

# **TECHNIQUE-BASED EXPLOITATION OF LOW GRAZING ANGLE SYNTHETIC APERTURE RADAR IMAGERY OF SHIP WAKES**

Graham J Orme

A dissertation submitted in partial fulfilment of the requirements for the degree of

Doctor of Philosophy

of

Electronic and Electrical Engineering

University College London

Supervisor

Prof Hugh Griffiths

Electronic and Electrical Engineering Dept

University College London

## Declaration

### **DECLARATION**

I, Graham J Orme, declare that the work conducted within this thesis is my own. Where previous accomplishment has been built upon, the source or sources are specifically referenced and acknowledged.

Signed

Graham J Orme

## **ABSTRACT**

The pursuit of the understanding of the effect a ship has on water is a field of study that is several hundreds of years old, accelerated during the years of the industrial revolution where the efficiency of a ship's engine and hull determined the utility of the burgeoning globally important sea lines of communication. The dawn of radar sensing and electronic computation have expanding this field of study still further where new ground is still being broken.

This thesis looks to address a niche area of synthetic aperture radar imagery of ship wakes, specifically the imaging geometry utilising a low grazing angle, where significant non-linear effects are often dominant in the environment. The nuances of the synthetic aperture radar processing techniques compounded with the low grazing angle geometry to produce unusual artefacts within the imagery. It is the understanding of these artefacts that is central to this thesis. A sub-aperture synthetic aperture radar technique is applied to real data alongside coarse modelling of a ship and its wake before finally developing a full hydrodynamic model for a ship's wake from first principles. The model is validated through comparison with previously developed work. The analysis shows that the resultant artefacts are a culmination of individual synthetic aperture radar anomalies and the reaction of the radar energy to the ambient sea surface and spike events.

### IMPACT STATEMENT

The main focus of the work in this thesis aims to examine the appearance of, until now unexplained, artefacts in synthetic aperture radar (SAR) imagery of the region in close proximity to moving ships and their associated wakes taken from low grazing angles. The problem lies under overlapping layers of specialist areas of interest that need to be combined in order to provide a satisfactory answer. It is the low grazing angle imaging geometry that makes the already complex combination of SAR imagery and sea clutter scattering particularly unique. The low grazing angle environment is more complex than higher angles as non-linear effects of sea clutter scattering begin to become dominant and higher grazing angle SAR imagery is much more abundant as a data source and is hence more widely studied and understood.

The nature of SAR imaging and its associated phenomena will be utilised particularly with regard to the azimuthal displacements of moving scatterers. A sub-aperture analysis, where an individual SAR image will be deconstructed chronologically, will be used to elicit a greater breadth of characterisation data from a full SAR image containing the artefacts. Fundamental principles of radar scattering from sea clutter will be invaluable to explain both ubiquitous artefacts within the SAR imagery of the sea surface and features within the target ship's wake. The generation of wakes by ships from the perspective of hydrodynamic modelling will be utilised as a foundation for a full SAR simulation of a target ship and its wake. The model output can then be readily compared to real imagery to confirm the modelling hypotheses.

Individual areas of novel work will benefit academically, which include the sub-aperture algorithm, the range-Doppler algorithm and the integrated point ship wake model. Data



## Impact Statement

found from the application of the sub-aperture technique from the reaction of sea clutter features will allow for improved analysis and modelling of sea clutter scatterers. The understanding of the phenomenon will benefit the understanding and modelling of the environmental impact of shipping on littoral waterways and perhaps the wider oceanographic field where SAR has been used for ship detection. In a similar way, there may be benefits to the defence industry where SAR and inverse-SAR (ISAR) are used for ship identification.

## **ACKNOWLEDGEMENTS**

This work could not have been conducted without the stalwart support and guidance of my supervisor, Hugh Griffiths, to whom I am very grateful for enabling me to conduct this study outside of a traditional university setting and in a field that is so close to my personal interest. I am also especially indebted to Keith Ward, Darren Muff, Bob Hill and David Blacknell for their years of critique and guidance, for continually challenging me and always being able to answer the questions I could not. My thanks also go to Claire Stevenson, Matthew Nottingham, Andy May and Paul Brennan for their helpful inputs and support. Thank you to the wider Igence Radar team whose modelling work specifically contributed to the validation section of this thesis. The specificity of this study could not have been accomplished without access to data and imagery owned by the UK Ministry of Defence and the support of its multiple subject matter experts. Finally, I am ever grateful for the support of my family who tolerate the many hours sacrificed in production of this work.

## CONTENTS

Technique-based exploitation of low grazing angle synthetic aperture radar imagery of ship wakes.....	1
Declaration.....	i
Abstract.....	ii
Impact Statement .....	iii
Acknowledgements.....	v
Contents .....	vi
List of Figures .....	xi
List of Tables .....	xxv
List of Symbols.....	xxvi
List of Abbreviations .....	xxx
1 Chapter 1 – Introduction.....	1
1.1 SAR Imaging of Ship Targets .....	1
1.2 Research Question.....	5
1.3 Novel Contributions .....	5
2 Chapter 2 – Research Context .....	7
2.1 Introduction .....	7
2.2 Background of SAR .....	7

## Contents

2.3	Stripmap SAR Geometry .....	14
2.4	Spotlight SAR Geometry .....	20
2.5	Ocean Remote Sensing.....	24
2.6	Geometric Focussing .....	26
2.7	Wake Models.....	31
2.8	Clutter Scattering.....	47
2.9	SAR Imaging Analysis Tools.....	55
2.10	Sub-Aperture Processing Methods.....	68
2.11	Summary .....	71
3	Chapter 3 – Sub-aperture Analysis .....	72
3.1	Introduction .....	72
3.2	Technique Description .....	72
3.3	Technique Application .....	74
	Image Intensity Variation.....	78
3.4	Target Return Variation .....	80
3.5	Sea Clutter Appearance.....	82
3.6	Wake Bloom Striations .....	85
3.7	Wake Bloom Location .....	87
3.8	Summary .....	89
4	Chapter 4 – Theoretical SAR Modelling.....	90
4.1	Introduction .....	90

## Contents

4.2	Problem Identification.....	90
4.3	Model Hypothesis .....	93
4.4	Target Vessel Displacement and Ambiguities .....	98
4.5	Wake Bloom.....	99
4.6	Orbital Velocity.....	106
4.7	White Water .....	110
4.8	Final Construction.....	112
4.9	Summary .....	113
5	Chapter 5 – Range Doppler Algorithm Modelling.....	114
5.1	Introduction .....	114
5.2	Algorithm Considerations .....	114
5.3	Model Details .....	115
5.4	Model Application.....	117
5.5	Model Output Analysis .....	122
5.6	Sub-Aperture Algorithm Validation.....	124
5.7	Sub-Image Intensity Variation .....	126
5.8	Summary .....	135
6	Chapter 6 – Hydrodynamic Modelling.....	137
6.1	Introduction .....	137
6.2	Point Source Model Derivation.....	137
6.3	Alternative Derivation.....	151

## Contents

6.4	Point Source Wake Model.....	161
6.5	Radar Scattering Model.....	163
6.6	Summary .....	165
7	Chapter 7 – Model Validation .....	167
7.1	Introduction .....	167
7.2	Thin Ship Model.....	167
7.3	Surface Pressure Ship Model .....	170
7.4	Integrated Point Ship Model .....	172
7.5	Summary .....	174
8	Chapter 8 – Final Analysis .....	175
8.1	Introduction .....	175
8.2	Wake Bloom Envelope.....	175
8.3	Wake Bloom Tail .....	178
8.4	Wake Bloom Skew .....	183
8.5	Wake Bloom Striations .....	191
8.6	Summary .....	194
9	Chapter 9 – Conclusions and Future Work .....	195
9.1	Introduction .....	195
9.2	Conclusions .....	195
9.3	Suggested Future Work.....	199
9.4	Summary .....	200

## Contents

10	References.....	202
----	-----------------	-----

## LIST OF FIGURES

Figure 1: Chip-out of full SAR image, taken in X-band, showing the artefact associated with the target ship and the general lack of traditional wake pattern that is to be explained in this study. The chip-out is roughly 2 km x 2 km square.....	2
Figure 2: Diagram showing the relationship between the antenna size and its beam pattern; the larger the antenna the finer the beamwidth. ....	8
Figure 3: Diagram showing the concept of the Doppler beam sharpening (DBS) technique where the received frequency of the radar return can be used to refine the scatterer bearing from the sensor.....	9
Figure 4: Diagram showing the conceptual result of coherent summation of radar returns on the synthetic beamwidth and hence the improved achievable resolution compared to the real radar. ....	10
Figure 5: Diagram showing the change of scene range through a simple collection geometry for a maximum synthetic aperture length for a swath of the scene centre point. Knowledge of the change in range through the collect is required in order to 'focus' the SAR imagery.....	11
Figure 6: Diagram showing the 3 main SAR imaging footprint techniques and how the real radar beam is steered to achieve each collect. ....	13
Figure 7: Diagram showing the general construction of the stripmap SAR geometry.....	15
Figure 8: Graphs showing the expected range variation of 3 scatterers within a SAR scene collected using the stripmap SAR geometry. The right-hand plot shows the expected hyperbolic relationship the scatterer ranges have with the time parameter $u$ of the collection. ....	17
Figure 9: Diagram showing the spotlight SAR geometry where the real radar beam in continually focussed on a single patch during the extended synthetic aperture. ....	21



## List of Figures

Figure 10: Diagram showing the use of the real radar boresight and cross-boresight isorange contours to determine suitable dimensions for the spotlight SAR collection.....	22
Figure 11: Diagram showing the range migration variation of 3 scatterers within a spotlight SAR scene. The scatterer data is centred around the scene centre, therefore scatterer number 1 is considered stationary and the others vary accordingly. ....	23
Figure 12: Graphs showing the non-hyperbolic range migration of the spotlight SAR geometry from the same scatterers as in Figure 8.....	23
Figure 13: Diagram showing the basic imaging geometry used to define the geometric focussing technique.....	27
Figure 14: Diagram describing the generic location and motion of the target scatterer at $(x_p, y_p)$ .....	28
Figure 15: Diagram showing the collection construction for the geometric focussing (GF) technique. In the ideal case the target, or targets, have velocity that is perpendicular to the synthetic aperture. ....	29
Figure 16: Diagram showing a comparison of a static target scatterer with a moving target within the GF construct.....	30
Figure 17: Chip-out of a SAR image taken using the GF technique. The sensor motion and imaging angle are indicated with the blue arrows. The ship is moving away from the sensor towards the bottom-left of the image. The chip-out is roughly 2 km x 2 km square.....	31
Figure 18: Diagram showing the locus of the points that contribute to the standing wave pattern around a moving ship.....	34
Figure 19: Diagram showing the locus of the points of the wave energy generated by a moving ship. The angle $\theta_{ACD}$ can be determined through the examination of the right angled triangle as drawn. ....	35

## List of Figures

Figure 20: Diagram showing the geometric construction used to determine the lines of constant phase within the Kelvin wake.....	36
Figure 21: Graph showing a plot of (2.50) and (2.51) with parameter $L_p = [1, 5]$ . ....	40
Figure 22: Kelvin wake plot showing lines of constant phase (Lamb, 1932). The pattern can be seen to be bounded by the limiting angle of $39^\circ$ .....	41
Figure 23: Plot of drag coefficient, $C_T$ , against Froude number, $F_r$ . The plot shows the solid line from Michell's integral as well as experimental results from Tuck et al. (2008). ....	43
Figure 24: Diagram showing the generic dimensions for the generation of a Rankine ovoid. The red line denotes the boundary of the ovoid where the flow is always tangential to the surface ( <a href="http://www-mdp.eng.cam.ac.uk">www-mdp.eng.cam.ac.uk</a> ). ....	44
Figure 25: Diagram showing the flow of fluid around the Rankine ovoid and the internal flow from source to sink. The red line denotes the boundary where the internal and external flows are separated ( <a href="http://www-mdp.eng.cam.ac.uk">www-mdp.eng.cam.ac.uk</a> ).....	44
Figure 26: Chip-out from full SAR image taken from the SEASAT system showing the narrow V-shaped wake behind a ship (Case et al., 1984).....	46
Figure 27: Chip-out from full image where fine wave patterns on the surface of the water can be seen to be formed through velocity bunching. The bright arcing and overlapping features are formed from the interaction of the outflow of the Columbia River (Alpers et al., 1981)..	48
Figure 28: Plots of amplitude against time for different polarisation (VV at top, HH at bottom) returns from a patch of Bragg scattering sea surface (Walker, 2001).....	51
Figure 29: Plots of amplitude against time for different polarisation (VV at top, HH at bottom) returns from a whitecap scatter event (Walker, 2001). ....	53
Figure 30: Plots of amplitude against time for different polarisation (VV at top, HH at bottom) returns from a burst scatter event (Walker, 2001).....	54

## List of Figures

Figure 31: Along track interferometric technique used by Lombardo et al. (2006) to separate a full antenna into multiple phase centres to elicit velocity information from a particular scatterer through the SAR imaging process.....	56
Figure 32: Plot showing the linear approximation of the quadratic phase history used by Moreira (1992) in the real-time SAR algorithm. ....	57
Figure 33: Sub-aperture image set, top row, showing a slight variation in returns from fields due to anisotropic scattering. The use, by Ferro-Famil et al. (2002), of the mean scattering parameter $\alpha$ and the entropy $H$ produce the bottom two rows of image data giving an analyst greater information with which to understand the nature of the scatterers within the scene...	58
Figure 34: Diagrams showing the construction of the simulated imaging geometry used by Zhang et al. (2010). The sub-aperture approach taken allows for many targets to be grouped into range rings to reduce the number of computations required in fast-time. ....	60
Figure 35: SAR sub-images of Chen and Wu (2009) showing the target response of two ships in close formation have in multiple polarisations.....	61
Figure 36: Subsequently processed images from Figure 35 with examples of the effect of processing techniques that Chen and Wu (2009) applied. Sub-image (d), the optical coherence product, is a compound of the other three techniques and results in a strong contrast between the two ships and the surrounding sea clutter. ....	62
Figure 37: Images processed by Greidanus (2006). The left images are simple processed 500 m x 500 m SAR image tiles of individual ships. The right images have been sub-aperture processed with different colours attributed to different polarisation combinations. The dual peak feature was of keen interest and attributed to wave motion. ....	63
Figure 38: Image chip-outs from Madsen (2010). The left column shows the initial image on the top row with its coherence image below where a decorrelation artefact can be seen in	

## List of Figures

both. The right column shows the corrected image and coherence map after processing by the aperture splitting technique.....	64
Figure 39: Plots of simulated point targets taken at high squint angles, Yeo et al. (2001). The left column images are processed using a standard step-transform whereas the right column is the same target processed using their high squint SAR algorithm. ....	65
Figure 40: Spigai et al. (2008) show the behaviour of targets with different characterisation properties having used a radar spectrogram technique to decompose the original full SAR image.....	66
Figure 41: Image comparison conducted by Zhang et al. (2010) where the real image on the left has been processed for speckle reduction using a four sub-aperture split technique to produce the image on the right.....	67
Figure 42: Flow diagram showing the stages used in the sub-aperture algorithm that is used to generate the multiple sub-images from the initial processed complex SAR image. ....	73
Figure 43: Chip-out from full X-band SAR image showing imaging geometry of sensor orientation and direction of motion with scale bars (axis markings denote 500 m). The blue triangle represents the orientation and direction of motion of the radar platform and the blue arrow represents the direction of the sensor boresight during the collection. ....	74
Figure 44: Annotated chip-out from full SAR image highlighting key areas of interest including the proposed target vessel returns, the artefact associated with the target vessel wake and a segment of the background sea clutter.....	75
Figure 45: Sub-image 1 of 7 from full SAR image. ....	75
Figure 46: Sub-image 2 of 7 from full SAR image. ....	76
Figure 47: Sub-image 3 of 7 from full SAR image. ....	76
Figure 48: Sub-image 4 of 7 from full SAR image. ....	77

## List of Figures

Figure 49: Sub-image 5 of 7 from full SAR image. ....	77
Figure 50: Sub-image 6 of 7 from full SAR image. ....	78
Figure 51: Sub-image 7 of 7 from full SAR image. ....	78
Figure 52: Side-by-side comparison of sub-images 1, 4 and 7 to illustrate the variation of overall image intensity through the sub-aperture set. It can be seen that the intensity peaks in the centre of the aperture and dims at either end. ....	80
Figure 53: Annotated chip-out from full SAR image highlighting the area around target vessel return that is to be examined in the next Figure.....	81
Figure 54: Side-by-side comparison of target vessel return location from beginning of the aperture to the end. The annotations shows the extent of the vessel return from bow to stern in each sub-image. Sub-image 1 was not used as the target vessel return was too weak compared to the background clutter to display satisfactorily. The comparison shows the bulk movement of the target vessel return through the aperture.....	81
Figure 55: Annotated sub-image 4 from the sub-aperture set highlighting the appearance of a fringe pattern within the background clutter and individual circled highlights of proposed sea spike returns. Note that the highlighted spikes are some of the many spikes observed within the image but not a complete plot of all spikes.....	83
Figure 56: Side-by-side comparison of chip-outs from 3 sub-images from the full sub-aperture set. The chip-outs are geographcially identical and show the consitent azimuthal location of the fringe pattern through the aperture. The internal structure of each fringe peak and trough can be seen to change through the aperture. The end sub-images 1 and 7 were not used as the background clutter is significantly dimmed compared to sub-images 2 and 6 so sub-images 2 and 6 make for an improved display.....	83

## List of Figures

Figure 57: Annotated chip-out from full SAR image highlighting the area of sea clutter containing spike returns that is to be examined in the next Figure.....	84
Figure 58: Unannotated and annotated chip-outs from 4 sub-images (2, 3, 4 and 5) highlighting the location of 3 spike returns. The relative distribution of the spike returns can be seen to vary azimuthally through the sub-aperture set. Each spike return can be seen to follow a similar pattern of intensity growth to a peak and then decay. It can be seen that each spike peaks at a different time within the aperture indicating that that is scatterer related rather than a pan-image property. ....	85
Figure 59: Annotated chip-out from full SAR image highlighting the area of proposed wake return that is to be examined in the next Figure.....	86
Figure 60: Annotated sub-image 4 showing the approximate location of repeating linear features that run azimuthally through the wake return. Note the annotations purposefully terminate to allow for clearer display of the striations underneath.....	87
Figure 61: Annotated chip-out from full SAR image highlighting the area of proposed wake return that is to be examined in the next Figure.....	88
Figure 62: Annotated chip-out from sub-images 1 and 5 showing the assessed centreline of each wake artefact. The centreline can be seen to move azimuthally through the sub-aperture set. The bulk movement of the artefact is smooth and consistent through all of the sub-images. ....	88
Figure 63: Chip-out from from full SAR image showing imaging geometry of sensor orientation and direction of motion with scale bars (axis markings denote 500 m). ....	90
Figure 64: Annotated chip-out from sub-aperture set highlighting the fringe pattern of bunched returns that runs through the entire image.....	92

## List of Figures

Figure 65: Annotated chip-out from full SAR image highlighting the locations of the apparent target vessel returns compared with the known true location of the vessel, and, the location of the proposed wake return.....	93
Figure 66: Diagram showing the imaging geometry of the geometric focussing (GF) technique.....	94
Figure 67: Diagram showing the relative azimuthal displacement of the primary target vessel return to the true location as a result of the SAR imaging process. ....	95
Figure 68: Plot showing the measured azimuthal displacements of a group of target vessels against the expected displacements predicted using the imaging geometries and (4.53).....	96
Figure 69: Diagram showing the superposition of the azimuthal ambiguities of the azimuthally displaced primary target vessel return that is a result of the SAR imaging process.....	97
Figure 70: Plot of moving target vessel using the GF technique to show the relative displacements of the primary target returns and the azimuthal ambiguities compared to the footprint of the real radar for range bracket 80 – 120 km.....	99
Figure 71: Chip-out from full SAR image showing the extent of the proposed wake artefact in relation to the true location of the target vessel. ....	100
Figure 72: Annotated photographic image taken from the stern of a merchant vessel (ferry) facing rearwards. The image contains wake structures of the Kelvin wake and the turbulent wake. The image shows breaking wave events associated with the cusp waves of the Kelvin wake and highlights the white-water associated with the turbulent wake. ....	105
Figure 73: Diagram showing the orbital motion of water particles within a surface wave field. ....	106

## List of Figures

Figure 74: Plot showing the superposition of the extremes of the wake bloom onto a plot of the azimuthally displaced primary return from the target vessel with its azimuthal ambiguities. The extremes of the bloom artefact are plotted from the maximum and minimum orbital velocities of the water particles from within the transverse Kelvin wake.	112
Figure 75: Flow diagram showing the stages of the range Doppler algorithm (RDA) written to generate a simulated SAR image from a user defined target array. ....	115
Figure 76: Diagram showing the collection geometry for the RDA algorithm and the determination of some of the terms used for the model.....	116
Figure 77: Plot of the RDA up-chirp linear frequency modulated pulse used for the processor. ....	117
Figure 78: Diagram showing the distribution of the target scatterer array locations and appended velocities. The placement and velocities are designed to simulate the ship and extremities of its wake bloom. ....	118
Figure 79: Plot of the interim output of the RDA showing the raw video phase history of the scene using the RDA. Prior to matched filtering, it can be seen that the information contained within the history of each of the scatterers occupy the same space in the time and frequency domains, which must be resolved in order to focus the image. ....	119
Figure 80: Plot of the interim output of the RDA showing the range compressed return from the scene. Even at this stage of the processing the smear artefact associated with the radial motion of the primary target vessel begins to appear as a non-vertical tilt to the plot. ....	119
Figure 81: Plot showing the azimuthal compression function for the scene. In this case, with the given geometry of the collection its can be seen that the azimuth chirp induced by the motion creates a down-chirp pattern in this pseudo-waveform. ....	120



## List of Figures

Figure 82: Plot of the interim output of the RDA following range migration correction of the scene.....	120
Figure 83: Plot of the final output of the RDA, a simulated SAR image of the target scene. The ambiguous returns from the target vessel can be seen azimuthally displaced, as expected, from the wake bloom region. The wake bloom azimuthal distribution can be seen to follow the predicted power law decay with target range from the target vessel. Imperfections within the processor have also allowed for the appearance of range and azimuth sidelobes around each of the scatterers.....	121
Figure 84: Zoomed section of basic plot of the immediate vicinity of the target vessel showing the ambiguous target returns and the extents of the wake bloom for ready comparison with Figure 83. ....	121
Figure 85: Image plot for comparison of 2 target vessel returns. The target return on the left of the image is moving at $10 \text{ ms}^{-1}$ whereas the target return on the right is stationary but otherwise identical. The comparison shows the increased defocus of the moving target and the reduced intensity of the return. ....	123
Figure 86: Image plot of sub-image 1 of 3. ....	125
Figure 87: Image plot of sub-image 2 of 3. ....	125
Figure 88: Image plot of sub-image 3 of 3. ....	126
Figure 89: Diagram showing the theoretical distribution of the amplitude of signal frequency from an azimuth slice of a generic SAR image. ....	127
Figure 90: Diagram showing the theoretical distribution of the amplitude of signal frequency from an azimuth slice of a generic SAR image that has been unweighted.....	128

## List of Figures

Figure 91: Diagram showing the distribution of window functions that can be used to sample the unweighted image spectrum to form a sub-aperture set. In this case there are 5 windows that have a 50% overlap. ....	128
Figure 92: Diagram showing the frequency-time relationship of the azimuthal match filter input used in a generic SAR processor to conduct azimuthal compression. Note that the non-linear extremes of the relationship are generally not used, only the central linear section. ..	129
Figure 93: Diagram showing the superposition of the expected frequency response from 2 azimuthally displaced static targets. ....	130
Figure 94: Diagram showing the azimuthally compressed returns for the 2 targets of Figure 93 using the matched filter signal of Figure 92. ....	130
Figure 95: Diagram showing the location and velocity characteristics of 5 target scatterers used to simulate the appearance of an azimuth slice from the wake bloom artefact. ....	132
Figure 96: Contour plot of the simulated SAR image output of the RDA of the target scene shown in Figure 95. The spread of the slice of the bloom can be seen and has been chosen to be of representative scale for the real bloom of Figure 71. ....	132
Figure 97: Sub-image azimuthal plot 1 of 4 from Figure 96. ....	133
Figure 98: Sub-image azimuthal plot 2 of 4 from Figure 96. ....	134
Figure 99: Sub-image azimuthal plot 3 of 4 from Figure 96. ....	134
Figure 100: Sub-image azimuthal plot 4 of 4 from Figure 96. ....	135
Figure 101: Surface plot of (6.256) for $t = 10$ s. The plot shows the propagating wave pattern away from the points source at the $x,y$ plane origin.....	161
Figure 102: Diagram showing the geometry of the polar integration for composing the ship wake. ....	162

## List of Figures

Figure 103: Surface plot of (6.259). The point target is moving as per the previous modelling as a velocity of $7.72 \text{ ms}^{-1}$ . The plot demonstrates the development of the wave field of the point target into the Kelvin wake where the cusp waves and the tranverse wake can be seen. ....	163
Figure 104: Image plot of (6.259). The point target is moving as per parameters in Table 2. The Kelvin wake cusp waves and the tranverse wake can be seen bounded by the angle of $39^\circ$ .....	163
Figure 105: Contour plot of the simulated SAR image generated from the Kelvin wake input of Figure 104.....	165
Figure 106: Contour plot of $k$ -space spectrum of (7.264). The characterisitc ‘hour-glass’ shape can be seen that is common for the Kelvin wake. ....	169
Figure 107: Image plot of (7.264) showing the Kelvin wake generated by a Rankine ovoid source using Michell’s thin-ship methodology.....	169
Figure 108: Contour plot of the simulated SAR image generated from the Kelvin wake input of Figure 107.....	170
Figure 109: Contour plot of $k$ -space spectrum of (7.265). The characterisitc ‘hour-glass’ shape can be seen as in Figure 106. ....	171
Figure 110: Image plot of (7.265) showing the Kelvin wake generated by a pressure distribution source using Munk et al.’s methodology.....	171
Figure 111: Contour plot of the simulated SAR image generated from the Kelvin wake input of Figure 110.....	172
Figure 112: Contour plot of the $k$ -space spectrum of (6.259). The characterisitc ‘hour-glass’ shape is visible but somewhat distorted.....	173

## List of Figures

Figure 113: Image plot of (6.259) showing the Kelvin wake generated by a point source following the methodology developed in Chapter 6.....	173
Figure 114: Contour plot of the simulated SAR image generated from the Kelvin wake input of Figure 113.....	174
Figure 115: Log-log plot of the simulated SAR image bloom azimuthal extents with range for the thin-ship model (7.264). The vertical and horizontal error bars have been derived from the accuracies of the measurement process.....	176
Figure 116: Log plot of the simulated SAR image bloom azimuthal extents with range for the pressure distribution model (7.265). The vertical and horizontal error bars have been derived from the accuracies of the measurement process.....	177
Figure 117: Log plot of the simulated SAR image bloom azimuthal extents with range for the point ship model developed here (6.259). The vertical and horizontal error bars have been derived from the accuracies of the measurement process.....	177
Figure 118: Contour plot of the gradient of the surface of the wake behind a ship.....	179
Figure 119: Reduced contour plot of the gradient of the surface of the wake behind a ship. The reduced number of contours illustrates the likely areas in the Kelvin wake field where waves will most consistently and predictably break. In this case the contours show the regions bounded by wave steepness that is greater than 0.05 or less than -0.05. ....	181
Figure 120: Plot of wake amplitude wavenumber product, i.e. wave steepness, variation with target aft range showing the power law decay directly along the centreline of the target vessel's transverse wake. The breaking wave threshold of Melief et al. (2006) of 0.38 would suggest waves would break in the closest 150 m to the target vessel.....	182
Figure 121: Chip-out from full SAR image annotated to show the assessed likely area of rough water within the wake bloom.....	182

## List of Figures

Figure 122: Diagram showing the variation of the impact of shadowing with differing grazing angles. ....	185
Figure 123: Diagram showing the likely impact of shadowing on the extremes of the wake bloom. ....	186
Figure 124: Plot showing the wave amplitude of the transverse waves within the Kelvin wake against aft range from the target vessel. The plot is taken along the centreline of the wake. ....	186
Figure 125: Plot of wave gradient in the along-target-track direction against aft range. The plot is taken along the centreline of the wake. The horizontal threshold at -0.058 shows where the steepness of the wake breaches the criterion for shadowing being present. ....	187
Figure 126: Diagram showing the situations of shadowing where the Doppler spectrum of the wave can be seen to be bounded due to the proportion of the wave phase that is observable by the sensor. ....	188
Figure 127: Diagram showing the sense of the impact of the shadowing of the waves on the bloom artefact with relation to the imaging geometry. ....	189
Figure 128: Plot of wave amplitude against aft range taken from the transverse waves along the centreline of the wake. The line of best fit has been derived from the power law decay assessments in Figure 115, Figure 116 and Figure 117. ....	190
Figure 129: Chip-out of full SAR image annotated to show the zoomed areas for Figure 130. ....	191
Figure 130: Side-by-side comparison of areas within the wake bloom showing elongated and short azimuthal striation structure. The area of the wake bloom nearest the target vessel also shows a diffuse haze return. ....	192

**LIST OF TABLES**

Table 1: Basic initial sensor parameters .....	98
Table 2: RDA collection scene and radar parameters.....	116
Table 3: Simulation parameters including developed target dimensions. ....	168

## List of Symbols

### LIST OF SYMBOLS

$c, e, g, i, \pi$	Universal constants
$r, \theta, z, t$	Cylindrical polar coordinates
$r_s, \theta_s, z_s, t$	Ship reference frame cylindrical polar coordinates
$x, y, z, t$	Cartesian coordinates
$x_p, y_p, z_p$	Spatial coordinate of a given point
$a$	Exponential identity parameter
$A$	Amplitude
$A_o$	Amplitude origin / datum
$a_x, a_y, a_z$	Acceleration components
$a( \quad )$	Hydrodynamic and stationary phase function term
$A( \quad )$	Transfer function term
$\alpha$	Integration and stationary phase parameter
$b( \quad )$	Hydrodynamic and stationary phase function term
$\beta_k$	Spatial frequency bandwidth
$c_g$	Wave group velocity
$c_p$	Wave phase velocity
$D_A$	Real aperture dimension

## List of Symbols

$\delta_{az}$	Azimuthal resolution
$\delta_r$	Range resolution
$\delta r$	Delta function with respect to radial coordinate
$\Delta_B$	Bessel differential operator
$\varepsilon$	Stationary phase small valued constant
$\eta$	Surface elevation
$\eta_{Re}$	Real value of surface elevation
$F_r$	Froude number
$f_s$	Radar pulse repetition frequency (PRF)
$\mathcal{F}_x\{ \}$	Fourier transform with respect to $x$
$\mathcal{F}_x^{-1}\{ \}$	Inverse Fourier transform with respect to $x$
$f(x, y) \text{ vs } F(k_x, k_y)$	Source function and Fourier transform pair
$f( \ )$	Hydrodynamic and stationary phase function term
$h_z$	Height of sensor along $z$ axis
$H( \ )$	Transfer function term
$\mathcal{H}_r\{ \}$	Hankel transform
$\mathcal{H}_r^{-1}\{ \}$	Inverse Hankel transform
$\theta_b$	Beamwidth



## List of Symbols

$\theta_{inc}$	Angle of incidence
$\theta_x$	Specified angle dimension variable
$J_o( \ )$	Bessel function of the first order of the first kind
$k$	Spatial frequency
$\lambda$	Wavelength
$L_s$	Ship length dimension
$L_x$	Specified length dimension variable
$\underline{n}$	Surface normal vector
$\underline{\hat{r}}$	Unit radial vector
$p$	Integration and stationary phase parameter
$p_0$	Integration and stationary phase parameter
$P$	Pressure
$P_o$	Pressure origin / datum
$P( \ )$	Transfer function term
$q$	Integration and stationary phase parameter
$R$	Range
$R_o$	Range – a given origin / datum
$\mathcal{Re}\{ \ }$	Real value operator

## List of Symbols

$\rho$	Density
$s$	Integration and stationary phase parameter
$S(\ )$	Transfer function term
$\sigma_{rel}$	Relative radar cross section
$T$	Period
$T_{SAR}$	Time taken to form a given synthetic aperture
$\tau$	Integration and stationary phase parameter
$\tau_0$	Integration and stationary phase parameter
$u$	Sub-aperture parameter
$\underline{v}$	Generic velocity
$v_x, v_y, v_z$	Velocity components
$v_{orb}$	Wave particle orbital velocity
$v_{rdr}$	Radar velocity
$v_s$	Ship velocity
$v_{tgt}$	Target velocity
$\Delta x_v$	Image displacement due to velocity
$\Delta x_s$	Image displacement due to PRF
$\varphi$	Velocity potential

## List of Symbols

$\varphi(r, z, t)$ <i>vs</i> $\Phi(k, z, t)$	Potential function and Hankel transform pair
$\psi$	Phase
$\omega$	Angular frequency

**LIST OF ABBREVIATIONS**

AIS	automatic identification system
BBC	bottom boundary condition
CAT	computer aided tomography
CCD	coherent change detection
CFAR	constant false alarm rate
CSA	chirp scaling algorithm
DBC	dynamic boundary condition
DBS	Doppler beam sharpening
DI	dynamic imaging
DMR	dual mode radar
FFT	fast Fourier transform
FMCW	frequency modulated continuous wave
GF	geometric focussing
GIF	graphical interchange format
GMTI	ground moving target indication/indicator
GPS	global positioning system
HF	high frequency
IFFT	inverse fast Fourier transform

## List of Abbreviations

ISAR	inverse synthetic aperture radar
KBC	kinematic boundary condition
LFM	linear frequency modulation
MTI	moving target indication/indicator
NITF	NATO Standard Image Transmission Format
$P_d$	probability of detection
PFA	polar format algorithm
PRF	pulse repetition frequency
PSF	point spread function
RCS	radar cross section
RDA	range Doppler algorithm
RMA	range migration algorithm
RVP	residual video phase
SAR	synthetic aperture radar
SNR	signal to noise ratio
TBP	tomographic back projection
TDA	time domain algorithm
VHF	very high frequency
UHF	ultra-high frequency

## List of Abbreviations

## **1 CHAPTER 1 – INTRODUCTION**

### **1.1 SAR Imaging of Ship Targets**

Synthetic aperture radar (SAR) is a radar imaging technique that has evolved over the past 70 years in order to provide the radar operator with high-resolution imagery capable of covering wide areas of target area either day or night and through most weathers. Many systems have been developed, both space-based and fitted to aircraft, to be able to provide such imagery that use a variety of computational algorithms to process the radar returns. Due to the desirable capabilities of SAR, it has been successfully used for many applications both civilian and military. One of the main benefits of SAR as a sensor is that the mechanisms of the radar signal scattering can be quite intricate and responsive to the composition and behaviour of the target. As such, a significant amount of target information can be gleaned by the radar and analysed by the operator. Therefore, a proper understanding of the phenomenology is essential to maximise the extraction of target information from SAR imagery. This thesis considers the imaging of ship targets and their wakes collected at comparatively low grazing angles with respect to the sea surface and at comparatively low radar velocities. This combination of parameters has the effect of exaggerating some of the traditional SAR phenomena as well as introducing some non-linear features as a result of the sea clutter that becomes dominant at such angles.

This introduction is provided as a road map to summarise the intent and content of each of the following chapters of this thesis in order to guide the reader through its structure. The core of this thesis was borne from a specific artefact found in imagery taken of moving ship targets whilst attempting to develop a technique to subtly improve the apparent resolution of standard processed SAR imagery. The artefact, more appropriately a presentation of several artefacts, was somewhat unexpected but was consistent across many collections. These

collections included varying imaging geometries, scene environmental conditions and target vessels. It was quickly found that the artefact had not been explained before in literature and was almost entirely not present in any other published imagery. Figure 1 shows the general presentation of the artefact that was found in a low grazing angle X-band SAR image. Key areas to note are the general lack of standard ship wake patterns common in other imagery and the presence of an intense azimuthally distorted bloom near the primary return from the target vessel. In the context of this image, the azimuth dimension runs vertically through the image. The understanding and explanation of this phenomenon became the principal objective of this thesis.

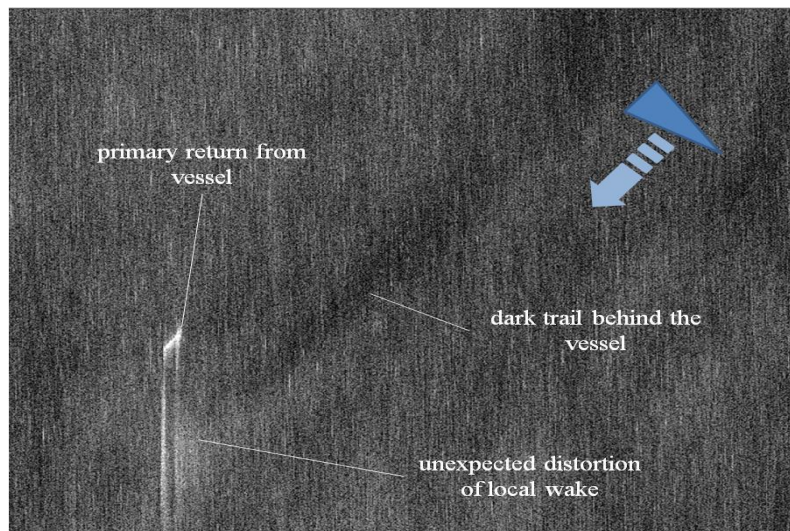


Figure 1: Chip-out of full SAR image, taken in X-band, showing the artefact associated with the target ship and the general lack of traditional wake pattern that is to be explained in this study. The chip-out is roughly 2 km x 2 km square.

Such an objective is suitable for specific study as it will add a small but relevant piece of knowledge to an area of SAR research that is less thoroughly understood than most. The use of SAR as a sensor in the maritime environment is not particularly common and is most rare when the sensor is low to the surface producing a low grazing angle image and when the sensor is not travelling particularly fast compared to the moving target. This combination of



parameters exacerbates the natural distortions that are a side-effect of the SAR imaging process and the low grazing angle image means that the sea clutter presents its most non-linear features to the radar for sampling. This makes this artefact a potent combination and somewhat special. Much of the thesis itself is concerned with the analysis and understanding of SAR and the interaction of SAR with the given environment. The publication of the process of understanding should also lend itself to assisting future researchers and operators in their own development in the field.

The method that will be applied in the thesis has several phases. Firstly, as much information shall be gleaned from the original image artefacts as possible. In order to achieve this, a sub-aperture SAR technique will be developed to deconstruct the fully processed SAR image and examine hidden detail within the image spectra. Following this, a staged modelling process will occur that gradually increases in complexity. At each stage, the validity of the modelling and the appearance of the artefact components will be demonstrated and analysed. A fully functional, dedicated SAR algorithm will be developed to demonstrate initial theoretical predictions from the basic modelling. Then an in-depth model for the image scene will be derived from the first principles of hydrodynamics and validated against extant wake models. This will then provide a significant body of evidence and understanding that will be used to analyse the artefact and draw conclusions.

This thesis content will start with Chapter 2 that lays the foundation for the context of the novel elements of this thesis through review of some of the key and broader areas of study that have already been established by previous work. This chapter will begin with an explanation of the root of the specific area of study from work already completed in preparation for the transfer thesis prior to the submission of this dissertation. This will show where the wake artefact originated. Then the literature of other authors' work that relates to

the field of study including generic ship wakes, sea clutter and scattering, SAR imaging analysis tool theory and functional approaches taken to implementation.

Chapter 3 marks the beginning of the novel contributions of this study. It begins with the application of the sub-aperture analysis techniques that were recommended on completion of the transfer thesis as a suitable mechanism to deconstruct the SAR image containing the wake artefact. The algorithm designed and method of implementation are described in detail and the results are analysed. The analysis provides some immediate answers, however, several features attributed to the target vessel return, the wake and the generic sea clutter provide questions that require further thought. In order to answer some of these, Chapter 4 looks at the development of a basic imaging and scene model that can be used to understand the presentation of the features of both the full SAR image, of the ship and its wake, and the sub-aperture images. The basic model looks at an explanation through the combination of the known SAR image phenomena of azimuthal displacement of moving scatterers and ambiguous returns. At the basic model level, the detailed consideration of sea clutter scattering is ignored until subsequent chapters. The chapter shows that the combination of the basic tenets of SAR imaging can be combined to produce a predicted image construct that satisfactorily mirrors the real SAR image.

In order to test the basic model prediction in more detail and to greater rigour, a SAR imaging algorithm is written so that a test scene can be generated to validate the output. For this, the range Doppler algorithm (RDA) is used as a structure, chosen for its clarity and pedigree as a SAR processing algorithm. This RDA model is used first look at validating the prediction of the basic model then used to investigate specific characteristics identified through the sub-aperture analysis.

To further develop the complexity and relevance of the modelling to more accurately examine the wake artefact a hydrodynamic model is derived from first principles in Chapter 6. The initial model looks at modelling the impact to the surface elevation of water from a point source. The point source model is then used to generate a wake by moving the point and integrating the impact over the time. The output is satisfactorily shown to produce a classic Kelvin wake form. In order to validate this detailed model, the output is compared to two established wake models from other authors in Chapter 7. The comparison is made through both assessment of surface elevation and through the implementation of a radar scattering model to the surface elevation. A good comparison is made that shows the model developed in Chapter 6 holds sufficient weight to provide a new approach for final analysis of the image data. Of note, some interesting differences between previous models and new are noted that lead to useful topics for consideration in future work.

The thesis culminates in Chapter 8 where the bulk of data analysis is conducted. Outputs from the sub-aperture analysis, the basic model, RDA model and modelling from first principles are all drawn upon to examine the many characteristics of the wake artefact and the appearance of the sea clutter. Conclusions and suggested routes for future study are summarised in the final Chapter 9.

### **1.2 Research Question**

The explicit aim of this thesis is to understand and explain the origin and mechanism that creates the wake artefacts that occur in SAR imagery of a moving ship taken from a low grazing angle as shown in Figure 1.

### **1.3 Novel Contributions**

The following are claimed to be the novel contributions of this thesis:

## Chapter 1 – Introduction

- A sub-aperture SAR processing application, based on the Python language, that allows SAR analysts to gain understanding of moving targets within a complex SAR image has been developed.
- The compound near-field artefacts from a moving ship target are constructed from extant SAR theory.
- A SAR processor, based on the range Doppler algorithm, has been developed to include a raw fast-time receive signal to accurately model SAR phenomena.
- A SAR image simulator of a ship wake is developed through use of a full hydrodynamic model from first principles.
- Finally, through use of the application of SAR theory to hydrodynamic modelling of the near field wake of a ship, an understanding of the origin of the wake artefact is developed.

## **2 CHAPTER 2 – RESEARCH CONTEXT**

### **2.1 Introduction**

This chapter will lay the foundation for the main body of the thesis by describing the origin of the problem that is to be solved and then by reviewing previous work by other researchers. The previous work will focus on several fields of study that will be needed to complete the analysis of the ship and wake artefact including the development of modelling of ship wakes, the scattering of generic radar waveforms from sea clutter and then the application of sub-aperture SAR techniques from a theoretical and practical perspective. Awareness of these overlapping fields will provide background knowledge and context as to where this thesis sits.

### **2.2 Background of SAR**

Synthetic aperture radar (SAR) is a term used to describe a host of advanced radar equipment and signal processing techniques that have been developed throughout roughly the last 70 years. The primary aim of the field of study has been to enhance the azimuthal resolution of a radar system beyond the conventional diffraction limits of a physical antenna aperture. The result, through the multitude of means developed, is now the production of near-photographic quality radar imagery of a target scene that can be taken from a variety of platforms over very large areas through most weather during the day or night. This has led the field to be of great benefit to scientific, commercial and military communities. Knowledge of the history of SAR is important to understanding the phenomenology of the imagery because it has been through the progression of the field that challenges have been met and overcome with improvements of hardware and processing techniques. Each method has brought with it its own character that is contained within the images produced. It is through the understanding of these characters that greater value can be brought to the final product.

## Chapter 2 – Research Context

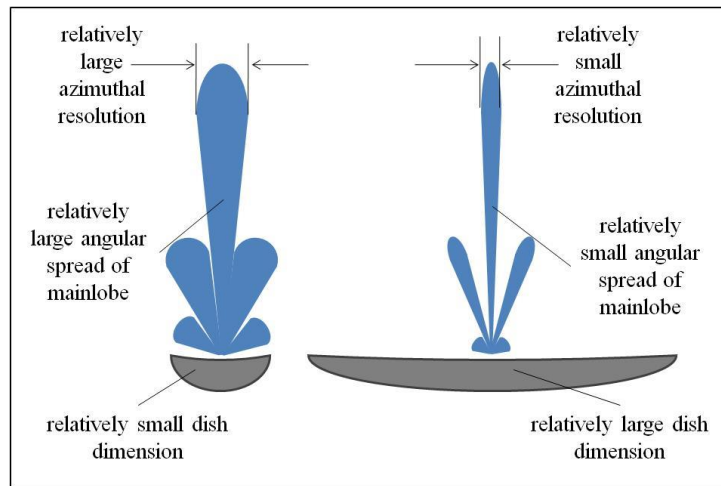


Figure 2: Diagram showing the relationship between the antenna size and its beam pattern; the larger the antenna the finer the beamwidth.

Many, including Sherwin et al. (1962), attribute the origin of SAR to be traced to the early 1950s where Wiley, working for the Goodyear Aircraft Corporation, first developed the theory of Doppler beam sharpening (DBS). The DBS techniques aimed at using the Doppler signature of ground scatterers within a side-looking radar beam to enhance the aperture limited azimuthal resolution. Conventional azimuthal resolution is determined by the beamwidth of the radar in use. The beamwidth is classically determined by the physical size of the aperture of the radar and the wavelength of the emitted energy, as shown in Figure 2. Particularly with airborne radars there are physical constraints to the size of antennas that can be used, which has a knock-on limitation to the achievable resolution. DBS initially aimed at filtering the received signals from the side-looking beam by Doppler frequency. The theory being that if the near zero-Doppler fraction of the beam could be isolated then the effective azimuthal resolution of the beam could be significantly improved. The compromise however was that due to the filtering there was a reduction in power received and therefore reduced sensitivity. The DBS technique was demonstrated by a group from the University of Illinois in 1953 using an airborne X-band radar, described by Brown et al. (1969). Wiley (1985)

## Chapter 2 – Research Context

swiftly developed the DBS technique in order to counter the reduced sensitivity by coherent summation of the returns within the radar beam, which produced the first form of what was then called ‘unfocussed’ radar. The DBS technique is illustrated in Figure 3.

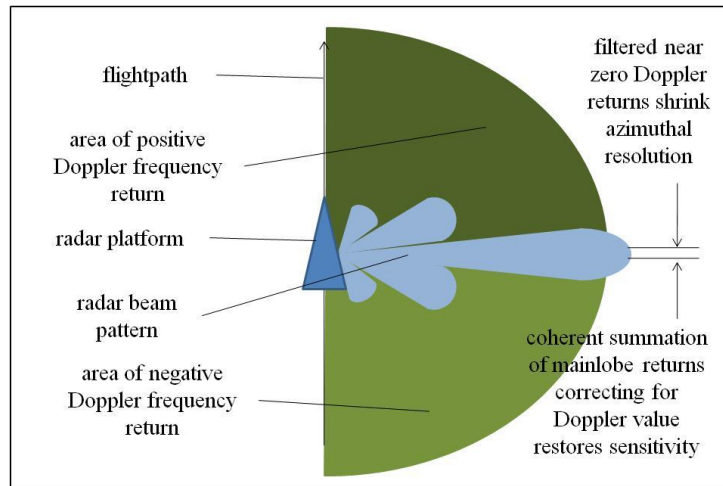


Figure 3: Diagram showing the concept of the Doppler beam sharpening (DBS) technique where the received frequency of the radar return can be used to refine the scatterer bearing from the sensor.

Independently, similar processing techniques were being developed by Cutrona et al. (1960) of the University of Michigan and Sherwin of the University of Illinois. Their approaches were termed spatially-induced SAR and were the first to be labelled as SAR due to the notion of the construction of a single large array through the summation of spatially and temporally separated pulses, as shown in Figure 4. The essential element of SAR processing was to enable the azimuthal compression of the signal by matched-filtering the phase history of the sequential received pulses from across the synthetic aperture, thereby improving the azimuthal resolution to the order of the range resolution.

## Chapter 2 – Research Context

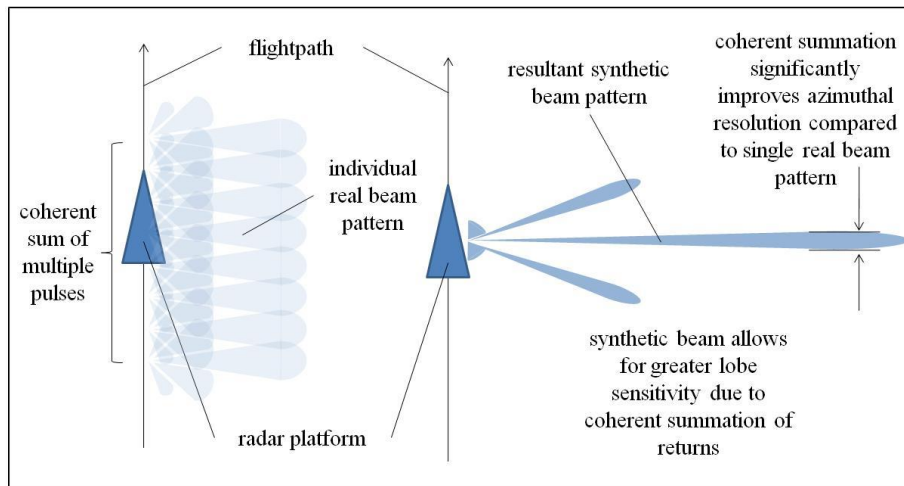


Figure 4: Diagram showing the conceptual result of coherent summation of radar returns on the synthetic beamwidth and hence the improved achievable resolution compared to the real radar.

Cutrona developed the first optical SAR processor in 1957, which paved the way for the primary means of processing until the end of the 1960s (Cutrona et al., 1966). Optical processing used a construction of lenses to decode the information for recording onto photographic film, which was the preferred method due to the high data rate and bandwidth required by the system that could not be conducted by digital processing means at the time.

As the DBS technique relied on the compression of an arbitrary scatterer's Doppler signature from across a radar beam to a focussed point it suffered from a phenomenon called range migration. Range migration is the result of a point scatterer transiting through multiple range bins during the imaging process, as shown in Figure 5 and described by Brown et al. (1969). This would be especially noticeable for fine range resolutions and for large cross-range scene collects. The problem with the technique was that there was no correction included for the curvature of the radar wavefronts. Consequently, a phase correction has to be included in the processing that would effectively bend the path of the sensor to maintain constant separation between the collection aperture and the scene centre (Luttrell and Oliver, 1986). Within the framework of the optical processor, the range migration could be mitigated by the inclusion



## Chapter 2 – Research Context

of a conical lens, as shown by Cutrona et al. (1966). By taking range migration into account, SAR was considered ‘focussed’ and could theoretically achieve azimuthal resolutions of the order of half the real aperture of the radar system. This development was an improvement in system performance by an order of magnitude and produced resolutions of a similar value to the range achievable range resolutions of the systems of the day, shown by Brown (1967).

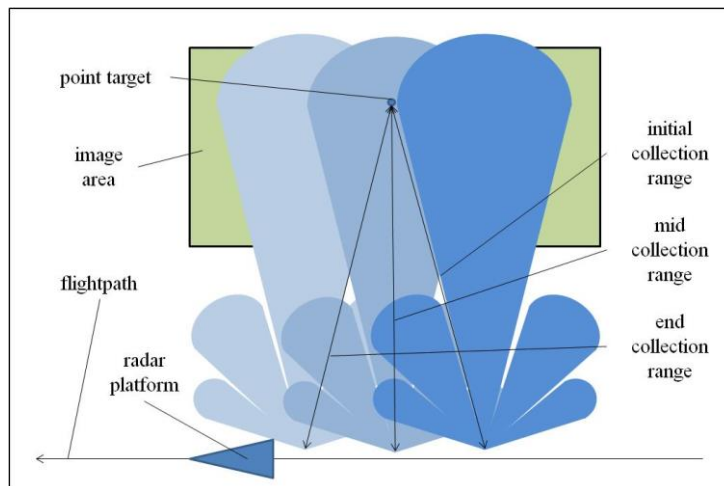


Figure 5: Diagram showing the change of scene range through a simple collection geometry for a maximum synthetic aperture length for a swath of the scene centre point. Knowledge of the change in range through the collect is required in order to ‘focus’ the SAR imagery.

During the 1970s, there were sufficient improvements in digital computation to enable SAR processing to be conducted by non-optical means. This was of great interest particularly to the military for the improvements in system architecture and potential future capabilities. The first fully digital system was developed by Kirk (1975), which also incorporated an early form of digital motion compensation. The digital age of SAR created new avenues for development and led to the dominance of the Fourier synthesis view of the SAR process and evolved a consistent signal processing framework. The first orbital SAR sensor was an experimental system call QUILL that was flown as a proof of concept mission in 1964. In 1978, the first mainstream orbital SAR was launched on the SEASAT-1 satellite. Barber

## Chapter 2 – Research Context

(1983) explains that orbital SAR involved greater challenges due to the increase in range migration, satellite motion compensation, orbital eccentricity and atmospheric effects from both the troposphere and the ionosphere. Developments also brought ‘range walk’ into consideration, which is the phenomenon where the scatterer apparently transits through the scene during the collect. It is the linear variation in target scatterer range through the aperture as a result of the relative motion of the radar and the scene footprint. This is exacerbated where collection dimensions are large. Such problems, combined with the advent of new digital resources, led to the development of new SAR processing algorithms. The first family of these were termed range-Doppler algorithms (RDA) and were first developed by Wu of the NASA Jet Propulsion Laboratory in 1976 (Wu, 1978). These incorporated second order terms of the range variation and opened the possibilities for off-broadside squinted SAR, scanning DBS and spotlight SAR, as shown in Figure 6. The spotlight mode of SAR, where the beam is steered onto a target during the collect, was first devised by Walker (1980) while working with Brown on imaging rotating objects and objects traversing a static radar site. This method limits the scene dimensions to that of the real radar beam but allows for greater azimuthal resolution as the Doppler bandwidth of the received pulses from scatterers is greater than for the side-looking stripmap mode due to the increased azimuthal angle through which the collect is taken. The difference of the frequency collect from stripmap mode was that the spotlight SAR collect could be stored as pulses in a polar format in order to simplify subsequent processing. The resultant focussing algorithm, the polar format algorithm (PFA), used the scene centre response as a reference with which to apply correction to the entire image in a neat process. The minor problem was that scatterers that do not have the same polar format phase histories as the reference signal experience defocusing, which is true for scatterers away from the scene centre.

## Chapter 2 – Research Context

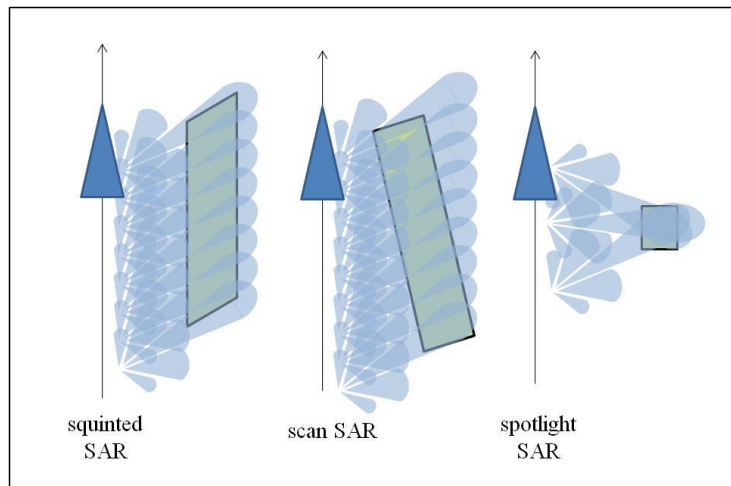


Figure 6: Diagram showing the 3 main SAR imaging footprint techniques and how the real radar beam is steered to achieve each collect.

Further improvement in computational capabilities since the 1990s has allowed the development and use of more complex algorithms that have been designed to remove certain approximations and assumptions within the SAR process in order to improve the output imagery (Clemente and Soraghan, 2010). The first of these was developed by Rocca et al. in 1988 from inclusion of a field of study of seismic waves (Rocca, 1989). With strong emphasis on multi-dimensional Fourier signal processing, their method applied a phase correction to each pulse and applied a Stolt interpolation to correct for curvature of the radar wavefronts, which has been the foundation for much work on resolution including the likes of Carrara et al. (1995) and Jakowatz et al. (1995). Amongst other labels, this algorithm has been called the wavenumber algorithm or range-migration algorithm (RMA). Although there was a resultant improvement in image quality there were new limitations that included the necessity for greater motion compensation as the phase correction effectively straightened the line of collect and increased computational memory was required to cope with the higher frequency and up-sampling of the signal. The process of deramp-on-receive was developed to reduce the bandwidth of the required digitisation on the receive channel. Carrara et al.

(1995) show that this involves mixing of a raw copy of the output pulse with the received signal to strip out relevant information for processing. Although computationally beneficial there was a resultant induced error termed residual video phase (RVP), which causes artefacts within the imagery most notable at high squint where the range from the scene centre or stabilisation point is greatest, Oliver (1991) who produced considerable work on the understanding of SAR imagery artefacts.

Standard RMA has had several evolutions. Following the 1992 International Geoscience and Remote Sensing Symposium (IGARSS), an improvement to the RMA was proposed in 1994 termed the chirp scaling algorithm (CSA) (Raney et al., 1994). The CSA removed the need to use interpolation by storing the output pulse in chirp form rather than the deramped version. Similar to the earlier RDAs, the CSA does not correct for high range-rate terms and therefore limits the maximum scene size. The second main evolution that occurred early in the 21<sup>st</sup> century has been tomographic back projection (TBP), which was based on signal processing used in computer aided tomography (CAT) (Reigber et al., 2007). This technique corrects for the curvature of the wavefronts and builds the imagery in a layered approach by coherent combination of subsequent information with an original scene. Finally, the time domain algorithm (TDA) has been proposed. It is designed to fully correct for each pixel within the image for the collection process and is therefore highly computationally dependent. Regardless of the technological burden the TDA should produce imagery that only contains artefacts that result from broken assumptions or SAR theory rather than a combination of processing and principal artefacts (Guerrierio et al., 2005).

### **2.3 Stripmap SAR Geometry**

It would be thorough to consider all forms of SAR but due to its low level of use in modern SAR systems the detail concerning Doppler beam sharpening (DBS), as first devised by

Wiley in the 1950s, will be omitted in favour of the two more prevalent developments. The first construction for consideration is the stripmap geometry. In the stripmap model the SAR platform moves along a line arbitrarily parallel with the  $x$  axis in the  $x$ - $z$  plane at speed  $v$  at height,  $h_z$ , in the  $z$  axis direction above the image, the  $x$ - $y$ , plane. The real radar beam is projected sideways from the platform at the scene area that is to be imaged and is maintained at a fixed squint angle in relation to the platform's flightpath and at a fixed grazing angle in relation to the image plane. In this configuration the real radar beam is swept across the scene area in a swath as the platform transits along its flightpath. As the platform transits the length of the synthetic aperture,  $D_{SAR}$ , it will pulse its real radar at interval distances,  $u$ , along the aperture. It is assumed that the stop-start approximation is valid as the pulse length is much shorter than the parametric interval of  $u$ , which can be used as an indicative gauge of the validity of the stop-start approximation when comparing standard SAR geometries for given platform velocities (Skolnik, 1980). Figure 7 illustrates the stripmap SAR geometry.

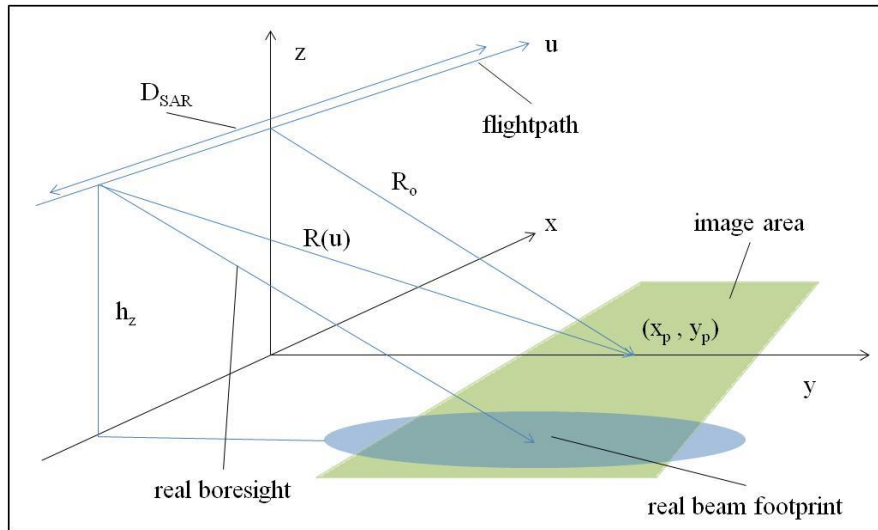


Figure 7: Diagram showing the general construction of the stripmap SAR geometry.

## Chapter 2 – Research Context

In order to determine the azimuthal resolution, it is necessary to consider the response of a point scatterer within the stripmap model. Therefore, for a point scatterer located on the image plane at  $(x_p, y_p)$  the range from the platform is  $R$  and can be considered a function of the parameter  $u$ :

$$R(u) = \sqrt{(u - x_p)^2 + y_p^2 + h_z^2} \quad (2.1)$$

If  $R_o$  is taken to be the range at closest point of approach of the point scatterer to the flightpath:

$$R(u) = \sqrt{(u - x_p)^2 + R_o^2} \quad (2.2)$$

Rearranging shows that the path of the point scatterer through the imaged scene, from the reference frame of the platform, is hyperbolic:

$$R(u) = R_o \sqrt{1 + \frac{(u - x_p)^2}{R_o^2}} \quad (2.3)$$

Using the binomial expansion for the square root segment of (2.3):

$$\sqrt{1 + x} \approx 1 + \frac{1}{2}x - \frac{1}{8}x^2 + \dots \quad (2.4)$$

Assuming that the scene dimensions are much smaller than the range of the swath,  $R_o \gg (u - x_p)$ , terms with greater than quadratic powers can be discarded:

$$R(u) \approx R_o \left\{ 1 + \frac{1}{2} \frac{(u - x_p)^2}{R_o^2} \right\} \quad (2.5)$$

$$R(u) = R_o + \frac{1}{2} \frac{(u - x_p)^2}{R_o} \quad (2.6)$$

Expanding:

$$(u - x_p)^2 = u^2 + x_p^2 - 2ux_p \quad (2.7)$$

and substituting (2.7) into (2.6):

$$R(u) = R_o + \frac{x_p^2}{2R_o} + \frac{u^2}{2R_o} - \frac{ux_p}{R_o} \quad (2.8)$$

From this second order approximation (2.8) of the hyperbolic range function (2.3) the decomposition of the range migration, which is the deviation of the range of the point scatterer from  $R_o$ , can be seen. This is illustrated in Figure 8 for 3 different point targets.

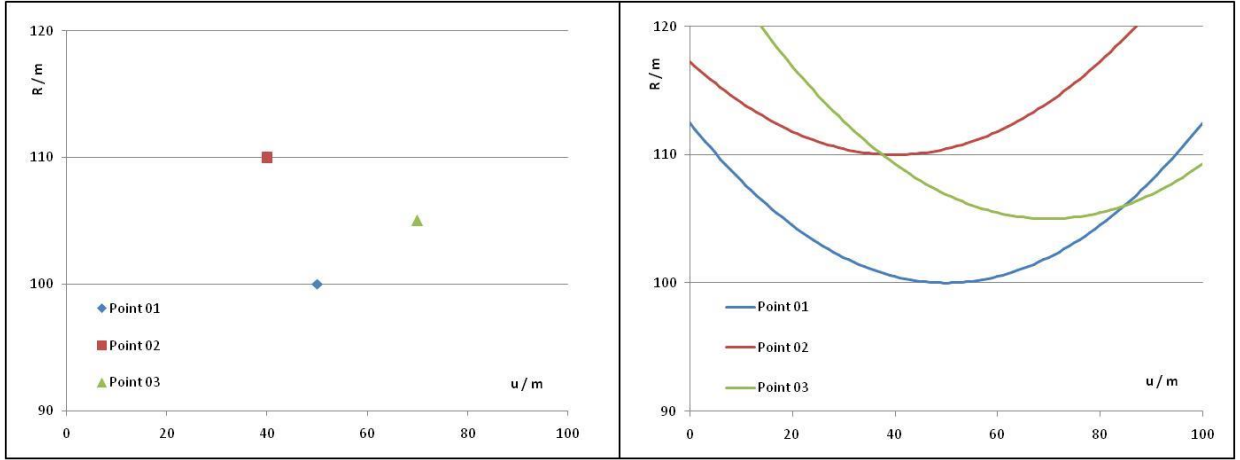


Figure 8: Graphs showing the expected range variation of 3 scatterers within a SAR scene collected using the stripmap SAR geometry. The right-hand plot shows the expected hyperbolic relationship the scatterer ranges have with the time parameter  $u$  of the collection.

When the phase,  $\psi$ , is considered as a function of the parameter  $u$ , due to the round-trip time of the radar energy:

$$\psi(u) \approx -\frac{4\pi}{\lambda} R(u) \quad (2.9)$$

Substituting (2.8) into (2.9) gives

$$\psi(u) \approx -\frac{4\pi}{\lambda} \left( R_o + \frac{x_p^2}{2R_o} + \frac{u^2}{2R_o} - \frac{ux_p}{R_o} \right) \quad (2.10)$$

From (2.10) the instantaneous spatial frequency,  $k_{u,i}$ , can be determined to demonstrate that the stripmap model effectively implements a spatial chirp in the azimuthal dimension. The spatial chirp property can then be used to determine the achievable azimuthal resolution of stripmap SAR:

$$k_{u,i} = \frac{d}{du} \psi(u) \quad (2.11)$$

$$k_{u,i} = -\frac{4\pi}{\lambda} \frac{1}{R_o} (u - x_p) \quad (2.12)$$

A single point scatterer can only provide information to the signal processor when it is within the footprint of the real radar beam, therefore the parameter  $u$  will be limited to vary from zero to the length of the synthetic aperture,  $D_{SAR}$ , during the collect. Therefore, the spatial frequency bandwidth,  $\beta_k$  will be given:

$$\beta_k = \frac{2D_{SAR}}{\lambda R_o} \text{ cyclesm}^{-1} \quad (2.13)$$

From (2.13) the space-bandwidth product for the spatial chirp can be determined:

$$\beta_k u = \frac{2D_{SAR}^2}{\lambda R_o} \quad (2.14)$$

Analogous to pulse compression where the achievable range (fast time) resolution,  $\delta_r$ , through matched filtering can be computed as the ratio of the pulse duration to the time-



## Chapter 2 – Research Context

bandwidth product, the azimuthal resolution,  $\delta_{az}$ , can be computed as the ratio of the spatial pulse extent and the space-bandwidth product:

$$\delta_{az} = \frac{D_{SAR}}{\beta_k u} \quad (2.15)$$

Substituting (2.15) into (2.14):

$$\delta_{az} = \frac{\lambda R_o}{2D_{SAR}} \quad (2.16)$$

The real beamwidth,  $\theta_b$ , limits the maximum spatial extent of the swath,  $D_{SAR\ max}$  for the point scatterer:

$$D_{SAR\ max} = R_o \theta_b ; \theta_b = \frac{\lambda}{D_A} \quad (2.17)$$

where  $D_A$  is the dimension of the real aperture in the  $x$  axis direction. Substituting (2.17) into (2.16) gives the minimum achievable azimuthal resolution for the stripmap model,  $\delta_{az,min}$ :

$$\delta_{az,min} = \frac{D_A}{2} \quad (2.18)$$

This result is somewhat counterintuitive to conventional radar theory as the resolution and the antenna dimensions are normally inversely proportional. With SAR, the smaller the real antenna the larger the real beamwidth, which means that a particular target can remain within the real beam for longer in time or space and therefore provide more information to the signal processor for spatial compression. This increased amount of information then allows the SAR processor to refine the resolution more than real radar.

The last two terms in (2.8) constitute what is called range migration, which is the deviation from the exact spatial chirp construction. The range migration, as demonstrated by the two

residual terms, is composed of two primary factors: the range walk, which is the difference in range of a point scatterer from the start to the end of the synthetic aperture collection; and the range curvature, which is the variation in the quadratic term of  $R(u)$ .

## **2.4 Spotlight SAR Geometry**

The beginnings of the development of spotlight SAR can be traced back to the work conducted during the 1960s at the University of Michigan. Walker utilised techniques inherent in spotlight SAR in order to compensate for errors induced in SAR imaging of rotating objects using standard radar imaging techniques (Walker, 1980). This technique has since become a field of research in itself and is now termed Inverse SAR (ISAR). From this work the early form of the polar format algorithm was developed. Through consideration of the spotlight geometry problem as a tomographic construction the use of the projection slice theorem was introduced later by Munson, which added further mathematical elegance to the formulation of spotlight imagery (Munson et al., 1983). The principal difference between stripmap SAR and spotlight SAR is the use of the real radar beam during the collection of the target area. In spotlight the SAR the real beam is fixed on a patch on the surface and continually steered towards the fixed point as the platform forms the synthetic aperture in the same manner as an optical spotlight tracks a target. Figure 9 illustrates the spotlight SAR geometry.

## Chapter 2 – Research Context

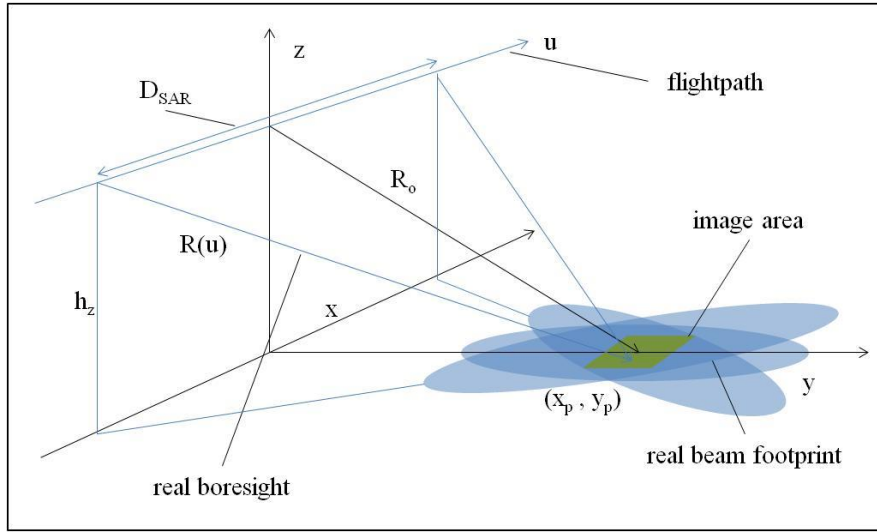


Figure 9: Diagram showing the spotlight SAR geometry where the real radar beam is continually focussed on a single patch during the extended synthetic aperture.

As the beam is fixed over the target area, the physical extent of the target area must fit within the footprint of the real beam for the entirety of the collection so must therefore be smaller than the extent of the stripmap model collect, if identical real radar beams are used for both collects. The main benefit of prolonging the collection of returns from the target area beyond that of the stripmap model is that the sensor receives more information concerning the reflectivity of the scene from the extended viewing angle and hence an increased Doppler bandwidth. As it is the bandwidth of the returns that essentially determines the achievable resolution of the image, the increased bandwidth of the scatterers induced by platform motion allows the azimuthal resolution to be improved beyond the theoretical limits of the stripmap model.

Due to the motion of the real beam through the extent of the synthetic aperture, the data received for processing has a different form than the hyperbolic relationship shown in Figure 8. Generically, each pulse sample of the scene can be considered by separating the scene frame of reference into along real boresight and its perpendicular. In this way, each range bin

is a summation of all scatterers along the line perpendicular to the boresight at the range of the bin. This is true as long as the range to the scene is much greater than the size of the scene, which is a fair assumption in most cases. As the scene collection progresses, the boresight and cross-boresight frame of reference changes gradually. The gradual change of the frame along with the receive Doppler variation gives the processor the requisite information to plot the locations of the scatterers within the scene. The footprint deconstruction is shown in Figure 10.

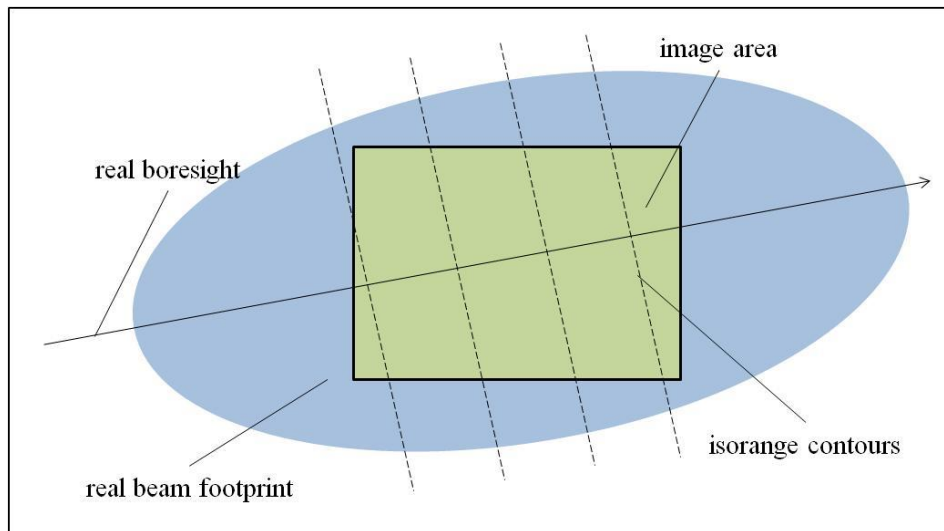


Figure 10: Diagram showing the use of the real radar boresight and cross-boresight isorange contours to determine suitable dimensions for the spotlight SAR collection.

This model is sufficiently accurate when the isorange contours can be considered straight within the scene area, otherwise the curvature of the contours must be taken into account in the imaging process. An unfocussed image can be formed from the collected data directly, which has similar but more extreme scatterer range migration issues to the stripmap SAR geometry, shown in Figure 11.

## Chapter 2 – Research Context

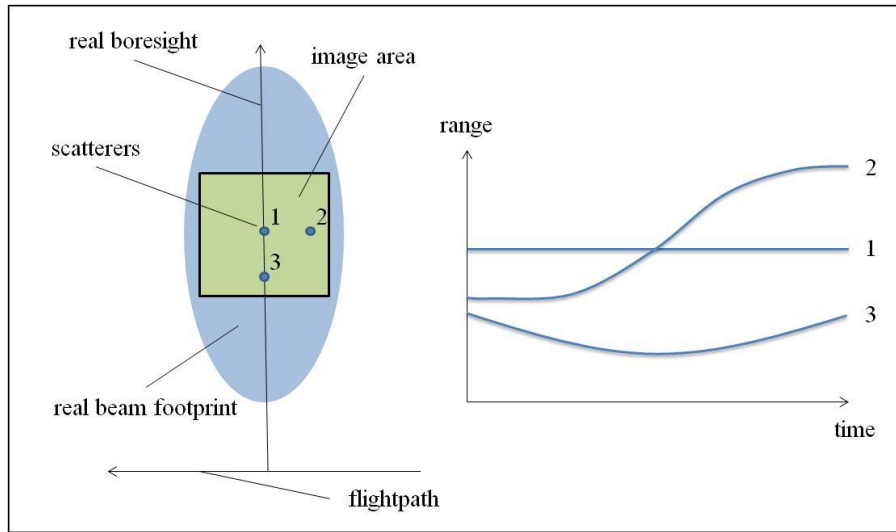


Figure 11: Diagram showing the range migration variation of 3 scatterers within a spotlight SAR scene. The scatterer data is centred around the scene centre, therefore scatterer number 1 is considered stationary and the others vary accordingly.

Figure 11 illustrates the primary problem with the spotlight SAR geometry; the algorithm that must be developed to focus the collection data must be able to compensate for the large non-hyperbolic range migration of the scatterers through the image collection. Figure 12 can be used for comparison of the range migration seen using the same distribution of scatterers as for the stripmap model in Figure 8.

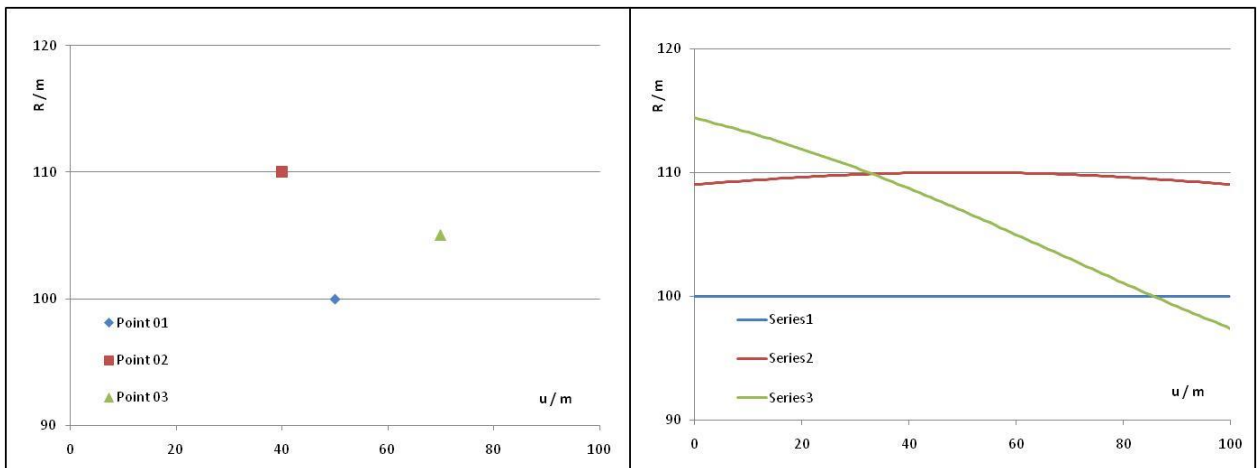


Figure 12: Graphs showing the non-hyperbolic range migration of the spotlight SAR geometry from the same scatterers as in Figure 8.

## **2.5 Ocean Remote Sensing**

Remote sensing of the ocean utilising SAR arguably began with the launch of SEASAT-1 in 1978. Unfortunately, it only ran for 105 of the planned days but such was the imagery produced that it is still used in scientific research many years later. SEASAT-1 was part of an early generation of Earth observing satellites that grew out of the beginnings of the space race of the 1960s. Many of the original sensors were in the visible band but the SAR sensor on board SEASAT-1 showed that high-quality radar imagery could be obtained in this way. Unlike the use of real aperture radar at very long range, SAR was able to provide the desirable resolutions from orbit that so benefitted the surface observations. The success of the project paved the way for further investigative work using similar remote sensing on the Shuttle Imaging Radars that had multiple derivatives of SIR-A, SIR-B and SIR-C starting in 1981 and running through until 1994. Also, multinational development occurred with the deployment of sensors such as the European project ERS-1 and the Japanese JERS-1. These next generation of sensors aimed at improving spatial resolution and experimenting with alternate bands. The use of orbital sensors proved that wide area observation of the oceans could be achieved efficiently and economically with useful revisit frequency for extended periods. Satellites remain the primary means for marine environment monitoring with the benefit of assisting scientists with forecasting, disaster monitoring, early warning, resource surveying and management. Progressive development of technology and demand persisted through to the latest generation of surface observing satellites that include the likes of marine observing RADARSAT-2 that is capable of imaging large 500 km swaths of ocean at a variety of incidence angles and also provides fully polarimetric information.

Specifically, the high spatial resolution of the SAR imagery of the ocean has allowed for the study of targets within the sea clutter and the detailed study of the sea clutter itself. Shipping

## Chapter 2 – Research Context

and other man-made phenomena, such as oil spills and particularly the identification of ships and their associated wakes have been the subject of continual scientific and commercial interest. Far from being a space-based field, much has also been accomplished with airborne sensors. The Raytheon ASARS-2 has been a longstanding fit to the Lockheed U-2 Dragon Lady where the long range and high resolution helped overcome the impact of having to fit a sensor to an aircraft that could fly at newly accomplished cruise altitudes. Though this system was primarily focused on ground surveillance there were many systems developed for the maritime domain including the Searchwater fitted to the UK RAF Nimrod MR2 and the AN/APS-137 fitted to the USN P3-C Orion. These sensors carried capable-enough imaging techniques but did not fully embrace SAR as a function. As such, airborne maritime SAR has been a rarer and more recent commodity. Currently, with the proliferation of advanced radar techniques more easily deployable, there is an increased number of platforms that are SAR capable in the maritime domain such as the USN MQ-4C Triton and the Boeing P-8 Poseidon. Their imaging capabilities, such as the application of ISAR, allow for improved recognition at range of moving surface targets, which is of great value when understanding the surface water battlespace. Away from commercially produced systems, in the experimental field, much has also been achieved in the study of the surface of the oceans in terms of system development and the phenomena themselves. For instance, much was learned from the early space-based systems to influence the development of the AIRSAR system on the NASA DC-8, which has been used in many fields of research in its time of operation. When considering specific research aimed at developing the understanding of interaction of hydrodynamics and radar, there have been some major series of experimental projects by various groups. To name a few, the Joint Canada-US Ocean Wave Investigation Project (JOWIP), the SAR Internal Wave Signature Experiment (SARSEX), the Tower

Ocean Wave and Radar Dependence (TOWARD) experiment and the US/UK Lock Linnhe experiments all have looked to progress the scientific understanding of the interaction of the radar sensor with the hydrodynamics of the water and include the understanding of the SAR algorithm nuances (Ward et al., 2006 and Stapleton, 1989).

## 2.6 Geometric Focussing

The term geometric focussing (GF) was given to a technique that was developed as part of the early work towards this thesis investigating a method to improve the focus of moving scatterers within SAR imagery. Rather than introducing additional layers of computation or altering the SAR processing steps, which have been considered by other authors, the GF technique looked to improve the focus of a moving scatterer through manipulation of the imaging geometry. For a known target velocity, it was found that an imaging could be constructed that would achieve this aim. The geometry for GF is initially constructed as per Figure 13 where a side-looking SAR sensor images a target area within which lies the target scatterer at location  $(x_p, y_p)$ . The sensor position, as it moves between  $-L$  and  $+L$  along the  $x$  axis, is described by parameter  $u$  such that at any point along the sensor track the target can be described at range  $R(u)$ .



## Chapter 2 – Research Context

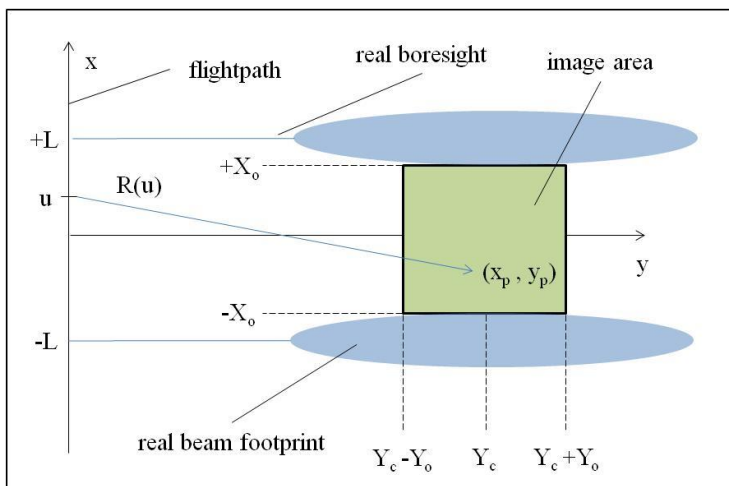


Figure 13: Diagram showing the basic imaging geometry used to define the geometric focussing technique.

Beginning with the moving target analysis of Raney (1970), the transfer function of the target can be written as

$$H(\omega, x - u, y) = A(\omega, x - u, y)e^{-2i\frac{\omega}{c}R(u)} \quad (2.19)$$

where  $A(\omega, x - u, y)$  contains the two-way antenna pattern and the amplitude factors. Using the transmitted pulse's spectrum,  $P(\omega)$ , the received signal,  $S(\omega, u)$ , can be given by

$$S(\omega, u) = P(\omega)A(\omega, x - u, y)e^{-2i\frac{\omega}{c}R(u)} \quad (2.20)$$

For a target scatterer with motion as per Figure 14, the function of  $R(u)$  can be expressed as a function of time,  $t$ :

$$R^2(t) = \left( v_{rdr}t - v_x t - \frac{a_x}{2}t^2 \right)^2 + \left( R_o - v_y t - \frac{a_y}{2}t^2 \right)^2 \quad (2.21)$$

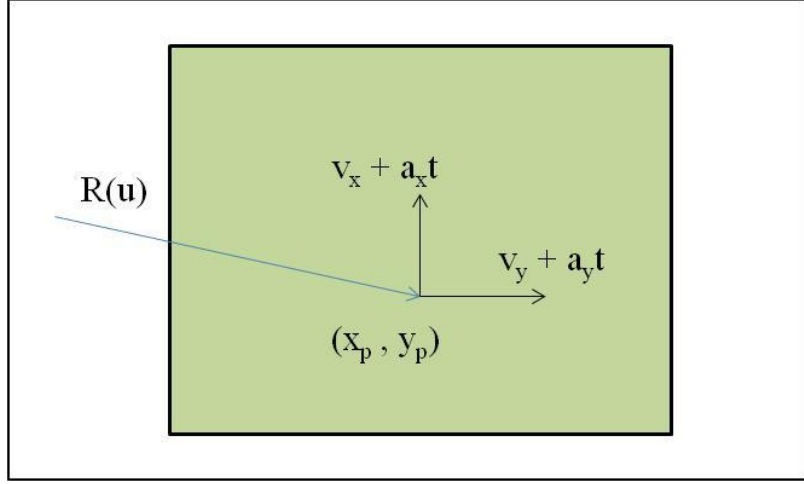


Figure 14: Diagram describing the generic location and motion of the target scatterer at  $(x_p, y_p)$ .

Taking linear approximations and ignoring quadratic terms of (2.21) gives

$$R(t) \approx R_o - v_y t + \left\{ (v_{rd} - v_x)^2 - R_o a_y \right\} \frac{t^2}{2R_o} \quad (2.22)$$

which, when substituted into (2.19), changes the transfer function to the form

$$S(\omega, u) = P(\omega) A(\omega, x - u, y) e^{-2i\frac{\omega}{c} \left[ R_o - v_y t + \left\{ (v_{rd} - v_x)^2 - R_o a_y \right\} \frac{t^2}{2R_o} \right]} \quad (2.23)$$

The main step of the GF technique is to construct the imaging scene such that the azimuthal velocity and target accelerations are near zero. This can be achieved with an image collection construction as shown in Figure 15.

## Chapter 2 – Research Context

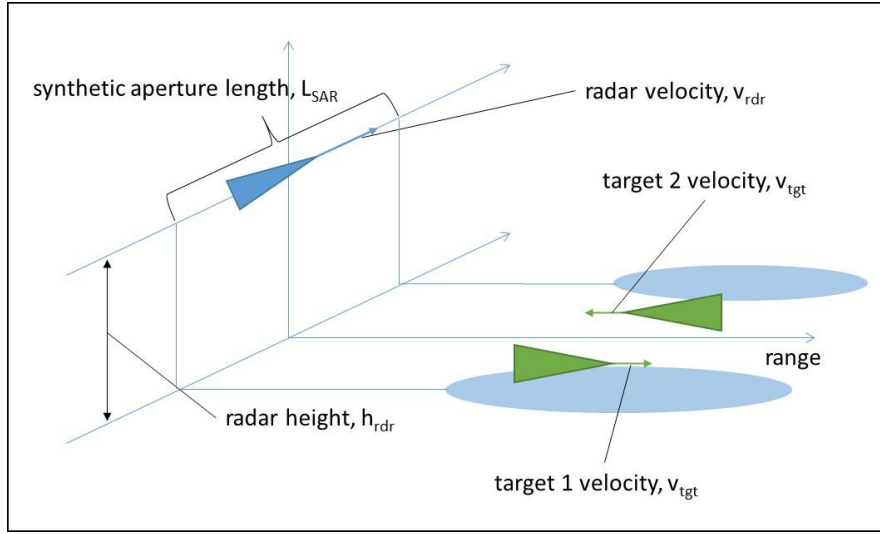


Figure 15: Diagram showing the collection construction for the geometric focussing (GF) technique. In the ideal case the target, or targets, have velocity that is perpendicular to the synthetic aperture.

Given this construct the third and fourth terms within the exponential of (2.23) can be considered negligible giving a simplified expression for the transfer function of the target scatterer

$$S(\omega, u) = P(\omega)A(\omega, x - u, y)e^{-2i\frac{\omega}{c}(R_0 - v_y t)} \quad (2.24)$$

The result of this is maximum azimuthal displacement of the target scatterer occurs when plotted within the image but with minimised azimuthal defocussing. As the target moves a specific distance in range during the imaging process there is still a residual range smear that can be predicted by the  $-v_y t$  term. Figure 16 shows the expected result of the GF technique.

## Chapter 2 – Research Context

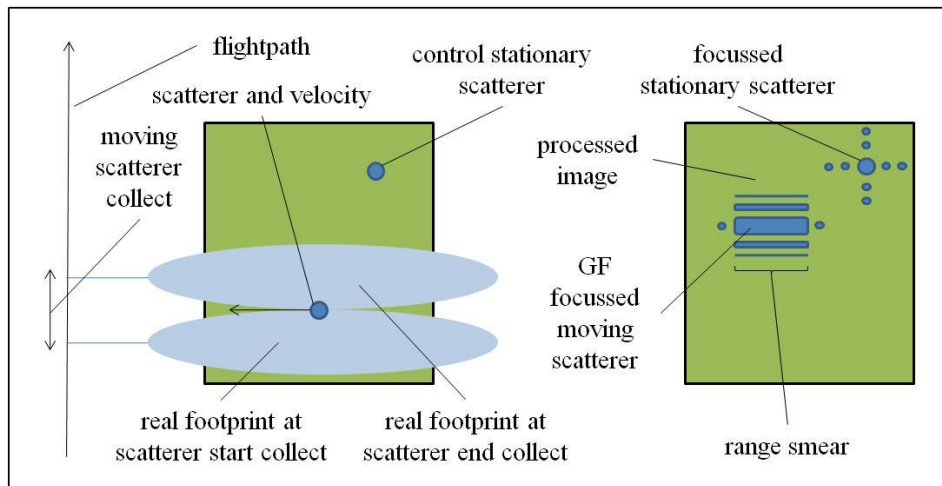


Figure 16: Diagram showing a comparison of a static target scatterer with a moving target within the GF construct.

In order to test this approach, the kingposts of ships (a distinctive mast near the bow of a ship) were chosen as a suitable target as the motion of non-cooperative targets could be predicted prior to imaging and AIS data could be used to analyse the results. Kingposts proved to be good targets as they are physically small enough to be considered point reflectors and are highly reflective being normally made of steel. As side effect of the GF technique used against ship targets was the appearance of an unintended and at the time unexplained ship and wake artefact. Figure 17 shows the result of the GF technique used against a ship target where the target vessel is displaced in azimuth, there is no discernible traditional wake pattern that is common in non-GF imagery and there is an unexpected distortion near the true location of the target vessel. It is this understanding of this non-standard combination of phenomena that is the focus of this thesis.

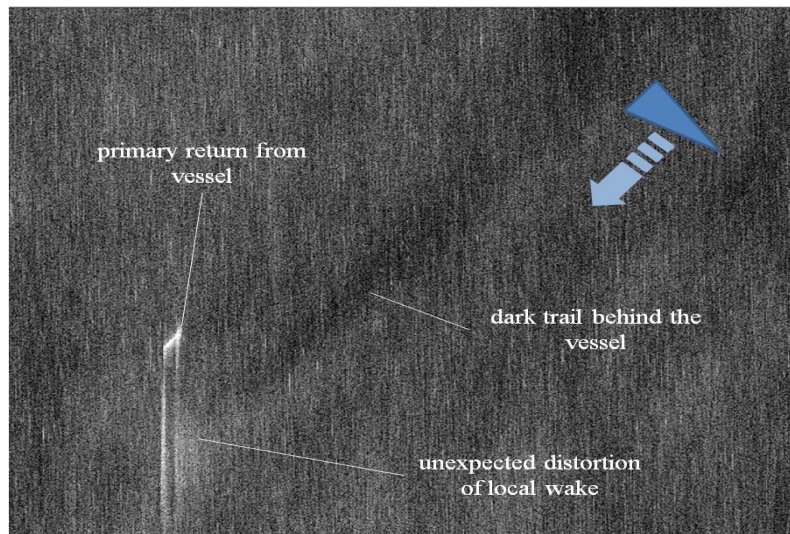


Figure 17: Chip-out of a SAR image taken using the GF technique. The sensor motion and imaging angle are indicated with the blue arrows. The ship is moving away from the sensor towards the bottom-left of the image. The chip-out is roughly 2 km x 2 km square.

## 2.7 Wake Models

As with many physical phenomena, the description of wave motion on the surface of water has been of general interest throughout much of modern recorded history. The 19<sup>th</sup> century saw a vast increase in the study and subsequent success that can be somewhat attributed to the demands of the industrial revolution. The application of more powerful and complicated engines to shipping and the vast increase in industrial transportation of goods globally factored as a potent purpose for the understanding and optimisation of ship-building in what was known to be a complex physical environment. This environment has been succinctly described by many, such as Tuck et al. (2004), as a boundary-value problem for Laplace's equation with several conditions. The disturbance of the surface is created with a body of some shape that has some condition, often the Neumann boundary condition; the free surface of the water with the atmosphere above holds a boundary condition of pressure, often related through Bernoulli's equation. The combination of these two conditions, which can be termed the Stokes' conditions, both of which are non-linear, must be applied to the free surface of the

## Chapter 2 – Research Context

water and then solved-for to satisfy Laplace's equation. This nasty combination of unknowns and non-linearity is why the ship wake problem, and conversely the hull-design problem, has persisted to the current era. There is no single model of truth that solves the problem and the many that have been developed over the last two hundred years each bring useful characteristics and varying limitations for the practitioner to develop and use effectively. Key to each approach are the assumptions used in the process, the method used to describe the disturbance as well as the intricacies of the modelling steps. This section will explore some the major breakthroughs that have paved the way for our current understanding. It claims in no way to be an all-encompassing study of the field but aims to highlight the main areas of the interest in order to provide perspective for the approach taken in the study.

Lord Kelvin, whose name is given to the major wake feature that all could recognise following the publication of his seminal paper 'On Ship Waves' in 1887, was the first to demonstrate the persistence of the characteristic wake angle through use of a moving impulse on the fluid surface coupled with the superposition of multiple waves emanating from the source (Kelvin, 1887). The approach showed that the pattern was the result of two main wave fields that change with the disturbance but the combination of the two has relative stability. The longer wavelength, transverse, waves are observed to travel mainly in the direction of the disturbance whereas the shorter wavelength, divergent, waves are observed to travel more parallel to the direction of travel of the disturbance. Underlying this construct is the dispersive nature of water waves in deep water. Deep water is often characterised as water that is deeper than the scale of the wavelength of the wave in question (Lighthill, 1978). Kelvin showed, through asymptotic approximation methods, that this pattern could be described with a consistent angle of  $39^\circ$ .

## Chapter 2 – Research Context

The basic constraint of this boundary can be shown quite simply through a geometric explanation. Consider a ship moving with constant speed,  $v_s$ , and generating waves in a stationary body of water. It is assumed that in this case the water is deep compared with the wavelength of the generated waves and the motion of the ship is constant and relatively slow compared with the wave velocity. The generated waves that are of particular concern in this case are those that will form the steady wake pattern and therefore must form standing waves in the frame of the ship otherwise they would eventually disperse and thus not form a continuous wake pattern. The constraint that holds true for this case is that the wave speed,  $c_s$ , must be equal to the speed of the source ship. Historically this was initially shown by consideration of waves that move in a stream through a canal where there was realistically only one dimension of propagation to calculate. However, when considering the water surface as a 2-dimensional plane the angle of propagation,  $\theta_s$ , away from the ship must be included in the constraint. As such, the required constraint is:

$$c_s = v_s \cos \theta_s \quad (2.25)$$

This relationship can be used to show an area of influence of the standing waves that are generated by the ship. The locus of the points where (2.25) is true is shown in Figure 18. The large circle shows the locus of the points from (2.25) where the ship moves from point A to point C. The smaller circle shows the locus of the points from (2.25) where the ship moves from point B to point C.

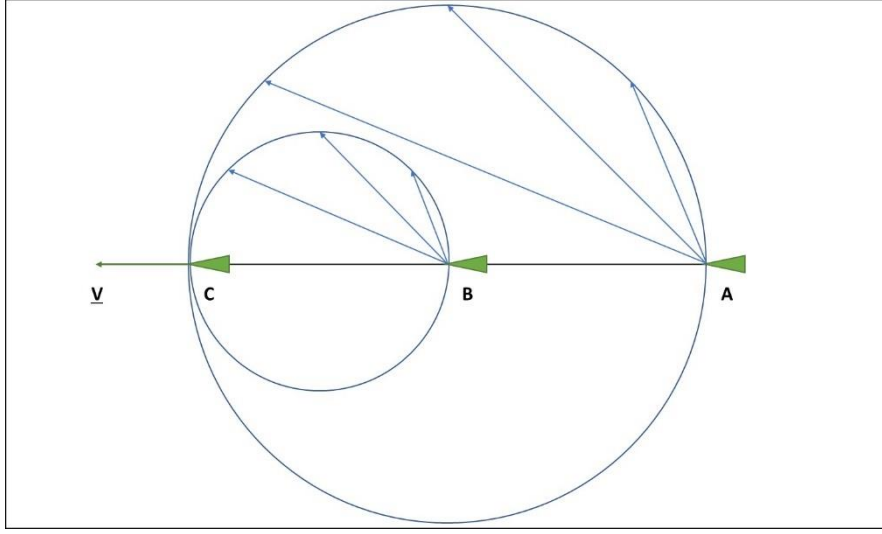


Figure 18: Diagram showing the locus of the points that contribute to the standing wave pattern around a moving ship.

The particularly interesting characteristic for water waves is that as the waves are dispersive the wave speed is dependent on the wavelength and therefore the wavelength of the waves that form the locus shown in Figure 18 vary across the circumference of the circle. The dispersion relationship for the waves gives the speed as:

$$c_s = \sqrt{\frac{g\lambda}{2\pi}} \quad (2.26)$$

From this it can be seen that the shorter wave speed vectors exist at greater angles of  $\theta_s$  and the longer wave speed vectors exist at angles that are more parallel to the line of advance of the ship. It is this variation that forms the overall shape of the Kelvin wake pattern.

However, a full understanding of the wave pattern is not required to determine its extent.

Continuing with the geometric analysis, the wave speed has been used to show the area of influence of the standing wave field. As the group velocity is equal to half the phase velocity, the energy of the waves that are produced by the ship in Figure 18 doesn't fully reach the extremes of the circles. In fact, the energy reaches half the distance between the



source and the edge as shown in Figure 19. The locus of the points that satisfy the group velocity form the dark-brown circles. The extent of the brown circles forms the extent of the standing wave pattern that moves with the ship. Therefore, the angle  $\theta_{ACD}$  is the source that gives the angle of the Kelvin wake.

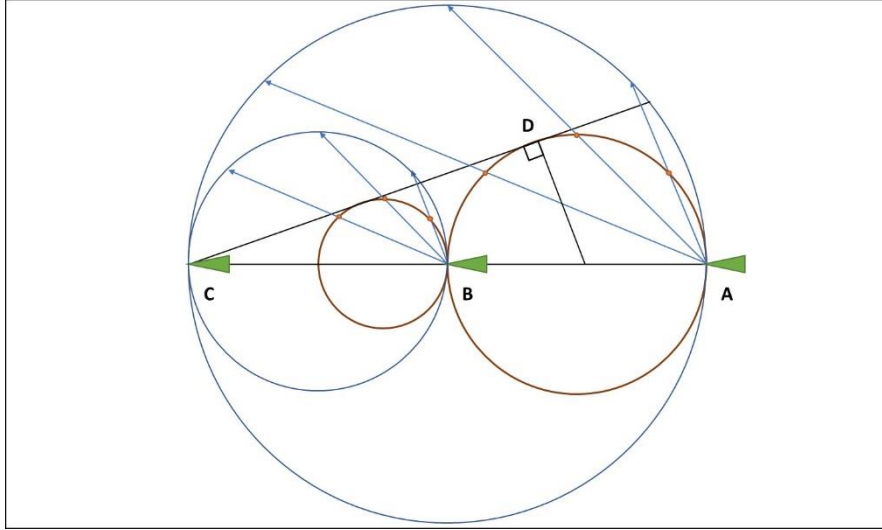


Figure 19: Diagram showing the locus of the points of the wave energy generated by a moving ship. The angle  $\theta_{ACD}$  can be determined through the examination of the right angled triangle as drawn.

Using the trigonometric construction in Figure 19, it can be simply shown that

$$\theta_{ACD} = \sin^{-1}\left(\frac{1}{3}\right) \approx 19.5^\circ \quad (2.27)$$

The pattern behind the wake can be discerned with a little more work through consideration of the lines of constant phase within the wave field. Using the construction, as shown in Figure 20, where the ship travels from point A to point C in a given time whilst travelling a constant speed,  $v_s$ , the point E indicates the direction and extent of travel of the wave of a given wavelength that travels at its related phase velocity for the angle  $\theta_{CAE}$  from the  $x$  axis.

## Chapter 2 – Research Context

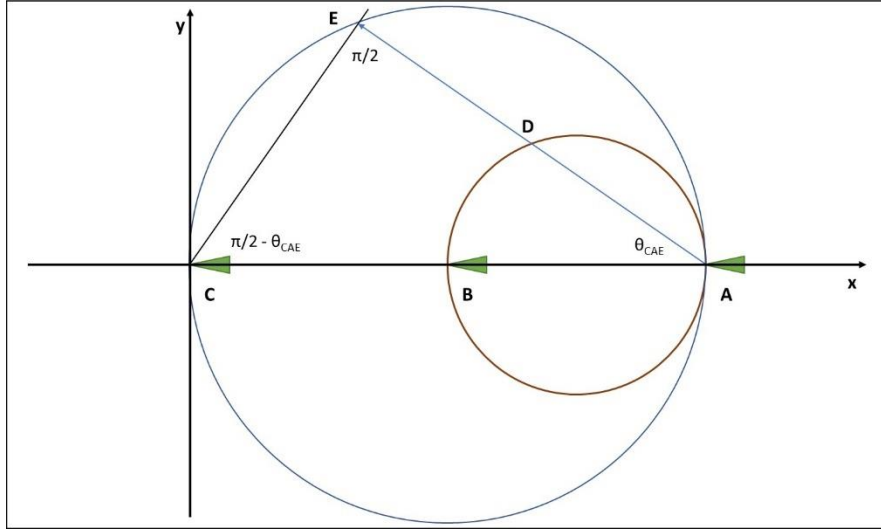


Figure 20: Diagram showing the geometric construction used to determine the lines of constant phase within the Kelvin wake.

From (2.25), it can be seen that in the context of Figure 20,

$$L_{AE} = L_{AC} \cos \theta_{CAE} \quad (2.28)$$

$$L_{AD} = \frac{1}{2} L_{AC} \cos \theta_{CAE} \quad (2.29)$$

In the given time for the ship to conduct its movement from A to C, the wave energy travelling towards E will have reached D in accordance with the group velocity. The location of D can be deduced using (2.29) as

$$x = L_{AC} \left\{ 1 - \frac{1}{2} (\cos \theta_{CAE})^2 \right\} \quad (2.30)$$

$$y = \frac{1}{2} L_{AC} \cos \theta_{CAE} \sin \theta_{CAE} \quad (2.31)$$

It can also be seen that the wave crest of Figure 20, which is perpendicular to the wave vector, makes an angle of  $\pi/2 - \theta_{CAE}$  with the x axis. This can plainly be seen at the origin, coincident with C. The lines of constant phase exist when this gradient is maintained:

Chapter 2 – Research  
Context

$$\frac{dy}{dx} = \frac{\sin(\pi/2 - \theta_{CAE})}{\cos(\pi/2 - \theta_{CAE})} \quad (2.32)$$

$$\frac{dy}{dx} = \tan(\pi/2 - \theta_{CAE}) \quad (2.33)$$

$$\frac{dy}{dx} = \cot \theta_{CAE} \quad (2.34)$$

The relationships (2.30) and (2.31) can be used with the requirement of (2.34) to determine the location of the line of the wave crests.

$$\frac{dy}{dx} = \frac{dy}{d\theta} \frac{d\theta}{dx} \quad (2.35)$$

From (2.30),

$$\frac{dx}{d\theta} = \frac{dL_{AC}}{d\theta} \left\{ 1 - \frac{1}{2} (\cos \theta_{CAE})^2 \right\} + L_{AC} \cos \theta_{CAE} \sin \theta_{CAE} \quad (2.36)$$

From (2.31),

$$\frac{dy}{d\theta} = \frac{1}{2} \frac{dL_{AC}}{d\theta} \cos \theta_{CAE} \sin \theta_{CAE} + \frac{1}{2} L_{AC} \{ (\cos \theta_{CAE})^2 - (\sin \theta_{CAE})^2 \} \quad (2.37)$$

Therefore, using the relationship of (2.35) and then substituting (2.37) and (2.36) into (2.34),

$$\frac{dy}{d\theta} \frac{d\theta}{dx} = \cot \theta_{CAE} \quad (2.38)$$

$$\frac{dy}{d\theta} = \frac{dx}{d\theta} \cot \theta_{CAE} \quad (2.39)$$

$$\begin{aligned}
 & \frac{1}{2} \frac{dL_{AC}}{d\theta} \cos \theta_{CAE} \sin \theta_{CAE} + \frac{1}{2} L_{AC} \{(\cos \theta_{CAE})^2 - (\sin \theta_{CAE})^2\} \\
 &= \left[ \frac{dL_{AC}}{d\theta} \left\{ 1 - \frac{1}{2} (\cos \theta_{CAE})^2 \right\} \right. \\
 & \quad \left. + L_{AC} \cos \theta_{CAE} \sin \theta_{CAE} \right] \cot \theta_{CAE}
 \end{aligned} \tag{2.40}$$

Simplifying gives,

$$\begin{aligned}
 & \frac{1}{2} \frac{dL_{AC}}{d\theta} \cos \theta_{CAE} \sin \theta_{CAE} - \frac{dL_{AC}}{d\theta} \left\{ 1 - \frac{1}{2} (\cos \theta_{CAE})^2 \right\} \cot \theta_{CAE} \\
 &= L_{AC} (\cos \theta_{CAE})^2 \\
 & \quad - \frac{1}{2} L_{AC} \{(\cos \theta_{CAE})^2 - (\sin \theta_{CAE})^2\}
 \end{aligned} \tag{2.41}$$

$$\begin{aligned}
 & \frac{1}{2} \frac{dL_{AC}}{d\theta} \cos \theta_{CAE} \sin \theta_{CAE} - \frac{dL_{AC}}{d\theta} \cot \theta_{CAE} \\
 & \quad + \frac{1}{2} \frac{dL_{AC}}{d\theta} (\cos \theta_{CAE})^2 \cot \theta_{CAE} \\
 &= L_{AC} (\cos \theta_{CAE})^2 - \frac{1}{2} L_{AC} (\cos \theta_{CAE})^2 \\
 & \quad + \frac{1}{2} L_{AC} (\sin \theta_{CAE})^2
 \end{aligned} \tag{2.42}$$

$$\begin{aligned}
 & \frac{1}{2} \frac{dL_{AC}}{d\theta} (\cos \theta_{CAE} \sin \theta_{CAE} - 2 \cot \theta_{CAE} + (\cos \theta_{CAE})^2 \cot \theta_{CAE}) \\
 &= \frac{1}{2} L_{AC} \{(\cos \theta_{CAE})^2 + (\sin \theta_{CAE})^2\}
 \end{aligned} \tag{2.43}$$

$$\frac{1}{2} \frac{dL_{AC}}{d\theta} \cot \theta_{CAE} \{(\sin \theta_{CAE})^2 - 2 + (\cos \theta_{CAE})^2\} = \frac{1}{2} L_{AC} \tag{2.44}$$

$$-\frac{dL_{AC}}{d\theta} \cot \theta_{CAE} = L_{AC} \tag{2.45}$$

$$\frac{dL_{AC}}{d\theta} = -L_{AC} \tan \theta_{CAE} \quad (2.46)$$

The differential equation of (2.46) can be solved to determine the coordinates of the locus of the wave crests,

$$\frac{dL_{AC}}{L_{AC}} = -\tan \theta_{CAE} d\theta \quad (2.47)$$

$$\ln L_{AC} = \ln \cos \theta_{CAE} + \ln L_p \quad (2.48)$$

$$L_{AC} = L_p \cos \theta_{CAE} \quad (2.49)$$

Here, in (2.49),  $L_p$  is a constant of integration that serves as a parametric determiner for the wave crest pattern of interest. Substituting (2.49) back into (2.30) and (2.31) gives the equations for the lines of the wave crests:

$$x = L_p \cos \theta_{CAE} \left\{ 1 - \frac{1}{2} (\cos \theta_{CAE})^2 \right\} \quad (2.50)$$

$$y = \frac{1}{2} L_p (\cos \theta_{CAE})^2 \sin \theta_{CAE} \quad (2.51)$$

Figure 21 shows a plot of (2.50) and (2.51) where the parameter  $L_p$  takes the values [1,5].

## Chapter 2 – Research Context

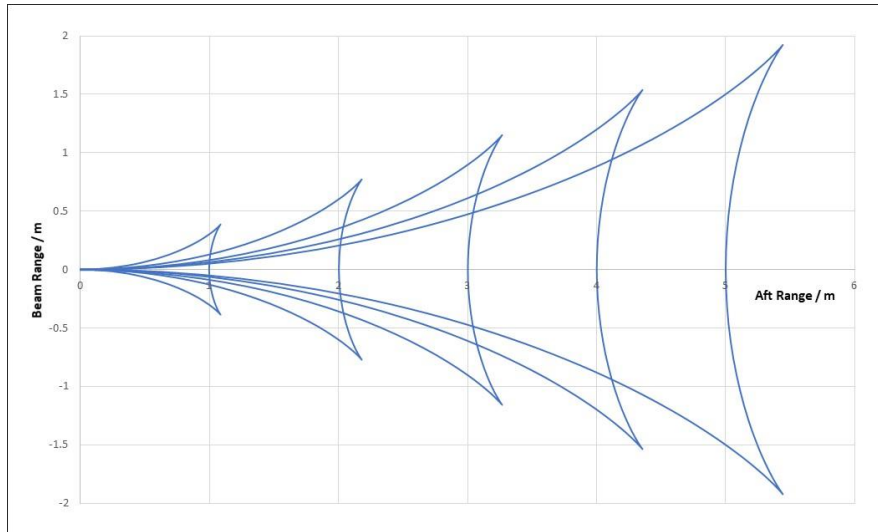


Figure 21: Graph showing a plot of (2.50) and (2.51) with parameter  $L_p = [1, 5]$ .

Below, Figure 22 shows an annotated diagram of the wave field where the varying gradients of the wave crests relative to the line of advance of the ship can be considered as a superposition of 2 separate wave patterns. The divergent field has a smaller gradient and moves relatively slowly away from the line of advance of the ship whilst remaining relatively parallel to its track. Whereas, the transverse field moves at roughly the speed of the ship along the line of advance with the wave crest almost perpendicular to its track. At the angular extent of the pattern, where the gradients of the transverse and divergent wave field match, the cusp waves can be found. Due to the superposition of the wave fields at this angle, the amplitude of the cusp waves is shown to be normally greater than the rest of the waves within the pattern.

## Chapter 2 – Research Context

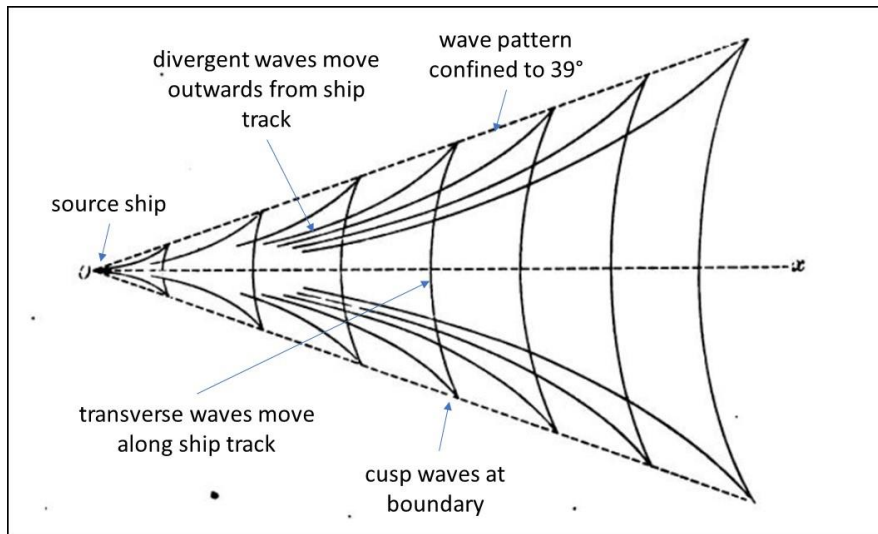


Figure 22: Kelvin wake plot showing lines of constant phase (Lamb, 1932). The pattern can be seen to be bounded by the limiting angle of 39°.

At a similar time to Kelvin, Froude utilised a more practical approach to generate understanding and usable results for the benefit of real-ship use. Froude used a scaling method that centred on the use of a towing tank with physical models of ships. The scaling method, using the law of gravitational similarity developed by Reech in 1844, allowed Froude to complete studies on the resistance of flow. Froude's work could be considered distinct also due to his treatment of the viscous action of the fluid flow as well as the wave effect (Gotman, 2007). Many models neglect viscous action, which is often a fair assumption for simplification, as the far field appears to have limited impact from viscous mechanisms. This is not true for the near-field where the displacement is small from the wetted surface of the hull, Tuck (2004). Froude's name is still attached to a widely-used method for general characterisation of shipping, the Froude number,  $F_r$ :

$$F_r = \frac{v_s}{\sqrt{gL_s}} \quad (2.52)$$

## Chapter 2 – Research Context

Arguably the pivotal work that began the true use of the theoretical science of water waves into a form that could be used to positively influence the practical application desired was Michell's work using 'thin-ships' (Michell, 1898). Michell used the linearised form of the boundary conditions and the thin ship approach in an attempt to determine the overall resistance felt on a hull in a given flow. The purpose was to understand how much energy was transposed by a vessel into the generation of the wake. The vessel design could then be optimised through the minimisation of the drag function. The construct used the notion of fluid with infinite depth and the thin ships that do not have real physical size, the 'hull' is confined to the longitudinal axis, but the impact the 'hull' has on the fluid is generated by a factor that is dependent on the steepness of the hull shape presented to the flow of water around it. Unfortunately, Michell's work remained under-used for roughly 20 years when it was followed by the likes of Havelock (1934), Wigley (1926) and Weinblum (1959) who applied constraints on the hull models to specifically calculate Michell's integral and produce curves of calculated wave resistance. The calculated results from Michell's work still provide a fair description of the expected drag albeit with the presence of some 'hump' and 'hollow' features that have proven to be a topic for subsequent study, an example of such is shown in Figure 23.



## Chapter 2 – Research Context

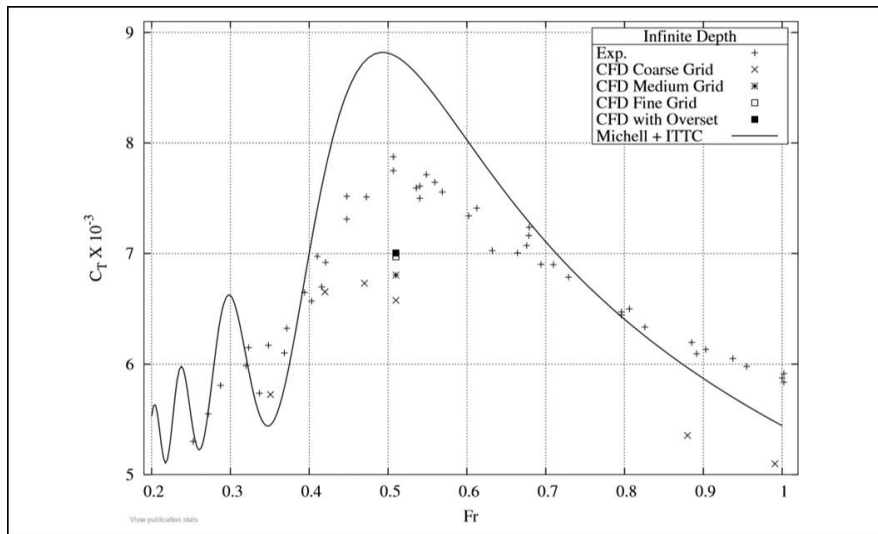


Figure 23: Plot of drag coefficient,  $C_T$ , against Froude number,  $Fr$ . The plot shows the solid line from Michell's integral as well as experimental results from Tuck et al. (2008).

Michell's approach using thin ships that generate small waves removed the need for the nonlinear Stokes conditions on the free surface but instead used the linear condition of Kelvin on the undisturbed surface. As such this approach is often termed the Michell-Kelvin problem. Havelock's addition to the body of work was considerable from the theoretical angle; it also included the use of the double model, proposed by Foettinger, that was particularly useful for the experimental approach to separate the wave resistance experienced by a vessel from the total resistance. A key feature of Havelock's work was through the use of singularities in the description of the ship's hull through the double model, for instance through the use of the Rankine ovoid description that uses a paired source and sink for fluid flow emulation of a ship's hull, as shown in Figure 24 and Figure 25 (Gotman, 2007). Kochin conducted similar theoretical work to Havelock and was able to produce an integral solution function that still bears his name and which was similar in nature to Michell's original.

## Chapter 2 – Research Context

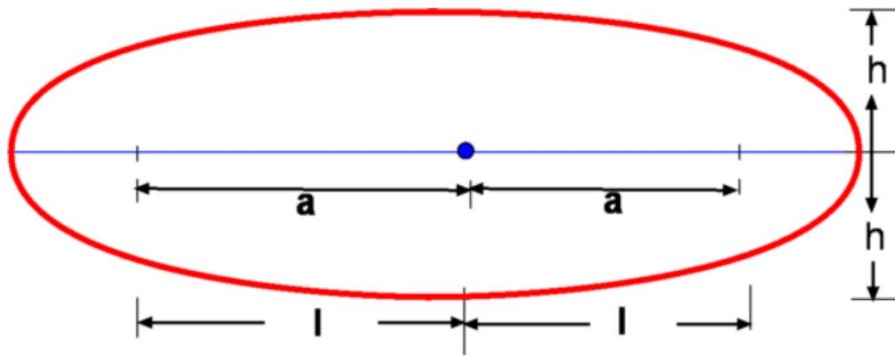


Figure 24: Diagram showing the generic dimensions for the generation of a Rankine ovoid. The red line denotes the boundary of the ovoid where the flow is always tangential to the surface ([www-mdp.eng.cam.ac.uk](http://www-mdp.eng.cam.ac.uk)).

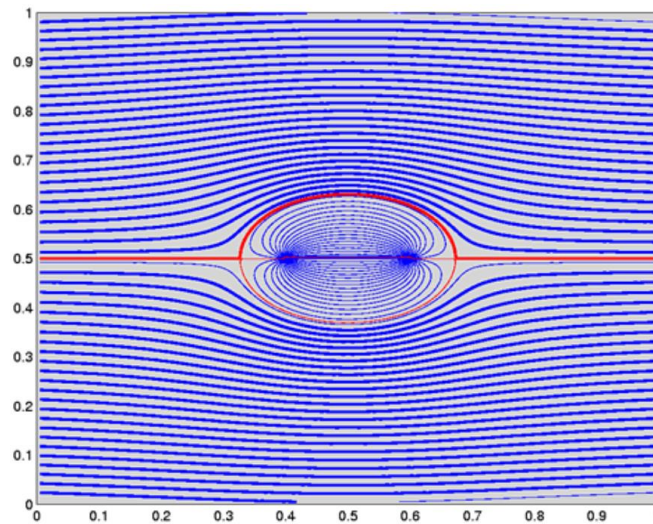


Figure 25: Diagram showing the flow of fluid around the Rankine ovoid and the internal flow from source to sink. The red line denotes the boundary where the internal and external flows are separated ([www-mdp.eng.cam.ac.uk](http://www-mdp.eng.cam.ac.uk)).

The advent of electronic computation saw a renewed vigour for the subject as the restrictions placed on assumptions or particular hull models could begin to be lifted. Albeit, not until the modern era would full nonlinear descriptions be considered easy. Well-developed theories for wave production had been established from theorised sources that included surface pressure distributions, thin ships, singularity distributions and flat ships (Tuck, 1975). The use of electronic computation allowed exploration into the nonlinear conditions and more ‘real’ hulls through techniques such as the finite difference approach, finite element approach

## Chapter 2 – Research Context

and boundary element method. Common to these was the use of a computational mesh to iterate cell disturbances or other characteristics through the timeline (Pethiyago, 2016). Not focussed just on the additional use of computation, many continued to develop the science, such as Lighthill and Witham (1955) who significantly expanded the concept of the kinematic approach to wave motion. The kinematic approach looks to describe a flow with a single velocity for a given position, governed by the continuity equation (Lighthill and Whitham, 1955).

A further resurgence of interest in the modelling of ship wakes has grown from the space era through the addition of satellite imagery. Initially from the SAR imagery from SEASAT in 1978 but also from many other platforms and sensors such as Rabaud and Moisy's recent observations of multiple ship 'wakes' using satellite photography (Fang et al., 2011 and Pethiyago, 2016). Both the appearance of expected ship wakes and also the appearance of strange unexpected phenomena have been the cause of deep scientific study in the area. A prominent example of this is the modelling conducted by Munk et al. (1987) using the SEASAT SAR imagery in an attempt to explain the appearance of narrow V-shaped wakes that do not fit with the classical Kelvin wake model as can be seen in Figure 26.

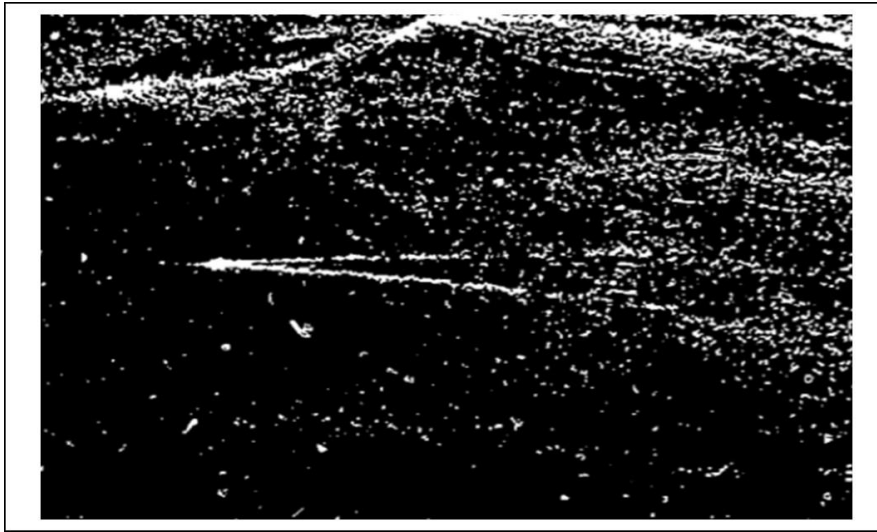


Figure 26: Chip-out from full SAR image taken from the SEASAT system showing the narrow V-shaped wake behind a ship (Case et al., 1984)

The addition of the use of radar as the imaging mechanism brought a fascinating new angle to the way in which the wakes could be measured. Such has been the increase in publication that it is worthwhile examining the developed models rather than simply the personalities involved. Historically, the ‘classical’ approach of the 19<sup>th</sup> century with its thin ship approach with linearised modelling has since been termed the Michell-Kelvin theory. This has evolved over time with the addition of the work of others. The Neumann-Kelvin theory that was developed by Brard and Guevel altered the thin ship idea to a line integral around the wetted waterline of the vessel – termed a boundary-integral flow representation (Noblesse et al., 2013).

In order to formulate results the approach used a more numerical method for the generation of solutions. Tuck et al. (2002) conducted a comparison of the Neumann-Kelvin approach with the Michell-Kelvin and an exact body and surface condition approach, termed the Neumann-Stokes theory, to measure the relative accuracies. The ‘ship’ used for the comparison was a submerged ellipsoid and the free surface elevation was the test criterion.

The Neumann-Kelvin and Neumann-Stokes models were found to have an average 5% error, which was considered good. There were occasions, however, when an error of 50% arose when comparing the Michell-Kelvin approach to the Neumann-Stokes (Furth, 2014).

Noblesse et al. followed the Neumann-Kelvin approach with a modification that resurrected some of the analytical approach of Michell to create the Neumann-Michell theory. This analytical approach touched on previous ideas that Noblesse et al. (2013) put forward with the use of ‘slender-ships’ also attributed to Hogner. The ship model in the case of the Neumann-Michell theory is to use an integration over the surface of the hull. Such was the success of the model that the humps and hollows predicted by the thin-ship or slender-ship approaches are largely eliminated with no noticeable computational effort.

## **2.8 Clutter Scattering**

The scattering of radar energy from the surface of the sea has been shown to be the result of the combination of multiple processes. These processes are affected by external factors that likewise alter the scattering effect. This section will describe some of the primary areas for concern that need to be considered in order to generate a realistic scattering model. In bulk terms the factors can be broken down into those that are the result of the choices of the sensor, which is the simpler topic, and those that are natural characteristics of the environment. Advanced models do exist to take account of many of the effects, some focussed on specific areas of interest and some more generic, but it is true to say that limitations in understanding still exist and remain an area of study

From the perspective of the sensor there are two key elements. The first is the grazing angle at which the radar observes the scene, the second is the set of parameters at which the radar operates. Reduction in the grazing angle makes the modelling of the sea surface gradually more complex. At high grazing angles of roughly greater than 50deg the sea can be fairly

## Chapter 2 – Research Context

accurately modelled using Kirchhoff's laws of electromagnetic scattering from a conducting surface (Ward et al., 2006). At the high grazing angles the angle of incidence with respect to the surface of the sea is such that the appearance of the wave and surface features, assuming that both are relatively small in amplitude and therefore maintaining the linear nature of the modelling, are all unobscured and the relative velocities that affect the radar scattering are roughly limited to the orbital velocities of the water molecules. A common effect in this case that is observed in SAR imagery is velocity bunching as shown in Figure 27. This is caused by the SAR imaging process's use of relative Doppler frequency of return as a determining factor in the azimuthal plotting of a scatterer's location. As the orbital velocities oscillate with the wave field pattern, an artificial wave pattern is induced in the resultant image as the moving scatterers bunch and spread in line with the azimuthal displacement process, as described by Alpers et al. (1981).

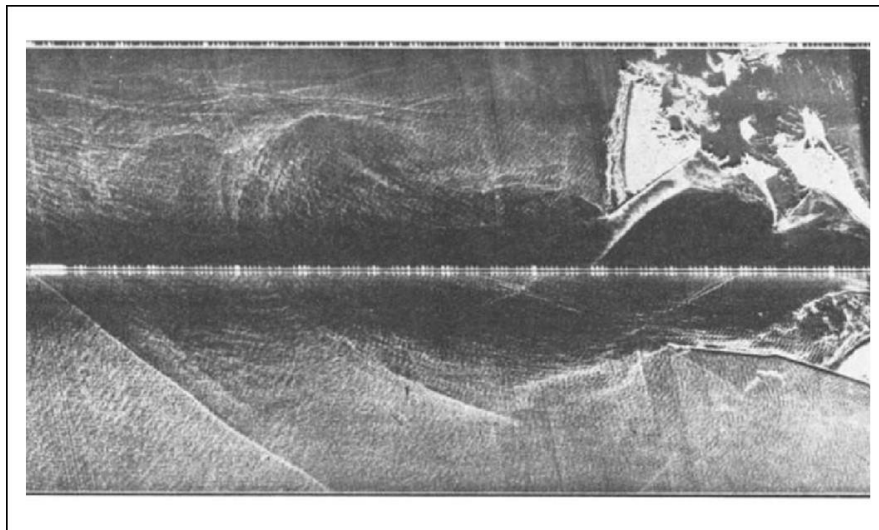


Figure 27: Chip-out from full image where fine wave patterns on the surface of the water can be seen to be formed through velocity bunching. The bright arcing and overlapping features are formed from the interaction of the outflow of the Columbia River (Alpers et al., 1981)

Alpers et al. describe how this effect naturally has a degrading effect on the azimuthal resolution of the SAR imagery due to radial velocity of the scatterers and, as it is a more

## Chapter 2 – Research Context

predictable process in smooth seas, can be factored-out to improve the resolution of an image post-processing. The aspect at high grazing angles also allows for a relatively balanced scattering of polarisations. However, this is much more complicated as the grazing angle is reduced. In the intermediate region, down to roughly 10deg, the grazing angle plays much less of a part in the reflectivity, often called the plateau region. The wave shape and features play the significant part in the radar returns. Bragg scattering becomes the dominant mechanism, which has in this case a strong VV polarisation, and the wave velocities that are engendered by wind and tide effects influence the scene (Walker, 2001). Below the intermediate region mechanisms such as wave shadowing, breaking and multipath scattering further complicate the environment and necessitate specific attention (Ward et al., 2006).

The second major factor is the radar itself, and central to this is the frequency band at which it operates. The band will have a significant impact on the scattering mechanism that will dominate the return. The presence and distribution of the required scatterers will vastly change the image that the radar returns dependent on band. For instance, X-band is dominated by Bragg scattering from the gravity-capillary waves due to the similarity of the dimension of the gravity-capillary waves and the wavelength of a generic X-band sensor (Guo et al., 2009). Conversely, a HF radar has much less focus on the ripples and can readily interact with the large-scale swell of the open sea (Anderson, 1991). The resolution cell size is also worth consideration here as a useful comparison can be made with the scale of the surface wave pattern, which has general rules that govern the magnitude of the most common and routine waves. In this case the resolution cell size determines how much each cell return ‘sees’ of any given wave pattern and what wave features, and therefore scattering mechanisms, contribute to that return (Watts et al., 2005)

## Chapter 2 – Research Context

The sea surface features are more diverse, unpredictable and complex than the radar and thus continue to provide unanswered questions for researchers. A first examination can begin by assuming that the surface of the sea is a simple superposition of multiple waves of varying frequencies that behave in an entirely linear way. This is known to be not entirely accurate as breaking waves and non-linear wave interactions are clearly visible, however, the assumption is not entirely without merit as the treatment of the sea in such a way can produce relatively effective Doppler spectrum models of the sea surface, as shown by Liu et al. (2012). Even with such an assumption a primary mechanism for the scattering variation can be explained. Particularly linked to the Bragg scattering from small-scale waves, tilt modulation is key to explaining the scattered energy. The small-scale waves are seen to ‘ride’ on the large-scale swell. The angle that the local small-scale waves are presented to incident radar energy then has a powerful effect on the reflectivity. The small angle of incidence gives the waves, locally to the front face of a wave approaching the radar, a high reflectivity compared to the higher incidence angle of the back face of the same wave (Lyzenga, 1986).

On top of the tilt modulation effect, in a similar manner to SAR imagery of a land target, the image remains constrained by speckle. In this sense, speckle is a phenomenon within SAR imagery that gives an apparent uniform surface a mottled texture due to the summation and interference of the returns from multiple individual scatterers within each resolution cell. The phenomenon is common in coherent imaging systems, for example holography, which is the case in most SAR configurations, as long as the number of scatterers per resolution cell is large, where Bragg scattering is the primary mechanism (Ward et al., 2006), a plot of which can be seen in Figure 28. The final main effect to add to this constrained model is the use of shadowing. Shadowing becomes more of a factor for small grazing angles but cannot be discounted in the intermediate region where isolated large waves may occur to compound the



model. Watts et al. (2005) explain that shadowing and multipath effects are a direct result of the shape of waves within a scene and subsequently play a significant part in determining the polarisation dependence of the scattered returns. In this case, the multipath effects are radar rays that leave the transmitter and find a route that allows them to return to the receiver having reflected more than once on the surface.

In order to improve a model of the sea clutter further the stochastic effects of the surface need to be taken into account as, although isolated in cases, the intensity of each is such that they play a large part in the overall radar response. As the sources of the clutter are even less mechanically predictable than the tilt modulation and the Doppler spectrum modelling the ability to produce a determinate model is limited. However, much success has been achieved through use of statistical approaches that address the temporal and spatial properties of the clutter as well and a measure of the correlation (Leonard et al., 2002). Presumably originally used as a descriptive term to explain the spikiness of the reflectivity of real sea clutter at low grazing angles, sea ‘spikes’ are the key feature that needs to be added.

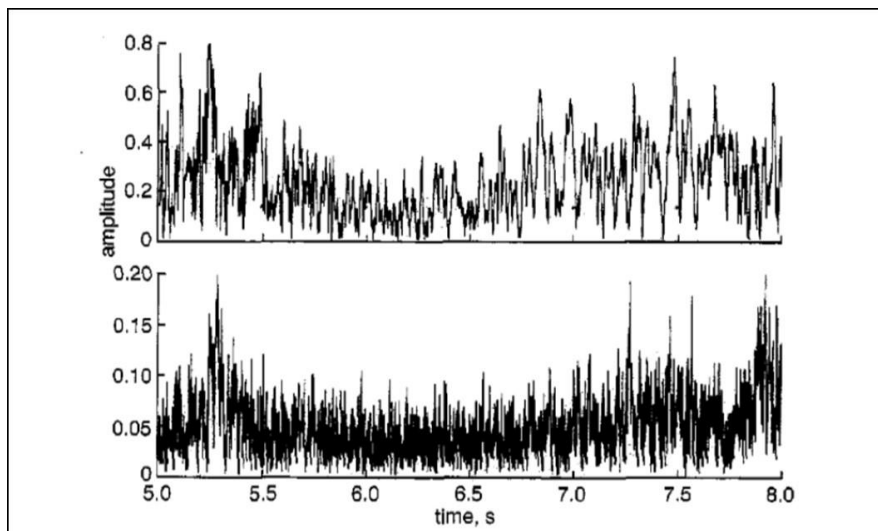


Figure 28: Plots of amplitude against time for different polarisation (VV at top, HH at bottom) returns from a patch of Bragg scattering sea surface (Walker, 2001).

## Chapter 2 – Research Context

Spikes have been long attributed to wave breaking events with considerably resilient mechanism constructions (Watts et al., 2005). The Bragg scattering produced by the many independent contributions locally gives rise to a Gaussian statistic. It has been noted that the Bragg scattering is dominated, in magnitude terms, by its VV polarisation. Bragg scattering also shows low Doppler velocities and a short decorrelation time, which implies a relatively broad spectrum (Melief et al., 2006). The swell, which is of a much larger scale than the Bragg susceptible waves, has a longer correlation time than is seen in the localised speckle features from the Bragg mechanism. The return from the texture or the local mean level can be modelled well with a gamma distribution (Watts et al., 2005). In order to include the spiked features within the observed statistics, using hypotheses that the spike is associated with breaking wave phenomena, the K distribution with a gamma distribution texture has been suggested and shown to be a good fit by several authors including Ward et al. (2006). Further analysis has expanded the field. A breaking wave event has been shown to include two prominent mechanisms that contribute slightly differently to the overall clutter picture. Through use of temporal, Doppler and polarisation analysis it is readily achievable to discern the mechanism.

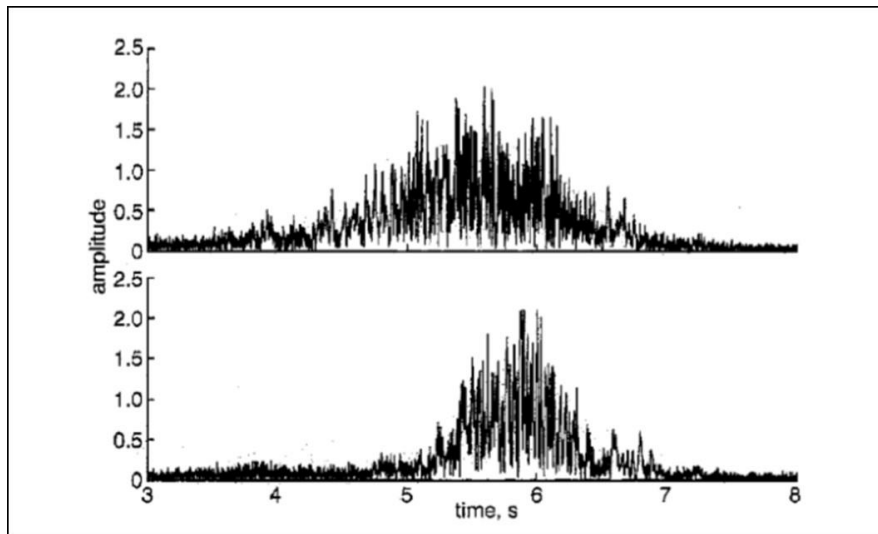


Figure 29: Plots of amplitude against time for different polarisation (VV at top, HH at bottom) returns from a whitecap scatter event (Walker, 2001).

Firstly, the whitecap effect is proposed to be caused by the chaotic breaking rough water that can be seen visually when the tips of a breaking wave turn a distinct white colour. The timescale of the whitecap effect is of the order of seconds but are seen to be noisy in structure such that they decorrelate quickly, in the order of milliseconds, as shown in Figure 29 (Walker, 2001). The whitecaps also demonstrate a much more even polarisation profile, with respect to the relative magnitudes of the polarisation channels, than the Bragg scatter and also a higher Doppler frequency. The spectrum of the Doppler frequencies can also be seen to be broader than Bragg (Watts et al., 2005). This is strong evidence to show that the more random scatterer orientation in the rough and white-water at the top of the wave, where the greater particle velocity can be found, is the source for this mechanism and as such is given the name whitecap. Alpers et al. (1981) considered the use of Rayleigh scattering to explain the whitecap appearance due to the hypothesis that the bubbles within the water and water droplets above the wave crest may contribute a significant Rayleigh scatter mechanism to the return. Although there was some caveat given to the number of bubbles that would be

sufficient to be able to make the mechanism significant it was concluded that the Rayleigh mechanism would not normally be dominant.

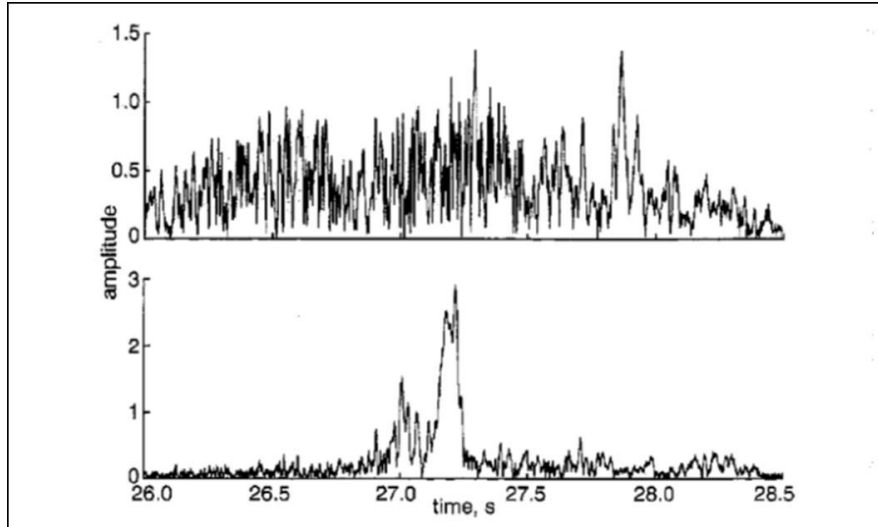


Figure 30: Plots of amplitude against time for different polarisation (VV at top, HH at bottom) returns from a burst scatter event (Walker, 2001).

Secondly, bursts are another feature created by breaking waves. These are specular returns, often stronger in intensity than the whitecaps, that are much shorter lived on a timescale of fractions of a second, Melief et al. (2006). They have a velocity characteristic similar to the velocity of the top of a wave, again supporting the proposed mechanism source. A burst is likely to remain coherent over its timescale and, an interesting property, has a strong polarisation opposite to the Bragg scatterer; the bursts are higher HH polarised compared to their VV effect, as seen in Figure 30 (Walker, 2001). Walker also noted that this effect is particularly strong close to the Brewster angle. This has brought some to conclude, including Holiday et al. (1998), that the source of the burst effect is from the steepening and immediately breaking section of a wave front. Melief et al. (2006) have specifically examined the velocity observation of the burst effect. It was found that the burst often exhibits a Doppler velocity that is greater than the ambient maximum. It was also shown that

large burst events could occur that would extend over several range cells, for certain given resolution cell dimensions. Similarly, it was shown by Ward et al. (2006) that a jet of water could be produced during large breaking event that travels forwards and hits the leading face of the steepened breaking wave. Again examining the statistical descriptions of the clutter, the KA distribution that was originally described by Middleton has been shown to produce a good fit for the expected returns from sea clutter that includes Bragg scattering, whitecaps and bursts (Watts et al., 2005). Within these, the discrete spike events are proposed to have an occurrence frequency described by the Poisson distribution and the intensity of their contribution is given by the exponential distribution. Watts et al. used such a model to the extremes of using a rough sea to show that the composite tilt modulation model that takes into account multipath effects and breaking waves produces good results against experimental measurements for sea clutter at low grazing angles.

## **2.9 SAR Imaging Analysis Tools**

The use of sub-aperture techniques is by no means new for the purpose of additional analysis of a SAR image. There are multiple reasons for the extra processing steps. The purpose of using such a technique in this case is to gain further information concerning the extended azimuthal bloom artefact within the image, as Figure 1, to either identify the source or at least provide evidence for analysis that will follow. First, it is necessary to understand the characteristics of sub-aperture processing, any limits or constraints imposed by its use and select a suitable path ahead.

**Target velocity estimation.** The separation of a given aperture into multiple sections of given time durations allows for detailed analysis of the velocity of a scatterer within the scene. Constraints are put on the accuracy of the estimation. The estimation of the cross-range velocity can be achieved in a similar manner to range velocity estimation by measuring

the range displacement sub-image to sub-image but is significantly coarser than the estimation of the radial velocity due to the different image phenomena incurred by the different components of the target velocity. Lombardo et al. (2006) suggest use such of a technique with along-track interferometry to obtain accurate estimations of sea surface currents, as shown in Figure 31.

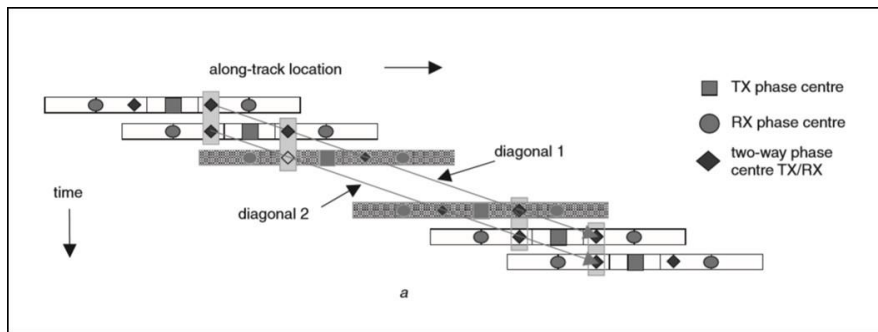


Figure 31: Along track interferometric technique used by Lombardo et al. (2006) to separate a full antenna into multiple phase centres to elicit velocity information from a particular scatterer through the SAR imaging process.

**Moving target relocation.** The natural progression, once target velocity has been approximated, is to manipulate the SAR image such that the moving target is relocated and refocussed. If successful, this allows for detailed analysis of the target once focused, effectively, back to where it should be within the image plane and undistorted by the standard SAR imaging phenomena. Gu (2018) explains that conventional algorithms, such as Map Drift, Contrast Optimisation and Phase Gradient Autofocus, have shown success at refocussing the smeared returns of moving targets but add considerable computational burden. Calloway and Donohoe (1994) argue that the limitations on such autofocus techniques are that they only estimate greater-than-first-order parameters. Through the use of a sub-aperture approach, the estimation of the motion in the slant-range direction can be made more accurately, which is very important in reducing Doppler centroid shift and reduction of any additional range walk. Low-order phase error results in the widening of the

mainlobe of the point spread function whereas the high-order phase error raises the side-lobes of the point spread function. The sub-aperture approach estimates the drift between pairs of maps in order to ascertain the linear trend in the phase function. The two-stage approach of estimation of linear phase term for range walk, shown in Figure 32, and then an interpolation step for higher-order range curvature correction is successfully applied by Moreira (1992).

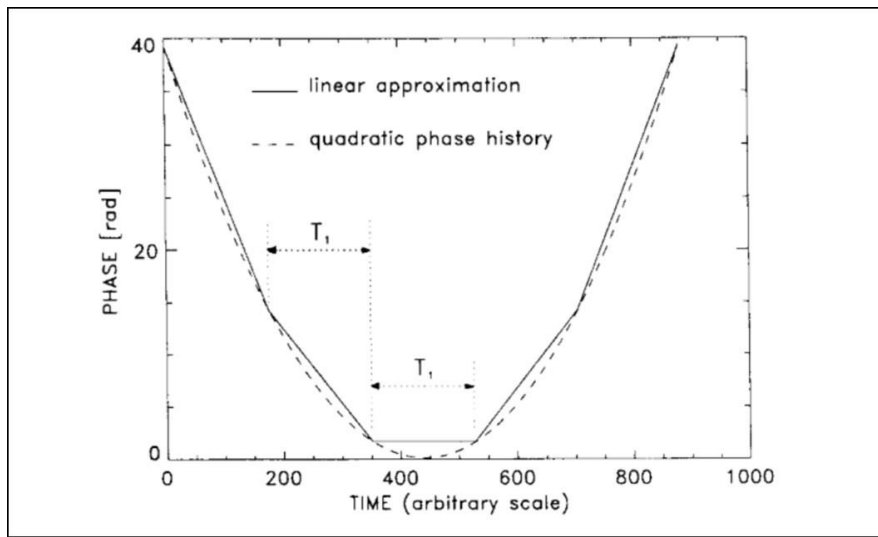


Figure 32: Plot showing the linear approximation of the quadratic phase history used by Moreira (1992) in the real-time SAR algorithm.

**Target identification.** Particularly through the use of multiple polarimetric sub-channels, sub-aperture analysis can be used to divulge greater detail about the composition or structure of a given target than would be otherwise possible. This is due to the naturally differing reflectivity or reactivity of a target to illumination with respect to imaging angle. It is normally a fundamental assumption of the SAR imaging process that a given target is an isotropic scatterer but inspection of any given real target would find that this is hardly ever the case. Lombardo et al. (2006) proposed artificially splitting the active phased array of the COSMO-SkyMed radar to obtain multiple receive channels. Ferro-Famil et al. (2002) have extended this analysis using an eigenvector/eigenvalue decomposition theorem to establish

two main parameters for pure scattering mechanisms, as shown in Figure 33: the indicator of the nature of mean scattering and the entropy that indicates the random behaviour of the global scattering, thereby allowing non-stationary target segmentation.

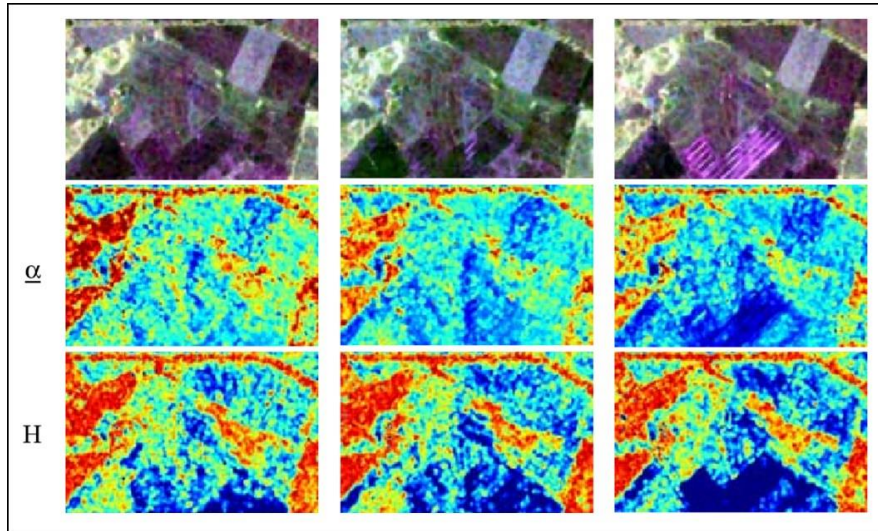


Figure 33: Sub-aperture image set, top row, showing a slight variation in returns from fields due to anisotropic scattering. The use, by Ferro-Famil et al. (2002), of the mean scattering parameter  $\alpha$  and the entropy  $H$  produce the bottom two rows of image data giving an analyst greater information with which to understand the nature of the scatterers within the scene.

**Computational burden.** By dealing with sub-apertures rather than full data-sets, there can be significant reductions in computational burden as each sub-aperture. If the size in time or frequency domain is chosen selectively, essentially if the domain is considerably smaller than the whole, then the apertures can be dealt with in a linear fashion by the approximation that the quadratic phase terms are negligible. This modelling step opens multiple data manipulation possibilities for real-time SAR processing as explained by Moreira et al. (1994). The application of such techniques to space-based sensors, where linear range cell migration dominates, is significantly advantageous through the reduction of downlink data rate requirements. Veneziani et al (1995) use segmented sub-aperture data from the AVIOSAR-580 and ERS-1 alongside a method based on Wigner distribution analysis of SAR data to create a fast autofocus that benefits from the computational simplicity of using shorter



periods of time rather than the total SAR integration. This resulted in imagery of 1 m resolution rather than the 3 m resolution of the conventional technique.

The benefits of sub-aperture processing through the ease of computational burden has been applied to the synthetic environment as well as for real radar. Accurate, fast-time, radar simulation is very computationally intense, which is exacerbated for a SAR simulator due to the need to store large numbers of coherent data samples prior to batch processing to form the resultant image. Similar techniques that allow processing steps to be simplified for a real radar can also be applied in principle to a simulated process to alleviate the burden whilst still producing satisfactory simulated outputs. Zhang et al. (2010) have shown success in this approach using their echo simulation algorithm SAR processor. It first uses a 1D FFT in range to establish the central pulse's signal of each sub-aperture then a first-order approximation model in azimuth to generate the other pulses' signals. Due to the simplification of the approximation, particularly against target scenes that contain high numbers of scatterers, the sub-aperture approach displays speeds of processing up to 34 times faster than conventional control processes. The geometry is shown in Figure 34.

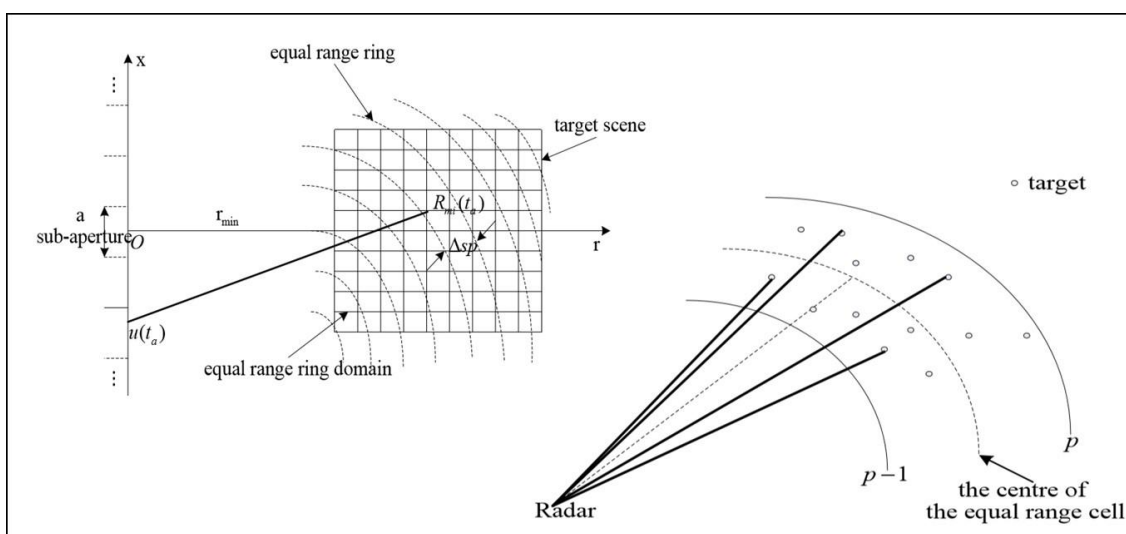


Figure 34: Diagrams showing the construction of the simulated imaging geometry used by Zhang et al. (2010). The sub-aperture approach taken allows for many targets to be grouped into range rings to reduce the number of computations required in fast-time.

**Ship detection.** It is noted by Chen and Wu (2009) that the difference in reflectivity of the sea surface with polarimetric channel forms an important option in the detection of ships. The comparative reflectivity of the sea surface to the target vessel is normally largest in VV, more so than HH but there are many dependencies on the condition of the surface of the sea and inclement weather that can play a major factor in this comparison. An example of the comparative reflectivity of a sea and target scene under different polarisation conditions is shown in Figure 35.

## Chapter 2 – Research Context

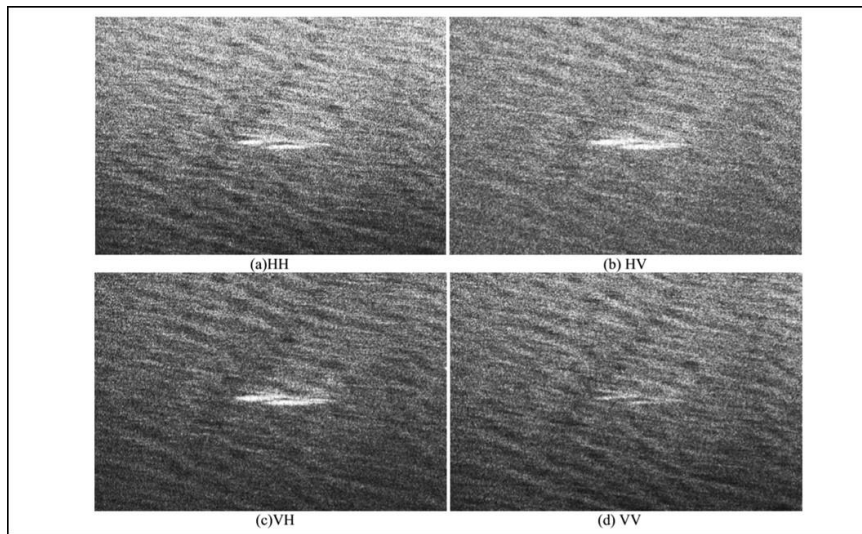


Figure 35: SAR sub-images of Chen and Wu (2009) showing the target response of two ships in close formation have in multiple polarisations.

Due to the relative size of a ship to the resolution cell and that the sea surface is a summation of many time-dependent scatterers, a ship can be considered to have deterministic scattering behaviour. It is postulated that the HH polarisation channel is best for the detection of shipping as the background sea surface reflectivity is lower than in the VV or the co-polarised VH channel but the ship return will be roughly the same and therefore offer a greater detectable signature. It should be noted that there is some dispute between authors on this subject as to the best channel to select for this purpose. Chen and Wu expand on the previously studied ship detection capabilities of RADARSAT-1, ERS-1/2 and ENVISAT by examining RADARSAT-2, ALOSPALSAR and TerraSAR-X using termed ‘optical coherence techniques’ to remove sea clutter from the images and reveal the ship targets, as shown in Figure 36.

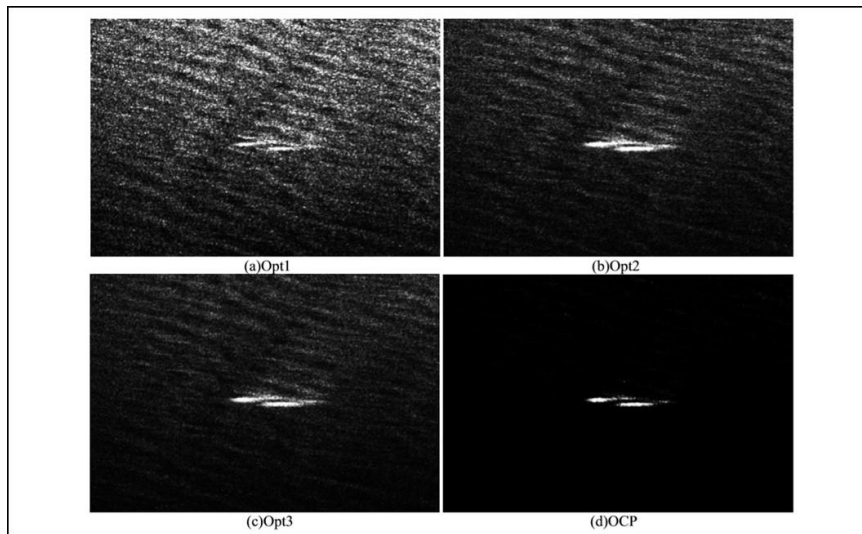


Figure 36: Subsequently processed images from Figure 35 with examples of the effect of processing techniques that Chen and Wu (2009) applied. Sub-image (d), the optical coherence product, is a compound of the other three techniques and results in a strong contrast between the two ships and the surrounding sea clutter.

Greidanus (2006) terms the acquisition of different polarisation channels by sub-aperture SAR as an alternate polarisation technique. The characteristic of this approach allows the inspection of different polarisation channels to be equivalent to different, non-overlapping sub-apertures. This is used in an attempt to explain the appearance of individual ships as two peaks, attributed to wave motion, seen in RADARSAT imagery shown in Figure 37.

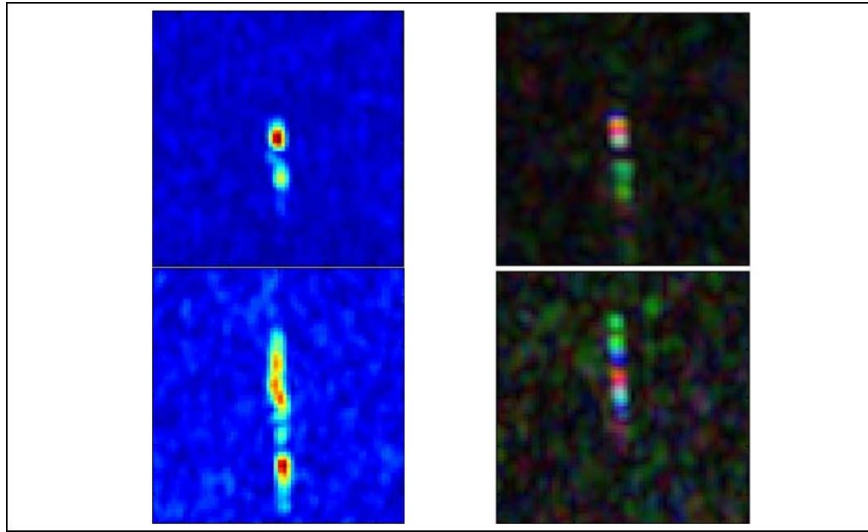


Figure 37: Images processed by Greidanus (2006). The left images are simple processed 500 m x 500 m SAR image tiles of individual ships. The right images have been sub-aperture processed with different colours attributed to different polarisation combinations. The dual peak feature was of keen interest and attributed to wave motion.

**Optimising hardware processing.** Acknowledgment that the hardware that conducts the processing of imagery is characteristically discrete allows for certain optimisations to be attempted. By way of example used by Moreira (1992), in the image construction for the DLR airborne SAR (E-SAR), using a sub-aperture approach groups the data required into batches. These batches were each given to a dedicated processing unit and thereby decreased processing time.

**Temporal analysis.** Decomposition of a SAR image can provide great detail of a target due to the, normally, extended period over which an image is collected. This decomposition can directly display the time-based dependence of the target area through the SAR collection or by inference, due to the known and expected relative motion of the sensor to the target scatterer, the directional dependence of the target backscatter can be measured. Ainsworth et al. (1999) use a Fourier transform-based technique on the complex imagery, in the azimuth direction, to recreate the phase history of EMISAR.

Ainsworth generates a blunt form of temporal analysis, joint time-frequency, where the sub-aperture approach is used to generate multiple images from an original single-look, high-resolution master complex image. The resolution is somewhat sacrificed but the resultant image set creates a time series of the activity captured within the time of the synthetic aperture of the primary collection.

**Advanced processing.** The coherence of the SAR sensor allows for fairly ready application of advanced image processing techniques to the imagery, such as coherent change detection and interferometry. Madsen (2010) have demonstrated use of sub-aperture SAR techniques coupled with interferometric splitting of a wide antenna beam to examine the height estimations of the imagery pixels in detail from look to look. The imagery result was shown to generate more distinct and accurate topographic approximations.

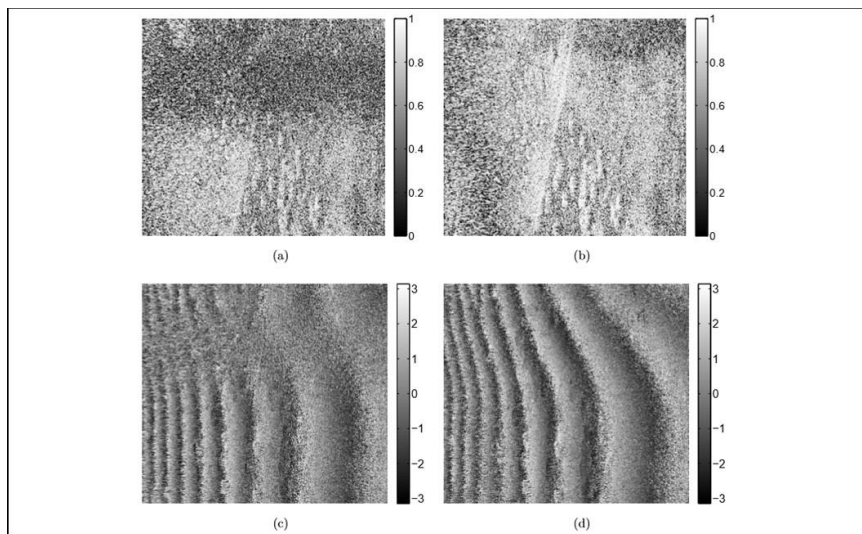


Figure 38: Image chip-outs from Madsen (2010). The left column shows the initial image on the top row with its coherence image below where a decorrelation artefact can be seen in both. The right column shows the corrected image and coherence map after processing by the aperture splitting technique.

**High squint SAR.** Due to the large range walk, high squint imagery is very hard to achieve for the earlier lower dimensional imaging techniques, such as the range-Doppler algorithm

family. Higher complexity techniques, such as the wavenumber or chirp-scaling algorithms, have since shown ability within this footprint of a given sensor. However, Yeo et al. (2001), demonstrate the use of a sub-aperture processing technique that can be effectively used to counter the effects of the quadratic, and higher-order, phase terms. This almost pseudo-linearisation is only valid in this region as the sub-apertures are smaller than the whole and artificially reduce the range migration needing to be considered at each step. The effect of the approach is shown in Figure 39.

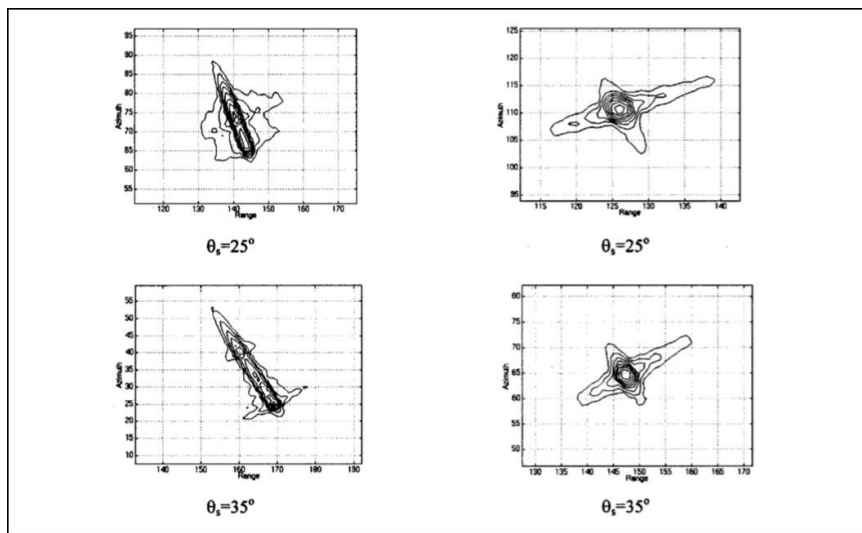


Figure 39: Plots of simulated point targets taken at high squint angles, Yeo et al. (2001). The left column images are processed using a standard step-transform whereas the right column is the same target processed using their high squint SAR algorithm.

**Target scatterer characterisation.** Having discussed the benefits of the use of sub-aperture analysis to realise detail of the target with regard to the angular dependent scatterers, it is worth note that the principle can be further extended. Other qualities that lead to variation within the sub-apertures can be the result of target scatterer material and that of the surrounding surfaces. Singh et al. (2010) extend the azimuthal sub-aperture analysis techniques to include decomposition of the range dimension also using single look complex data of the high-resolution spotlight from the TerraSAR-X. The broad range chirp of the



sensor allows for comparable use of the range dimension to azimuth and the combination of both creates a form of processing termed time-frequency analysis, proposed by Spigai et al. (2008). The output is a 4-dimensional function that can be readily viewed by an analyst in 2-dimensional form as radar spectrograms. An example of this is shown from Singh et al. (2010) at Figure 40. Whereas the SAR image of each of the insets in Figure 40 have the purpose of finding what the target looks like, the spectrogram allows the radar analyst to visually examine the behaviour of the target scatter or scatterers through the collection period by use of the frequency or spatial frequency domain. This allows for further classification of scatterers that would otherwise look almost identical in the processed SAR image.

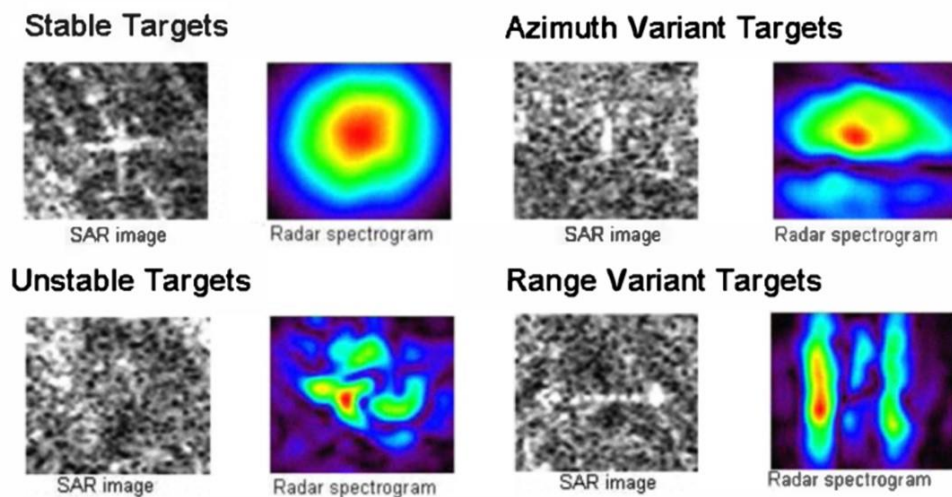


Figure 40: Spigai et al. (2008) show the behaviour of targets with different characterisation properties having used a radar spectrogram technique to decompose the original full SAR image.

**Speckle noise reduction.** The appearance of speckle in SAR imagery has already been explained as a natural result of the use of a coherent imaging technique and will remain within the image regardless of the length of the synthetic aperture. However, due to the noisy quality of the phenomenon, and its variation when compared to the more stable scatterer returns from coherent image scatterers, the use of sub-aperture processing does allow an opportunity to reduce the effect of the speckle on a resultant image. Zhang et al. (2010) use



an algorithm where the relative pixel returns from four sub-apertures are compared to produce a filtered final image that has noticeably reduced speckle. The final images presented do appear to have lost some of their analytical quality by a reduction in spatial resolution albeit with improved noise reduction.

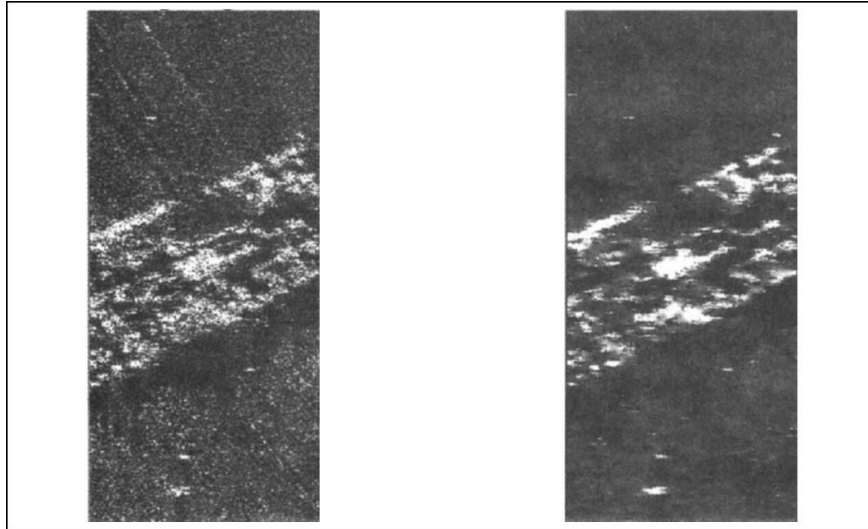


Figure 41: Image comparison conducted by Zhang et al. (2010) where the real image on the left has been processed for speckle reduction using a four sub-aperture split technique to produce the image on the right.

The previously described coherent scatterer detection, at Figure 35, is similar to the speckle noise reduction approach but from the perspective of maximising coherence rather than reducing incoherence

**Flash reduction.** It should be noted that the term used here is different from the term in optical sensing. Flash, here, is an angular dependent increase in radar cross section that has the effect of overloading a full aperture SAR image even though the effect is only present for a small time of angular segment of the aperture. A development of the target characterisation where the target is known to have angular dependent scattering properties is to correct the degradation to a final image that can be caused by angular dependent glint of a target.

Ainsworth et al. (1999) discuss that after the separation of an image data-set into sub-

apertures, those that contain the glint artefact can be identified and nulled prior to image re-composition. The filtered final image can be seen to be much improved as a result of the sub-aperture manipulation.

## **2.10 Sub-Aperture Processing Methods**

**Multiple channels.** The sub-apertures can be formed at source through the design of the sensor. Lombardo et al. (2006) propose the use the radar of COSMO-SkyMed by splitting the active antenna into multiple receive channels and thereby create the sub-apertures required for their processing. This is a similar approach to displaced phase centre approach used in moving target indication. The use of such a technique has great advantages through the control of clutter and the algorithm required for image processing is very simple meaning that there is little penalty for conducting the processing on-board, which is of particular benefit for a space-based sensor. However, there are limitations imposed on the PRF tuning that is required to compensate for the rotation of the earth, satellite orientation and platform motion errors that all add to the computational load of the process. Further, high PRFs are not generally desirable for space-based platforms due to the inherent range ambiguities that are subsequently introduced. A need to carefully choose the PRF in order to balance range and Doppler ambiguities is a common problem for all radar systems. One particular advantage that Moriera argues for with regard to hardware design is through the use of parallel processing. In this case, each chain requires a dedicated processor but if achieved then the time is significantly reduced. Such an aim was put under development for the C-band DLR airborne SAR system (Moriera, 1992).

**Polarisation channels.** In a similar way to the multiple channel approach, radar design that enables the transmission and collection of all combinations of polarised radar energy creates sub-aperture channels that can be used for processing. The use of different polarisation

channels between the apertures has added benefits with regard to supplying the operator with a greater spectrum of information concerning the target reflectivity as well as creating the opportunity for sub-aperture processing. This approach has been successfully applied by Greidanus (2006) by separating the azimuth bandwidth of RADARSAT data into three non-overlapping apertures against ship targets. The use of the three sub-apertures was shown to improve the standard ship detection mechanism of thresholding the multilook intensity over the local clutter levels by having three images rather than a single to perform the target-clutter separation. By matching the sub-aperture point spread functions to the target size further optimised the threshold detection method.

**Raw signal.** Without specific hardware design already in place, the sub-aperture techniques can be achieved through use of the raw fast-time video phase history from the real radar processor. In this case, the received pulses are grouped into batches that are both time and physically displaced. This creates differing phase centres and very separate image data-sets that can be independently processed as per a larger SAR image. Moreira et al. (1994) used a batch processing technique to particularly good effect for the optimisation of space-based performance with a real-time sub-aperture algorithm. The sub-apertures generated from the raw video phase history are processed in an unfocussed form, which negates the need for quadratic phase corrections. The resultant images are coherently summed to produce the final output. Particularly useful in C- and X-band where most of the range cell migration is linear, the overall approach has shown comparable results to the impulse response function of a conventional method but at significantly reduced down-link data rates. There are many options available for the structure of the sub-apertures. The overall collect is limited by the real radar characteristics and the parameters imposed by the full synthetic aperture generation. However, freedom to use the full recorded raw signal allows for the optimisation

depending on the intent of the product. Madsen (2010) uses five overlapping sub-apertures from within the 20° real L-band beam to conduct scene height estimation in order to improve the coherent change detection and interferometric images. Yeo et al. (2001) use the step transform, as part of their application of sub-aperture processing in high squint cases and identify that the spacing of the sub-apertures is important in setting the data ready for transformation. An overlap ratio of 0.6 is used in order to reduce frequency aliasing and prevent image degradation. Of note, in this case of high squint, the conjugated reference signals that are used to multiply the complex raw signal with are scaled to include the varying azimuth chirp rate that is expected in that geometry.

**Processed signal.** A simpler method than fast-time video phase history use is through the manipulation of the processed complex SAR image data. From the complex data-set, the sub-apertures can be formed through the un-weighting, division of the spectrum and then separation. Each batch is then weighted and processed individually. The use of the complex SAR data alone makes this approach readily achievable for all hardware types and does not have the significant data burden of the fast-time approach. There are pitfalls and errors that are built in to the interpretation of this method mainly due to the non-specific separation of the sub-apertures, either by time and/or displacement, which will be touched upon in Chapters 3 and 5.

**Step transform.** The step transform is a common technique used in the processed signal space where the sub-apertures are formed through the multiplication of the SAR data-set with over-lapping conjugate reference signals. The batches are transformed via FFT and time-delayed before being formed into each sub-image through an FFT process. As with all sub-aperture processes, there is under-sampling that results in the degradation of the resultant image compared to the full aperture output, normally through reduced image resolution.

## **2.11 Summary**

This chapter has aimed to establish the context of research problem and where within the wider field of research the thesis methods developed sit. The origin of the ship and wake artefact in SAR has been described from the use of a geometric focussing (GF) technique from low grazing angles. Key previous work in the multiple fields of ship wake modelling, sea clutter scattering and sub-aperture SAR processing have been introduced. All of which will be required to progress towards a satisfactory answer as to what the ship and wake artefact is and how it forms within the SAR image. Having reviewed previous work, the next chapter will begin the new analysis of the artefact, starting with application of a bespoke sub-aperture technique to deconstruct the full SAR image in order to improve the understanding of the problem.

### **3 CHAPTER 3 – SUB-APERTURE ANALYSIS**

#### **3.1 Introduction**

For the purpose of the investigation into the wake phenomenon, a sub-aperture approach was chosen to breakdown the appearance of the target within the image with the aim of aiding the understanding of the mechanism that underlies the artefacts. As a moving target, the ship and its wake are fitting for the application of a sub-aperture technique, as has been suggested for moving targets by multiple sources. The chapter will explain the details of the particular approach that has been chosen and how it has been implemented in this case. The output of the sub-aperture technique is presented with subsequent analysis of the results. It will be shown that the application of the approach did not provide evidence to allow a direct answer to be drawn for the artefact. However, several interesting phenomena are identified relating to variation of the image intensity, variation of the target vessel return, appearance of the background sea clutter and the appearance of specific striated features with the proposed wake artefact. Explanations for these phenomena are presented but many require further modelling that is signposted for later chapters.

#### **3.2 Technique Description**

The method chosen initially was to take a similar approach to that used by Chen et al. (2011). In this case, the complex image is the input to the sub-aperture process. The image data is unweighted in azimuth so that once the sub-apertures are formed the image intensity of each of the sub-images is not degraded when formed. The spectrum of the complex image is then sampled using a set of filters to select the section of the spectrum with which to process into new sub-images. The specific number of the filters is, in this case, made selectable for the user giving flexibility depending on the scene collection metadata and geometry. This flexibility should also allow the operator greater analytical freedom to apply

### Chapter 3 – Sub-aperture Analysis

scrutiny to the scene when used as a mainstream processing tool. Prior to re-processing, the sub-datasets are zero-padded and windowed using the Hamming window function to reduce the major sidelobe effects in the new sub-images. IFFTs are then used to generate the new sub-images. The output for the process is a selectable number of evenly spaced, overlapping, sub-aperture images from the main aperture of the collect derived from the complex processed original image in .gif format. The chosen output format makes image display and manipulation post-processing universal, easy and of low computational load. In order to achieve this process, a script has been written using Python 2.7.10 that performs the data read from the complex NATO Standard Image Transmission Format version 2.1 (NITF2.1) image and all necessary manipulation to output to Graphic Interchange Format (GIF). The flow diagram at Figure 42 shows the stages of the algorithm written to achieve this processing.

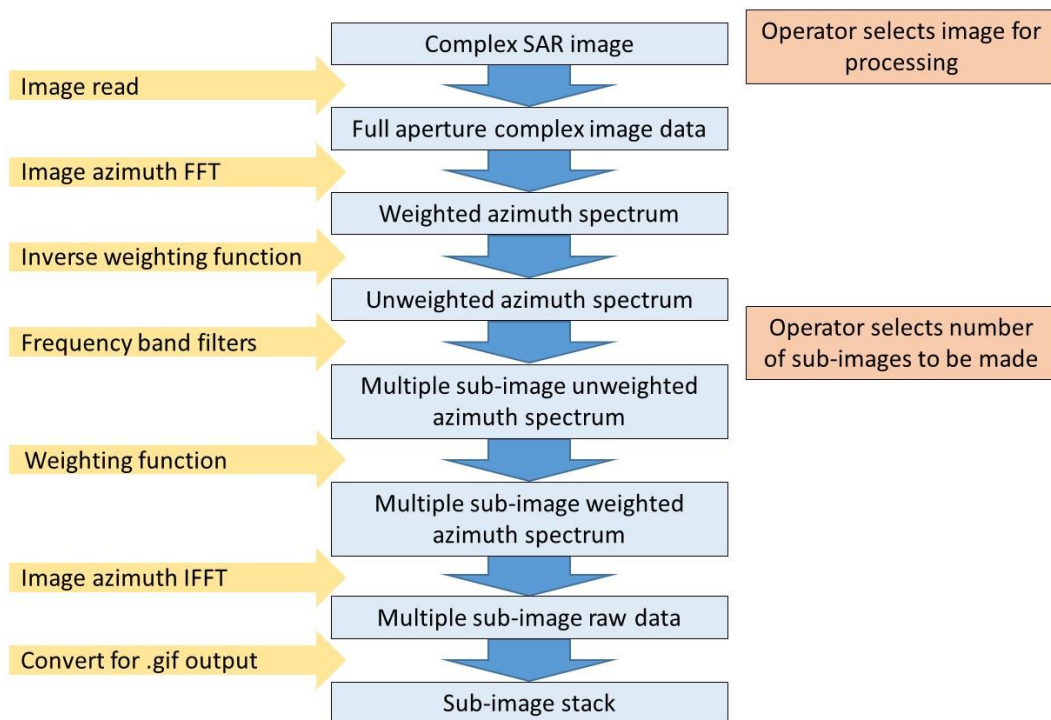


Figure 42: Flow diagram showing the stages used in the sub-aperture algorithm that is used to generate the multiple sub-images from the initial processed complex SAR image.

### 3.3 Technique Application

The formulated sub-aperture technique has been applied to multiple target signatures to deconstruct the wake artefact. Figure 43 shows a segment from the full aperture image, which has been included for context. Within the image, several key elements of the scene can be identified, including: the wake signature; the returns from the target vessel including at least one visible alias; and, background sea surface clutter. Annotations of these artefacts can be seen in Figure 44 including the orientation of the sensor to the target vessel that is tracking northbound through the image.

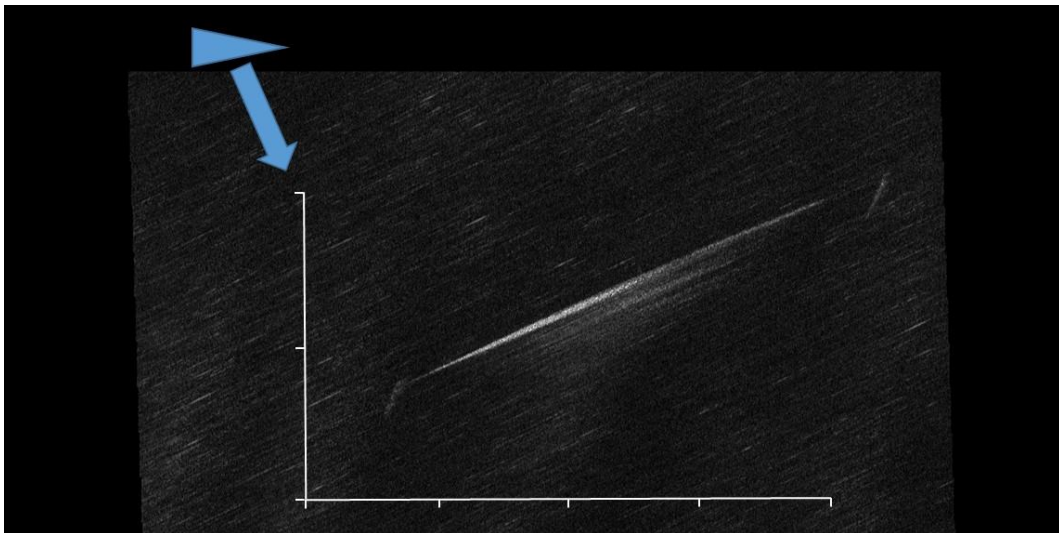


Figure 43: Chip-out from from full X-band SAR image showing imaging geometry of sensor orientation and direction of motion with scale bars (axis markings denote 500 m). The blue triangle represents the orientation and direction of motion of the radar platform and the blue arrow represents the direction of the sensor boresight during the collection.



### Chapter 3 – Sub-aperture Analysis

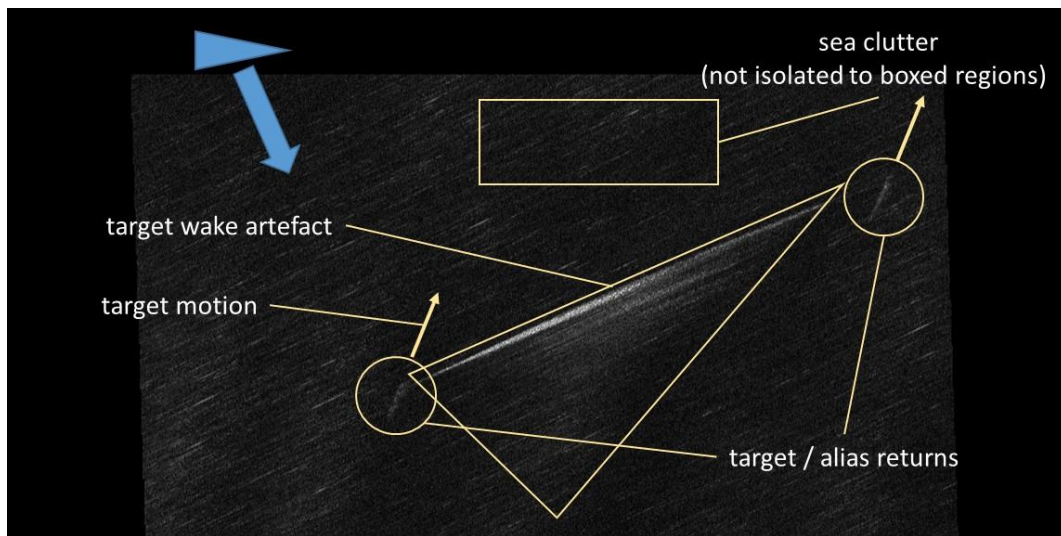


Figure 44: Annotated chip-out from full SAR image highlighting key areas of interest including the proposed target vessel returns, the artefact associated with the target vessel wake and a segment of the background sea clutter.

A set of sub-aperture images taken from this collection are shown in Figure 45 - Figure 51.

In order to create the set, the original was split into seven sub-sets with a 60% overlap and processed. The split has reduced the resolution roughly by a factor of two, as predicted by Ainsworth et al. (1999), but the main elements of the scene can still be identified readily for interpretation.



Figure 45: Sub-image 1 of 7 from full SAR image.

### Chapter 3 – Sub-aperture Analysis

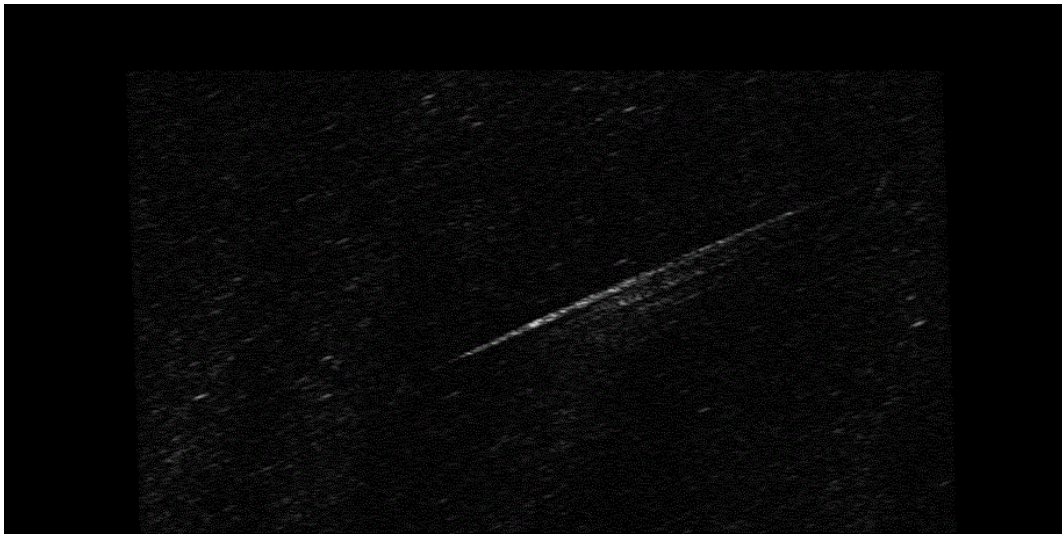


Figure 46: Sub-image 2 of 7 from full SAR image.

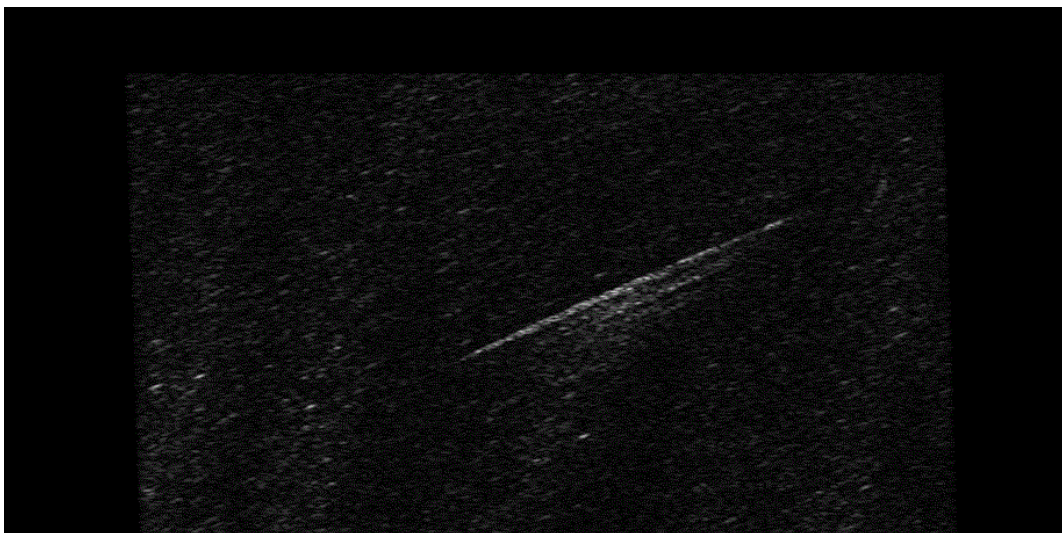


Figure 47: Sub-image 3 of 7 from full SAR image.

### Chapter 3 – Sub-aperture Analysis

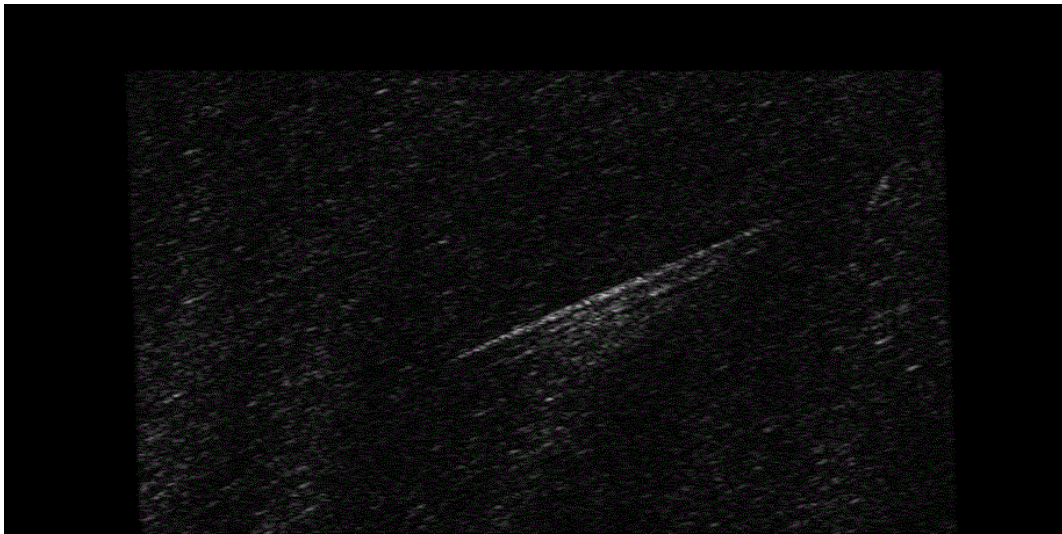


Figure 48: Sub-image 4 of 7 from full SAR image.

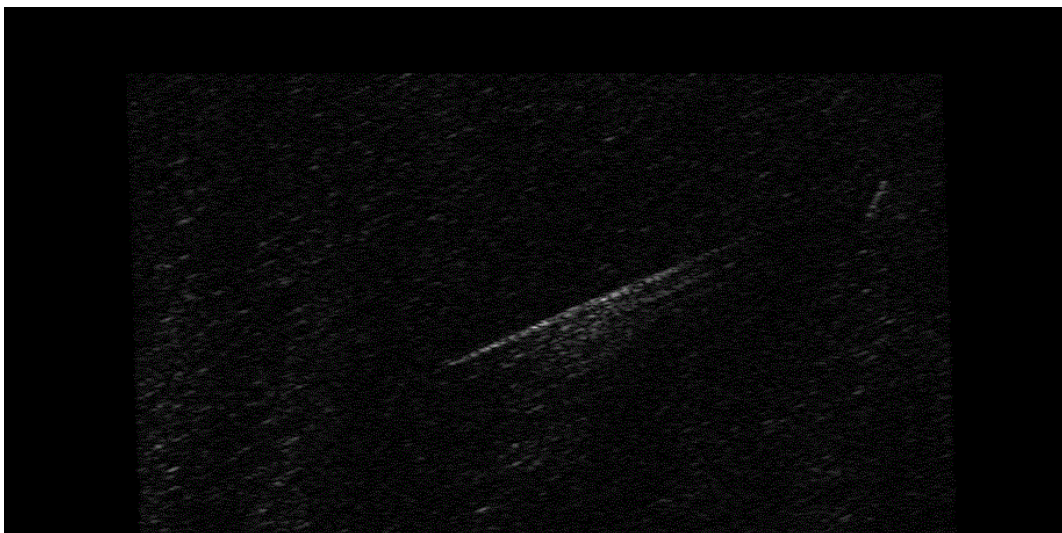


Figure 49: Sub-image 5 of 7 from full SAR image.



## Chapter 3 – Sub-aperture Analysis

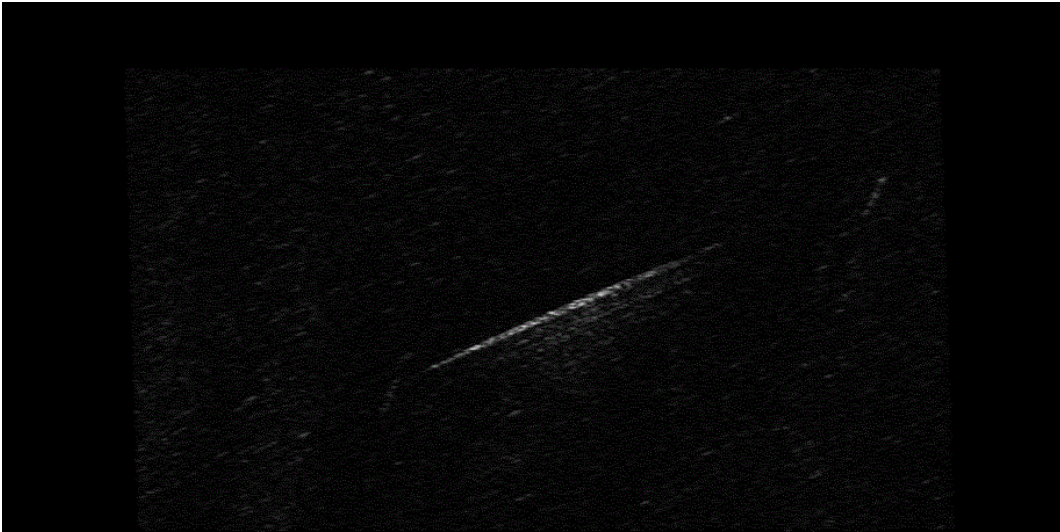


Figure 50: Sub-image 6 of 7 from full SAR image.



Figure 51: Sub-image 7 of 7 from full SAR image.

### **Image Intensity Variation**

It can be seen from inspection of the sub-aperture image set that there is a noticeable, albeit small, variation of image intensity through the aperture. The pattern begins with a lower intensity that rises to a peak in the centre image of the aperture before falling to the end. This variation can be seen from the superposed cropped image stack at Figure 52 where the initial

### Chapter 3 – Sub-aperture Analysis

sub-image,1, is compared with a mid-collect sub-image, 4, and the final sub-image, 7. The variation between end to mid sub-image is a factor of 0.101 dB using the mean image intensity as a measure. This is most likely due to an inability of the inverse weighting function applied in the sub-aperture technique to correct for the variation of the magnitude of the phase history signal in the full aperture spectrum. This could be a specific failing for this particular image but it is also possible that a global characteristic could exist. If global then the noise data that would be greatest at the edges of the spectrum, and therefore have the effect of dulling the outermost sub-images, could readily be the cause of the intensity variation. There is an inverse weighting function built in to the sub-aperture algorithm. This has been designed, for ease, to be predictive to restore the edges of the full image spectrum to a usable intensity rather than expend computational power to fully correct the phase history. On reflection, it would be a simple step to either iterate the weighting or insert a feedback circuit to refine the intensity scaling into a more moderated set. However, there appears to be no analytical need to increase the computational burden in order to smooth the images as all are usable. In its current configuration, the algorithm runs quickly enough ( $\sim 10$  s) to be used to provide almost immediate output. Finally, although artificial, the gentle variation of the intensity of each sub-aperture image gives the analyst non-intrusive feedback as to which section of the full aperture is being displayed when the sub-aperture images are displayed in succession. For these reasons, the image intensity variation was not corrected.

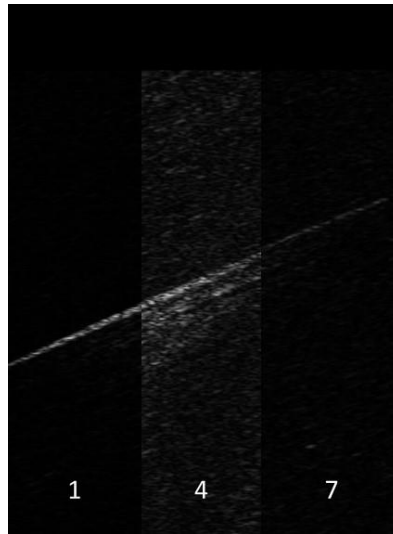


Figure 52: Side-by-side comparison of sub-images 1, 4 and 7 to illustrate the variation of overall image intensity through the sub-aperture set. It can be seen that the intensity peaks in the centre of the aperture and dims at either end.

### 3.4 Target Return Variation

The target vessel and alias returns vary in two main ways through the sub-aperture set.

Firstly, the intensity varies in bulk through the set, in line with the overall image intensity variation. There is also a small variation of intensity where comparing the right image to the left. The left return, sub-image image 1, all but disappears into the background clutter from the midpoint of the aperture to the end, sub-image 7. At minimum intensity, the target vessel is -3.8 dB darker than the mid sub-image. Unlike the overall intensity variation, the dynamic range of the target vessel return varies by 4.53 dB across the aperture. This is assessed to be due to being a less sharp alias of the primary return from the target vessel and therefore has a reduced processed return when the full aperture is split. This is likely also due to a slightly increased defocus on the more extreme alias return. A quantitative demonstration of this effect is presented in section 5.5. Secondly, the small motion of the target vessel along its track that occurs during the sensor collection can be seen as a small movement of the vessel up-image as it progresses through the sub-aperture set. Knowledge of the timespan of the

### Chapter 3 – Sub-aperture Analysis

aperture allows for the calculation/confirmation of the velocity of the target vessel. Figure 54 shows a zoomed in side-by-side comparison of this longitudinal location shift of the target vessel within the image. The illustrated markers show the extremes of the vessel and the shift between the sub-images.

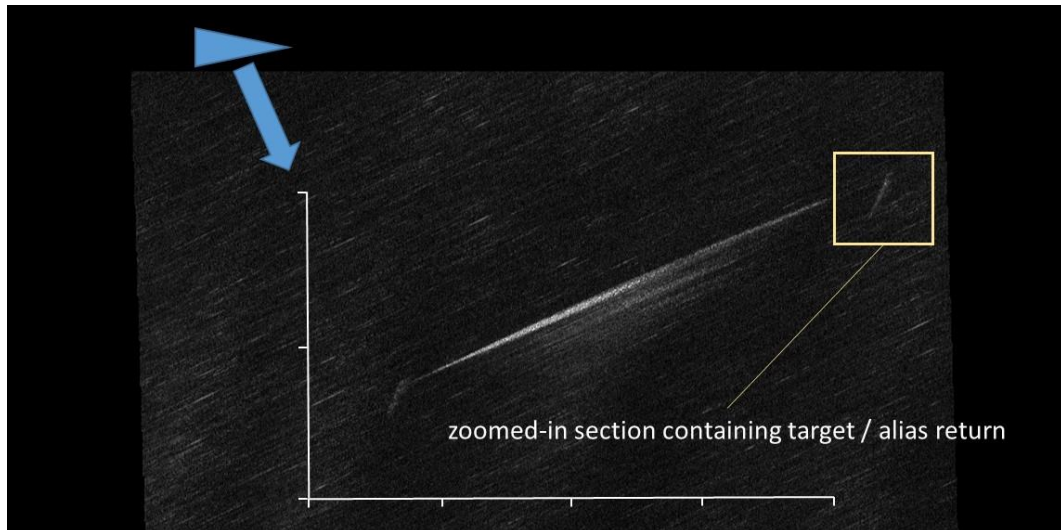


Figure 53: Annotated chip-out from full SAR image highlighting the area around target vessel return that is to be examined in the next Figure.

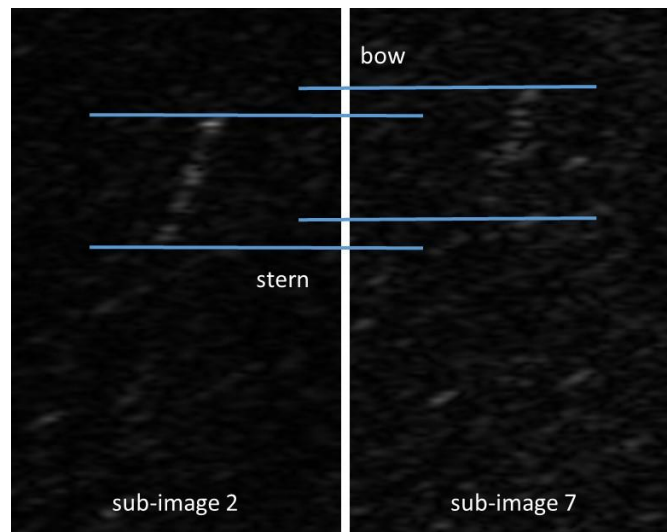


Figure 54: Side-by-side comparison of target vessel return location from beginning of the aperture to the end. The annotations shows the extent of the vessel return from bow to stern in each sub-image. Sub-image 1 was not used as the target vessel return was too weak compared to the background clutter to display satisfactorily. The comparison shows the bulk movement of the target vessel return through the aperture.

### 3.5 Sea Clutter Appearance

The appearance of the background sea clutter noticeably changes from the full aperture to the sub-aperture set. The distribution of the many, small but intense, returns shows that they are short lived compared to the full aperture and are ubiquitous across the scene. These are likely to be sea spike returns from the surface wave pattern that exhibit this behaviour as described by Watts et al. (2005) due to their high intensity compared to the background returns and the narrow azimuthal width that reads directly across from their Doppler spectrum. As the spikes are formed from the returns from parts of the background surface wave pattern that is fair to assume to be always moving then the location of the spikes in the image is distorted by the imaging process. This motion is predicted and has been measured as part of the expected Doppler velocity spectrum of spike events (Walker, 2001). The range from the sensor will be accurate but the azimuth coordinate will be unrepresentative of the actual wave's location. As the spikes can form from a somewhat chaotic process the actual locations will remain unknown but it could be possible to determine the approximate magnitude of the azimuthal displacement with knowledge of the average surface conditions of the tidal flow and wind speed. The second feature of the background clutter that is shown more clearly in the sub-aperture images is the gentle/weak 'fringe' pattern that runs throughout the image. Again, as with the sea spike effects, the pattern can be seen across the entire image area and exhibits fairly uniform distribution. The scale of the pattern would suggest that the source of the artefact is related to the background swell of the sea surface rather than the more visible surface waves related to sea state. As the surface is again moving, the formation of the pattern will have a certain degree of velocity bunching/distortion involved in the mechanism, so is not strictly representative of the scale of the swell but this could be calculated (Marghany, 2004). Figure 55 shows annotations of the background sea clutter effects.



### Chapter 3 – Sub-aperture Analysis

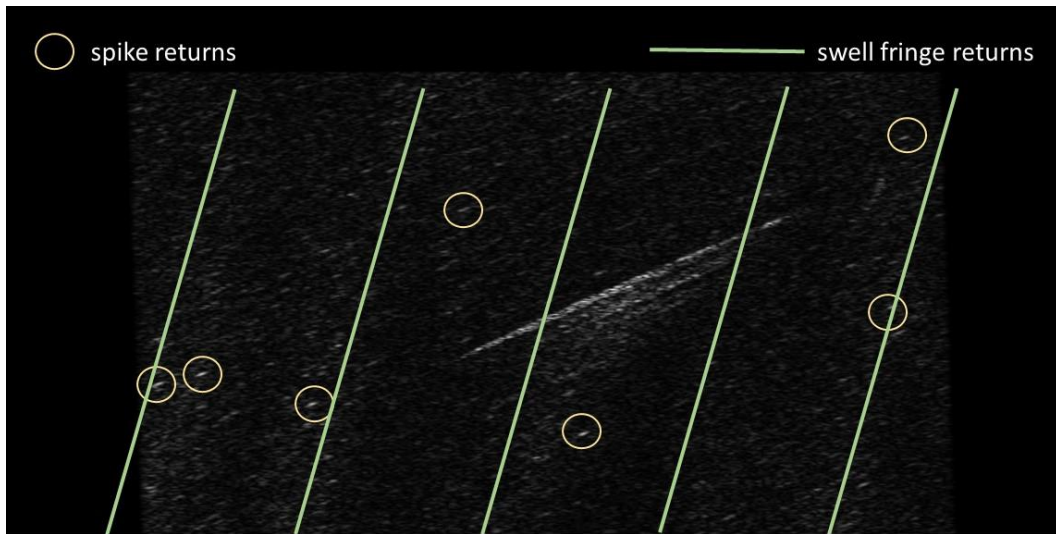


Figure 55: Annotated sub-image 4 from the sub-aperture set highlighting the appearance of a fringe pattern within the background clutter and individual circled highlights of proposed sea spike returns. Note that the highlighted spikes are some of the many spikes observed within the image but not a complete plot of all spikes.

Figure 56 shows a time comparison of the fringing effect that runs through the sub-aperture. The fringes are apparent in all the sub-images and maintain their locations. The spike returns within the fringes however flow readily through the fringes. The inter-fringe areas within the sub-images shows fewer spike events and lower intensity scatter returns by  $-0.223$  dB variation in mean image intensity and an overall increase of  $-12.6$  dB to the image dynamic range.

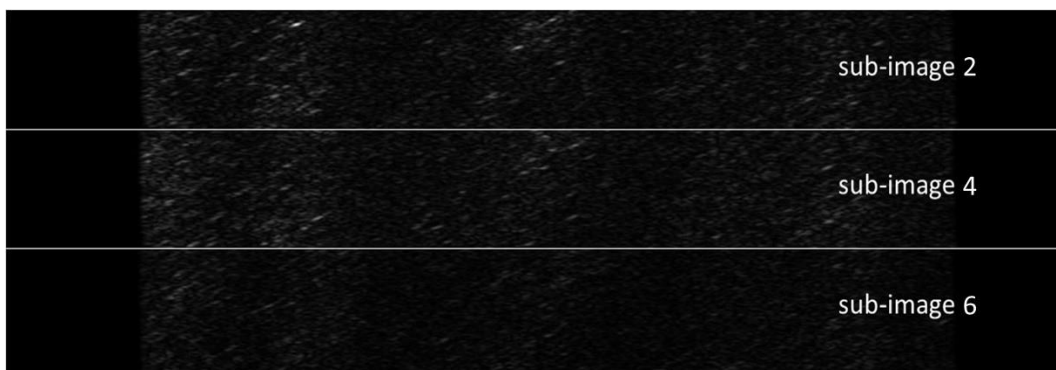


Figure 56: Side-by-side comparison of chip-outs from 3 sub-images from the full sub-aperture set. The chip-outs are geographically identical and show the consistent azimuthal location of the fringe pattern through the aperture. The internal structure of each fringe peak and trough can be seen to change through the aperture. The end sub-images 1 and 7 were not used as the background clutter is significantly dimmed compared to sub-images 2 and 6 so sub-images 2 and 6 make for an improved display.

### Chapter 3 – Sub-aperture Analysis

Figure 58 shows a zoomed in section of the sea clutter region where spike events are prominent. The figure contains sections from four of the sub-aperture stack in sequence to illustrate the chronological variation in the displacement and the intensity of the spike returns. The upper four sub-image sections are unannotated for visibility and the lower four images are annotated copies of the upper four to highlight the assessed sea spikes and their variation sub-image to sub-image. The range of the events remains constant through the aperture but slight azimuthal variation is observed. Observed results from Watts et al. (2005) show that it would be expected that burst events would have almost no azimuthal motion as they appear to give a very constant absolute Doppler return back to a sensor. The three spike returns that are highlighted in Figure 58 move  $38.8 \pm 4.2$  m through the aperture.

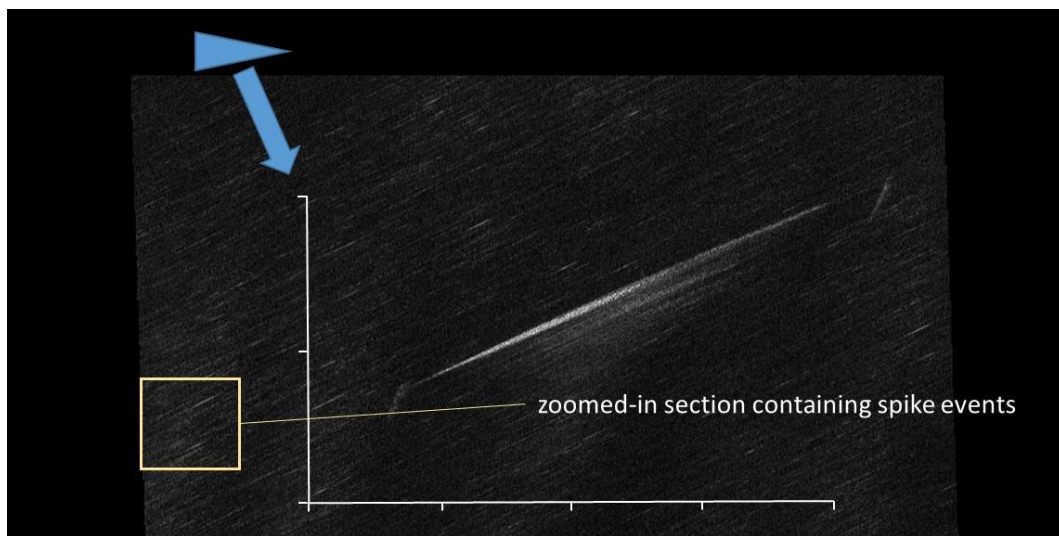


Figure 57: Annotated chip-out from full SAR image highlighting the area of sea clutter containing spike returns that is to be examined in the next Figure.

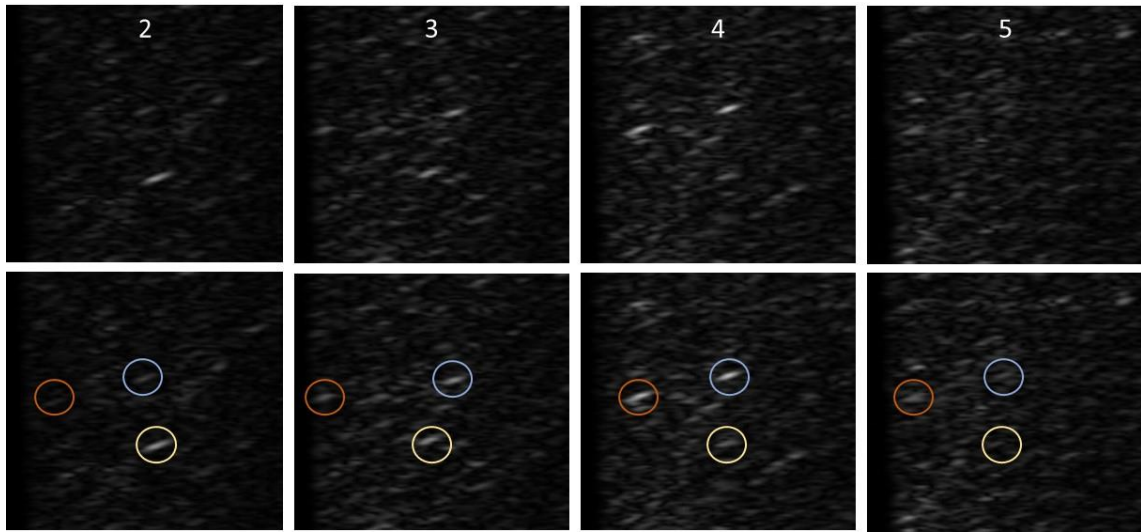


Figure 58: Unannotated and annotated chip-outs from 4 sub-images (2, 3, 4 and 5) highlighting the location of 3 spike returns. The relative distribution of the spike returns can be seen to vary azimuthally through the sub-aperture set. Each spike return can be seen to follow a similar pattern of intensity growth to a peak and then decay. It can be seen that each spike peaks at a different time within the aperture indicating that that is scatterer related rather than a pan-image property.

### 3.6 Wake Bloom Striations

Several of the full aperture images of ships that contain the bloom artefact in question contain a ‘striation’ effect where azimuthal linear features exist throughout the overall artefact. In this case, the full aperture image can be seen to contain a hint to such an effect albeit somewhat smoothed in this case. However, in the sub-aperture images, consistently throughout, these linear features are much clearer. Looking downstream through the bloom, the striation pattern displays a moderate level of banding that exhibits a fairly regular spatial interval in range although not exact. The similar extent of the smearing in azimuth and its similarity in location to the rest of the bloom might suggest that the striations and the bloom have a common source mechanism. The difference in intensity, the striations being slightly brighter within the images, are reminiscent of spike events. However, as can be seen from the spike events in the sea clutter of Figure 58, there is a significant difference in azimuthal width. This could be explained by the sea clutter spike events being caused by isolated individual waves and the bloom having a much higher concentration of scatterers over an

### Chapter 3 – Sub-aperture Analysis

area, or there could be a different mechanism. In this case the sea clutter events could be due to bursts that are known to have much reduced Doppler velocity spread than whitecap returns that could form the bloom artefact. The spikes that form ubiquitously in the clutter background show a maximum azimuthal width of the order  $23 \pm 2$  m whereas the striations show a maximum of  $596 \pm 125$  m. Using Ward et al.'s (2006) plot for the measured Doppler spectrum of whitecap returns from a given range cell, it would be expected that a whitecap return could have azimuthal spread up to 1060 m for this given geometry. Counter to this though, it would be unlikely, if it were the case that the bloom striation artefact was just a result of the whitecaps, that there were no whitecaps anywhere else within the imaged area. This is a particularly useful consideration to take into the more detailed modelling stage in the next chapters; the sharpness, consistency and uncertainty suggests that this is a novel feature of interest and worth consideration. Figure 60 shows the linear striations in question.

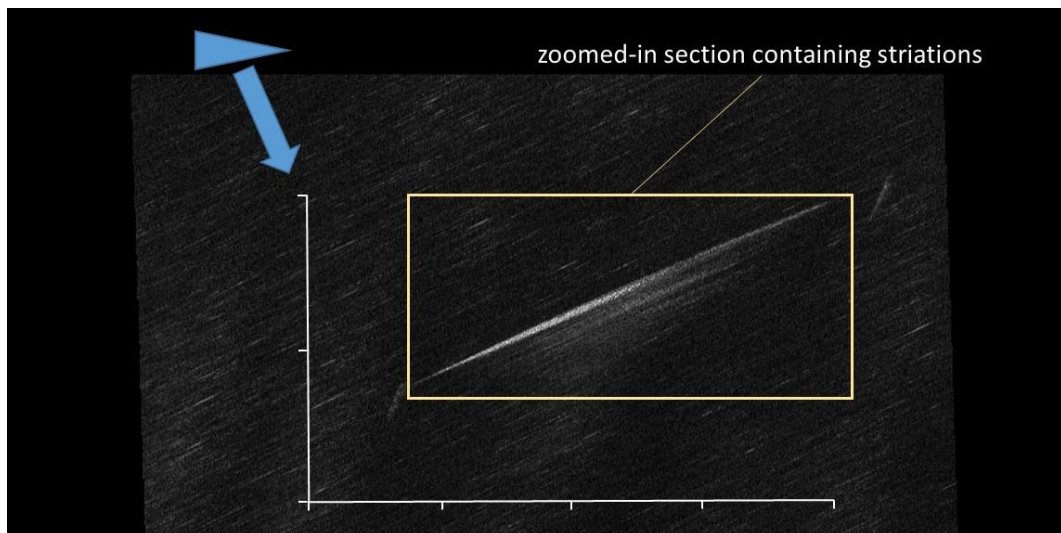


Figure 59: Annotated chip-out from full SAR image highlighting the area of proposed wake return that is to be examined in the next Figure.

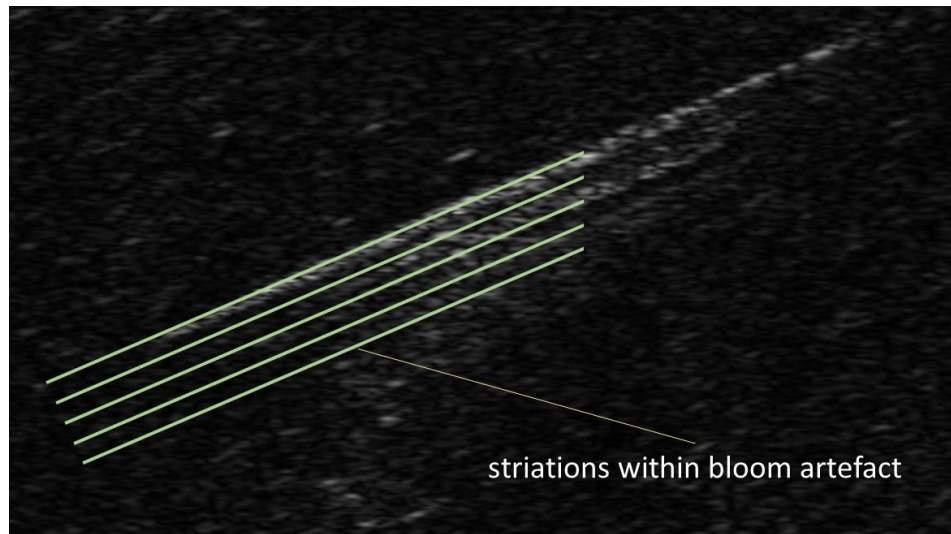


Figure 60: Annotated sub-image 4 showing the approximate location of repeating linear features that run azimuthally through the wake return. Note the annotations purposefully terminate to allow for clearer display of the striations underneath.

The separation of the striations in Figure 60 gives an average of 29.8 m.

### 3.7 Wake Bloom Location

It is evident from the sub-aperture set that the majority of the bloom artefact does not change its construction through the images but does change its location in azimuth. The change in azimuth is a gradual, linear progression through the aperture and at no point reverses.

Compared to the overall width of the bloom, the change in azimuthal displacement of 356 m is small and can be seen in Figure 62.



### Chapter 3 – Sub-aperture Analysis

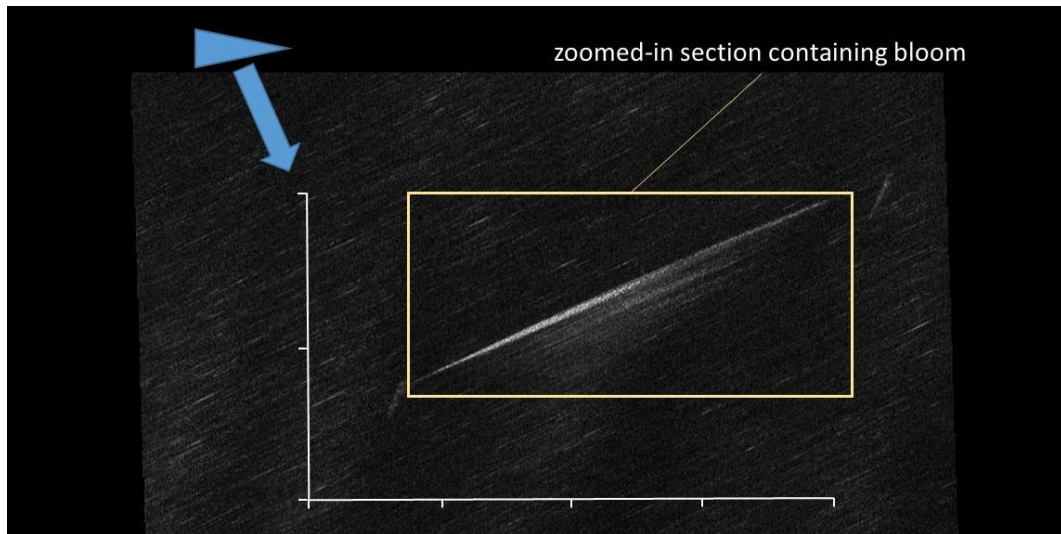


Figure 61: Annotated chip-out from full SAR image highlighting the area of proposed wake return that is to be examined in the next Figure.

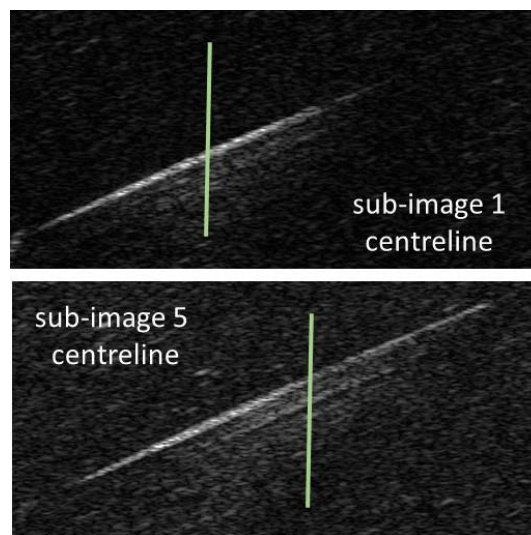


Figure 62: Annotated chip-out from sub-images 1 and 5 showing the assessed centreline of each wake artefact. The centreline can be seen to move azimuthally through the sub-aperture set. The bulk movement of the artefact is smooth and consistent through all of the sub-images.

This phenomenon would suggest that there is a dependent relationship between the Doppler spectrum of the bloom and sub-image time as it is the Doppler velocity that the SAR processor is using to determine the azimuthal coordinate of each scatterer in the scene. This indeed would be a useful characteristic to take forward. The appearance of this phenomenon,

## Chapter 3 – Sub-aperture Analysis

as it is in this case, in a single image only, there is a strong probability that this effect could be caused by an error in the autofocus processing for the image. If indeed it is, then the effect is caused by the autofocus not fully correcting the azimuthal distribution of scatterers so that they are not aligned as they should be. The side effect is that, when sub-divided, the misaligned scatterers appear to move through the image. If the effect were the result of a misalignment through the autofocus process then all the image scatterers would appear to move through the image in a similar sense and rate, which is indeed the case here.

Without returning to the original image and re-processing it would be hard to be certain as to the cause of the phenomenon. To supplement the understanding of this effect and for balance, a different cause is proposed in Chapter 5. It will be proposed that the phenomenon is, at least in part, an unintended side effect of the sub-aperture processing.

### **3.8 Summary**

Having assessed the results of the sub-aperture technique, it can be concluded that it was very worthwhile. The technique alone has not produced an absolute answer in itself as to the mechanism and construction of the ship artefacts but the analysis has unearthed multiple layers of complex structure and hints as to what the root source of the phenomena could be. These are useful starting points for further analysis that will follow in the next chapters. Chapter 4 will examine the same collected scene but from a particular perspective of SAR phenomena and use the basic assumptions and understanding of SAR to build a simple collection model that will add further understanding as to the scattering mechanisms behind the now known deconstructed segments of the ship artefact.

## 4 CHAPTER 4 – THEORETICAL SAR MODELLING

### 4.1 Introduction

In the previous chapters the basic wake components and phenomenological effects of sea clutter have been described. On top of this, a sub-aperture technique has been applied to the SAR image of a moving ship in order to deconstruct the image and further understand the mechanisms behind the artefacts in the image. The analysis has produced some answers but has more importantly highlighted areas for further investigation. It is the aim of this chapter to discuss a proposed cause for the components of the image using understanding of SAR processes and demonstrate the theoretical appearance of such a mechanism using a simple worked example. This will lay the foundation for the application of a more rigorous mathematical model to determine a detailed explanation for the artefacts that have resulted from the previous work.

### 4.2 Problem Identification

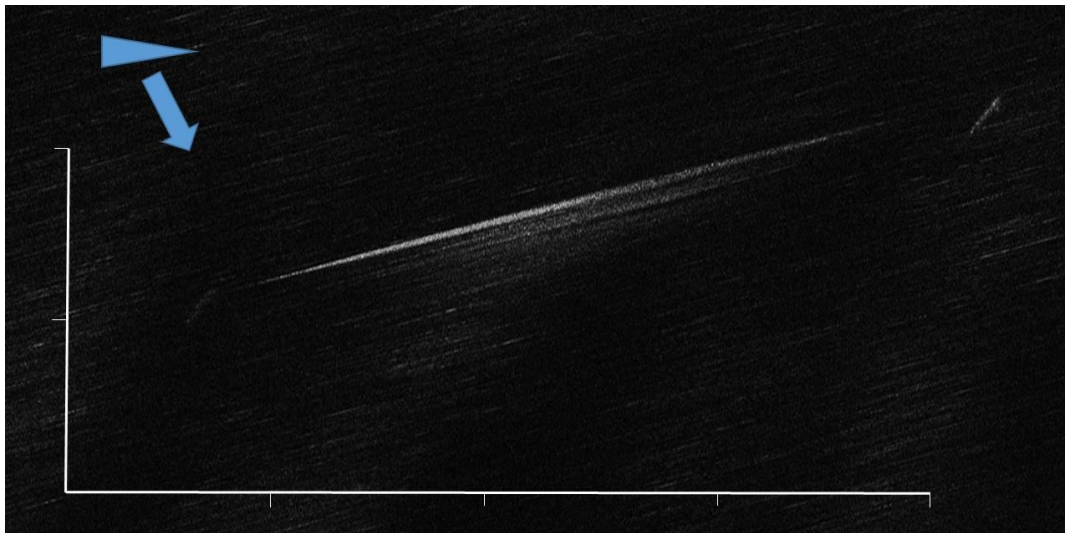


Figure 63: Chip-out from full SAR image showing imaging geometry of sensor orientation and direction of motion with scale bars (axis markings denote 500 m).



## Chapter 4 – Theoretical SAR Modelling

Figure 63 shows the common appearance of the area near a generic target ship observed using the previously developed Geometric Focussing (GF) technique where the image geometry is manipulated to ensure the image is collected close to the mean line of advance of the ship (either up-track or down-track). The purpose of the GF technique is to minimise cross range motion, which dramatically enhances the focussing capability of a particular target scatterer due to nuances within the SAR processing. A side effect of the GF technique is that it maximises other artefacts, particularly azimuthal displacements, and therefore presents an unfamiliar image of a ship wake to the operator that is a combination of unusual SAR image artefacts. Therefore, the effect on the target vessel and its wake must be understood before it can be effectively used. The crux of the subsequent problem here is to determine the key elements of the image: what parts of the artefact are caused by the main vessel; what is caused by the wake of the vessel; and finally, what is caused by the background clutter. The interaction of these components within the image and the appearance of phenomena that are an effect of the breaking of the SAR processing assumptions, will lead to a basic model for the scene. If the basic model can be shown to sufficiently explain the general appearance of the artefacts within the image then a more comprehensive model will be built to thoroughly test the developed hypothesis.

The first artefact, which is being taken first almost to discount it and remove it from the following consideration for the moment, is the wide-spread low intensity mottled return that runs through the entire image. Its low intensity and wide-spread appearance would align with the supposition that this is caused by the background sea clutter that contains areas of increased radar reflectivity that distort the picture from a uniform background intensity. Not knowing the exact meteorological conditions at the time of collection, no precise comment can be passed as to the relative strength of the returns due to high or low sea state when

## Chapter 4 – Theoretical SAR Modelling

compared to the returns from other sections of the artefact. The banding that is highlighted in Figure 64 roughly falls in line with the explanation of Tunaley et al. (1989) for a swell where the orbital motion of the water particles within the wave surface have the result of bunching within the image when the azimuthal displacement of the SAR process is applied. An example of a simulation of this is readily shown by Yoshida (2012) and practically applied to real imagery, in this case ERS-1, by Marghany (2004). It is worth a note that velocity bunching is normally described, and strongest, from high grazing angle geometries as the observed particle velocities and surface elevations are in phase and therefore magnify the effect.

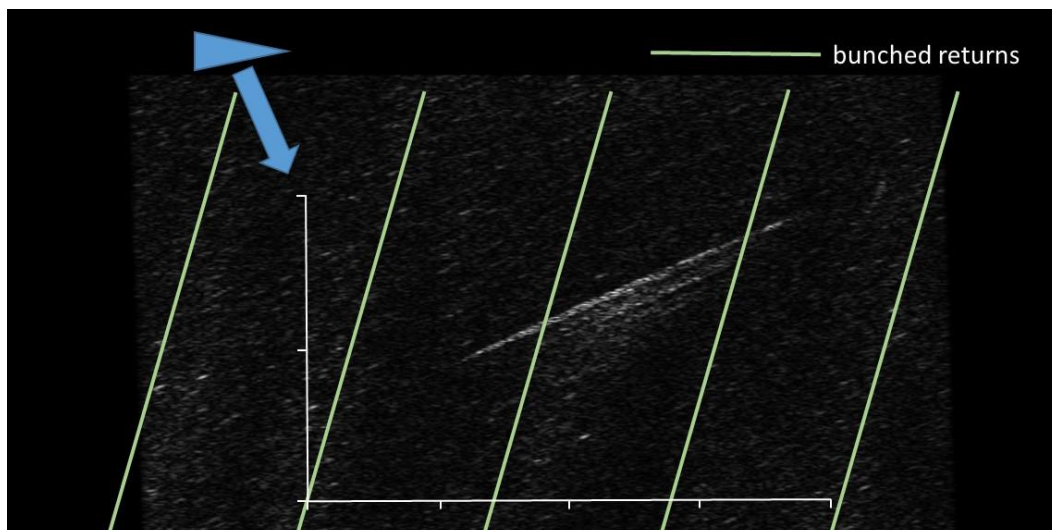


Figure 64: Annotated chip-out from sub-aperture set highlighting the fringe pattern of bunched returns that runs through the entire image.

The next element to consider is the location of the vessel returns within the image. Figure 65 shows the locations of identified apparent target vessel signatures as well as the location of the true vessel given by open source AIS data. With the true target location known and the apparent target locations considered, the remaining smeared artefact can be deduced as wake-associated. These features are annotated in Figure 65.

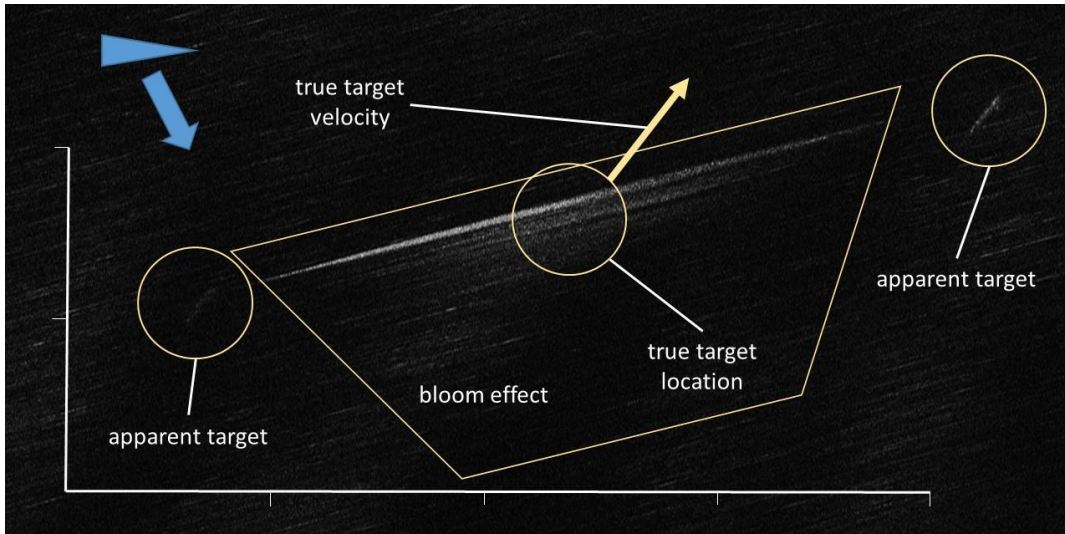


Figure 65: Annotated chip-out from full SAR image highlighting the locations of the apparent target vessel returns compared with the known true location of the vessel, and, the location of the proposed wake return.

### 4.3 Model Hypothesis

Due to the GF method that was used to construct the image, the large magnitude of the azimuthal displacement of moving scatterers must first be acknowledged and must not be underestimated in its effect on the image. For a GF imaging geometry as shown in Figure 66 where the radar platform is moving at velocity  $v_{rdr}$  and the target vessel is moving with velocity  $v_{tgt}$  perpendicularly towards the radar on boresight, the azimuthal displacement of the target within the resultant SAR image,  $\Delta x_v$ , is given by Oliver et al. (1998) as:

$$\Delta x_v = R \frac{v_{tgt}}{v_{rdr}} \quad (4.53)$$

## Chapter 4 – Theoretical SAR Modelling

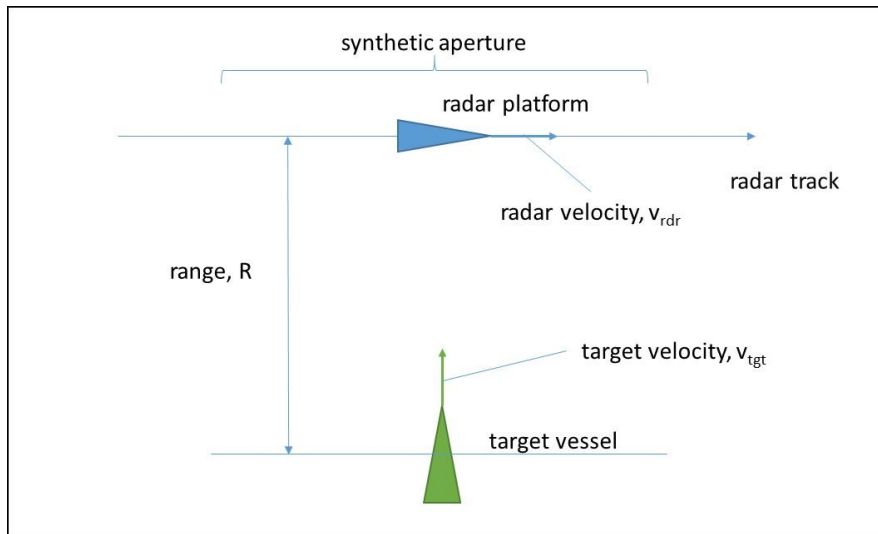


Figure 66: Diagram showing the imaging geometry of the geometric focussing (GF) technique.

The ratio  $\frac{R}{v_{rdr}}$  is used as a common rough factor to describe the SAR imaging construct.

Kasilingham et al. (1990) show that the ratio is key to describing the realistic azimuthal resolution and when observing the ocean surface, in particular, it is also key to understanding the velocity bunching effect of the moving scatterers within the scene. They also suggest that there is a criterion for the selection of an optimum ratio in order to attain the best focus for the image that is dependent on the sea state and the maximum wavelength of the sea swell.

## Chapter 4 – Theoretical SAR Modelling

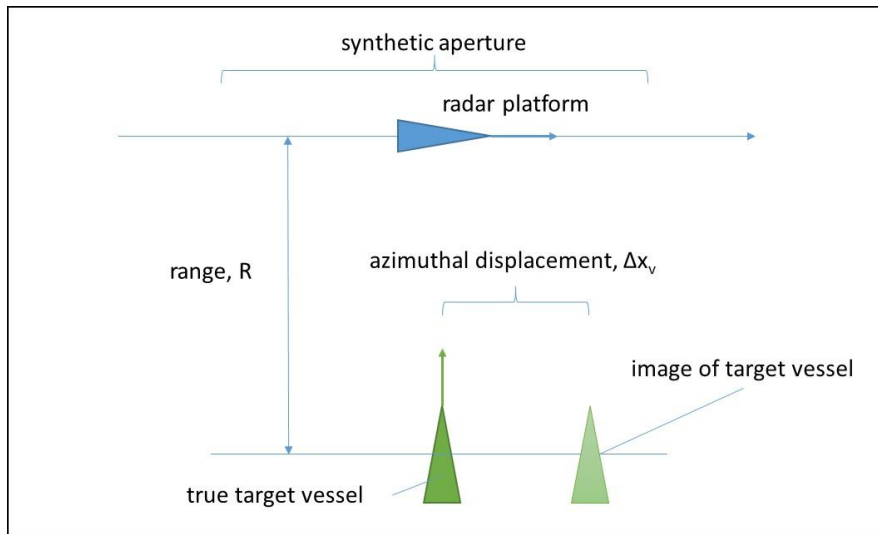


Figure 67: Diagram showing the relative azimuthal displacement of the primary target vessel return to the true location as a result of the SAR imaging process.

Equation (4.53) shows that anything that is physically connected to the main target vessel will suffer from an azimuthal displacement from its true position in the image by a factor that is proportional to the magnitude of its velocity. It is assumed that the velocity of the radar is a constant under control and knowledge of the operator. The displacement of the vessel within the image will also have a specific sense as indicated in Figure 67, the orientation of the displacement is dependent on the imaging geometry and the relative velocity of the target vessel. Examination of the imagery against truth data from open source AIS logs shows that the displacement of the apparent main vessel return and the true position of the vessel are inconsistent and commonly in error greater than that which could be explained by the accuracy of the direct measurements. This mismatch can be seen from Figure 68. Therefore, the bulk azimuthal displacement cannot be the only phenomenon that is having an effect on the positioning of the target ship within the image.

## Chapter 4 – Theoretical SAR Modelling

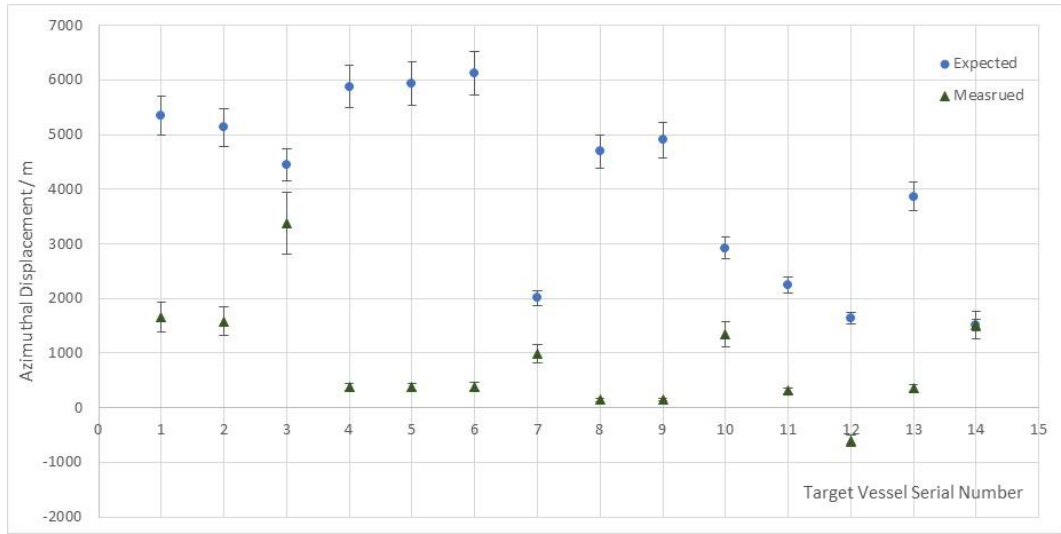


Figure 68: Plot showing the measured azimuthal displacements of a group of target vessels against the expected displacements predicted using the imaging geometries and (4.53)

Due to the general low PRF of SAR and the generally large magnitude of the azimuthal displacement, the azimuth ambiguities must be taken into account. The azimuth ambiguity is a side effect of the sampling of the scene data at the PRF and the ‘misunderstanding’ of the SAR processor of the meaning of the ambiguous frequency as another displacement in azimuth. The azimuthal displacement,  $\Delta x_s$ , in metres, caused by the sampling frequency is given by Skolnik (1980) as:

$$\Delta x_s = \frac{\lambda f_s R}{2v_{radr}} \quad (4.54)$$

where  $\lambda$  is the wavelength of the radar in metres and  $f_s$  is the PRF in Hz. The displacement of the ambiguity is taken from the displaced image location of the primary vessel return not from its true location within the image. The displacement caused by the ambiguity may produce a single additional artefact at one multiple of the displacement from the datum or, which is more likely, it will repeat several times. This repetition is akin to the PRF induced repetition within the frequency domain apparent in Fourier analysis. Figure 69 shows the

## Chapter 4 – Theoretical SAR Modelling

superposition of the azimuthal displacement of the target vessel due to its velocity and the azimuthal displacement due to the PRF induced ambiguities.

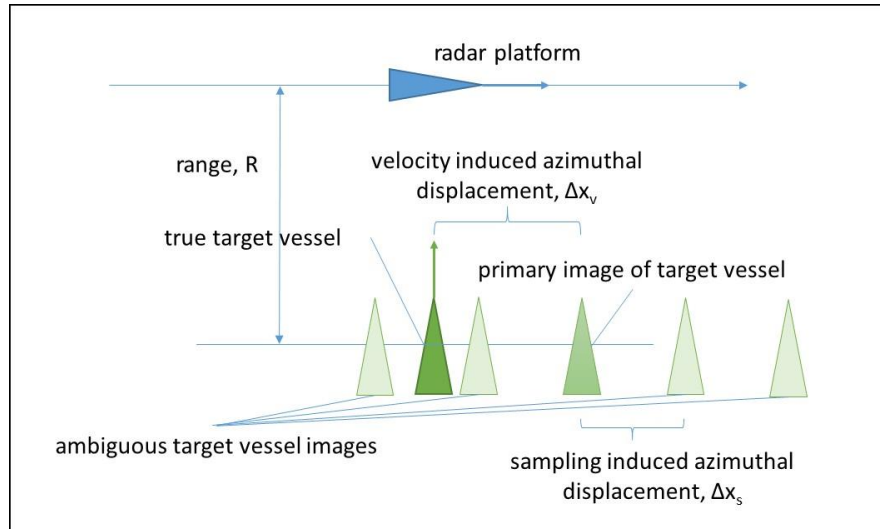


Figure 69: Diagram showing the superposition of the azimuthal ambiguities of the azimuthally displaced primary target vessel return that is a result of the SAR imaging process.

The combination of the main azimuth displacement and then the multiple repetitions of the primary return caused by the azimuth ambiguity creates a ‘comb-like’ pattern of multiple targets along the azimuth line of the true target position. Not all of these returns will be visible within the image due to the envelope of the real radar that modifies the intensity of the processed SAR image to only show targets that would be ‘seen’ within the true radar beam. Management of this characteristic is often specifically by design to avoid the appearance of ambiguous returns that may lead to confusion when being analysed by an operator (Stimson, 2014).

The combination of the azimuthal displacement of the primary return from the target vessel and the azimuth ambiguities, all modified in amplitude by the overall envelope of the real radar beam, would create a composite of several replicas of the target vessel along the same azimuth line in the image. It can be seen on Figure 63 there exist two apparent targets on the

same azimuthal line but displaced from the true target location, which has been cross-referenced with AIS data. The unequal displacement of 38.7 m left and right from the true location supports the notion that the datum for the two apparent targets is not simply the true target location but is based on some separate mechanism.

#### 4.4 Target Vessel Displacement and Ambiguities

Using (4.53) and (4.54), a model for the scene can be produced. Table 1 shows figures used for the worked example used in this chapter. The radar characteristics are for a generic X-band aircraft mounted sensor and the speed selected for the target vessel is based on the average transitory speed of merchant shipping from AIS. This figure generally derives from the running efficiency of time versus cost. The dimension,  $D$ , is the diameter of the antenna.

target velocity	$v_{tgt} / \text{ms}^{-1}$	7.72
radar velocity	$v_{rdr} / \text{ms}^{-1}$	205.78
wavelength	$\lambda / \text{m}$	0.03
PRF	PRF / Hz	320
real antenna length	$D / \text{m}$	1

Table 1: Basic initial sensor parameters

With these figures, the basic scene can be plotted. A range bracket of 80 – 120 km is used to examine the uniqueness of the scene construction across the possible collection geometries. The antenna dimension and the wavelength are used to calculate the real radar beamwidth, which is plotted onto Figure 70 as the solid lines to indicate the surface footprint of the real radar. A total of five target vessels have been inserted into the plot all with initial zero azimuthal displacement but are spaced at every 10 km along the ‘Target Range’ axis. The primary return for each target is plotted using the square icon and any azimuth ambiguities are plotted using circles.



## Chapter 4 – Theoretical SAR Modelling

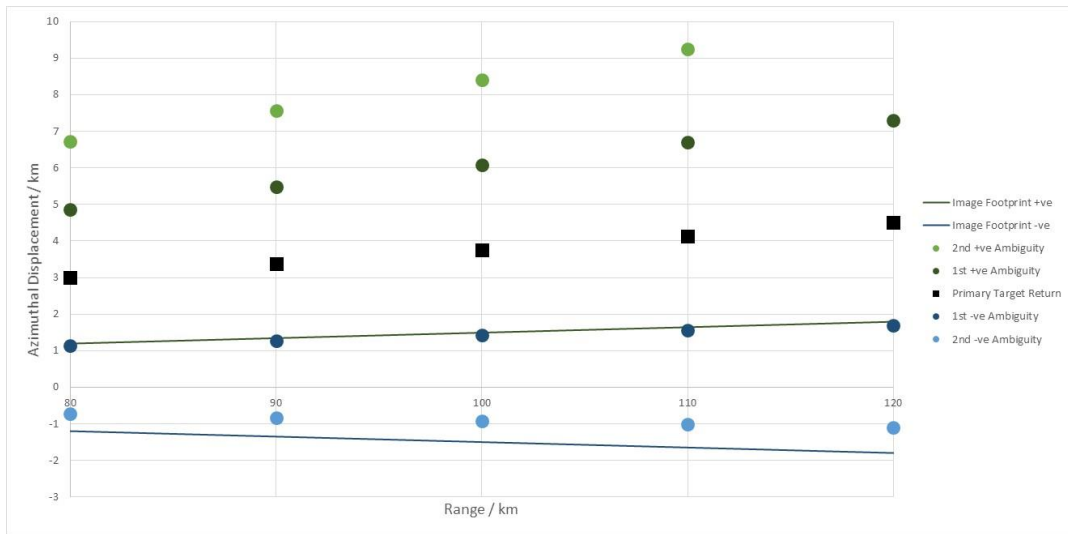


Figure 70: Plot of moving target vessel using the GF technique to show the relative displacements of the primary target returns and the azimuthal ambiguities compared to the footprint of the real radar for range bracket 80 – 120 km.

The first observation of note is that due to the  $\frac{R}{v_{rdr}}$  ratio, in this case for a range of 100 km the ratio is 486 s, the azimuthal displacements are large. To such an extent of multiple kilometres that, in the given framework, the primary return will not be seen within the image unless the vessel radial velocity is of the order of 2 kts or greater, which is very slow for a real maritime target vessel. Also, it can be seen from Figure 70 that there readily exists the circumstance where multiple ambiguous returns appear within the footprint of the image. It is encouraging also to see that, given the distribution of the ambiguities, there is a fair likelihood that an ambiguous return will be located near the true location of the target vessel. This is a relatively common phenomenon, as shown in Figure 68. This characteristic can be considered to be due to the relative speeds of the aircraft and the target as in (4.53).

### 4.5 Wake Bloom

The remaining phenomenon that this model does not yet explain is the strongly reflective blooming effect that the AIS data shows is plotted in the vicinity of the true position of the target vessel in the image, as shown in Figure 71.

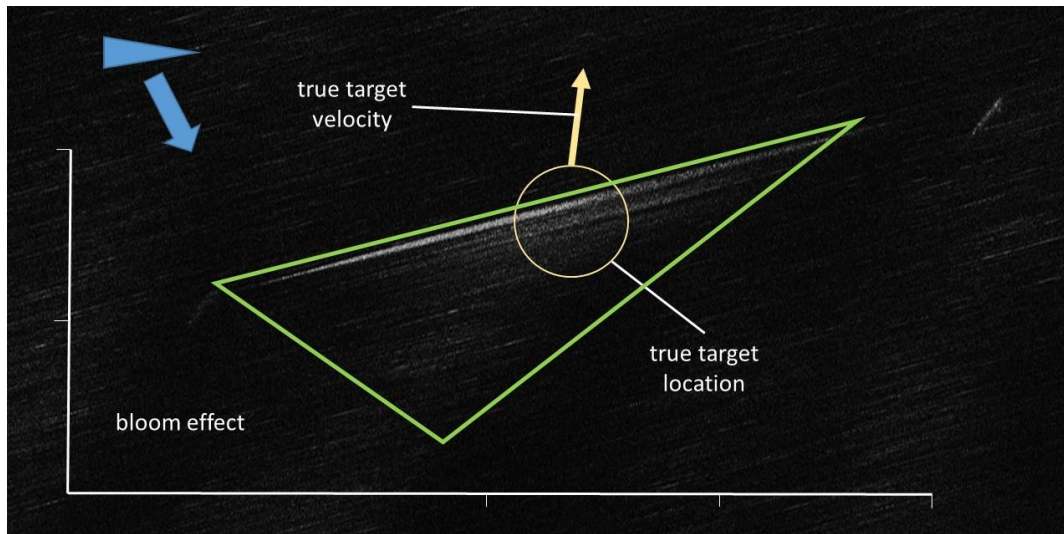


Figure 71: Chip-out from full SAR image showing the extent of the proposed wake artefact in relation to the true location of the target vessel.

The blooming effect, through examination of several images, shows common characteristics. Firstly, the bloom appears to be associated with range from the radar and the comparative position of the target vessel; the bloom only extends behind the vessel with regard to where it has travelled from. Secondly, when compared along the range axis the bloom is wider at one extreme of range compared to the other; the bloom is at its widest near the bow of the target vessel and then decays in range towards and beyond the stern downstream of the target vessel. Thirdly, the intensity of the image shows that bloom is very reflective by comparison to both the background sea clutter and even the returns from the main target; this is surprising as the target vessel is generally made of a very good conductor whose geometric construction would mean it would have an enhanced radar cross section, however, the ambiguous returns would be expected to be reduced in brightness when compared to the amplitude of the primary return due to defocussing. These characteristics were apparent in imaging geometries where the target vessel was moving towards and away from the sensor and at various ranges.

## Chapter 4 – Theoretical SAR Modelling

The existence of the bloom starting in line with the bow of the vessel, and then always behind the stern of the vessel, would support the assessment that the cause is vessel-wake associated. The lack of any traditional wake appearance in the imagery (the expected wake constructions have already been described in Chapter 2) is not an uncommon situation as there are many elements to the possible wakes that are imaging geometry and sensor specific, as noted by Alpers et al. (1998). This is therefore not concerning but what is intriguing is the consistent appearance of an unexplained artefact that may be wake related.

The decay of the bloom is also fascinating as there appear to be two elements to the decay. Firstly, the azimuthal width of the bloom, and secondly, the intensity of the bloom decay with range from the target vessel, both of which are quite stark and sharp with the section of the bloom nearest the true vessel location being significantly brighter and wider than the rest. It would be reasonable to assume that as it is known that the sea surface is moving that the azimuthal width of the bloom may be caused by the azimuthal displacement of the scatterers that form the artefact. This would mean that the scatterers in closest proximity to the target vessel are travelling faster than those to the rear of the vessel. As the bloom occurs either side of the mean line of advance of the true target vessel location, it is also reasonable to argue that the motion that causes the displacement within the bloom is either side of zero relative velocity. There is an apparent minor skew to the azimuthal width relative to the true location of the target vessel but it is consistently only minor. From (4.53), and using the measured dimensions for bloom width of  $596 \pm 125$  m from section 3.6, the azimuthal bloom in Figure 71 would result in a magnitude of scatterer velocity of  $0.41 \pm 0.05$  ms<sup>-1</sup>. For such radial velocities, both positive and negative, either side of a near-zero relative velocity datum the underlying cause must be oscillatory in nature. If it were not, then significant sections of the sea would be moving, permanently as a flow, towards and away from every moving

vessel, which has not been identified by any other means. This would also not be realistic from a conservation of energy and hydrodynamic perspective. It makes more sense to argue that the most likely source of this oscillation and associated radial velocities is the orbital velocities of the water particles in the wake of the target vessel. The wake, the combination of all forms of wake previously described, has greatest wave elevation nearest to the source vessel and decays as the individual waves emanate from the source. The greater the wave elevation then the greater the maximum and minimum orbital velocities of the water that would be observable. This could account for the decay of the azimuthal width of the bloom.

The second element of the decay of the bloom is the decay of the intensity of the bloom with range rearwards from the target vessel. This is particularly noticeable in the imagery as a link to the characteristic that the whole bloom artefact is of a higher amplitude within the image than the surrounding background scatterers. So, assuming for the moment that these factors are linked, there should be some characteristic about the source of the bloom artefact that makes its radar cross section higher than average within the image and whatever the source is its distribution or strength as a scatterer is physically associated with being nearer the target vessel. Still always being behind the vessel, and roughly balanced either side of the zero relative velocity line, would maintain that it is wake associated. There are several ready possibilities that might manifest a suitable RCS distribution to appear in imagery as the bloom does. The source of the scattering mechanism could be directly linked to the white foam riding on the water's surface. This would make sense as the target vessel generates foam from the breaking water and the turbulent flows around the bow and stern. The foam exists in highest concentration directly near the target vessel but the bubbles eventually decay and return to the water equilibrium. There is disagreement in previous literature as to the effect on the reflectivity of foam riding on the water's surface. For instance, Alpers et al.

(1981) considered the contribution of bubbles to the increased reflectivity in a breaking wave via Rayleigh scattering. Their conclusion was that although the mechanism was sound in theory the Bragg scattering outweighed the Rayleigh as a primary source of the overall RCS. It was even suggested that the foam may not have been associated with an increase in the RCS and may form an impedance factor and reducing the overall Bragg scatter contribution. In this way, the whiter the water the less reflective it could be. To counter this conclusion, work, such as that conducted by Gunn et al. (2018) using bubbles in ice layers, has successfully shown that distributed bubbles form a valid radar reflector for a wide range of radar bands. The reflectivity does appear to be dependent on the physical bubble distribution, which may dissuade the use of the foam as a suitable explanation for the increased reflectivity in this case only because if the reflectivity is so sensitive to the distribution of bubbles it would be unwise to assume that a chaotic turbulent process for the bubble creation would be as consistent as the bloom artefact appears to be in the imagery. The main three sources for bubble generation in the vicinity of a target vessel are due to breaking waves, from frictional hull effects and directly from the vessel's propeller action on the water. The combination of these processes would be unlikely to repeatedly generate a common pattern.

An alternative scatterer source would be areas of rough water that have been created through the interaction of the target vessel and the sea surface. Much like the rough water that is at the heart of the whitecap scattering effect, Watts et al. (2005), the result when observed through a radar sensor is a significant spike in RCS. This would be further magnified through a SAR process due to the integration time of the image collection. The wake waves have the greatest energy when they are nearest the source vessel and therefore have the greatest amplitude near the vessel before the energy dissipates through the process of viscous dissipation, amongst other mechanisms (Lighthill, 1978). The greater the amplitude of the

## Chapter 4 – Theoretical SAR Modelling

waves the greater density of highly reflective tilted wave slopes per unit area of water. As the overall wake amplitude decays rearwards from the source vessel, so too would the reflectivity decay and therefore form a suitable explanation for the source mechanism for the bloom effect. The primary scattering mechanism in this case would remain Bragg-like but the extreme tilts that are induced by near-field wake would modify the RCS sufficiently to appear different to the tilt modulated returns from the ambient sea clutter that would also be governed by a similar scattering mechanism. It is difficult to conclude at this stage which mechanism is responsible for bloom scattering so will have to be taken forward.

Regardless of the source scattering coming from the foam riding on the surface of the wake or rough water the underlying wake pattern of the vessel is responsible for the Doppler signature of the returns, akin to the tilt modulation model, and determines the appearance of the bloom in the image, again as a side effect of the azimuthal displacement phenomenon. The orbital motion of the water particles in the wake pattern would be a major contributor to modification of the Doppler return of the water surface. The Kelvin wake of the target vessel generally, assuming roughly benign and standard conditions, provides the wave of greatest amplitude and therefore the waves that contain the greatest orbital velocities that would then determine the azimuthal envelope of the bloom artefact.

Linked to the tilt modulation explanation but could be treated as a separate entity, the breaking wave events within the near field wake of the source vessel could be a contender. The same large amplitude waves near the vessel would give rise to more, and larger, breaking wave events than the smaller amplitude waves at a greater distance from the vessel and it has already been cited that breaking waves lead to spikes in RCS. The whitecap events were shown to possess a broader Doppler spectrum that is non-coherent and lingers over a greater time-span than the burst effects but if these were to be the source it would mean that the

## Chapter 4 – Theoretical SAR Modelling

Doppler spectrum of the whitecaps would decay in magnitude with range from the vessel also to account for the decay of the azimuthal width of the bloom. This was not assessed specifically in the previously reviewed literature. The other question relating to this as a mechanism is with the noted link of the Doppler frequency of the detected spectrum associated with the whitecap effect; it has been noted in previous work, Watts et al. (2005) and Melief et al. (2006), that the whitecap events exhibit Doppler velocities higher than the ambient. The bloom artefact seems to show Doppler velocities higher than ambient but also more negative than ambient.

Figure 72 shows an optical scene from the immediate stern of a vessel where the combination of the tilt modulation of the Kelvin wake can be seen superposed with the turbulent wake. The white water can be seen forming at breaking wave events at Kelvin wake cusp waves, the foam can be seen riding the tile modulated wave patter and foam can be seen forming part of the turbulent wake from the hull friction and propellers.

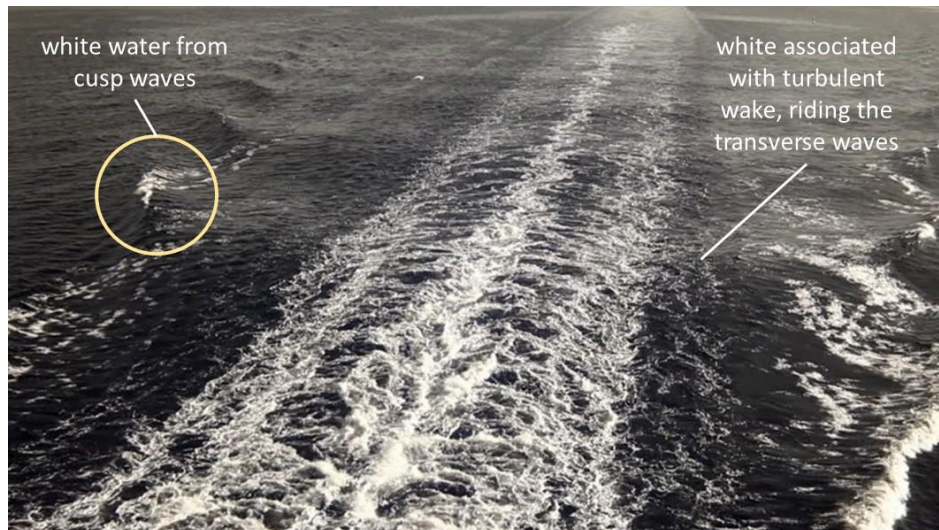


Figure 72: Annotated photographic image taken from the stern of a merchant vessel (ferry) facing rearwards. The image contains wake structures of the Kelvin wake and the turbulent wake. The image shows breaking wave events associated with the cusp waves of the Kelvin wake and highlights the white-water associated with the turbulent wake.

It is worth a note that there could likely be a contribution to the bloom effect from water directly in front of the vessel that receives the full frontal impact of the vessel moving through the water and reacts in an often chaotic manner as this section of water is often outside of modelling constraints but is easy to see when observing a ship in transit. The bow wave of a ship, even for those of moderate velocity, is an extreme breaking event that is very much non-linear in nature due to the large amplitude and proximity to the source. Both due to the presence of white water and steep surfaces it would be expected that this section of the wake to have high reflectivity, in line with the previous bloom artefact considerations, but would limit its distribution of effect to near the bow of the vessel where the source of the non-linearity lies. Any rough or white water created by the bow impact however must still be considered alongside the breaking events of the traditional non-near wake as there is no reason to assume these would have different lifetimes from those created by the other mechanisms.

#### 4.6 Orbital Velocity

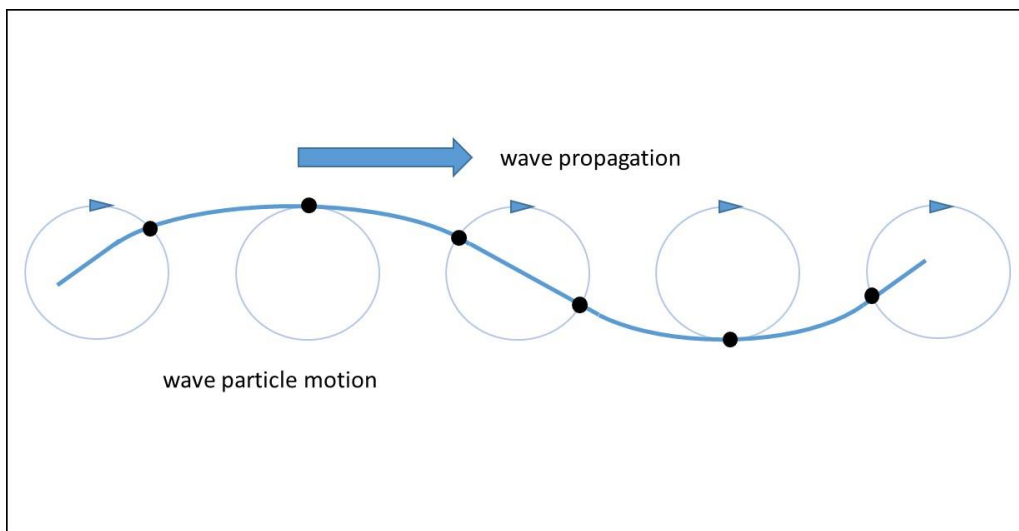


Figure 73: Diagram showing the orbital motion of water particles within a surface wave field.



## Chapter 4 – Theoretical SAR Modelling

Established theory based on the orbital velocity of the water can be used to predict the basic form that the bloom phenomenon would take if the orbital motion were the cause of the Doppler spectrum that results in the image appearance. However, this will not separate the Bragg scattering from the white-water scattering, this will be considered more carefully by other means. Using Airy wave theory behind the Kelvin wake derivation, as the wake pattern remains behind the source vessel and can be considered to effectively travel with it, the wake has phase velocity,  $c_p$ , equal to that of the ship,  $v_{tgt}$ :

$$c_p = v_{tgt} \quad (4.55)$$

Therefore, for the pattern to remain constant, the angular frequency is given by

$$\omega = kv_{tgt} \quad (4.56)$$

As the dispersion relation for deep water waves shows that there is a wavelength dependence on the phase velocity of a travelling wave the limitation of the wake velocity puts a limit on the maximum wavelength of waves that combine to form the Kelvin wake. The dispersion relation for deep water is

$$\omega^2 = gk \quad (4.57)$$

Substituting (4.56) for the angular frequency in (4.57) and rearranging gives

$$k = \frac{g}{v_{tgt}^2} \quad (4.58)$$

For a monochromatic 1-dimensional travelling wave the surface elevation,  $\eta$ , is given by

$$\eta(x, t) = A \cos(kx - \omega t) \quad (4.59)$$

where  $A$  is the wave amplitude in metres. Therefore

$$\frac{d}{dt}\eta(x, t) = A\omega \sin(kx - \omega t) \quad (4.60)$$

By considering the maxima of this expression for the velocity of the surface elevation, the maximum observable orbital velocity of the particles of this wave gives

$$v_{orb,max} = A\omega \quad (4.61)$$

Substituting for the angular frequency from (4.57) gives

$$v_{orb,max} = A\sqrt{gk} \quad (4.62)$$

Substituting the phase velocity from (4.55) into (4.62) gives

$$v_{orb,max} = A \frac{g}{v_{tgt}} \quad (4.63)$$

It can be seen from (4.62) that the magnitude of the velocity presented to the radial direction of the radar is dependent on the amplitude of the wake waves and the wavelength of the waves within the wake. When considering wavelength, the transverse wave component of the Kelvin wake pattern would both provide the greatest orbital velocity magnitude and would therefore also likely present the greatest Doppler velocity to the radar in the GF image construction. Note that in this orbital motion the greatest Doppler velocity is actually a magnitude either side of the zero-Doppler datum. There is something a little unreal about this assumption that can be accepted; the datum is unlikely to ever be exactly zero as the real sea is always moving. This movement is not the wind induced wave motion, even though this would result in a minor overall flow. The real sea is always affected by tidal forces that result in a small non-zero flow at almost all times of the day. This small non-zero quantity could explain the minor azimuthal skew of the bloom either side of the true target vessel location but this will be investigated more deeply later.

## Chapter 4 – Theoretical SAR Modelling

The evolution of the wake amplitude with respect to the distance from the source vessel has been studied and modelled by several authors (Cox and Macfarlane, 2019 and Doctors and Day, 2009). The resultant models that show good quantitative agreement with real-world measurement follow a power law whose factor is of the order of roughly -1/3. For comparison Stoker (1957) gives this value theoretically as -0.5 whereas Cox and Macfarlane's theory gives it as -0.4 but through observation of real events gives it as -0.33. Regardless of the minor disagreement, a working function can be used here:

$$A = A_o x^{-1/3} \quad (4.64)$$

where  $a_o$  is the initial amplitude of the wake waves in metres at the vessel and  $x$  is the distance in metres along the longitudinal axis that is parallel to the direction of travel of the vessel the positive direction is measured rearwards from the vessel.

Substituting (4.64) into (4.63) gives a final expression for the decay of the maximum orbital velocity of the transverse waves within the Kelvin wake field as

$$v_{orb,max} = \frac{A_o g}{v_{tgt}} x^{-1/3} \quad (4.65)$$

It can be seen from (4.65) that the appearance of the bloom is also dependent on the initial amplitude of the wake waves. Semi-empirical models, applied by Doctors and Day (2009), using Froude depth and length numbers as an approximation tool, show that this is also relatively predictable and is proportional to the square of the velocity of the vessel. The constant of proportionality is considered to be a result of the ability of the vessel to transfer its energy into the water through which it is travelling. Obviously, the vessel would prefer for efficiency purposes to avoid losing energy to its wake generation. If the constant of

proportionality that links the initial wave amplitude to the square of the ship velocity is  $A_1$ , then (4.65) becomes

$$v_{orb,max} = A_1 g v_{tgt} x^{-1/3} \quad (4.66)$$

In this simple worked example, the aim is to use realistic figures with a rough model to examine the possible causes for the overall artefact before applying a more detailed analysis. As such, for the initial wave amplitude, a realistic number can be used to allow the model to show the trend of the decay and the overall appearance of the artefact against the azimuthal displacements and ambiguities.

As the orbital motion to the wave particles will have a maximum and minimum velocity, shown from (4.63) to be dependent on the amplitude and wavelength, then the bloom appearance is a result of the spread of velocities that are presented to the radar during the image collection. The displaced extent of all the scattering events within the image is then bounded by the maximum and minimum velocities of the orbital motion. As the amplitude of the waves decay as a function of distance along the bow/stern line of the target vessel in accordance with the power law of (4.66)(4.64), the bounding maximum and minimum velocities also decay in accordance with the same power law. Therefore, the appearance of the bloom, from this theoretical proposition, should taper away from the vessel beyond the stern. Figure 74 shows a plot of such a bloom construction using (4.66) with  $A_1$  set to 0.3 m for a target vessel at a range of 100 km. The length of the decaying bloom in Figure 74 has been chosen as an arbitrary number for illustrative purposes only at this stage.

#### 4.7 White Water

Finally considering the case where the mechanism source is white water, the source of the return for the bloom will have a lifetime of its own. It has been suggested, Peltzer et al.

## Chapter 4 – Theoretical SAR Modelling

(1987), that this is dependent on environmental factors including wind speed, direction and sea state. Laboratory work by Callaghan et al. (2017) has shown that there is great variability to the decay time of the order of a factor of up to 50. Foam bubbles could dissipate in as little as 0.2 s or last until 10.4 s. In these timeframes the target vessel modelled here would transit, at most, less than 100 m. Therefore, on the scale that is being considered, similar to the image at Figure 63, if the white water is the cause of the bloom then the bloom must exist close to the source of the white water only. Other than sources attached to the target vessel itself, white water can be produced by breaking events within the wake. Rough bounds can be determined for the region of the wake that contains breaking wave events. Ward et al. (2006) use the downward acceleration of the wave field being greater than  $g/2$  as a discriminator and when the wave slope exceeds 0.58. Another measure is to use the product of the wave amplitude and the wavenumber that determines a breakable wave when it surpasses a threshold value. Melief et al. (2006) use

$$Ak \geq 0.35 \quad (4.67)$$

The value of the figure is not arbitrary but those that use this method cite quantitative or experimental observational sources for the magnitude. However, it does prove to be a reasonable predictor of breaking regions.

Also worth a note, with reference to Figure 72, the physical extent of bubble contaminated water is different depending on the source. This may relate to the life expectancy of the bubbles as noted by Callaghan et al. (2017). In Figure 72, the bubbles associated with the breaking wave events on the Kelvin wake cusps waves decay rapidly and do not extend beyond the subsequent phase of the wave. The turbulent wake bubbles however are much more persistent and extend for a great distance through the image. No calibrated measurable

scale can be attributed to the wake within the image so a comparison between the two will have to suffice for now.

#### 4.8 Final Construction

Figure 74 shows a plot of the combination of the expected returns from the target vessel as described by (4.53) and (4.54) superposed with the expected extreme bounds of the wake return using the orbital velocity of the transverse wake as (4.66).

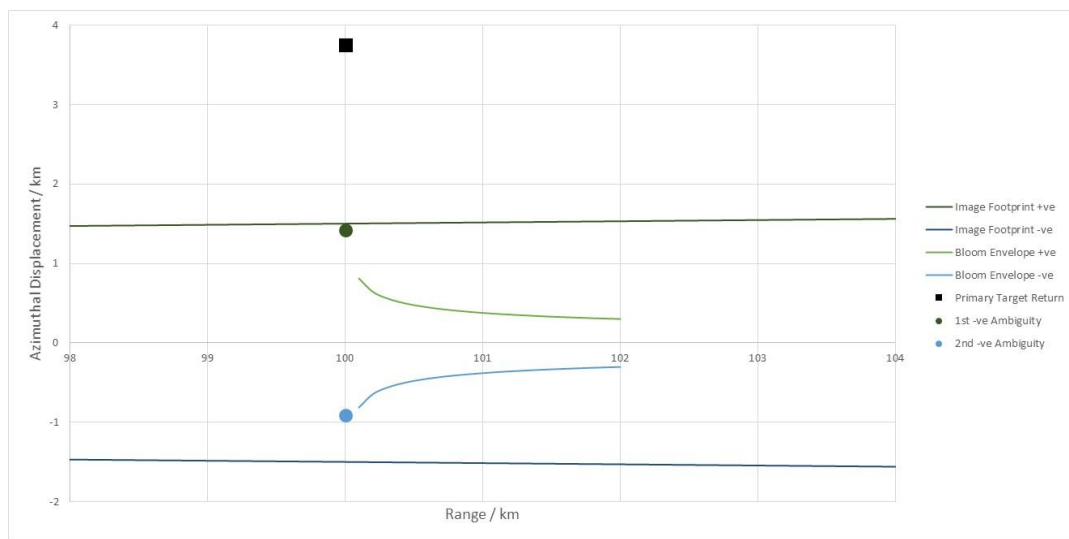


Figure 74: Plot showing the superposition of the extremes of the wake bloom onto a plot of the azimuthally displaced primary return from the target vessel with its azimuthal ambiguities. The extremes of the bloom artefact are plotted from the maximum and minimum orbital velocities of the water particles from within the transverse Kelvin wake.

In principle, the basic model behind Figure 74 shows the characteristics of the full SAR image, Figure 63. The appearance in the plot, however, is idealised owing to its generation from basic SAR theory of individual processing properties. The interaction between these phenomena is not included as yet and the cleanness of the output of Figure 74 is too precise to be able to conclude that the orbital velocity is the root or only cause of the bloom. However, the appearance is promising and suggests that modelling is progressing in the right direction.

#### **4.9 Summary**

This chapter has focussed on the application of basic SAR phenomena to produce a rough model that could explain, to a suitable degree of accuracy, the appearance of the artefacts with the real SAR image. The final model product used the azimuthal displacement from the primary return of the target vessel combined with the resultant azimuthal ambiguities from the primary displaced return and the orbital velocity of the wave particles. The final plot of the model shows promise but requires a more detailed approach to provide conclusive evidence as to what mechanisms are behind the artefacts in the real image. A key question, other than the reliability the previously discussed sources for the artefacts, is the reliance of the scattering on rough water or white water. The next chapter will expand on the realism of the developed model of this chapter by using a full SAR processing algorithm to validate and further understand the non-ideal interactions that have been covered in the basic model thus far.

## **5 CHAPTER 5 – RANGE DOPPLER ALGORITHM MODELLING**

### **5.1 Introduction**

The previous two chapters have focussed on identifying the underlying elements of the overall artefact seen when imaging a ship in the geometric focussing (GF) construct. The sub-aperture analysis and the application of the basic near-field model have gone some way in proposing answers to find the source mechanisms behind the phenomena associated with the primary target vessel return and its wake signature. However, many questions remain unanswered and the applied model should be improved. To that end, before developing a more mathematically comprehensive model for the ship wake in order to examine in detail its associated phenomenon in the GF construct, a step change of an improved sensor model will be conducted in order to validate the previously conducted idealised modelling and to further explore possible scattering artefacts associated with the scene.

### **5.2 Algorithm Considerations**

As this step aims to investigate the characteristic change of the target returns as a result of the generic SAR assumptions, the specific algorithm selected was not of highest importance. There are many SAR processing algorithms to choose from, each comes with its own characteristics but the underlying assumptions remain mostly constant. The output of the system model will be reviewed once complete to see if refinement of the chosen SAR processor is required. To that end, a simple processing algorithm has been chosen for modelling ease. However, as this model aims to understand quite intricate details of the SAR signals effort has been expended on making the signal return elements of the model sufficiently real. As such, the input to the processor comes from a fast-time simulation of a stipulated scene. It was known prior to implementation that such a model is necessarily



## Chapter 5 – Range Doppler Algorithm Modelling

computationally heavy due to the need to conduct pulse-to-pulse simulation but it should result in a clearer picture with regard to the SAR signal response to the target.

### 5.3 Model Details

In order to achieve this step, the range Doppler algorithm (RDA) was chosen from amongst the many options. The general RDA follows similar stages as detailed for this implementation, as at Figure 75, where the range compressed then put through an interpolation stage to correct for range cell migration before finally being azimuthally compressed to form the focussed image.

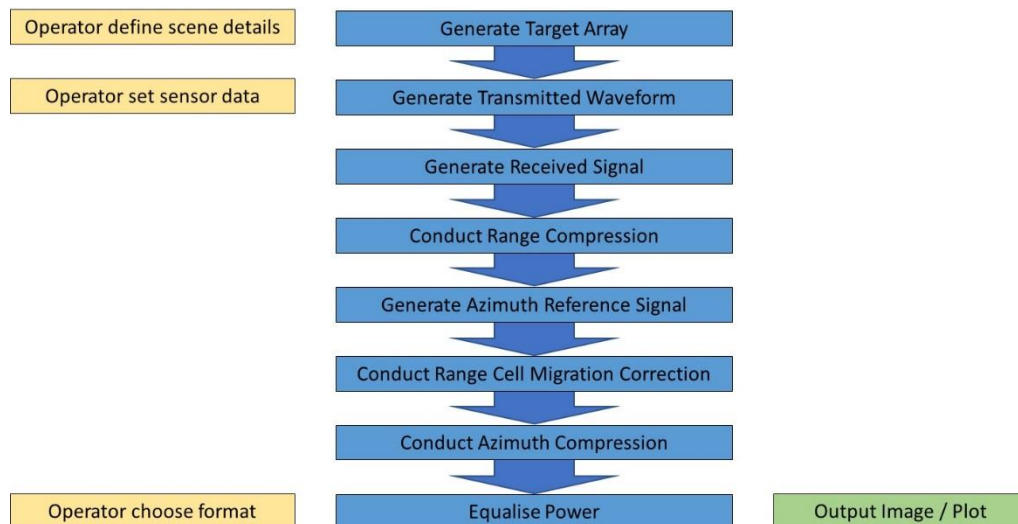


Figure 75: Flow diagram showing the stages of the range Doppler algorithm (RDA) written to generate a simulated SAR image from a user defined target array.

The image construction mechanisms for the RDA fit well with the underlying imaging geometry for the GF technique. The range migration correction interpolation, often the most cumbersome element of any SAR processor, within the RDA would make the model processing step on the less-burdensome side of the scale than compared to say the range migration algorithm. The image formation converts the phase history through two successive FFTs in range and azimuth. This aims to make for simple analysis once the processing is

## Chapter 5 – Range Doppler Algorithm Modelling

complete as both steps are independent and can easily be reversed. The collection geometry was chosen to follow the stripmap SAR geometry as Figure 76.

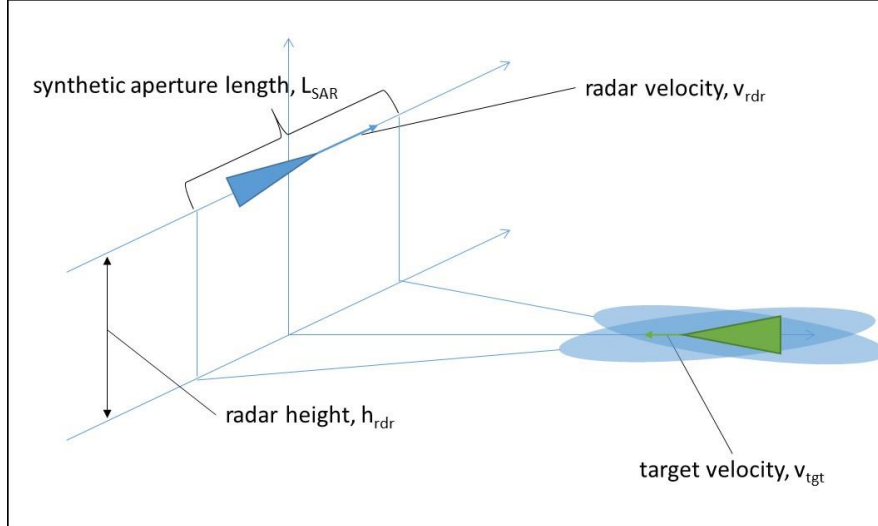


Figure 76: Diagram showing the collection geometry for the RDA algorithm and the determination of some of the terms used for the model.

Details of the algorithm design, parametric data and the waveform used for the SAR processor are at Table 2. The algorithm has been written using standard MATLAB toolsets.

target velocity	$v_{tgt} / \text{ms}^{-1}$	7.72
radar velocity	$v_{rdr} / \text{ms}^{-1}$	205.78
radar height	$h_{rdr} / \text{m}$	6096
SAR aperture duration	$T_{SAR} / \text{s}$	3
SAR aperture length	$L_{SAR} / \text{m}$	617.34
wavelength	$\lambda / \text{m}$	0.03
transmit bandwidth	$B_{tx} / \text{Hz}$	1.00E+08
pulse length	$t_{pulse} / \text{s}$	1.00E-06
PRF	$\text{PRF} / \text{Hz}$	320
number of azimuth bins	$az_{bin} / n$	960
number of range bins	$rng_{bin} / n$	1532
real antenna length	$D / \text{m}$	1
real beamwidth	$b_{width} / \text{deg}$	1.72

Table 2: RDA collection scene and radar parameters.

## Chapter 5 – Range Doppler Algorithm Modelling

The waveform used is an up-chirp linear frequency modulated with centre frequency of 10 GHz, pulse length of 1  $\mu\text{s}$  and PRF of 320 Hz. A plot of the pulse is at Figure 77.

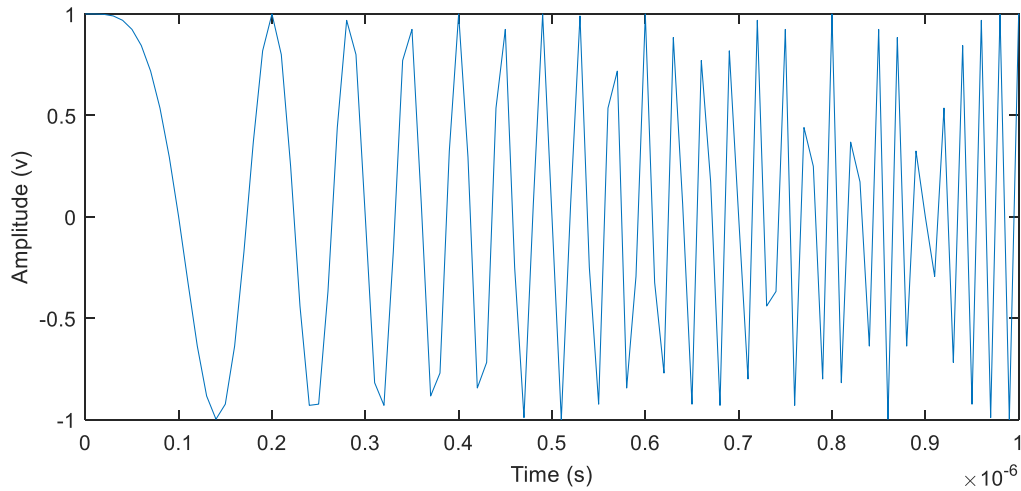


Figure 77: Plot of the RDA up-chirp linear frequency modulated pulse used for the processor.

### 5.4 Model Application

Due to the anticipated computational burden of the scatterer modelling, the full target scene is unachievable. Of the elements of the scene that could be omitted, background sea clutter was thought to be least damaging to the analysis and would buy-back a significant timescale of computation. The target vessel and the wake were thought to be the most important elements to consider. The target vessel itself, as it is considered to be all one entity, is relatively simple to implement. The vessel will move through the scene with a given velocity and the return will be given a relatively high RCS to fall in line with a realistic order of magnitude comparison with the wake scatterers. In this case each vessel scatterer was double the RCS of the wake scatterer. Multiple scatterers, similar to the deck layout of a merchant ship, could be considered. The wake model will initially focus on determining the azimuthal extent of the bloom artefact through modelling the maximum orbital velocity of the wake pattern at several points rearwards from the target vessel. The wake scatterers will be modelled by

## Chapter 5 – Range Doppler Algorithm Modelling

placing point reflectors with representative max and min radial velocities, as per (4.66), on the centreline of the target vessel's track. In line with the RCS of the target vessel scatterers, the wake scatterer RCS will be given a representative value to allow for comparison with the target vessel returns. A layout of the model input scene is shown in Figure 78. The most rearward extent of the wake scatterers remains arbitrary at this point as no single source for the decay and scattering mechanism has yet been identified.

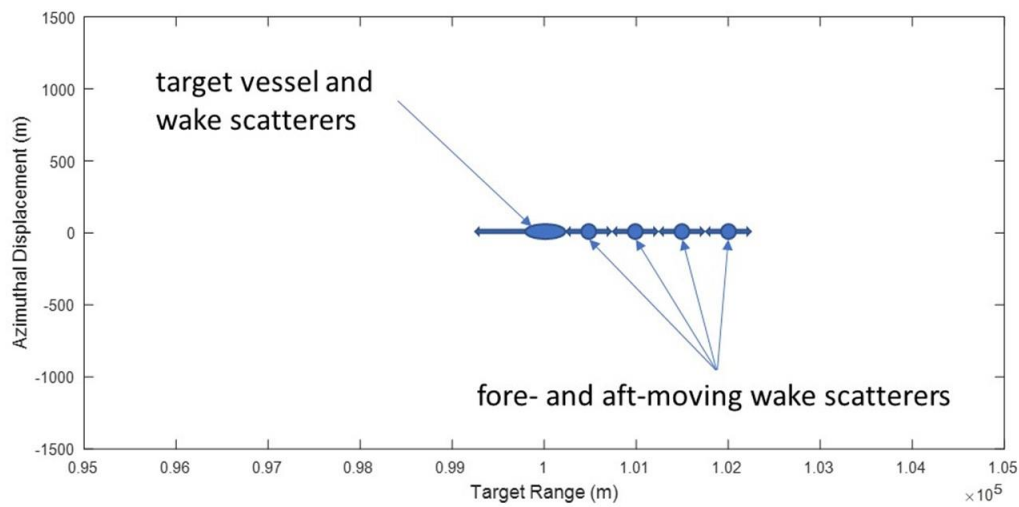


Figure 78: Diagram showing the distribution of the target scatterer array locations and appended velocities. The placement and velocities are designed to simulate the ship and extremities of its wake bloom.

Figure 79 to Figure 83 show plots of the outputs of the RDA algorithm as per Figure 75.

## Chapter 5 – Range Doppler Algorithm Modelling

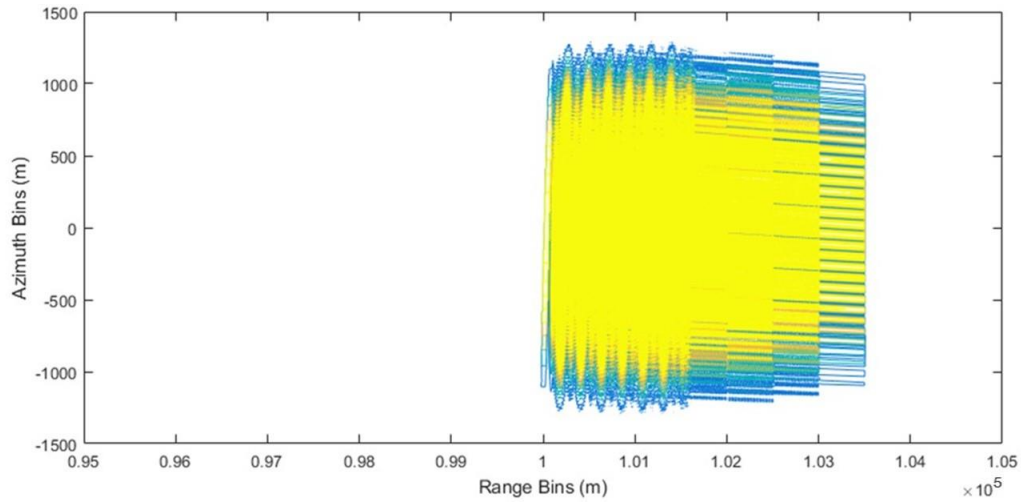


Figure 79: Plot of the interim output of the RDA showing the raw video phase history of the scene using the RDA. Prior to matched filtering, it can be seen that the information contained within the history of each of the scatterers occupy the same space in the time and frequency domains, which must be resolved in order to focus the image.

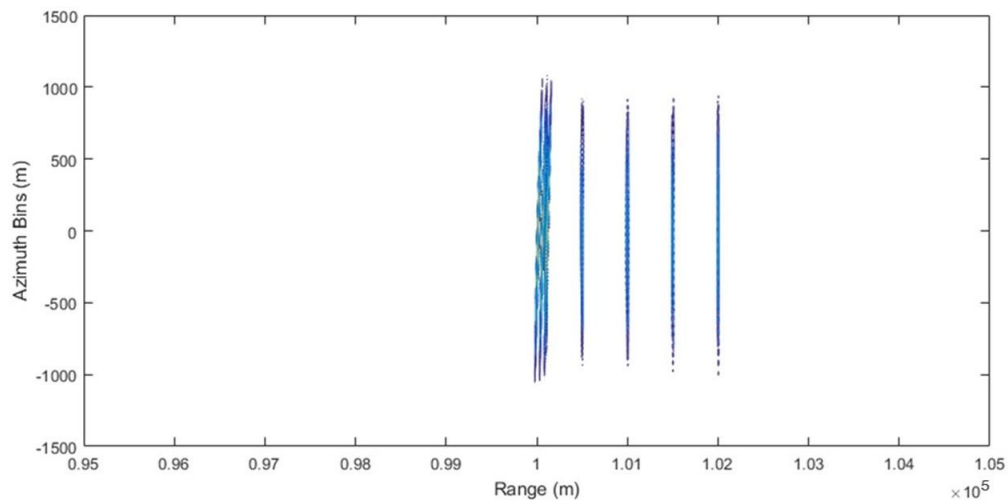


Figure 80: Plot of the interim output of the RDA showing the range compressed return from the scene. Even at this stage of the processing the smear artefact associated with the radial motion of the primary target vessel begins to appear as a non-vertical tilt to the plot.

## Chapter 5 – Range Doppler Algorithm Modelling

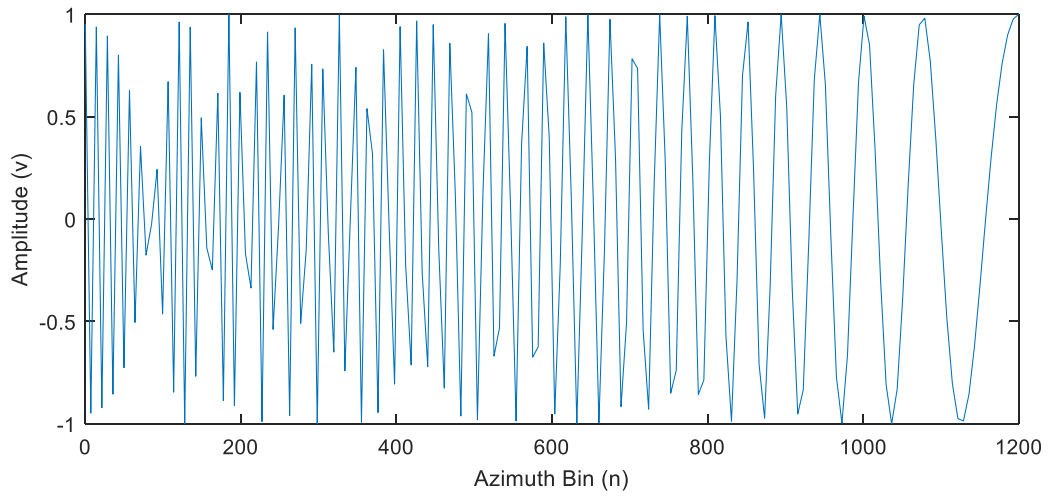


Figure 81: Plot showing the azimuthal compression function for the scene. In this case, with the given geometry of the collection its can be seen that the azimuth chirp induced by the motion creates a down-chirp pattern in this pseudo-waveform.

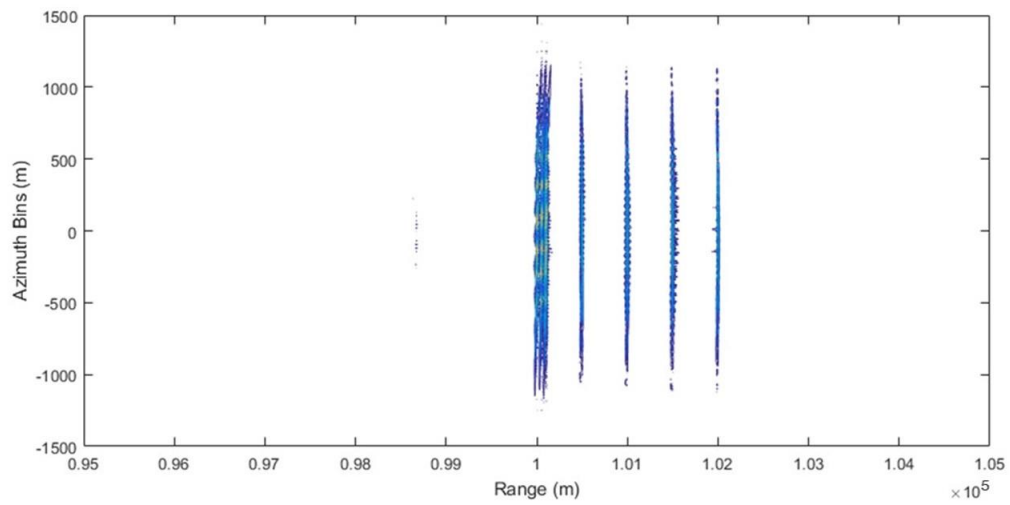


Figure 82: Plot of the interim output of the RDA following range migration correction of the scene.

## Chapter 5 – Range Doppler Algorithm Modelling

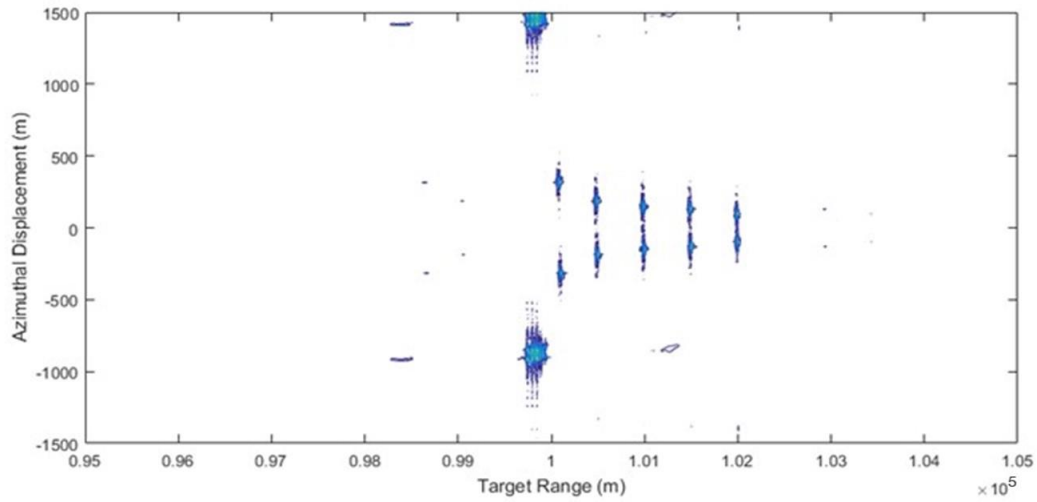


Figure 83: Plot of the final output of the RDA, a simulated SAR image of the target scene. The ambiguous returns from the target vessel can be seen azimuthally displaced, as expected, from the wake bloom region. The wake bloom azimuthal distribution can be seen to follow the predicted power law decay with target range from the target vessel. Imperfections within the processor have also allowed for the appearance of range and azimuth sidelobes around each of the scatterers.

Using equivalent figures for the dimensions of the scene from the previous simple model, the behaviour of the target vessel and the imaging geometry, the final output image Figure 83 can be compared with from the previous result from Figure 84, which is discussed quantitatively in the next section.

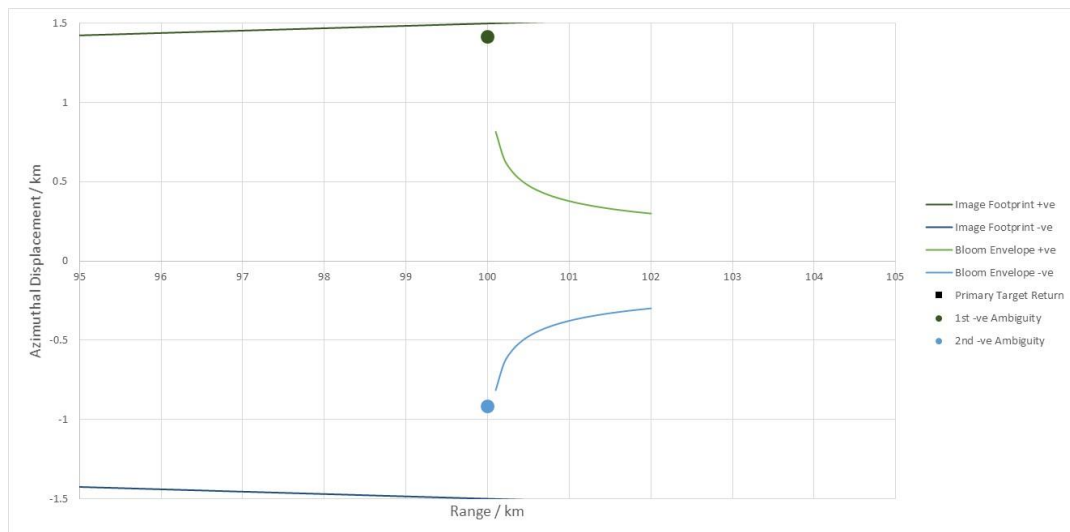


Figure 84: Zoomed section of basic plot of the immediate vicinity of the target vessel showing the ambiguous target returns and the extents of the wake bloom for ready comparison with Figure 83.

## 5.5 Model Output Analysis

The conclusions that can be drawn from this comparison, sadly do not add greater confidence in specifically identifying the source mechanism for the bloom artefact. However, the use of a more comprehensive SAR process technique, rather than the idealised equations, does show how the hypothesised scatterers would react to the SAR environment and thus provided confidence of the behaviour of the hypothesised source under SAR conditions.

The target vessel's appearance in the final imagery had several characteristics that have been replicated by the RDA. The displacement of the target correlates nicely with a mean squared error of 34.5 m in azimuth and 0.7 km in range. Also, using multiple stepped velocities for the target vessel from stationary to its final velocity of 15 kts, the wrap-around effect of the primary return and the first ambiguity can be demonstrated using the RDA processor. It can therefore be concluded as a general statement, given the likely relative velocities of the target vessel compared to an airborne sensor and the imaging geometry of the GF technique, the vessel returns are most likely to be ambiguous in nature rather than primary.

The focus of the target vessel returns in the real image Figure 63 and the intensity were observed to vary. The explanation through the ambiguity theory predicted that the focus of the return would decrease and the intensity would decrease as the returns became more ambiguous. In Figure 85, a moving target has been plotted next to a stationary version of the same target. The ambiguity is noticeably defocussed from the primary return, its scatterers appear more diffuse within the image plot. This can be confirmed through measurement of the mainlobe width of the returns. The primary return has an azimuthal width of 44.5 m compared to the ambiguous return that is 83.6 m. Also, the relative intensity has reduced by -1.24 dB compared with the primary return. From observation in the image, Figure 63, the comparable amplitude of the returns is -5.06 dB, which is considerably more of a drop than



## Chapter 5 – Range Doppler Algorithm Modelling

the theoretical case. This discrepancy could be a result of several possibilities; knowing which ambiguities are present within the original in order to make a fair comparison; not sufficiently approximating scene and sensor characteristics; or, it could be a result of the multitude of other scatterers that clutter the scene and distort the focussing stages of the algorithm.

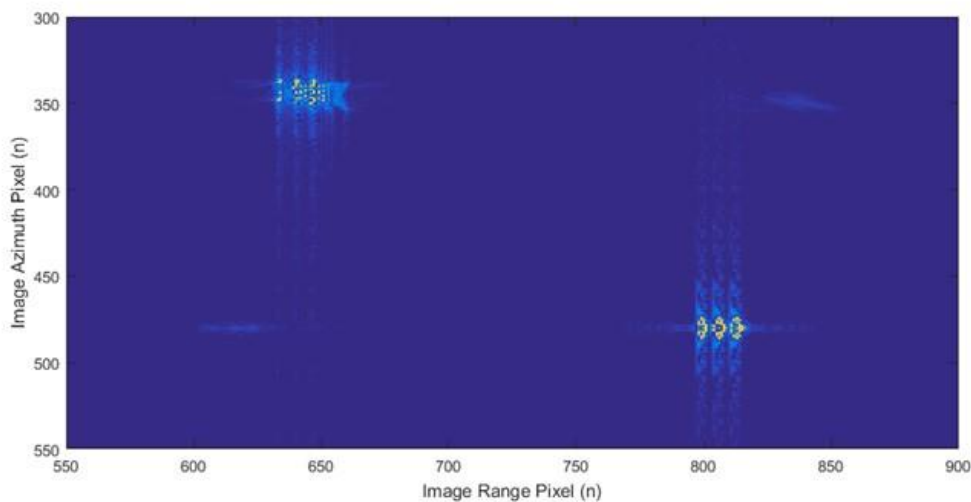


Figure 85: Image plot for comparison of 2 target vessel returns. The target return on the left of the image is moving at  $10 \text{ ms}^{-1}$  whereas the target return on the right is stationary but otherwise identical. The comparison shows the increased defocus of the moving target and the reduced intensity of the return.

The comparable reflectivity of the target vessel and the bloom scatterers is also worth a note.

The RDA cannot shed light on the actual values of the scatterer RCS's but as it is known what values were used for the initial parameters then comment can be passed on the effect that the process had and glean information about how good an initial approximation the parameters were. In this RDA case, the target vessel scatterers were given a RCS that was twice the magnitude of each of the wake scatterers. As can be plainly seen from Figure 83, the target vessel intensity dominates the image. This is not the case for the real image at Figure 63. Other GF images show that there is some variability as to the comparison.

However, in each case the target vessel is classed as a large merchant ship including tankers,

cargo, carriers, ro-ro ferries and container shipping. All vessels are large and highly reflective being primarily constructed from painted steel. Much work has been done by other authors in the past to categorise the RCS of shipping. The RCS function as determined by the azimuthal aspect of the vessel is a variable relationship but the outcome is normally high and in the region of 30-40 dBm<sup>2</sup> (Queen, 1971). Even when the aspect on the target vessel results in its lowest RCS, the bloom scatterers would have to be very reflective to compete with the primary vessel return within the final image. The spread of the bloom effect, coupled with the intensity that it shows, may be a result of a significantly larger number or area of scatterers that accumulate to produce the artefact in the image rather than having a small concentration of powerful reflectors. This is another consideration to take forward to the more comprehensive model in the next section.

## **5.6 Sub-Aperture Algorithm Validation**

The RDA model can also be used to validate the sub-aperture analysis taken. For this step, a single target vessel was simulated with a target velocity of 10 ms<sup>-1</sup> approaching the sensor, as the previous runs. The complex simulated SAR image from the RDA can then be input to the initial sub-aperture technique of Chapter 3. The result of this can be seen in Figure 86, Figure 87 and Figure 88. In this case the full aperture has been split into three sub-images which equates to a 1 s time difference between the centre reference point for each sub-image.

## Chapter 5 – Range Doppler Algorithm Modelling

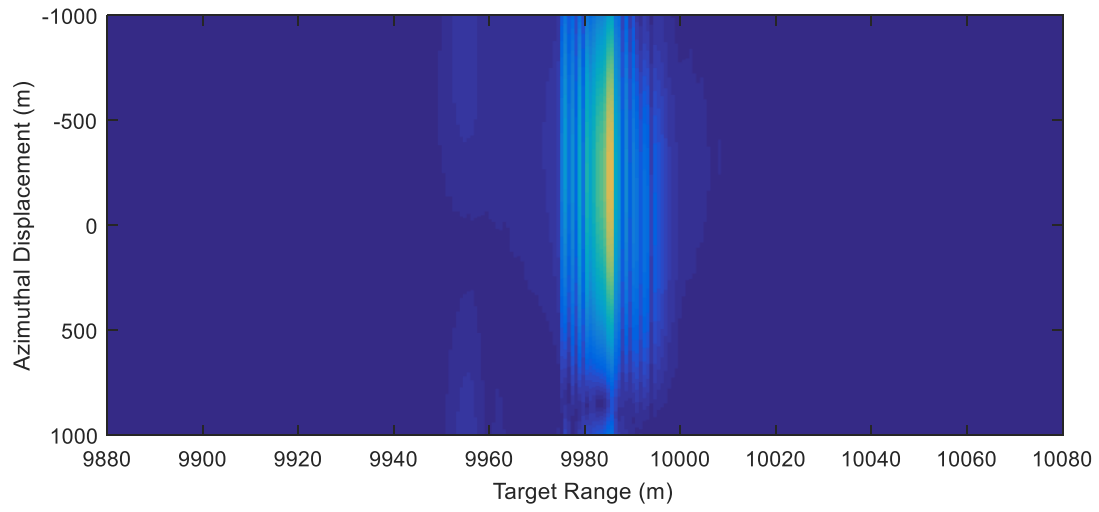


Figure 86: Image plot of sub-image 1 of 3.

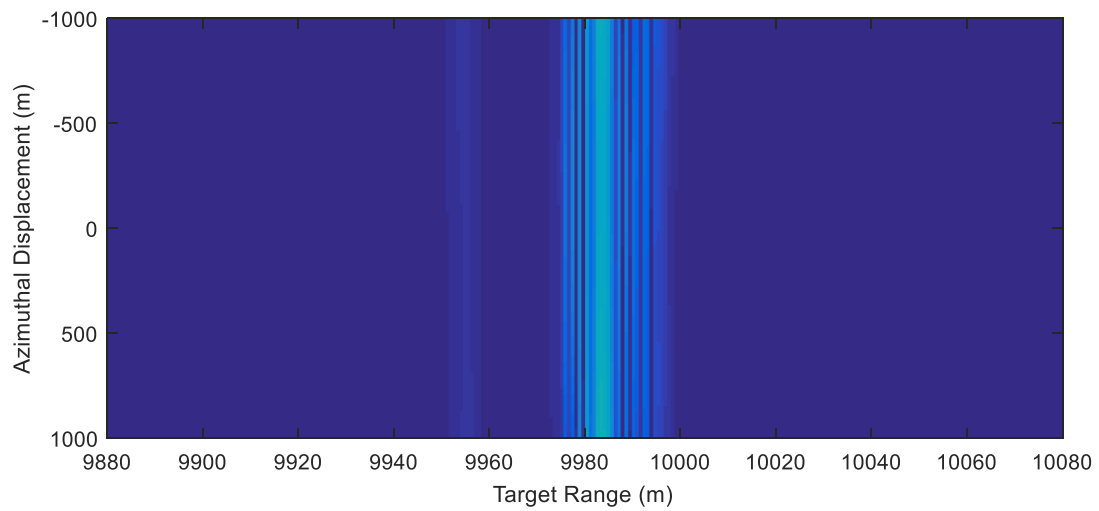


Figure 87: Image plot of sub-image 2 of 3.

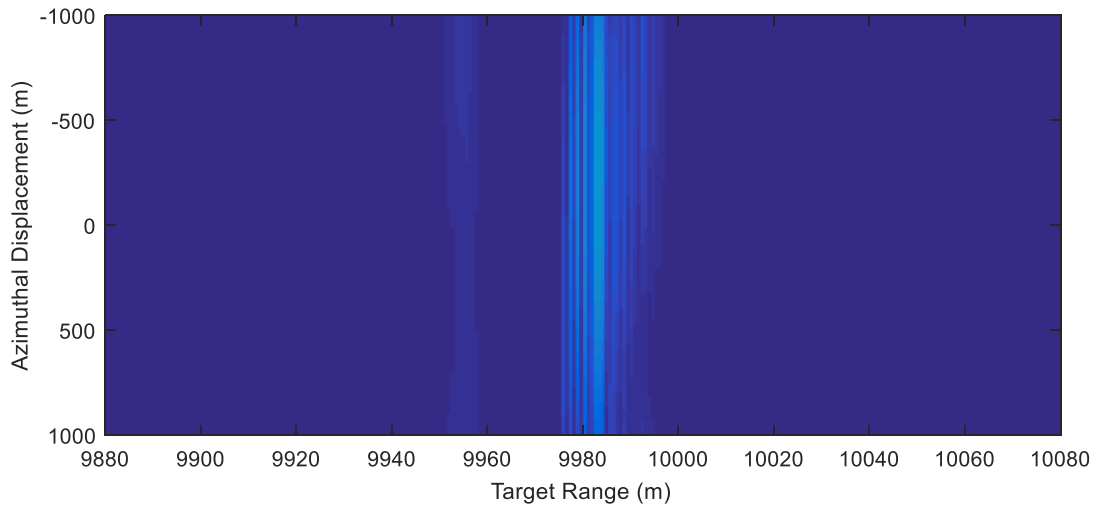


Figure 88: Image plot of sub-image 3 of 3.

The defocussing is a significant feature, which is not unsurprising given the full aperture length is only 3 s and the velocity of the sensor is  $205 \text{ ms}^{-1}$  but the important feature of the movement of the scatterer location through the sub-image set can be seen. The scatterer centre-point target range can be seen to reduce by 10 m between each sub-image, which falls in line with the expected track progression from the known input target velocity.

### 5.7 Sub-Image Intensity Variation

It was identified in Chapter 3 that the mean intensity of each generated sub-image varied through the full aperture in a smooth way beginning and ending with a minimum and rising to a peak intensity at the centre sub-image. It was explained that a likely cause of this phenomenon could be the mis-application of the autofocus during the initial processing of the real SAR image, which has since been highlighted through the sub-aperture deconstruction of the image. However, it was noted that an alternative explanation could be as a result of the particular sub-aperture technique being applied. The RDA model will allow for demonstration of this possible by-product.

## Chapter 5 – Range Doppler Algorithm Modelling

As the sub-images were formed through an algorithm that used the full bandwidth of the complex spectrum of the full aperture and essentially back-engineered the sub-apertures by specific selection, through frequency filtering, there is a risk of inducing a false link between apparent Doppler frequency and azimuth location. The theoretical output of the weighted azimuth spectrum from the flow diagram in Figure 42 should be of the form shown in Figure 89 for a standard SAR image.

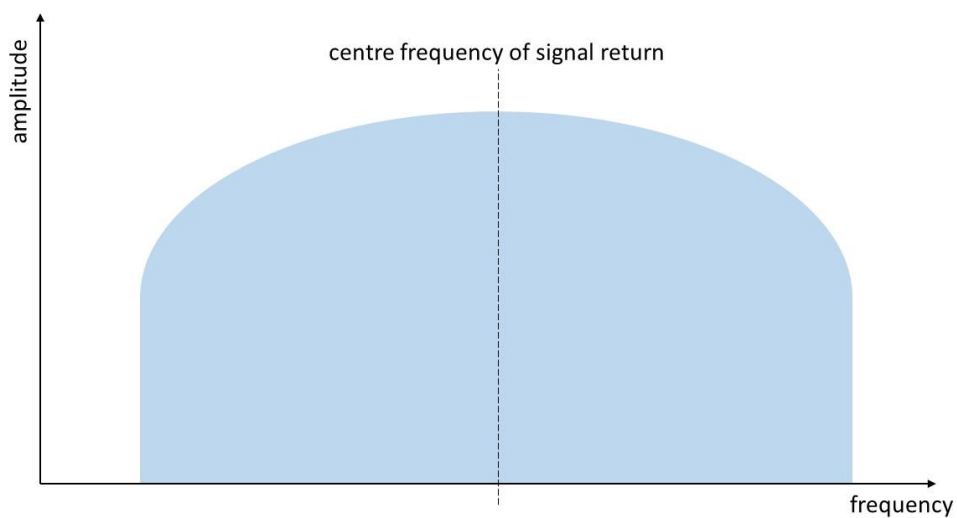


Figure 89: Diagram showing the theoretical distribution of the amplitude of signal frequency from an azimuth slice of a generic SAR image.

Once unweighted the spectrum should be of roughly equal intensity across the frequency bandwidth of the source image, as shown in Figure 90.

## Chapter 5 – Range Doppler Algorithm Modelling

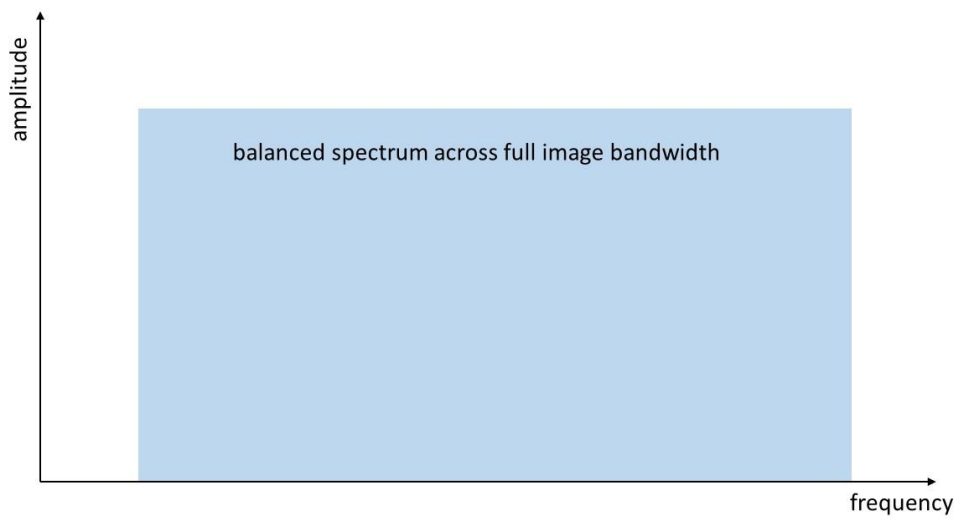


Figure 90: Diagram showing the theoretical distribution of the amplitude of signal frequency from an azimuth slice of a generic SAR image that has been unweighted.

From this unweighted spectrum the sub-image spectra are sampled using window filter functions as per Figure 91.

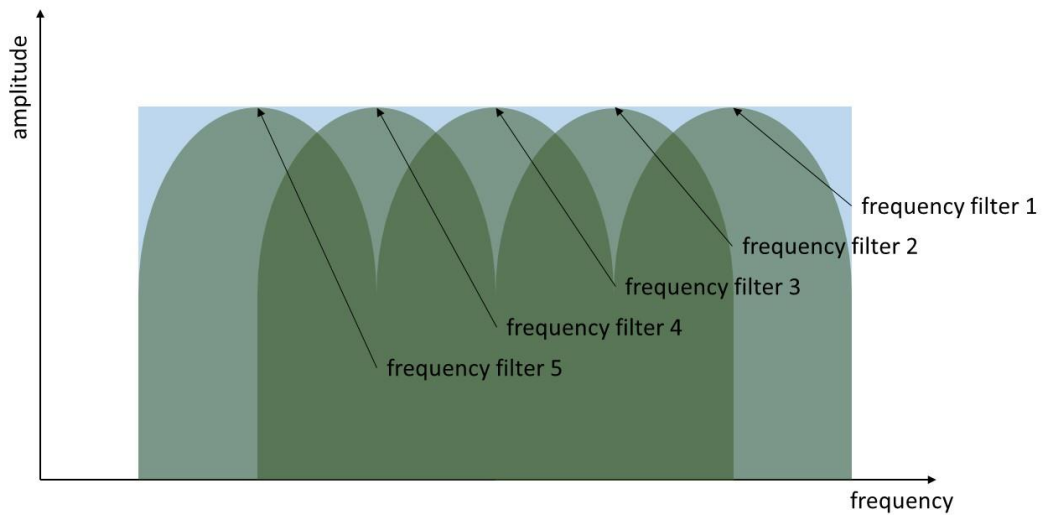


Figure 91: Diagram showing the distribution of window functions that can be used to sample the unweighted image spectrum to form a sub-aperture set. In this case there are 5 windows that have a 50% overlap.

Each of the frequency filtered segments of the full bandwidth are then subject to IFFT to reform a SAR image, albeit at reduced resolution due to the limitation imposed on the

## Chapter 5 – Range Doppler Algorithm Modelling

bandwidth used to form the new sub-image. However, from Figure 91, it can be seen that the magnitude of the higher frequencies within the bandwidth will be greater for the first sub-image than the last sub-image. This now needs to be compared with the expected return from a static scatterer, as per the initial underlying assumptions of the SAR process. The static scatterer should present the frequency profile to the radar through the image collection aperture as shown in Figure 92.

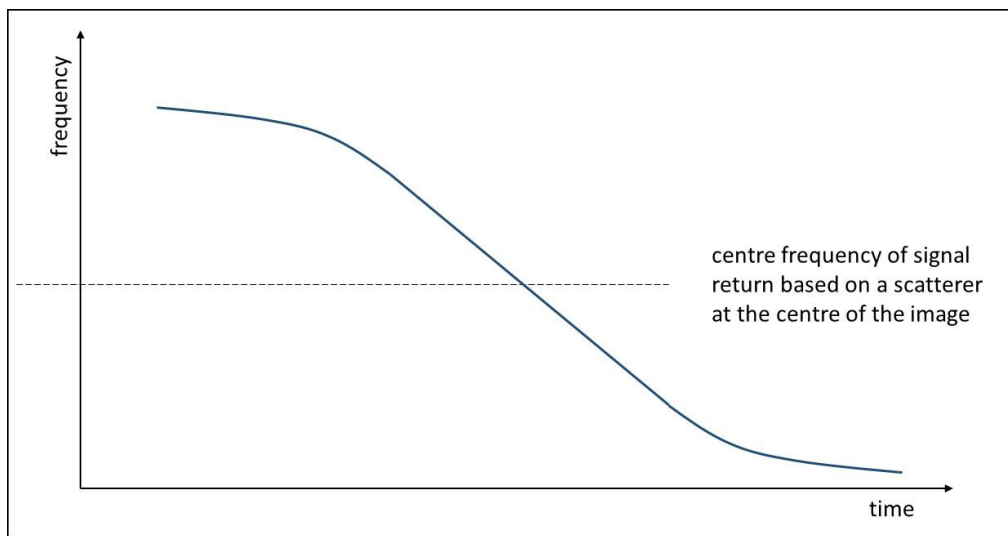


Figure 92: Diagram showing the frequency-time relationship of the azimuthal match filter input used in a generic SAR processor to conduct azimuthal compression. Note that the non-linear extremes of the relationship are generally not used, only the central linear section.

It is the correlation of this function within the returned raw radar signals that allows the SAR processor to conduct the azimuthal compression and hence improve its resolution over that of the real radar. It is by this same process that the azimuthal coordinate is determined for the scatterer. The expected return signals from two scatterers displaced by a fixed value are plotted in Figure 93. Once azimuthally compressed these will be plotted azimuthally displaced, as they should be.

## Chapter 5 – Range Doppler Algorithm Modelling

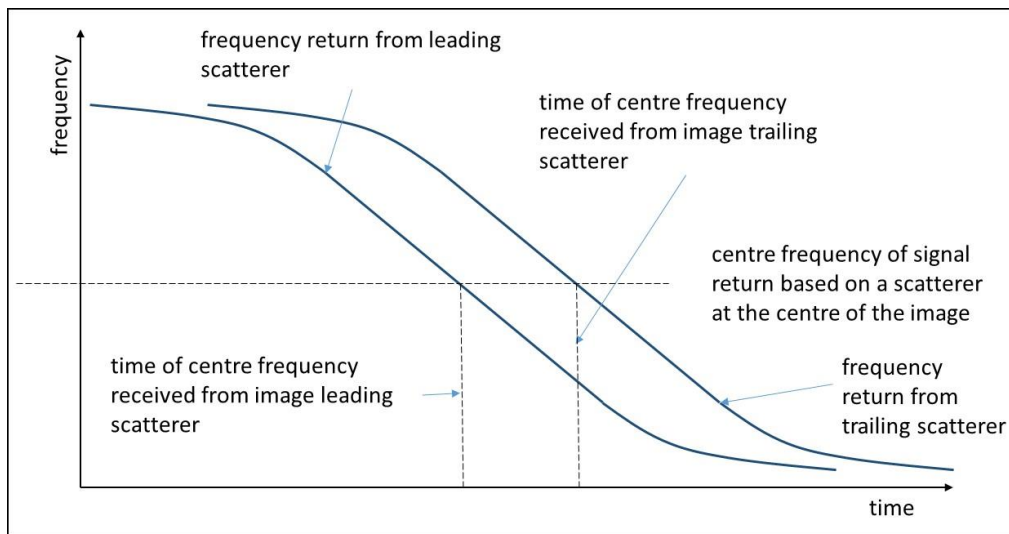


Figure 93: Diagram showing the superposition of the expected frequency response from 2 azimuthally displaced static targets.

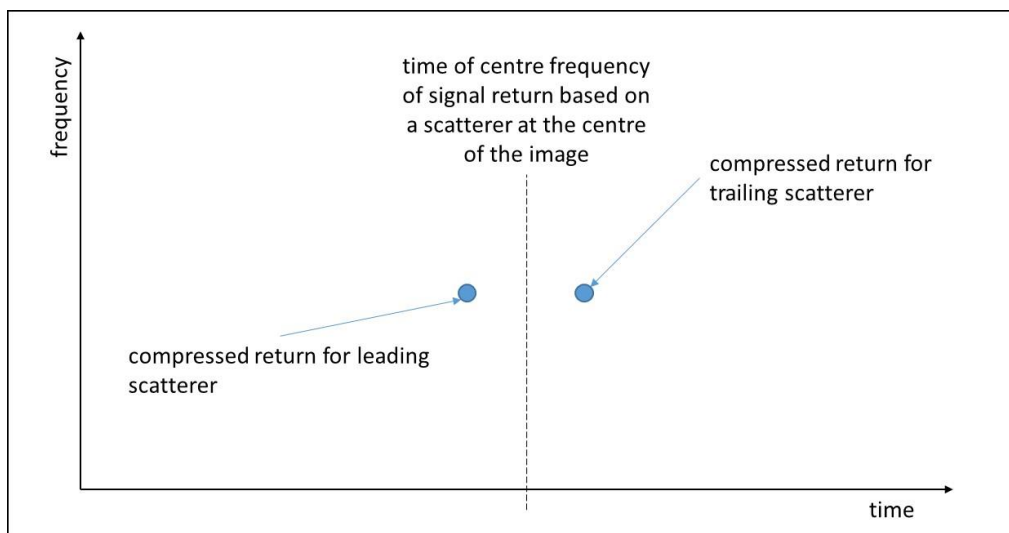


Figure 94: Diagram showing the azimuthally compressed returns for the 2 targets of Figure 93 using the matched filter signal of Figure 92.

It can be seen from the comparison of Figure 93 and Figure 94 that the scatterers are plotted azimuthally displaced dependent on their individual signal frequency history through the collect. In the simple case where there are very few scatterers within the scene, it is entirely possible that the sampling and IFFT will be able to fully compensate for the superposed spectra of the scatterers and return true locations for each. However, this may not be the case



for a highly complex scene where the spectra from a very large number of scatterers superpose. It is conceivable that enough of the individual scatterer spectra are lost in the sum. Therefore, assuming that the unweighted scatterer spectrum spans the width of several sub-image spectrum filters, the sampled first sub-image spectra that has passed through the high frequency filter will likely be plotted azimuthally displaced from the subsequent scatterers. This explanation is complicated by the non-static nature of the water surface that could easily throw some unknown factors into the processing but the generic case for near-zero and zero-centre motion has merit.

In order to demonstrate this cause of the phenomenon, the RDA processor was used with the initial scatterer plot as shown in Figure 95. A total of five identical scatterers were superposed at a target range of  $10^5$  m with an azimuthal displacement of zero. The scatterers were each given a different range velocity in order to simulate a range slice of the bloom artefact. The velocities given were  $[+1 \text{ ms}^{-1}, +0.5 \text{ ms}^{-1}, 0 \text{ ms}^{-1}, -0.5 \text{ ms}^{-1}, -1 \text{ ms}^{-1}]$ . The result of the RDA process from the initial scatterer distribution and parameters can be seen in Figure 96. It can be seen that the range slice of the bloom, although a little ‘digital’ in nature due to there being only five scatterers, is a suitable simulation of a real image.

## Chapter 5 – Range Doppler Algorithm Modelling

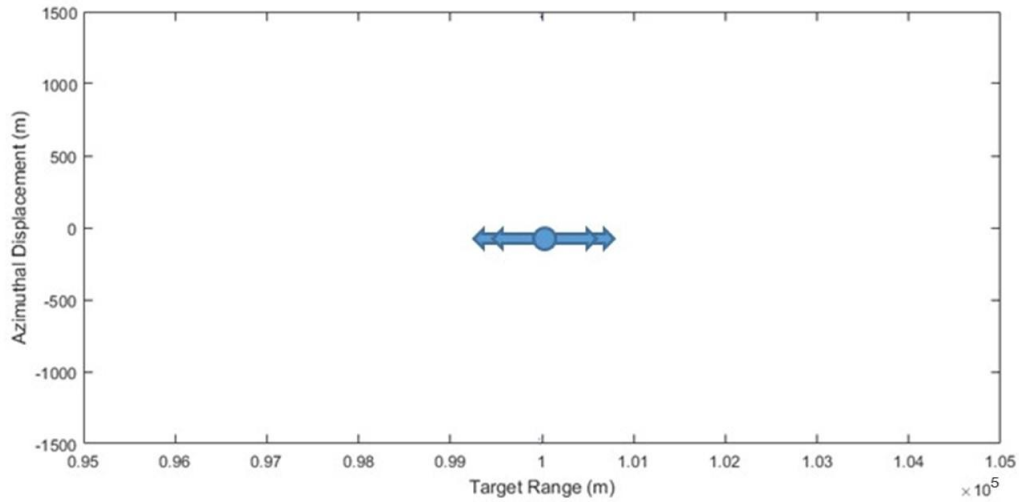


Figure 95: Diagram showing the location and velocity characteristics of 5 target scatterers used to simulate the appearance of an azimuth slice from the wake bloom artefact.

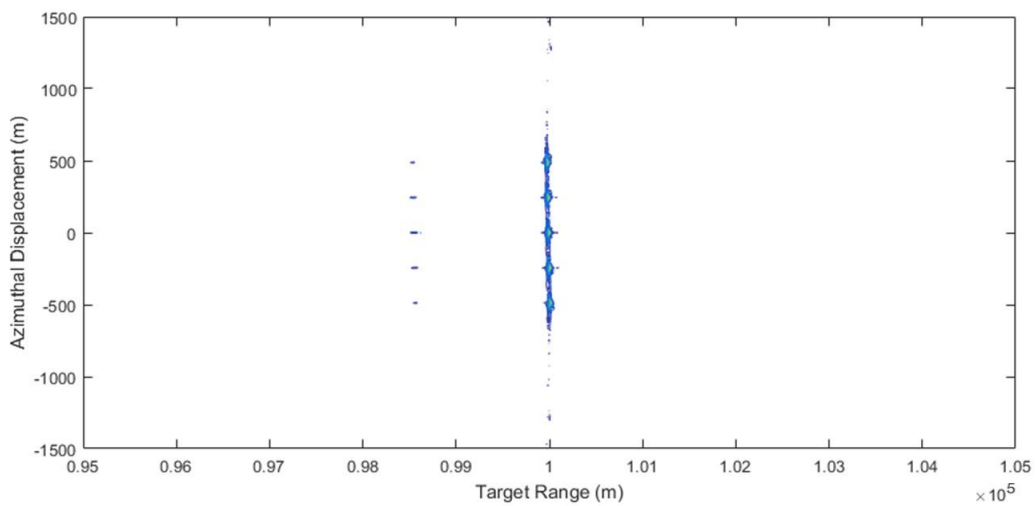


Figure 96: Contour plot of the simulated SAR image output of the RDA of the target scene shown in Figure 95. The spread of the slice of the bloom can be seen and has been chosen to be of representative scale for the real bloom of Figure 71.

The simulated complex SAR image of Figure 96 was then put through the sub-aperture image stages of Figure 42. In this case generating four sub-images. The presentation of the sub-images as contour or image plots make the distribution hard to see so a basic plot function is used in Figure 97 to Figure 100. The plots are taken perpendicular to the range direction of the bloom so that azimuthal displacement can be plotted against scatterer return intensity. In

this case to allow for easier interpretation and comparison between the sub-image plots, the intensity of each figure has been normalised within the set so that the maximum image intensity of each is equal to unity and each carry equal overall weight. Figure 97 is the result of the first chronological slice of the full aperture and the sequence runs through to Figure 100. Each figure plots that azimuthal line where target range equals  $10^5$  m. The overall maximum azimuthal width of the scatterer distribution does not appear to change through the set, the main bloom returns remain within  $\pm 800$  m. However, the peak intensity of the bloom does noticeably shift from +540 m in Figure 97, through a more central location, through to -390 m in Figure 100.

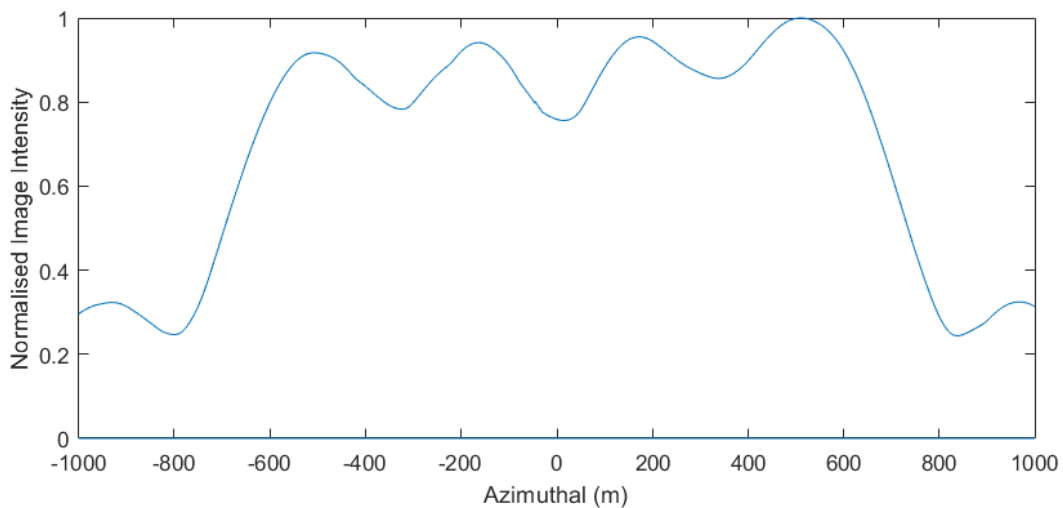


Figure 97: Sub-image azimuthal plot 1 of 4 from Figure 96.

## Chapter 5 – Range Doppler Algorithm Modelling

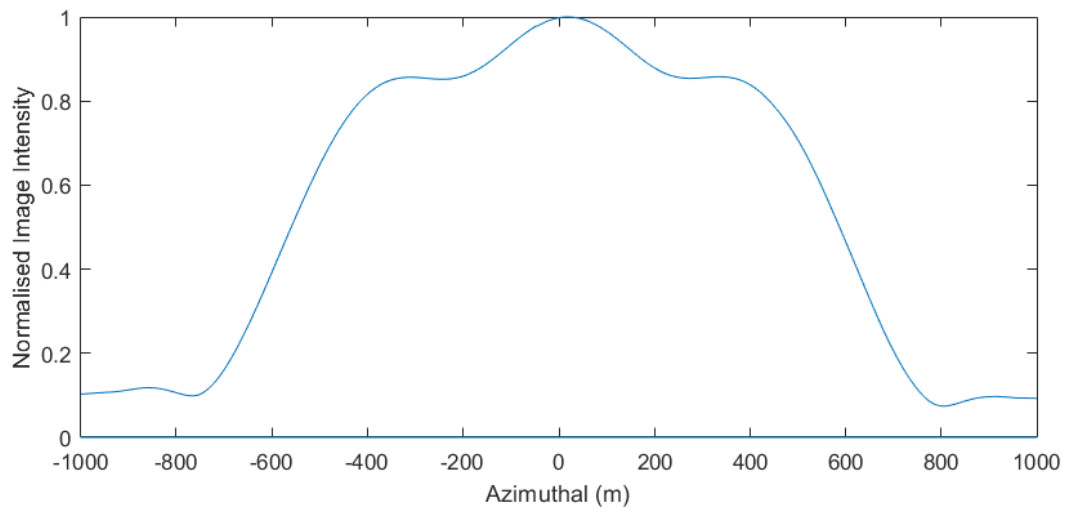


Figure 98: Sub-image azimuthal plot 2 of 4 from Figure 96.

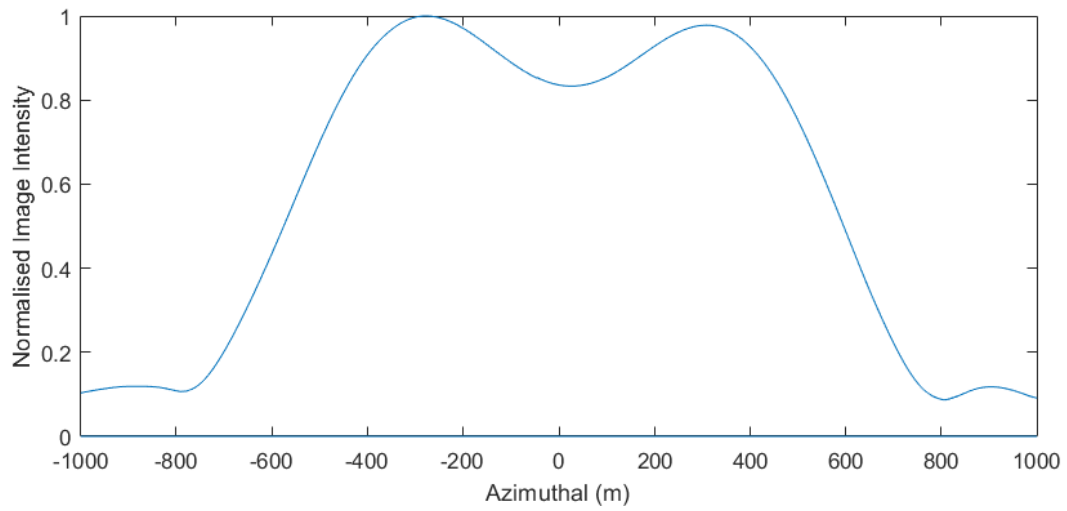


Figure 99: Sub-image azimuthal plot 3 of 4 from Figure 96.

## Chapter 5 – Range Doppler Algorithm Modelling

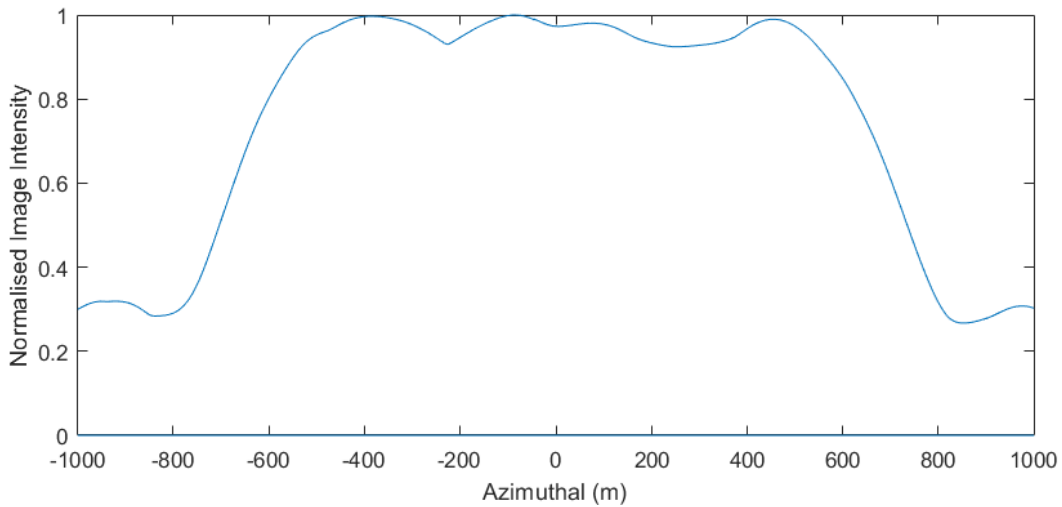


Figure 100: Sub-image azimuthal plot 4 of 4 from Figure 96.

Given that the autofocus processing is a valid reason for the azimuthal variation of the bloom artefact and given the manipulation of the real image, it cannot be ruled out at this time. Along with this alternative explanation, it is concluded that both likely contribute to the variation phenomenon. Further work would be required to split the two effects.

### 5.8 Summary

In this chapter the range Doppler algorithm (RDA) was selected as the full SAR processing technique to apply to a fully simulated fast-time return from a target scene in order to better understand the affect a SAR processing has on the modelled moving targets. The developed basic model from the previous chapters was used as an input to the RDA so that the model's assumptions could be validated and further tested. The RDA showed that the scatterers behave much in the way the pure SAR theory suggests that they should and showed some interesting features concerning the relative RCS of the targets. It was also useful, for completeness, to reassuringly demonstrate the effect of the previously used sub-aperture technique. There still remain unanswered modelling questions, which will now be more

## Chapter 5 – Range Doppler Algorithm Modelling

thoroughly tested with a rigorous mathematical model that starts from the first principles of the hydrodynamics of the target scene. The aim of the thorough model is to better explain the target scene to divulge the true dominant sources of the scattering.

## 6 CHAPTER 6 – HYDRODYNAMIC MODELLING

### 6.1 Introduction

The work of the previous chapters has demonstrated that the ship and wake scene artefacts that appear in the geometric focussing (GF) geometry are likely the result of a complex combination of scatterer behaviour within the scene itself and the reaction of the detected signal to the SAR processor. The rougher modelling conducted up to this point has not been able to fully explain the phenomena but has indicated that the underlying assumptions are worth further investigation. To that end this chapter will develop a more rigorous model that begins from first principles in order to generate a simulated SAR output that can be compared with the real image.

The model will be derived in stages. The first stage will aim to determine the response of a water surface to a point source disturbance. Due to the need to use the approximation method of stationary phase a verification step is used to confirm the result that also uses the asymptotic approximation for one of the Bessel functions within the derivation. The point source will then be moved across a static fluid surface through use of an integration over time with an applied velocity. The result of this integration will be a wake response from a point target. A ship model will then be generated by integrating the moving point source return over the length of a ship to produce a representative ship wake.

### 6.2 Point Source Model Derivation

From the conservation of mass of a given fluid

$$\nabla \cdot \rho \underline{v} = 0 \quad (6.68)$$

Adding the constraint that the fluid is incompressible so that the density remains constant

$$\nabla \cdot \rho \underline{v} = \rho \nabla \cdot \underline{v} \quad (6.69)$$

It therefore follows that

$$\nabla \cdot \underline{v} = 0 \quad (6.70)$$

The velocity can be represented by the existence of a velocity potential:

$$\underline{v} = \nabla \varphi \quad (6.71)$$

From this we can say that the velocity potential can be further described by Laplace's Law:

$$\nabla^2 \varphi = 0 \quad (6.72)$$

In cylindrical polar coordinates this can be expressed as

$$\frac{1}{r} \frac{\partial}{\partial r} \left( r \frac{\partial}{\partial r} \right) \varphi(r, \theta, z, t) + \frac{1}{r^2} \frac{\partial^2}{\partial \theta^2} \varphi(r, \theta, z, t) + \frac{\partial^2}{\partial z^2} \varphi(r, \theta, z, t) = 0 \quad (6.73)$$

With the intent to first solve the velocity potential for a point source on the surface of the fluid boundary with a view to then using the solution to generate a more complex wake pattern through moving the generated wave pattern it would be fair with an expected point source to consider the system to have rotational symmetry and therefore be independent of  $\theta$ . As such, (6.73) becomes

$$\frac{1}{r} \frac{\partial}{\partial r} \left( r \frac{\partial}{\partial r} \right) \varphi(r, z, t) + \frac{\partial^2}{\partial z^2} \varphi(r, z, t) = 0 \quad (6.74)$$

This differential equation for  $\varphi(r, z, t)$  can begin to be solved through the use of the Hankel transform applied to both sides. The form of the Hankel transform used is

$$\mathcal{H}_r\{\varphi(r, z, t)\} = \Phi(k, z, t) = \int_0^\infty r \varphi(r, z, t) \mathcal{J}_0(kr) dr \quad (6.75)$$



where  $J_o$  is the Bessel function of the first order of the first kind. Therefore

$$\mathcal{H}_r \left\{ \frac{1}{r} \frac{\partial}{\partial r} \left( r \frac{\partial}{\partial r} \right) \varphi(r, z, t) \right\} + \mathcal{H}_r \left\{ \frac{\partial^2}{\partial z^2} \varphi(r, z, t) \right\} = 0 \quad (6.76)$$

$$\int_0^\infty r \left[ \frac{1}{r} \frac{\partial}{\partial r} \left\{ r \frac{\partial}{\partial r} \varphi(r, z, t) \right\} \right] J_o(kr) dr + \frac{\partial^2}{\partial z^2} \Phi(k, z, t) = 0 \quad (6.77)$$

The first term is a special case of the Bessel differential operator acting upon  $\varphi(r, z, t)$ , in which case a property of the Hankel transform can be used to simplify the integral. The property states

$$\mathcal{H}_r \{ \Delta_B \varphi(r, z, t) \} = -k^2 \mathcal{H}_r \{ \varphi(r, z, t) \} \quad (6.78)$$

where  $\Delta_B$  is the Bessel differential operator. Substituting back into (6.77) the integral term gives:

$$-k^2 \Phi(k, z, t) + \frac{\partial^2}{\partial z^2} \Phi(k, z, t) = 0 \quad (6.79)$$

From inspection, this has a general solution of the form:

$$\Phi(k, z, t) = a(k, t) e^{kz} \quad (6.80)$$

where  $a(k, t)$  is, as yet, some unknown function of  $k$  and  $t$ . To progress further, the boundary conditions of the system can be used. Consider the motion of the 2D surface of a fluid of infinite depth, the boundary conditions for the elevation of the particles at the surface can be formulated. First, the kinematic boundary condition that ensures that particles that exist on the surface remain on the surface throughout the motion. This kinematic boundary condition (KBC) is given as:

$$\frac{\partial \eta}{\partial t} + \nabla \varphi \cdot \nabla \eta = \frac{\partial \varphi}{\partial z} \quad (6.81)$$

Secondly, the Bernoulli boundary condition that ensures continuity of pressure at the interface of the fluid. This Bernoulli boundary condition (DBC – sometimes referred to as the dynamic boundary condition) is given as:

$$\frac{\partial \varphi}{\partial t} + \frac{1}{2}(\nabla \varphi)^2 + gz = 0 \quad (6.82)$$

From the given situation of the state of the fluid a third boundary condition that describes the continued state of the velocity at the bottom tends to zero. This bottom boundary condition (BBC) is given as:

$$\frac{\partial \varphi}{\partial z} \rightarrow 0 \quad \text{as } z \rightarrow -\infty \quad (6.83)$$

The non-linearity of the boundary conditions makes progression of the derivation problematic in their current form. Taking the assumption that disturbances,  $\eta$ , around the  $z = 0$  plane and velocities are small then it is fair to use the linearised forms of the boundary conditions, which will make the next steps much more manageable, therefore for the KBC and DBC

$$\frac{\partial \eta}{\partial t} + \nabla \varphi \cdot \nabla \eta = \frac{\partial \varphi}{\partial z} \rightarrow \frac{\partial}{\partial t} \eta(r, t) = \frac{\partial}{\partial z} \varphi(r, z = 0, t) \quad (6.84)$$

$$\frac{\partial \varphi}{\partial t} + \frac{1}{2}(\nabla \varphi)^2 + gz = 0 \rightarrow \frac{\partial}{\partial t} \varphi(r, z = 0, t) = -g\eta(r, t) \quad (6.85)$$

The differential of the linearised DBC, (6.85), with respect to time gives

$$\frac{\partial^2}{\partial t^2} \varphi(r, z = 0, t) = -g \frac{\partial}{\partial t} \eta(r, t) \quad (6.86)$$

Substituting the linearised KBC, (6.84), into this result gives

$$\frac{\partial^2}{\partial t^2} \varphi(r, z = 0, t) = -g \frac{\partial}{\partial z} \varphi(r, z = 0, t) \quad (6.87)$$

The Hankel transform can be applied to solve this differential equation:

$$\mathcal{H}_r \left\{ \frac{\partial^2}{\partial t^2} \varphi(r, z = 0, t) \right\} = -g \mathcal{H}_r \left\{ \frac{\partial}{\partial z} \varphi(r, z = 0, t) \right\} \quad (6.88)$$

$$\frac{\partial^2}{\partial t^2} \Phi(k, z = 0, t) = -g \frac{\partial}{\partial z} \Phi(k, z = 0, t) \quad (6.89)$$

From the general solution to the Laplace equation in the given constraints, differentiation of (6.80) with respect to  $z$  gives

$$\frac{\partial}{\partial z} \Phi(k, z, t) = \frac{\partial}{\partial z} a(k, t) e^{kz} \quad (6.90)$$

$$= k a(k, t) e^{kz} \quad (6.91)$$

$$= k \Phi(k, z, t) \quad (6.92)$$

Substituting (6.92) back into (6.89) gives

$$\frac{\partial^2}{\partial t^2} \Phi(k, z = 0, t) = -g k \Phi(k, z = 0, t) \quad (6.93)$$

From this second order differential equation for  $\Phi$  with respect to  $t$ , another general solution can be discerned:

$$\Phi(k, z = 0, t) = b(k) e^{-i\sqrt{gk}t} \quad (6.94)$$

where  $b(k)$  is an unknown function of  $k$ . Taking the inverse Hankel transform with respect to  $r$  of both sides (6.94) gives

Chapter 6 – Hydrodynamic  
Modelling

$$\mathcal{H}_r^{-1}\{\Phi(k, z = 0, t)\} = \mathcal{H}_r^{-1}\{b(k)e^{-i\sqrt{gk}t}\} \quad (6.95)$$

Therefore

$$\varphi(r, z = 0, t) = \int_0^\infty kb(k)e^{-i\sqrt{gk}t}j_o(kr)dk \quad (6.96)$$

Starting from the linearised Bernoulli dynamic boundary condition (6.85) and using the developed solution for  $\varphi(r, z = 0, t)$  at (6.96):

$$\frac{\partial}{\partial t}\varphi(r, z = 0, t) = -g\eta(r, t) \quad (6.97)$$

$$\eta(r, t) = -\frac{1}{g}\frac{\partial}{\partial t}\varphi(r, z = 0, t) \quad (6.98)$$

$$= -\frac{1}{g}\frac{\partial}{\partial t}\int_0^\infty kb(k)e^{-i\sqrt{gk}t}j_o(kr)dk \quad (6.99)$$

$$= \frac{i}{\sqrt{g}}\int_0^\infty k^{3/2}b(k)e^{-i\sqrt{gk}t}j_o(kr)dk \quad (6.100)$$

The last boundary condition required to remove the unknown function  $b(k)$  is to stipulate the form of the surface elevation at the time  $t = 0$ . As such, here a point disturbance shall be used of the form

$$\eta(r, t = 0) = \frac{\delta r}{r} \quad (6.101)$$

From (6.100), this gives

$$\frac{i}{\sqrt{g}}\int_0^\infty k^{3/2}b(k)j_o(kr)dk = \frac{\delta r}{r} \quad (6.102)$$

## Chapter 6 – Hydrodynamic Modelling

Re-writing the left-hand side to group some of the independent elements of  $k$  into a new function of  $k$  can be written:

$$f(k) = k^{1/2}b(k) \quad (6.103)$$

Therefore

$$\frac{i}{\sqrt{g}} \int_0^\infty kf(k)\mathcal{J}_o(kr)dk = \frac{\delta r}{r} \quad (6.104)$$

It can be seen that this is a statement of the form of the inverse Hankel transform of  $f(k)$ , therefore (6.104) can be re-written

$$\frac{i}{\sqrt{g}} \mathcal{H}_r^{-1}\{f(k)\} = \frac{\delta r}{r} \quad (6.105)$$

Applying a Hankel transform to both sides and using the established property of the Hankel function:

$$\mathcal{H}_r\left\{\frac{\delta r}{r}\right\} = 1 \quad (6.106)$$

Therefore (6.105) becomes

$$\frac{i}{\sqrt{g}}f(k) = \mathcal{H}_r\left\{\frac{\delta r}{r}\right\} \quad (6.107)$$

$$f(k) = \frac{\sqrt{g}}{i} \quad (6.108)$$

Substituting this expression for  $f(k)$  back into (6.100) gives

$$\eta(r, t) = \frac{i}{\sqrt{g}} \int_0^\infty kf(k)e^{-i\sqrt{gk}t}\mathcal{J}_o(kr)dk \quad (6.109)$$

## Chapter 6 – Hydrodynamic Modelling

$$\eta(r, t) = \frac{i}{\sqrt{g}} \int_0^\infty k \frac{\sqrt{g}}{i} e^{-i\sqrt{gk}t} J_0(kr) dk \quad (6.110)$$

$$\eta(r, t) = \int_0^\infty k e^{-i\sqrt{gk}t} J_0(kr) dk \quad (6.111)$$

Equations in this form are hard to solve analytically and often have required asymptotic approximations and limited boundary conditions to produce a manageable result. Frequently used by Lord Kelvin to process integrals of this form, the application of the method of stationary phase is such an approximation method that, although sometimes lengthy, can produce usable simplifications.

As the Bessel function can be represented as:

$$J_0(kr) = \frac{1}{\pi} \int_{-\pi}^{+\pi} e^{ikr \cos \tau} d\tau \quad (6.112)$$

This can be used to expand the surface elevation equation (6.111):

$$\eta(r, t) = \frac{1}{\pi} \int_{-\pi}^{+\pi} d\tau \int_0^\infty k e^{ikr \cos \tau} e^{-i\sqrt{gk}t} dk \quad (6.113)$$

First, the integral over  $k$  will be considered. The form of the phase term within the integral allows for the use of the method of stationary phase. Two substitutions can be made to simplify the process:

$$p^2 = kr \text{ and } \alpha = \sqrt{\frac{g}{r}} t \quad (6.114)$$

Therefore

$$2p dp = r dk \quad (6.115)$$

$$dk = \frac{2p}{r} dp \quad (6.116)$$

Looking at the phase term of (6.113) and using the substitution of (6.114)

$$kr \cos \tau - \sqrt{gk}t = p^2 \cos \tau - \sqrt{gk} \frac{\sqrt{r}}{\sqrt{r}} t \quad (6.117)$$

$$= p^2 \cos \tau - \sqrt{kr} \frac{\sqrt{g}}{\sqrt{r}} t \quad (6.118)$$

$$= p^2 \cos \tau - p\alpha \quad (6.119)$$

Making the substitutions of (6.114), (6.116) and (6.119) back into (6.113) gives

$$\eta(r, t) = \frac{1}{\pi} \int_{-\pi}^{+\pi} d\tau \int_0^{\infty} \frac{p^2}{r} e^{i(p^2 \cos \tau - p\alpha)} \frac{2p}{r} dp \quad (6.120)$$

$$= \frac{2}{\pi r^2} \int_{-\pi}^{+\pi} d\tau \int_0^{\infty} p^3 e^{i(p^2 \cos \tau - p\alpha)} dp \quad (6.121)$$

For the method of stationary phase, set the phase term whose stationary point is to be found to be

$$f(p) = p^2 \cos \tau - p\alpha \quad (6.122)$$

$$\frac{\partial}{\partial p} (p^2 \cos \tau - p\alpha) = 2p \cos \tau - \alpha \quad (6.123)$$

$$\frac{\partial^2}{\partial p^2} (p^2 \cos \tau - p\alpha) = 2 \cos \tau \quad (6.124)$$

Therefore  $f(p)$  will be stationary where

$$2p \cos \tau - \alpha = 0 \quad (6.125)$$

Chapter 6 – Hydrodynamic  
Modelling

$$p_0 = \frac{\alpha}{2\cos \tau} \quad (6.126)$$

Using a Taylor series expansion of the function  $f(p)$  in the vicinity of  $p_0$ :

$$f(p) = f(p_0) + f'(p_0)(p - p_0) + f''(p_0) \frac{(p - p_0)^2}{2!} + \dots \quad (6.127)$$

$$f(p) \approx (p_0^2 \cos \tau - p_0 \alpha) + (2p_0 \cos \tau - \alpha)(p - p_0) \quad (6.128)$$

$$+ (2 \cos \tau) \frac{(p - p_0)^2}{2}$$

$$= p_0^2 \cos \tau - p_0 \alpha + 2pp_0 \cos \tau - p\alpha + 2p_0^2 \cos \tau + p_0 \alpha \quad (6.129)$$

$$+ \cos \tau (p - p_0)^2$$

$$= p_0^2 \cos \tau + 2pp_0 \cos \tau - p\alpha + 2p_0^2 \cos \tau + \cos \tau (p - p_0)^2 \quad (6.130)$$

Using the expression for  $p_0$ , (6.126) and rearranging for  $\alpha$  gives

$$\alpha = 2p_0 \cos \tau \quad (6.131)$$

Substituting (6.131) back into (6.130) gives

$$f(p) = p_0^2 \cos \tau + 2pp_0 \cos \tau - 2pp_0 \cos \tau - 2p_0^2 \cos \tau \quad (6.132)$$

$$+ \cos \tau (p - p_0)^2$$

$$= p_0^2 \cos \tau - 2p_0^2 \cos \tau + \cos \tau (p - p_0)^2 \quad (6.133)$$

$$= -p_0^2 \cos \tau + \cos \tau (p - p_0)^2 \quad (6.134)$$

$$= \cos \tau \{(p - p_0)^2 - p_0^2\} \quad (6.135)$$

Substituting the phase term (6.135) back into the integral of (6.121) and confining the integral region to the vicinity of the point of stationary phase:



## Chapter 6 – Hydrodynamic Modelling

$$\eta(r, t) = \frac{2}{\pi r^2} \int_{-\pi}^{+\pi} d\tau \int_0^\infty p_o^3 e^{i \cos \tau \{(p-p_o)^2 - p_o^2\}} dp \quad (6.136)$$

Rearranging the integrand:

$$\eta(r, t) = \frac{2}{\pi r^2} \int_{-\pi}^{+\pi} d\tau p_o^3 e^{-i \cos \tau p_o^2} \int_{p_o - \varepsilon}^{p_o + \varepsilon} e^{i \cos \tau (p-p_o)^2} dp \quad (6.137)$$

Further substitutions can be made to complete the integral for  $p$ :

$$s = q(p - p_o) ; \quad q^2 = \cos \tau \quad (6.138)$$

Therefore

$$\frac{ds}{q} = dp \quad (6.139)$$

Making the substitutions of (6.138) and (6.139) into (6.137) gives,

$$\eta(r, t) = \frac{2}{\pi r^2} \int_{-\pi}^{+\pi} d\tau p_o^3 e^{-i \cos \tau p_o^2} \frac{1}{q} \int_{-q\varepsilon}^{+q\varepsilon} e^{is^2} ds \quad (6.140)$$

Using an identity integral for the exponential term of the form

$$\int_{-\infty}^{+\infty} e^{-ax^2} dx = \sqrt{\frac{\pi}{a}} \quad (6.141)$$

Therefore

$$\int_{-q\varepsilon}^{+q\varepsilon} e^{is^2} ds \approx \sqrt{\frac{\pi}{-i}} \quad (6.142)$$

$$= \sqrt{\pi} e^{i\frac{\pi}{4}} \quad (6.143)$$

This gives

$$\eta(r, t) = \frac{2}{\pi r^2} \int_{-\pi}^{+\pi} d\tau p_o^3 e^{-i \cos \tau p_o^2} \frac{1}{\sqrt{\cos \tau}} \sqrt{\pi} e^{i \frac{\pi}{4}} \quad (6.144)$$

Rearranging

$$\eta(r, t) = \frac{2e^{i \frac{\pi}{4}}}{\sqrt{\pi} r^2} \int_{-\pi}^{+\pi} d\tau \frac{p_o^3}{\sqrt{\cos \tau}} e^{-i \cos \tau p_o^2} \quad (6.145)$$

This can be simplified. As

$$p_o = \frac{\alpha}{2 \cos \tau} \quad (6.146)$$

Therefore

$$\eta(r, t) = \frac{2e^{i \frac{\pi}{4}}}{\sqrt{\pi} r^2} \int_{-\pi}^{+\pi} \left( \frac{\alpha}{2 \cos \tau} \right)^3 \frac{1}{\sqrt{\cos \tau}} e^{-i \cos \tau p_o^2} d\tau \quad (6.147)$$

$$= \frac{2e^{i \frac{\pi}{4}} \alpha^3}{\sqrt{\pi} r^2 2^3} \int_{-\pi}^{+\pi} \left( \frac{1}{\cos \tau} \right)^{7/2} e^{-i \frac{\alpha^2}{4 \cos \tau}} d\tau \quad (6.148)$$

$$= \frac{\alpha^3 e^{i \frac{\pi}{4}}}{2^2 \sqrt{\pi} r^2} \int_{-\pi}^{+\pi} \left( \frac{1}{\cos \tau} \right)^{7/2} e^{-i \frac{\alpha^2}{4 \cos \tau}} d\tau \quad (6.149)$$

The method of stationary phase can then be applied to the phase term within the integral for  $\tau$ , let:

$$f(\tau) = \frac{1}{\cos \tau} \quad (6.150)$$

$$\frac{\partial}{\partial \tau} \left( \frac{1}{\cos \tau} \right) = \frac{\sin \tau}{(\cos \tau)^2} \quad (6.151)$$

$$\frac{\partial^2}{\partial \tau^2} \left( \frac{1}{\cos \tau} \right) = \frac{\cos \tau}{(\cos \tau)^2} + 2 \frac{\sin \tau}{(\sin \tau)^3} \quad (6.152)$$

## Chapter 6 – Hydrodynamic Modelling

Therefore  $f(\tau)$  will be stationary where

$$\frac{\sin \tau}{(\cos \tau)^2} = 0 \quad (6.153)$$

$$\tau_0 = 0 \quad (6.154)$$

A Taylor expansion of  $f(\tau)$  in the vicinity of  $\tau_0 = 0$  gives

$$f(\tau) \approx 1 + \frac{\tau^2}{2} \quad (6.155)$$

Substituting this phase term (6.155) back into (6.149) and confining the integral to the vicinity of  $\tau_0$  gives

$$\eta(r, t) = \frac{\alpha^3 e^{i\frac{\pi}{4}}}{2^2 \sqrt{\pi} r^2} \int_{\tau_0 - \varepsilon}^{\tau_0 + \varepsilon} \left( \frac{1}{\cos \tau_0} \right)^{7/2} e^{-i\frac{\alpha^2}{4} \left( 1 + \frac{\tau^2}{2} \right)} d\tau \quad (6.156)$$

$$= \frac{\alpha^3 e^{i\frac{\pi}{4}}}{2^2 \sqrt{\pi} r^2} e^{-i\frac{\alpha^2}{4}} \int_{\tau_0 - \varepsilon}^{\tau_0 + \varepsilon} e^{-i\frac{\alpha^2}{8} \tau^2} d\tau \quad (6.157)$$

Again, using the identity integral for the exponential term:

$$\int_{-\infty}^{+\infty} e^{-ax^2} dx = \sqrt{\frac{\pi}{a}} ; a = i \frac{\alpha^2}{8} \quad (6.158)$$

Therefore

$$\int_{\tau_0 - \varepsilon}^{\tau_0 + \varepsilon} e^{-i\frac{\alpha^2}{8} \tau^2} d\tau \approx \sqrt{\frac{8\pi}{i\alpha^2}} \quad (6.159)$$

$$= \sqrt{\frac{8\pi}{\alpha^2}} e^{-i\frac{\pi}{4}} \quad (6.160)$$

Substituting (6.160) back into (6.157) gives,

Chapter 6 – Hydrodynamic  
Modelling

$$\eta(r, t) = \frac{\alpha^3 e^{i\frac{\pi}{4}}}{2^2 \sqrt{\pi} r^2} e^{-i\frac{\alpha^2}{4}} \sqrt{\frac{8\pi}{\alpha^2}} e^{-i\frac{\pi}{4}} \quad (6.161)$$

$$= \frac{2^{3/2} \alpha^3 \sqrt{\pi} e^{i\frac{\pi}{4}} e^{-i\frac{\pi}{4}}}{2^2 \alpha \sqrt{\pi} r^2} e^{-i\frac{\alpha^2}{4}} \quad (6.162)$$

$$= \frac{\alpha^2}{2^{1/2} r^2} e^{-i\frac{\alpha^2}{4}} \quad (6.163)$$

As, from (6.114),

$$\alpha = \sqrt{\frac{g}{r}} t \quad (6.164)$$

Therefore (6.163) becomes

$$\eta(r, t) = \frac{1}{2^{1/2} r^2} \frac{gt^2}{r} e^{-i\frac{gt^2}{4r}} \quad (6.165)$$

$$= \frac{gt^2}{\sqrt{2} r^3} e^{-i\frac{gt^2}{4r}} \quad (6.166)$$

Taking the real valued functions of the expression for the surface elevation:

$$\mathcal{Re}\{\eta(r, t)\} = \mathcal{Re}\left\{\frac{gt^2}{\sqrt{2} r^3} e^{-i\frac{gt^2}{4r}}\right\} \quad (6.167)$$

$$\eta_{\mathcal{Re}}(r, t) = \frac{gt^2}{\sqrt{2} r^3} \cos \frac{gt^2}{4r} \quad (6.168)$$

The phase term for this function appears sensible at this point; the amplitude term is a little surprising due to the joint dependence on both  $t^2$  and  $r^3$ . The magnitude of the indices does suggest that the function will decay with range from the point source, as it should, but the  $t^2$

component suggests that it makes the amplitude of the wave grow with time – somewhat unreal.

### 6.3 Alternative Derivation

In order to check this derivation, with particular consideration given to understanding the impact of the approximations, a slightly altered formulation shall be completed using the asymptotic formulation for  $J_o(kr)$ . This stipulation does then confine the elevation solution to the far field.

Starting with the expression for the surface elevation at (6.111):

$$\eta(r, t) = \int_0^{\infty} k e^{-i\sqrt{gk}t} J_o(kr) dk \quad (6.169)$$

The Bessel function of the first order of the first kind can be approximated as

$$J_o(kr) \approx \frac{i}{\sqrt{2\pi kr}} \left\{ e^{i(kr + \frac{\pi}{4})} + e^{-i(kr + \frac{\pi}{4})} \right\} \quad (6.170)$$

Substituting this into (6.169), therefore

$$\eta(r, t) \approx \int_0^{\infty} k e^{-i\sqrt{gk}t} \frac{i}{\sqrt{2\pi kr}} \left\{ e^{i(kr + \frac{\pi}{4})} + e^{-i(kr + \frac{\pi}{4})} \right\} dk \quad (6.171)$$

$$= \frac{i}{\sqrt{2\pi r}} \int_0^{\infty} \sqrt{k} \left\{ e^{i(kr - \sqrt{gk}t + \frac{\pi}{4})} + e^{-i(kr + \sqrt{gk}t + \frac{\pi}{4})} \right\} dk \quad (6.172)$$

For ease, the two separate terms within the integral can be treated separately:

$$\eta(r, t) = \eta_1(r, t) + \eta_2(r, t) \quad (6.173)$$

where

Chapter 6 – Hydrodynamic  
Modelling

$$\eta_1(r, t) = \frac{i}{\sqrt{2\pi r}} \int_0^\infty \sqrt{k} e^{i(kr - \sqrt{gk}t + \frac{\pi}{4})} dk \quad (6.174)$$

$$\eta_2(r, t) = \frac{i}{\sqrt{2\pi r}} \int_0^\infty \sqrt{k} e^{-i(kr + \sqrt{gk}t + \frac{\pi}{4})} dk \quad (6.175)$$

So, making similar substitutions as before into  $\eta_1(r, t)$ :

$$p^2 = kr \text{ and } \alpha = \sqrt{\frac{g}{r}} t \quad (6.176)$$

Therefore

$$2p dp = r dk \quad (6.177)$$

$$dk = \frac{2p}{r} dp \quad (6.178)$$

The phase term (6.175) becomes,

$$kr - \sqrt{gk}t + \frac{\pi}{4} = p^2 - \sqrt{gk} \frac{\sqrt{r}}{\sqrt{r}} t + \frac{\pi}{4} \quad (6.179)$$

$$= p^2 - \sqrt{kr} \frac{\sqrt{g}}{\sqrt{r}} t + \frac{\pi}{4} \quad (6.180)$$

$$= p^2 - p\alpha + \frac{\pi}{4} \quad (6.181)$$

Completing the substitution of (6.176), (6.178) and (6.181) into (6.175) gives

$$\eta_1(r, t) = \frac{i}{\sqrt{2\pi r}} \int_0^\infty \frac{p}{\sqrt{r}} e^{i(p^2 - p\alpha + \frac{\pi}{4})} \frac{2p}{r} dp \quad (6.182)$$

$$= \frac{\sqrt{2}i}{\sqrt{\pi}r^2} \int_0^\infty p^2 e^{i(p^2 - p\alpha + \frac{\pi}{4})} dp \quad (6.183)$$

## Chapter 6 – Hydrodynamic Modelling

Again, the phase term is suitable for the method of stationary phase to be applied to solve the integral:

$$f_1(p) = p^2 - p\alpha + \frac{\pi}{4} \quad (6.184)$$

$$\frac{\partial}{\partial p} \left( p^2 - p\alpha + \frac{\pi}{4} \right) = 2p - \alpha \quad (6.185)$$

$$\frac{\partial^2}{\partial p^2} \left( p^2 - p\alpha + \frac{\pi}{4} \right) = 2 \quad (6.186)$$

Therefore  $f_1(p)$  will be stationary where

$$2p - \alpha = 0 \quad (6.187)$$

$$p_0 = \frac{\alpha}{2} \quad (6.188)$$

Using a Taylor series expansion of the function  $f_1(p)$  in the vicinity of  $p_0$ :

$$f_1(p) = f_1(p_0) + f_1'(p_0)(p - p_0) + f_1''(p_0) \frac{(p - p_0)^2}{2!} + \dots \quad (6.189)$$

$$f_1(p) \approx \left( p_0^2 - p_0\alpha + \frac{\pi}{4} \right) + (2p_0 - \alpha)(p - p_0) + (2) \frac{(p - p_0)^2}{2} \quad (6.190)$$

$$= p_0^2 - p_0\alpha + \frac{\pi}{4} + 2pp_0 - p\alpha - 2p_0^2 + p_0\alpha + (p - p_0)^2 \quad (6.191)$$

$$= p_0^2 + \frac{\pi}{4} + 2pp_0 - p\alpha - 2p_0^2 + (p - p_0)^2 \quad (6.192)$$

Rearranging (6.188) gives

$$\alpha = 2p_0 \quad (6.193)$$

Substituting (6.193) back in to (6.192) gives

## Chapter 6 – Hydrodynamic Modelling

$$f_1(p) = p_0^2 + \frac{\pi}{4} + 2pp_0 - 2pp_0 - 2p_0^2 + (p - p_0)^2 \quad (6.194)$$

$$= p_0^2 + \frac{\pi}{4} - 2p_0^2 + (p - p_0)^2 \quad (6.195)$$

$$= (p - p_0)^2 - p_0^2 + \frac{\pi}{4} \quad (6.196)$$

Substituting the phase term (6.196) back in to the integral (6.183) and restricting the integration to the region in the vicinity of  $p_0$ :

$$\eta_1(r, t) = \frac{\sqrt{2}i}{\sqrt{\pi}r^2} \int_0^\infty p_0^2 e^{i\{(p-p_0)^2 - p_0^2 + \frac{\pi}{4}\}} dp \quad (6.197)$$

$$= \frac{\sqrt{2}i}{\sqrt{\pi}r^2} p_0^2 e^{-ip_0^2} e^{i\frac{\pi}{4}} \int_{p_0-\varepsilon}^{p_0+\varepsilon} e^{i(p-p_0)^2} dp \quad (6.198)$$

Making a substitution to complete the integral for  $p$ , let

$$s = (p - p_0) \quad (6.199)$$

Therefore

$$ds = dp \quad (6.200)$$

This gives (6.198) the form

$$\eta_1(r, t) = \frac{\sqrt{2}i}{\sqrt{\pi}r^2} p_0^2 e^{-ip_0^2} e^{i\frac{\pi}{4}} \int_{-\varepsilon}^{+\varepsilon} e^{is^2} ds \quad (6.201)$$

Again, using the identity integral for the exponential term:

$$\int_{-\infty}^{+\infty} e^{-ax^2} dx = \sqrt{\frac{\pi}{a}} \quad (6.202)$$

Therefore, the integration within (6.201) becomes



## Chapter 6 – Hydrodynamic Modelling

$$\int_{-\varepsilon}^{+\varepsilon} e^{is^2} ds \approx \sqrt{\frac{\pi}{-i}} \quad (6.203)$$

$$= \sqrt{\pi} e^{i\frac{\pi}{4}} \quad (6.204)$$

Substituting (6.204) back into (6.201) gives

$$\eta_1(r, t) = \frac{\sqrt{2}i}{\sqrt{\pi}r^2} p_o^2 e^{-ip_o^2} e^{i\frac{\pi}{4}} \sqrt{\pi} e^{i\frac{\pi}{4}} \quad (6.205)$$

$$= \frac{\sqrt{2}i\sqrt{\pi} e^{i\frac{\pi}{4}} e^{i\frac{\pi}{4}}}{\sqrt{\pi}r^2} p_o^2 e^{-ip_o^2} \quad (6.206)$$

$$= \frac{\sqrt{2}i e^{i\frac{\pi}{2}}}{r^2} p_o^2 e^{-ip_o^2} \quad (6.207)$$

As,

$$p_o = \frac{\alpha}{2} \quad (6.208)$$

$$\eta_1(r, t) = \frac{\sqrt{2}i e^{i\frac{\pi}{2}}}{r^2} \left(\frac{\alpha}{2}\right)^2 e^{-i\frac{\alpha^2}{4}} \quad (6.209)$$

$$= \frac{i\alpha^2 e^{i\frac{\pi}{2}}}{2^{3/2}r^2} e^{-i\frac{\alpha^2}{4}} \quad (6.210)$$

The processing of  $\eta_1(r, t)$  can pause at this point to re-address  $\eta_2(r, t)$ , from previous:

$$\eta_2(r, t) = \frac{i}{\sqrt{2\pi}r} \int_0^\infty \sqrt{k} e^{-i(kr + \sqrt{gkt} + \frac{\pi}{4})} dk \quad (6.211)$$

So, making similar substitutions as before into  $\eta_2(r, t)$ :

Chapter 6 – Hydrodynamic  
Modelling

$$p^2 = kr \text{ and } \alpha = \sqrt{\frac{g}{r}} t \quad (6.212)$$

$$2pdp = rdk \quad (6.213)$$

$$dk = \frac{2p}{r} dp \quad (6.214)$$

The phase term of (6.211) becomes,

$$kr + \sqrt{gk}t + \frac{\pi}{4} = p^2 + \sqrt{gk} \frac{\sqrt{r}}{\sqrt{r}} t + \frac{\pi}{4} \quad (6.215)$$

$$= p^2 + \sqrt{kr} \frac{\sqrt{g}}{\sqrt{r}} t + \frac{\pi}{4} \quad (6.216)$$

$$= p^2 + p\alpha + \frac{\pi}{4} \quad (6.217)$$

Completing the substitution of (6.212), (6.214) and (6.217) into (6.211) gives

$$\eta_2(r, t) = \frac{i}{\sqrt{2\pi r}} \int_0^\infty \frac{p}{\sqrt{r}} e^{-i(p^2 + p\alpha + \frac{\pi}{4})} \frac{2p}{r} dp \quad (6.218)$$

$$= \frac{\sqrt{2}i}{\sqrt{\pi}r^2} \int_0^\infty p^2 e^{-i(p^2 + p\alpha + \frac{\pi}{4})} dp \quad (6.219)$$

Again, the phase term is suitable for the method of stationary phase to be applied to solve the integral:

$$f_2(p) = p^2 + p\alpha + \frac{\pi}{4} \quad (6.220)$$

$$\frac{\partial}{\partial p} \left( p^2 + p\alpha + \frac{\pi}{4} \right) = 2p + \alpha \quad (6.221)$$

$$\frac{\partial^2}{\partial p^2} \left( p^2 + p\alpha + \frac{\pi}{4} \right) = 2 \quad (6.222)$$

Therefore  $f_2(p)$  will be stationary where

$$2p + \alpha = 0 \quad (6.223)$$

$$p_0 = -\frac{\alpha}{2} \quad (6.224)$$

Using a Taylor series expansion of the function  $f_2(p)$  in the vicinity of  $p_0$ :

$$f_2(p) = f_2(p_0) + f_2'(p_0)(p - p_0) + f_2''(p_0) \frac{(p - p_0)^2}{2!} + \dots \quad (6.225)$$

$$f_2(p) \approx \left( p_0^2 + p_0\alpha + \frac{\pi}{4} \right) + (2p_0 + \alpha)(p - p_0) + (2) \frac{(p - p_0)^2}{2} \quad (6.226)$$

$$= p_0^2 + p_0\alpha + \frac{\pi}{4} + 2pp_0 + p\alpha - 2p_0^2 - p_0\alpha + (p - p_0)^2 \quad (6.227)$$

$$= p_0^2 + \frac{\pi}{4} + 2pp_0 + p\alpha - 2p_0^2 + (p - p_0)^2 \quad (6.228)$$

Rearranging (6.224) gives

$$\alpha = -2p_0 \quad (6.229)$$

And substituting into (6.228) gives

$$f_2(p) = p_0^2 + \frac{\pi}{4} + 2pp_0 - 2pp_0 - 2p_0^2 + (p - p_0)^2 \quad (6.230)$$

$$= p_0^2 + \frac{\pi}{4} - 2p_0^2 + (p - p_0)^2 \quad (6.231)$$

$$= (p - p_0)^2 - p_0^2 + \frac{\pi}{4} \quad (6.232)$$

## Chapter 6 – Hydrodynamic Modelling

Substituting this expression for the phase term back into the integral of (6.219) and restricting the integration to the region in the vicinity of  $p_0$ ,

$$\eta_2(r, t) = \frac{\sqrt{2}i}{\sqrt{\pi}r^2} \int_{p_0-\varepsilon}^{p_0+\varepsilon} p_o^2 e^{-i\{(p-p_0)^2 - p_o^2 + \frac{\pi}{4}\}} dp \quad (6.233)$$

$$= \frac{\sqrt{2}i}{\sqrt{\pi}r^2} p_o^2 e^{ip_o^2} e^{-i\frac{\pi}{4}} \int_{p_0-\varepsilon}^{p_0+\varepsilon} e^{-i(p-p_0)^2} dp \quad (6.234)$$

Making a substitution to complete the integral for  $p$ , let

$$s = (p - p_0) \quad (6.235)$$

Therefore

$$ds = dp \quad (6.236)$$

This gives

$$\eta_2(r, t) = \frac{\sqrt{2}i}{\sqrt{\pi}r^2} p_o^2 e^{ip_o^2} e^{-i\frac{\pi}{4}} \int_{-\varepsilon}^{+\varepsilon} e^{-is^2} ds \quad (6.237)$$

Again, using the identity integral for the exponential term:

$$\int_{-\infty}^{+\infty} e^{-ax^2} dx = \sqrt{\frac{\pi}{a}} \quad (6.238)$$

Therefore, the integral within (6.234) becomes

$$\int_{-\varepsilon}^{+\varepsilon} e^{-is^2} ds \approx \sqrt{\frac{\pi}{i}} \quad (6.239)$$

$$= \sqrt{\pi} e^{-i\frac{\pi}{4}} \quad (6.240)$$

This gives

## Chapter 6 – Hydrodynamic Modelling

$$\eta_2(r, t) = \frac{\sqrt{2}i}{\sqrt{\pi}r^2} p_o^2 e^{ip_o^2} e^{-i\frac{\pi}{4}} \sqrt{\pi} e^{-i\frac{\pi}{4}} \quad (6.241)$$

$$= \frac{\sqrt{2}i\sqrt{\pi} e^{-i\frac{\pi}{4}} e^{-i\frac{\pi}{4}}}{\sqrt{\pi}r^2} p_o^2 e^{ip_o^2} \quad (6.242)$$

$$= \frac{\sqrt{2}i e^{-i\frac{\pi}{2}}}{r^2} p_o^2 e^{ip_o^2} \quad (6.243)$$

As

$$p_o = -\frac{\alpha}{2} \quad (6.244)$$

$$\eta_2(r, t) = \frac{\sqrt{2}i e^{-i\frac{\pi}{2}}}{r^2} \left(\frac{\alpha}{2}\right)^2 e^{i\frac{\alpha^2}{4}} \quad (6.245)$$

$$= \frac{i\alpha^2 e^{-i\frac{\pi}{2}}}{2^{3/2}r^2} e^{i\frac{\alpha^2}{4}} \quad (6.246)$$

Recombining (6.210) and (6.246), as

$$\eta(r, t) = \eta_1(r, t) + \eta_2(r, t) \quad (6.247)$$

$$\eta(r, t) = \frac{i\alpha^2 e^{i\frac{\pi}{2}}}{2^{3/2}r^2} e^{-i\frac{\alpha^2}{4}} + \frac{i\alpha^2 e^{-i\frac{\pi}{2}}}{2^{3/2}r^2} e^{i\frac{\alpha^2}{4}} \quad (6.248)$$

$$= \frac{i\alpha^2 e^{i\frac{\pi}{2}}}{2^{3/2}r^2} \left( e^{i\frac{\alpha^2}{4}} + e^{-i\frac{\alpha^2}{4}} \right) \quad (6.249)$$

Using a standard application of de Moivre's theorem:

$$\cos x = \frac{1}{2} (e^{ix} + e^{-ix}) \quad (6.250)$$

$$2 \cos x = (e^{ix} + e^{-ix}) \quad (6.251)$$

Letting

$$x = \frac{\alpha^2}{4} \quad (6.252)$$

$$\eta(r, t) = \frac{2i\alpha^2 e^{i\frac{\pi}{2}}}{2^{3/2}r^2} \cos \frac{\alpha^2}{4} \quad (6.253)$$

$$= \frac{\alpha^2}{\sqrt{2}r^2} \cos \frac{\alpha^2}{4} \quad (6.254)$$

As

$$\alpha = \sqrt{\frac{g}{r}}t \quad (6.255)$$

$$\eta(r, t) = \frac{gt^2}{\sqrt{2}r^3} \cos \frac{gt^2}{4r} \quad (6.256)$$

As it can be seen, this alternative derivation of the surface elevation, using different approximation methods, has reassuringly returned the same form for both the phase and amplitude variation as the direct application of the stationary phase method that gave the result (6.168). Figure 101 shows a plot of the surface elevation derived from this function where the point disturbance occurs at the origin of the  $xy$ -plane.

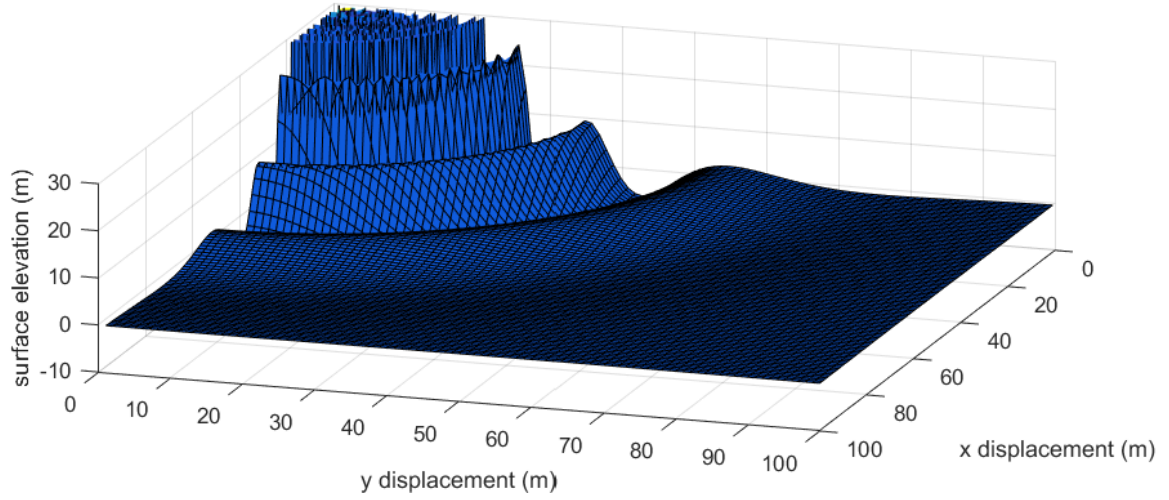


Figure 101: Surface plot of (6.256) for  $t = 10$  s. The plot shows the propagating wave pattern away from the points source at the  $x,y$  plane origin.

#### 6.4 Point Source Wake Model

The derivations for the wave term from a point source can begin to be used to form the wake from a ship by considering the ship's motion as a superposition of many delta impulses that each add ripples to the fluid surface. The ship is modelled to move with velocity,  $v_s$ , in the negative  $x$  direction. Restricting the ship's velocity,  $v_s$ , to remain constant allows the time function to be considered as a function of the distance,  $x$ , rear of the ship. The change in frame of  $r$  from the point source in polar coordinates centred on the point source to the reference frame of the ship means that the distance from the ship,  $r_s$ , and the polar angle in the ship frame,  $\theta_s$ , must be taken into account. The geometry is shown in Figure 102. Use of the cosine rule gives

$$r_s^2 = r^2 + v_s^2 t^2 + 2v_s r t \cos \theta_s \quad (6.257)$$

## Chapter 6 – Hydrodynamic Modelling

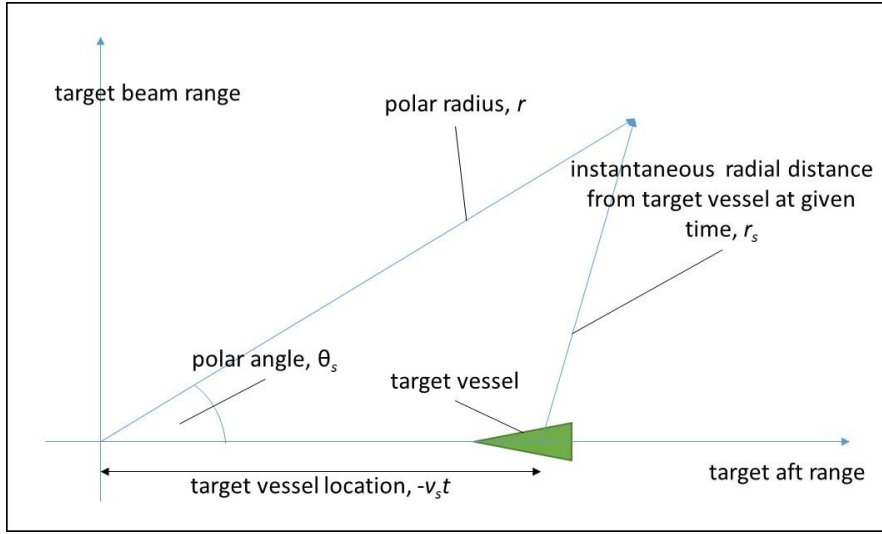


Figure 102: Diagram showing the geometry of the polar integration for composing the ship wake.

This gives the ship wake formed from the sum of point sources from the hydrodynamic method as:

$$\eta_{Re}(r, t) = \int_{-\infty}^0 \frac{gt^2}{\sqrt{2}r^3} \cos \frac{gt^2}{4r} dt \quad (6.258)$$

$$= \int_{-\infty}^0 \frac{gt^2}{\sqrt{2}(r^2 + v_s^2 t^2 + 2v_s r t \cos \theta_s)^{3/2}} \cos \frac{gt^2}{4(r^2 + v_s^2 t^2 + 2v_s r t \cos \theta_s)^{1/2}} dt \quad (6.259)$$

A 3D plot of (6.259) can be seen at Figure 103.



## Chapter 6 – Hydrodynamic Modelling

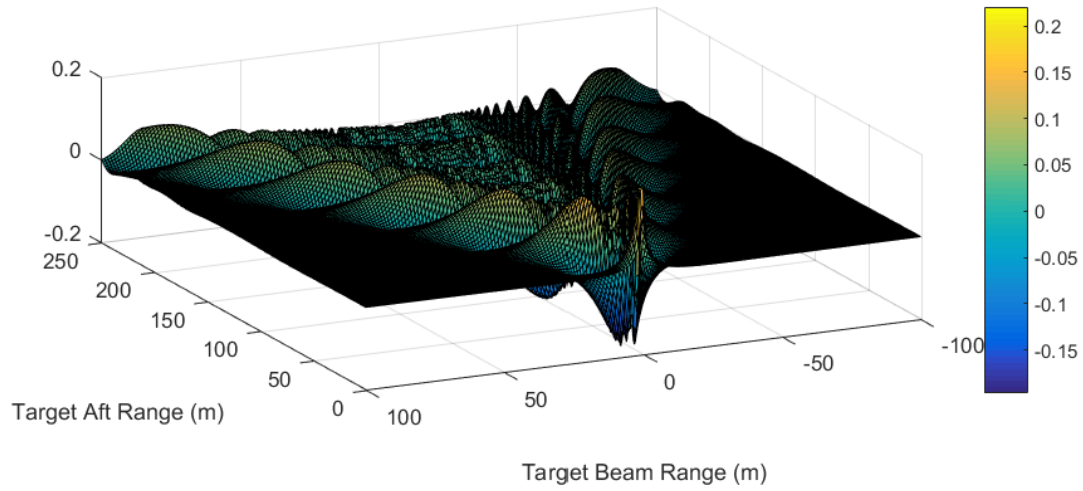


Figure 103: Surface plot of (6.259). The point target is moving as per the previous modelling as a velocity of  $7.72 \text{ ms}^{-1}$ . The plot demonstrates the development of the wave field of the point target into the Kelvin wake where the cusp waves and the transverse wake can be seen.

And a vertical projection can be seen at Figure 104.

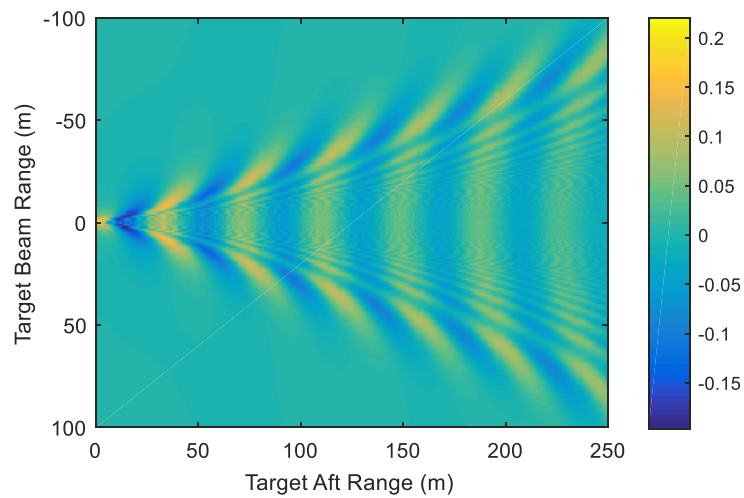


Figure 104: Image plot of (6.259). The point target is moving as per parameters in Table 2. The Kelvin wake cusp waves and the transverse wake can be seen bounded by the angle of  $39^\circ$ .

### 6.5 Radar Scattering Model

The radar scattering model is based on previously developed theory derived from the composite model for a generic sea surface. The model employed here is similar to the

application by Ward and Hill (2018). In line with the composite model, the surface wave spectrum is considered to be composed of two main groups of wave fields. The shorter wavelength waves, specifically waves that have wavelength of roughly less than twice the wavelength of the incident radar energy, are responsible for the Bragg scattering. The waves are considered in this case to be ubiquitous in nature. The longer wavelength waves, on which the shorter wavelength wave field rides, are the waves that are ultimately responsible for the tilt modulation effect that modifies the RCS of the scene. Therefore, the RCS is calculated through use of the normal to the slope of the surface elevation.

$$\underline{n} = \frac{1 - \nabla\eta}{\sqrt{1 + \|\nabla\eta\|^2}} \quad (6.260)$$

The reflectivity of the surface can be indicated as a relative RCS,  $\sigma_{rel}$ , through the dot product of the surface normal and the incident radar energy that has internal angle  $\theta_{inc}$ :

$$\sigma_{rel} = \underline{n} \cdot \hat{r} = \cos \theta_{inc} \quad (6.261)$$

In order to only consider the scattered returns that make it back to the sensor,  $\theta_{inc}$  is confined:

$$-\frac{\pi}{2} < \theta_{inc} < +\frac{\pi}{2} \quad (6.262)$$

As has been discussed, the motion of each scatterer has an impact on the mapped location within the SAR image. In order to sufficiently model this characteristic, the bulk displacement is considered but the higher order effects of defocussing and smearing are not. The time differentiation of the surface elevation is used to determine the velocities of each scatterer within the wake. These velocities are then used to map pixel-to-pixel the image locations.

$$\frac{\partial}{\partial t} \eta(r, t) = \frac{gt}{\sqrt{2}r^3} \left( 2 \cos \frac{gt^2}{4r} - \frac{gt^2}{2r} \sin \frac{gt^2}{4r} \right) \quad (6.263)$$

This is not an absolute calculation of the RCS of the scene but it does show comparative RCS within the scene. The final step in the imaging algorithm here is to normalise the image to allow for ready comparison between models. The output simulated SAR image from Figure 104 can be seen in Figure 105.

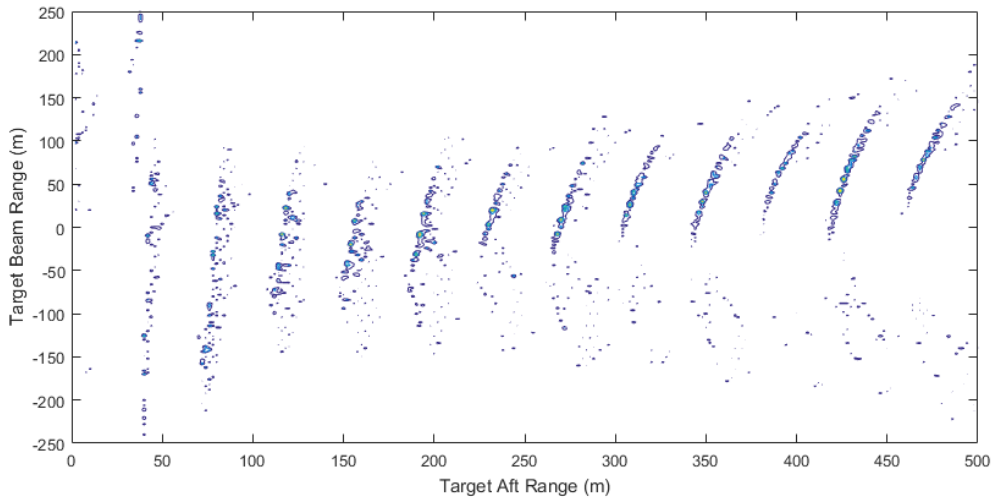


Figure 105: Contour plot of the simulated SAR image generated from the Kelvin wake input of Figure 104.

## 6.6 Summary

The purpose of this chapter was to develop a final detailed model of the scene that included the primary target vessel and its associated wake so that a more accurate simulated SAR image could be produced. This would allow for optimum analysis when compared with the real image and increase the understanding of the mechanisms behind the artefacts within the image. Such a model has been developed that has been built from a point source up to a full ship wake. The effect of the SAR processor has subsequently been added onto the model to produce a simulated SAR image. The next chapter will be a short validation of the developed

## Chapter 6 – Hydrodynamic Modelling

model that will be achieved by comparing the result of the integrated point ship model with established models from other authors.

## 7 CHAPTER 7 – MODEL VALIDATION

### 7.1 Introduction

In this section, the results of the integrated point ship model are presented as well as compared with other established models. A summary has already been discussed in Chapter 2 concerning the multiple other established models that have been developed through the history of the study of both the ocean surface but also the interaction of radar with the environment. For this comparison, two models were chosen that had similar aims as the one developed here but used alternate means to achieve the end state. The aim of the use of such a model set is to use the similarities of the models, and their previous pedigree, to reinforce the developed theory here as well as use the known differences to further investigate the discussed phenomenon as the models react slightly differently to the theoretical construct.

### 7.2 Thin Ship Model

The first model is a special case of the early thin-ship modelling completed by Michell (1898). The model follows a similar method to the application used by Lighthill (1967) where a Rankine ovoid is the source disturbance. This specific model was compiled by Ward and Hill (2018) in IDL and converted for use in MATLAB to sit alongside the model developed in chapter 6 and the surface pressure model to be shown in section 7.3. The fundamental expression used to determine the surface elevation of the water is

$$\eta(x, y) = \int_{-\infty}^{+\infty} \int_{-\infty}^{+\infty} F(k_x, k_y) \frac{ik_x v_s}{(\mathbf{k} \cdot \mathbf{v})^2 - gk} e^{kz} e^{ik \cdot \mathbf{x}} dk_x dk_y \quad (7.264)$$

where  $F(k_x, k_y)$  is the Fourier transform of the Rankine source term. In order to generate the overall elevation, the algorithm constructs the spectrum of the unaltered Kelvin wake and outputs the surface elevation through convolution with the source term. For consistency with

## Chapter 7 – Model Validation

previous sections and comparison with the simpler models, the input parameters remain unaltered. The parameters, including the additional details that relate to the dimensions of the target vessel, are shown at Table 3.

target velocity	v tgt / ms-1	7.72
target length	length tgt / m	100
target width	width tgt / m	10
radar velocity	v rdr / ms-1	205.78
radar height	h rdr / m	6096
SAR aperture duration	T SAR / s	3
SAR aperture length	L SAR / m	617.34
wavelength	lamda / m	0.03
transmit bandwidth	B tx / Hz	1.00E+08
pulse length	t pulse / s	1.00E-06
PRF	PRF / Hz	320
number of azimuth bins	az bin / n	960
number of range bins	rng bin / n	1532
real antenna length	D / m	1
real beamwidth	b width / deg	1.72

Table 3: Simulation parameters including developed target dimensions.

The calculated spectrum of the undisturbed Kelvin wake from the thin ship model can be seen at Figure 106.

## Chapter 7 – Model Validation

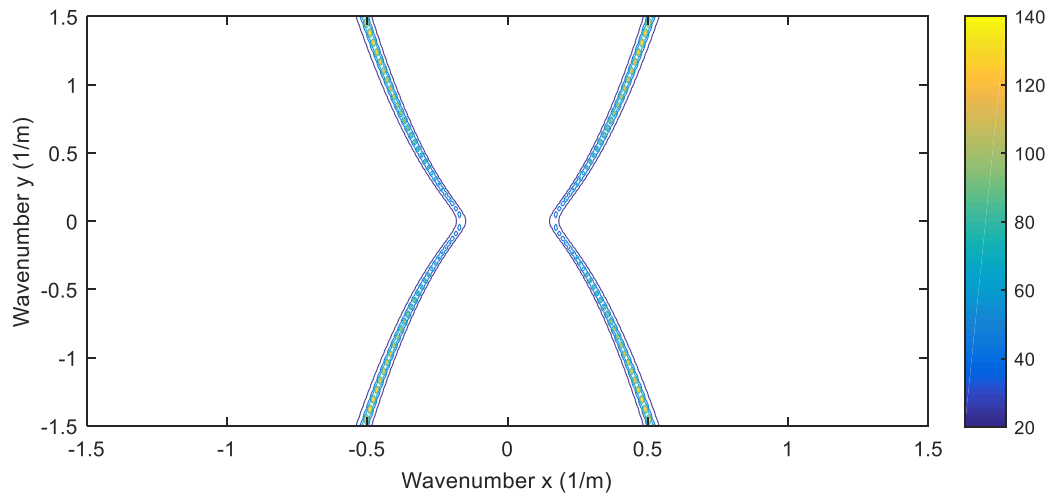


Figure 106: Contour plot of  $k$ -space spectrum of (7.264). The characteristic ‘hour-glass’ shape can be seen that is common for the Kelvin wake.

Once the convolution is complete, an inverse Fourier transform yields the output image of the surface elevation shown at Figure 107.

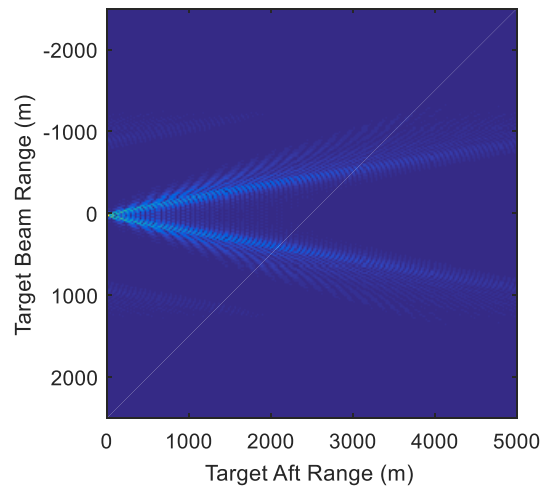


Figure 107: Image plot of (7.264) showing the Kelvin wake generated by a Rankine ovoid source using Michell’s thin-ship methodology.

The SAR processor step is then able to return the image that the radar sees of the calculated wake, shown at Figure 108.

## Chapter 7 – Model Validation

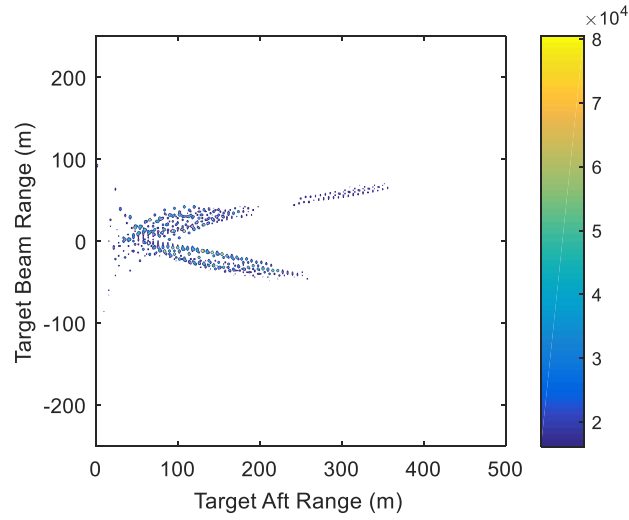


Figure 108: Contour plot of the simulated SAR image generated from the Kelvin wake input of Figure 107.

### 7.3 Surface Pressure Ship Model

The second model used here was not taken from previous code but developed directly from the work of Munk (1987) and Lyzenga et al. (1994) that uses a pressure distribution on the surface of the water to generate the wake. For this derivation, the surface elevation comes from a Fourier transform solution of the linearised boundary conditions and is given by

$$\eta(x, y) = -\frac{P_o}{(2\pi)^2 \rho g} \int_{-\infty}^{+\infty} \int_{-\infty}^{+\infty} \frac{k}{gk - (\mathbf{k} \cdot \mathbf{v})^2} e^{i\mathbf{k} \cdot \mathbf{x}} dk_x dk_y \quad (7.265)$$

This can be treated in a similar manner to the thin ship model by construction of the spectrum of the wake prior to combination with the pressure source. For ease of comparison the steps have been mirrored in Figure 109 to Figure 111 using the same input parameters as Table 3.



## Chapter 7 – Model Validation

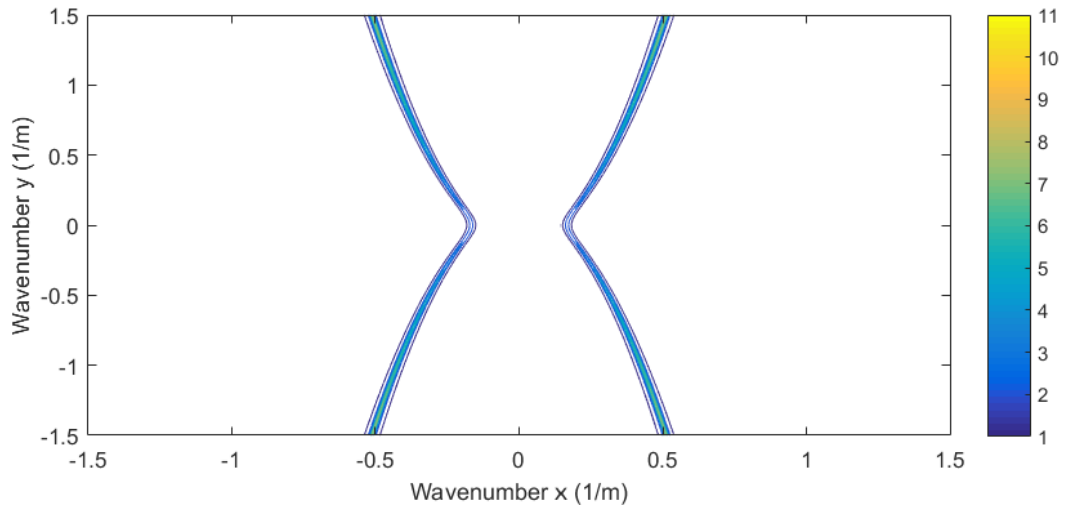


Figure 109: Contour plot of  $k$ -space spectrum of (7.265). The characterisitic ‘hour-glass’ shape can be seen as in Figure 106.

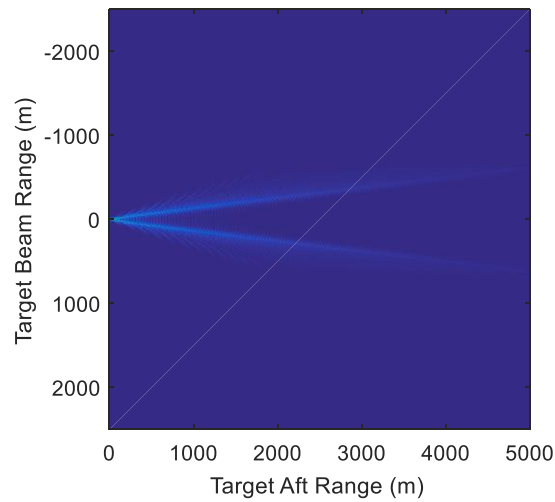


Figure 110: Image plot of (7.265) showing the Kelvin wake generated by a pressure distribution source using Munk et al.’s methodology.

## Chapter 7 – Model Validation

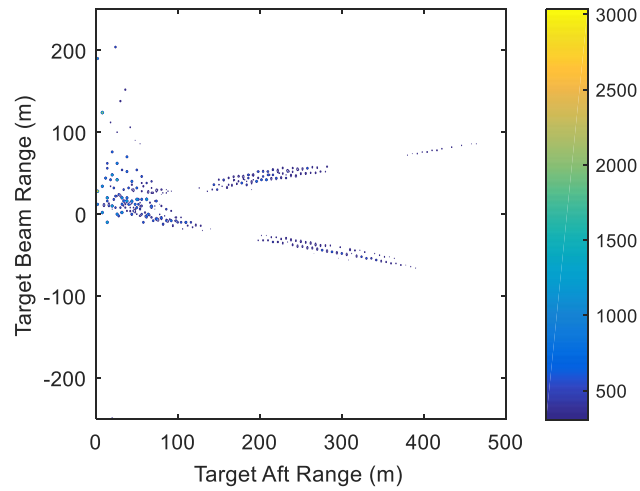


Figure 111: Contour plot of the simulated SAR image generated from the Kelvin wake input of Figure 110.

### 7.4 Integrated Point Ship Model

Finally, the model developed in the previous chapter is used to generate a simulated SAR image in line with the (7.264) and (7.265) using input parameters of Table 3. The processing steps of the wake generating algorithm could not be mirrored exactly, as they were with the surface pressure and thin ship models, to first generate a spectrum and then the final wake due to the direct way in which initial integral is conducted to form the final wake. The spectrum can however be produced post wake formation for comparison, which is shown at Figure 112. The large-scale wake produced by the model can be seen at Figure 113 and the simulated SAR image shown at Figure 114.

## Chapter 7 – Model Validation

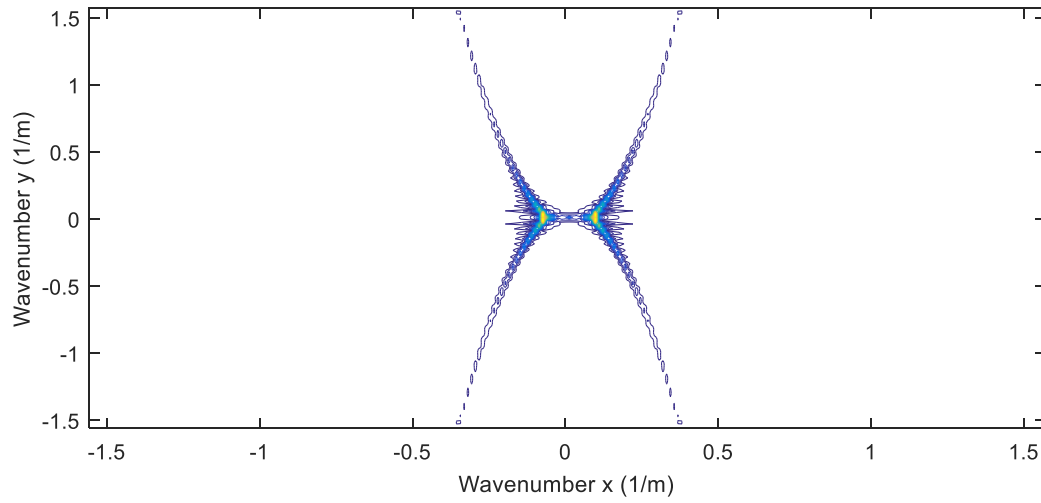


Figure 112: Contour plot of the  $k$ -space spectrum of (6.259). The characteristic 'hour-glass' shape is visible but somewhat distorted.

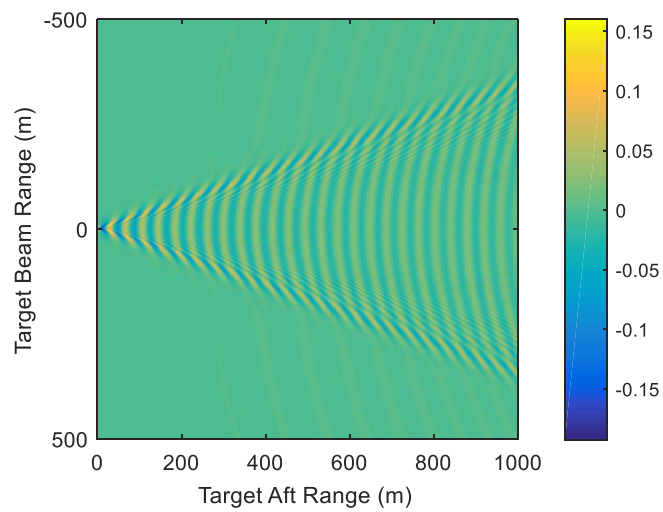


Figure 113: Image plot of (6.259) showing the Kelvin wake generated by a point source following the methodology developed in Chapter 6.

## Chapter 7 – Model Validation

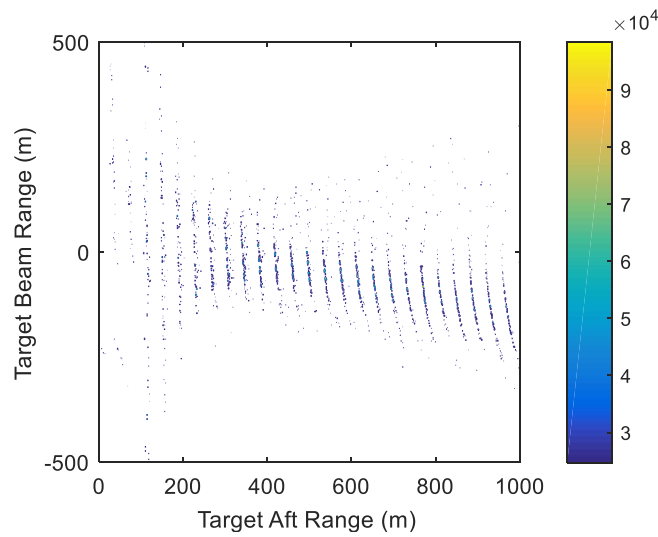


Figure 114: Contour plot of the simulated SAR image generated from the Kelvin wake input of Figure 113.

### 7.5 Summary

The purpose of the chapter has been to utilise two previously derived models to validate the output of the integrated point ship model. The generated  $k$ -space spectra, the surface elevations and the simulated SAR images have been used to show that the integrated point ship approach is satisfactory. The comparison has shown that there are differences between the outputs, which are intriguing and will be more fully analysed in the next chapter.

## **8 CHAPTER 8 – FINAL ANALYSIS**

### **8.1 Introduction**

Work in the Chapters 3, 4 and 5 used more simple constructions of the target scene to explain the appearance of both the target vessel returns and the bloom artefact. This was both encouraging but left some questions, particularly in relation to the wake bloom artefact, that flagged the need to examine further with a more comprehensive approach. The more detailed stage of hydrodynamic modelling of Chapter 6 has been completed and validated by comparison with alternative established wake models in Chapter 7. The work of this chapter will be to examine the output of the integrated point ship model against the real image.

### **8.2 Wake Bloom Envelope**

The orbital velocity model for the transverse waves within the Kelvin wake was able to produce an envelope shape as shown in Figure 74 that had a similar relationship of azimuthal width to aft distance from the vessel when compared to the bloom artefact within the SAR image. However, the reason for the resultant shape of this envelope was somewhat imposed on the simulation by the use of the model for the orbital velocity. The orbital velocity decay was based on sound modelling of both theoretical physical process of Stoker (1957) coupled with comparison with quantitative assessment of Cox and Macfarlane (2019). However, the model produced by both was known beforehand to have a power law structure so, although based on sound reason, did allow the distribution of the expected answer to be known before the result of the simulation was obtained. A sounder scientific process to show the source of the mechanism would be to have a model produce the required image distribution as a result of a hypothesis concerning the mechanism. This is now happily the case. The model does not only attempt to establish the extent of the envelope but looks to plot scatterers that fit within the envelope as well. The boundary is more real as a result both in its sharpness of

edge but also its shape within the simulated SAR image. In each case, the returns nearest the target vessels are large in azimuth and decay in width rapidly until a lingering tail remains.

Figure 115, Figure 116 and Figure 117 show analysis of the decay of the tail with the purpose of finding the coefficient of the power law decay. It can be seen from the  $R^2$  values that there is a reasonably good fit of the data with a power law decay. This is particularly so in the thin ship and surface pressure ship models and slightly less so in the integrated point ship model. The fit of the third is not quite as good as the first two. However, the power law exponents of decay -0.62, -0.46 and -0.24 are of the order predicted by the previous work of Stoker and Cox et al. It is possible that the narrowing of the wake artefact being asymmetric either side of the wake centreline could be a cause of the poorer fit of Figure 117 compared with Figure 115 and Figure 116. This asymmetric narrowing of the decay of the wake that can be seen in the simulated SAR image at Figure 105 and Figure 114. The wake width appears to decay well on the side of negative beam displacement and almost remain constant on the positive side. This asymmetry will be discussed shortly.

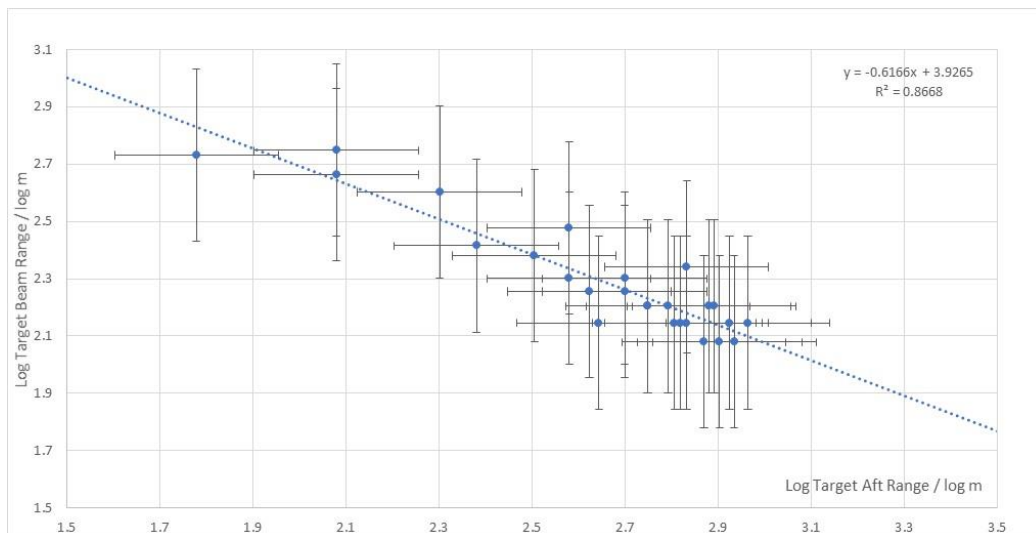


Figure 115: Log-log plot of the simulated SAR image bloom azimuthal extents with range for the thin-ship model (7.264). The vertical and horizontal error bars have been derived from the accuracies of the measurement process.

## Chapter 8 – Final Analysis

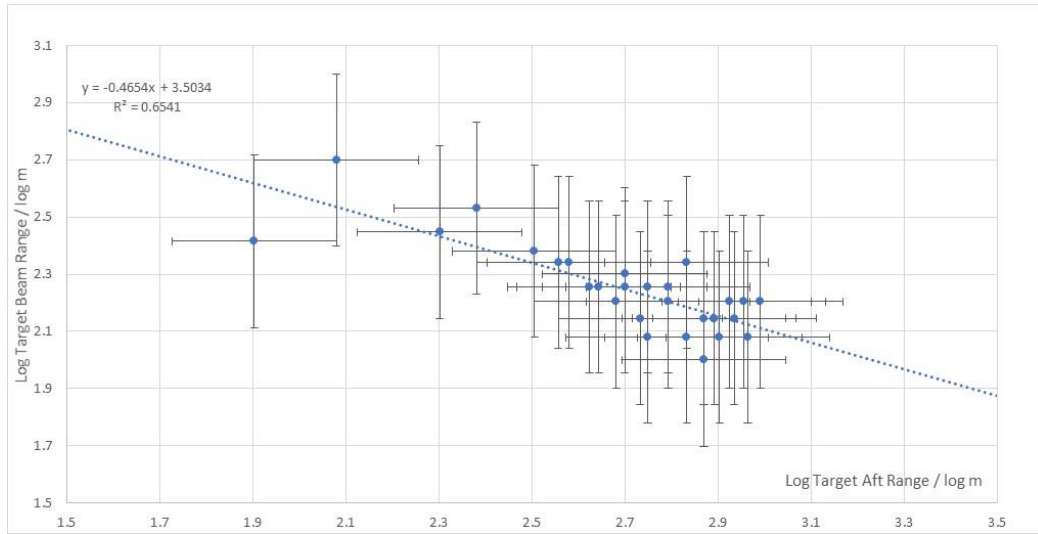


Figure 116: Log plot of the simulated SAR image bloom azimuthal extents with range for the pressure distribution model (7.265). The vertical and horizontal error bars have been derived from the accuracies of the measurement process.

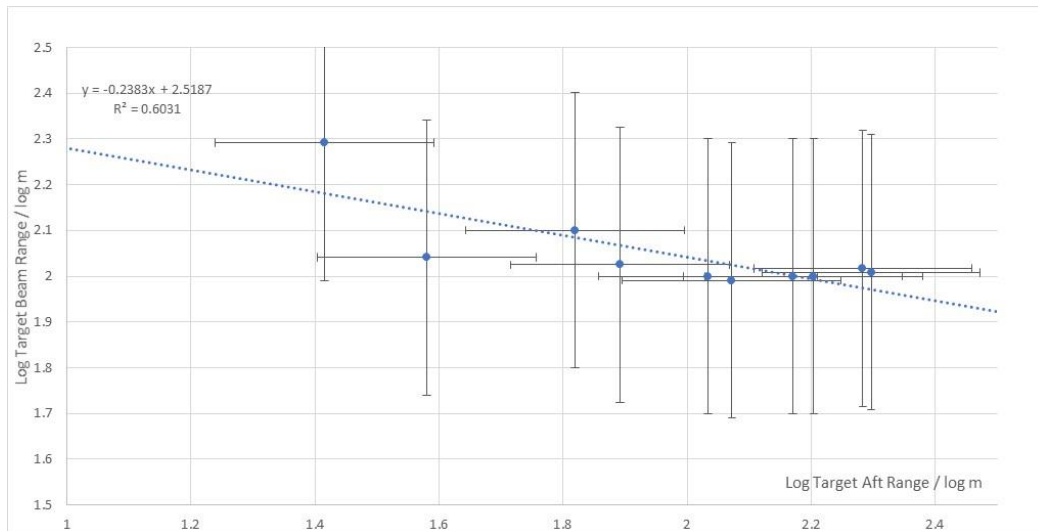


Figure 117: Log plot of the simulated SAR image bloom azimuthal extents with range for the point ship model developed here (6.259). The vertical and horizontal error bars have been derived from the accuracies of the measurement process.

As the theoretical mechanism behind the generation of the imagery phenomenon is essentially sinusoidal, i.e. equally positive and negative, then a boundary should exist in a manner similar to the simple case. This boundary would be determined by a symmetric spread of velocities of the wave orbital motion observed by the radar about a zero mean. However, for the real image, it must be understood that slight variation from the theoretical

perfect sinusoidal motion will blur the boundary. Surface roughness, wind and tide effects could quite easily induce such deviation and produce a limited but variable bloom in the imagery.

### **8.3 Wake Bloom Tail**

One aspect of the bloom artefact that the power law could not explain directly was the somewhat abrupt decay of the intensity as the distance downstream from the target vessel increased; at a particular aft range from the target the strong returns within the tail effectively ceased. Consideration was given to the location within the wake of white water and breaking events but a conclusive answer could not be given. The somewhat abrupt end to a bloom-like artefact is present in all three model simulated SAR images. Interestingly, none of the chosen models include white water as a scattering mechanism. The scatterer mechanisms used in the radar simulation element of the models focus primarily on the tilt modulation of the Bragg wave field. The appearance of the bloom intensity decays in all three models would therefore suggest that there exists a construct where tilt modulation generates a strong intensity response near the target vessel and remains reflective for some distance until a threshold aft of the target. Around such a threshold point, the reflectivity drops significantly and the wake return in the SAR image obscures into the background clutter. A point of note, the modelling assumptions did not specifically look to recreate breaking events as all remain within the linear parameter-space, however, the extremes of the tilt modulation could conceivably get waves into such shapes that they could exhibit burst-like characteristics. This supposition takes explanation for the burst scattering from Watts et al. (2005), understanding that there remains some disagreement as to the exact mechanism behind such events.

Examining the potential of the white water source a little further, using the quantitative approach of Melief et al. (2006), breaking events can occur where the wave amplitude and



wavenumber product is greater than 0.35, as shown in (4.57). Applying that criteria to the modelling could shed light on the region within the wake where waves may break and therefore generate white water. The issue with direct application of (4.67) is that the original work looked at situations with single and constant wavenumbers. It is clear here that this criterion does not apply given the inclusion of all possible wavenumbers in the construction of the model. However, an alternative approach is possible. Ward et al. (2006) cite a wave steepness limit 0.58, in a similar manner to the amplitude wavenumber product of Melief et al. (2006). Having already calculated the surface elevation for the given sources a direct derivative of the elevation will return the required slope, which can be compared to the limit noted by Ward et al. Figure 118 shows the plot of the gradient of the surface elevation in full detail.

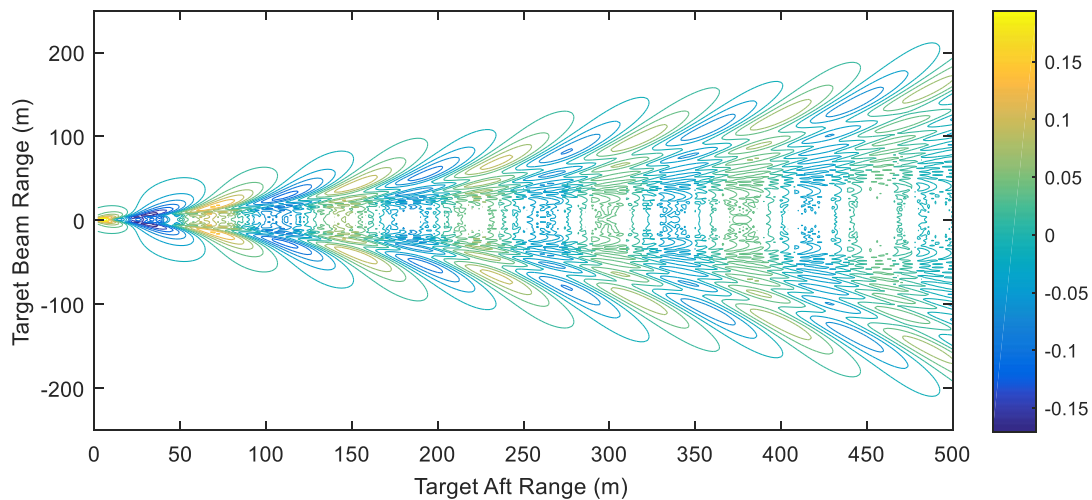


Figure 118: Contour plot of the gradient of the surface of the wake behind a ship.

In Figure 118 the wave gradient does not exceed the threshold of 0.58 indicating that there are no regions of the calculated wake that would break. A further plot is given that restricts the contours within the plot, Figure 119, to indicate where the breaking events are most likely

to occur if the amplitude of the waves were to increase gradually to breaking point. In this particular case, where the input parameters are as per Table 3, there is nowhere on the image that exceeds the threshold. This shows that in this case the wave field is smooth throughout. However, this will not always be the case as the surface elevation of the wake is dependent on the source vessel characteristics. The larger the vessel and the greater the velocity the greater the gradients of the wake will become. Figure 119 therefore indicates the areas of the wake of Figure 118 that will predictably and consistently break first given any increase in the vessel parameters. Breaking events also occur due to the interaction between the wake and the ambient wind-wave field. It is also worth a note that sea spikes are breaking-event-associated but it is not clear that a near-break cannot create a spike-like radar cross section. So, although the threshold was not breached in this case, the extremes of gradient remain a good indicator as to the extremes of radar cross section. This is a pleasing result as it would be expected from general observation of the wake of vessels that the cusp waves are routinely seen to break close to the source vessel and the magnitude of the break decays away from the vessel. This can be seen in the previously discussed photographic image at Figure 72.

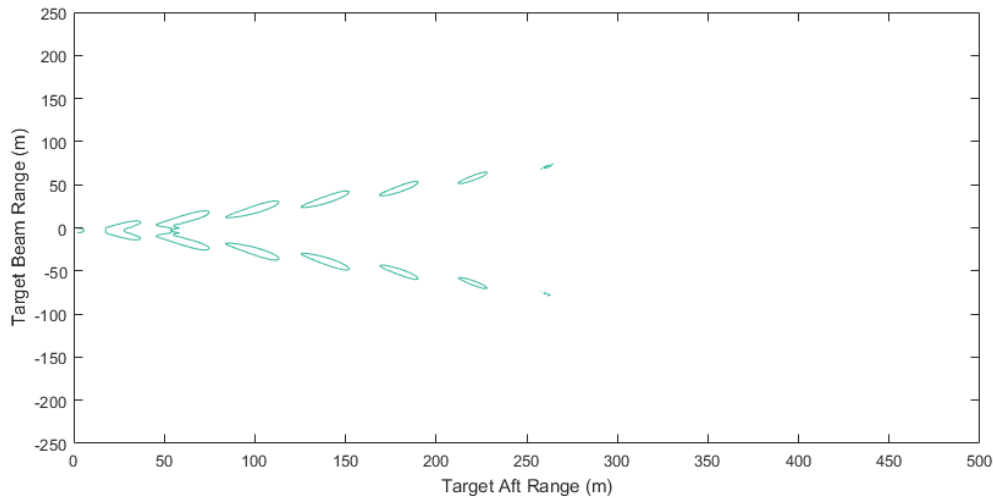


Figure 119: Reduced contour plot of the gradient of the surface of the wake behind a ship. The reduced number of contours illustrates the likely areas in the Kelvin wake field where waves will most consistently and predictably break. In this case the contours show the regions bounded by wave steepness that is greater than 0.05 or less than -0.05.

Due to the way waves of varying wavenumbers radiate to generate the Kelvin wake pattern, an approximation can be attempted that uses the Melief et al. threshold to compare against the slope threshold. By restricting the amplitude wavenumber product along the line of the transverse wake a relatively good approximation can be made of the risk of breaking. Figure 120 is plotted by taking a line along the centre of the wake to illustrate the magnitude of the amplitude wavenumber product. Of note, the power law decay of the amplitude can readily be seen from the shape of curve in Figure 120. Primarily though, the threshold of 0.35 is not exceeded in this case and it can be seen that the region where breaking waves most likely occur is very confined to the near field wake of the target vessel. The white water has been noted to exist for a certain measurable lifetime on the surface of the water. The measure of this time quantity has already been shown to be a highly variable figure that can change by a factor of roughly 50. From Callaghan et al. (2017), the longest persisting foam lasted 10.4 s. From this estimation of the lifetime of the foam created, there could exist a region of roughly 80.2 m aft of the vessel where scattering could be affected in quite a chaotic manner from

such water. This approximation is not very close to the measured haze region of Figure 121 that has aft range extent of  $215 \pm 20$  m suggesting that the foam is not a direct source mechanism for the haze.

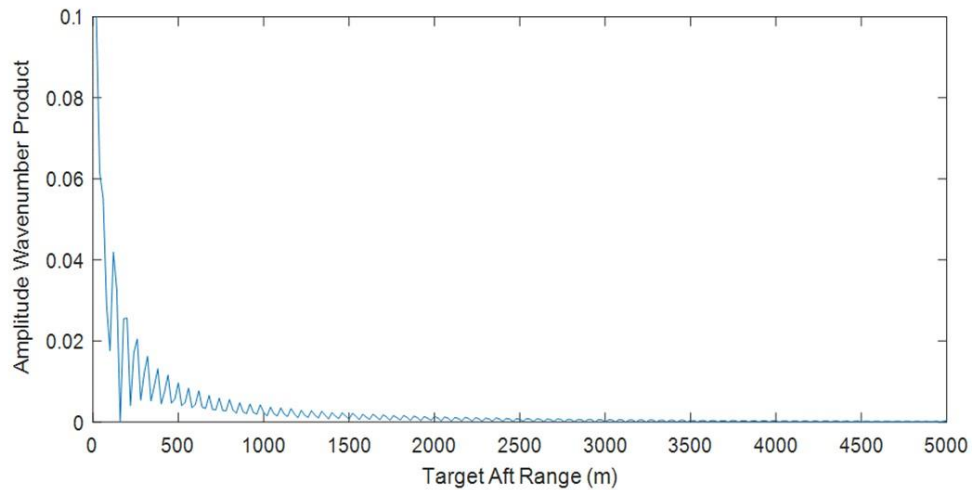


Figure 120: Plot of wake amplitude wavenumber product, i.e. wave steepness, variation with target aft range showing the power law decay directly along the centreline of the target vessel's transverse wake. The breaking wave threshold of Melief et al. (2006) of 0.38 would suggest waves would break in the closest 150 m to the target vessel.

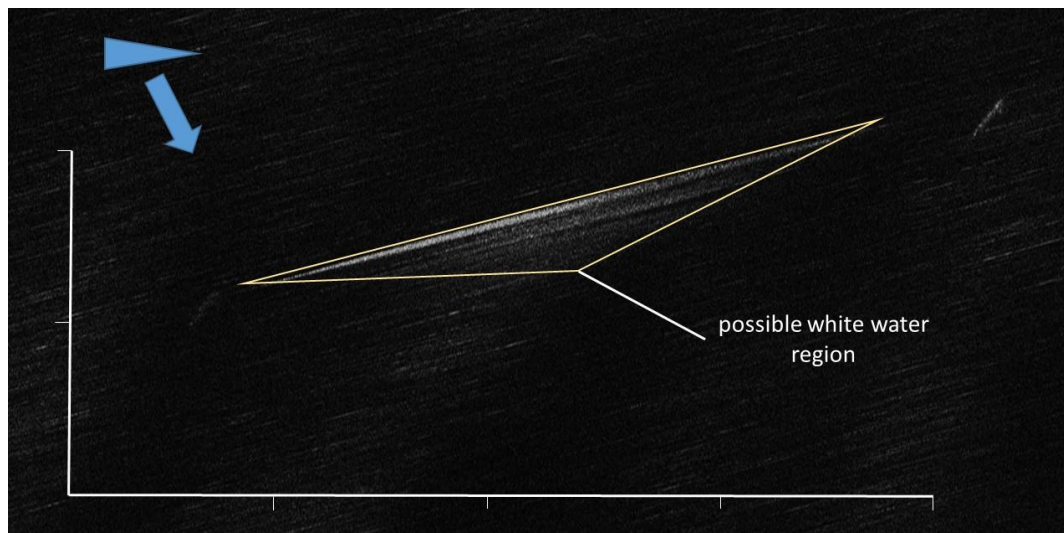


Figure 121: Chip-out from full SAR image annotated to show the assessed likely area of rough water within the wake bloom.

Figure 120 does show that the waves of greatest steepness occur on the centreline immediately rear of the vessel however in order to take the wider field into account the Kelvin wake crest waves should also be considered. The crest waves have greater amplitude than the transverse waves but have a shorter wavelength. Even so, in this case the wave steepness of the crest waves is not sufficient to generate breaking waves so have no impact on a potentially foam-covered region. When considering the real sea there are many factors that will cause waves to break beyond just the underlying Kelvin wake pattern as calculated here. The combination of the ambient sea state, the wind wave field and tidal flow are some of the primary factors that provide and describe the energy that is within the overall wave field. Breaking can readily occur in short timeframes when locally sufficient energy grows within a wave as an accumulation of these real environmental effects. When these are combined with the additional energy of a ship wake, the energy can then stimulate breaking events in the regions such as those suggested by Figure 119 even though in isolation the wave steepness is not predicted to exceed the necessary threshold.

### **8.4 Wake Bloom Skew**

A further phenomenon that could not be categorically answered by the previous section was the appearance of a small azimuthal skew to the bloom artefact in relation to the target vessel. The true location of the target vessel was of the order of 100 m off-centre within the leading edge of the bloom. Such a small skew, owing to the sensitivity of the azimuthal displacement of the SAR processing, has been proposed to be the result of a tidal effect or a result of the scattering mechanism being from whitecap returns that have a natural offset to their Doppler spectrum. Not knowing the precise tidal conditions of the image collection, the first proposition could not be confirmed or rejected. However, the final model at Figure 105 shows signs of such an azimuthal skew without the consideration of the tides. The magnitude

of the skew fits the order of magnitude that has been seen in the real image. Of note, the skew appears, albeit to a lesser extent within the thin ship and pressure ship models also. Ward et al. (2006) consider the offset spectra of whitecap events and assess this to be a result of the location of the rough water source being in the vicinity of the leading face of a breaking wave. The measured skew from the cited source would however give a target vessel location that was at a ratio of roughly 0.41:1 through the leading edge of the wake bloom, comparing the length of the bloom leading edge to the left of the true target location to that on its right. This is a stronger skew than is observed in the real image, 0.75:1.

Dissecting the modelling process, a possible explanation for the appearance of the skew could be due to the proportion of the full orbital motion of the water surface that is observed by the radar. As the tilt modulation aspect of the radar model partially takes shadowing into account then it is very possible that certain elements of the wake calculated are hidden from view of the sensor. This will be most pronounced when the amplitude of the surface elevation is at its greatest, which will normally be nearest the target vessel source. The skew is most noticeable along the azimuth line of the vessel where the greatest amplitude waves would be predicted. Figure 122 shows variation of the shadow region of a surface wave.

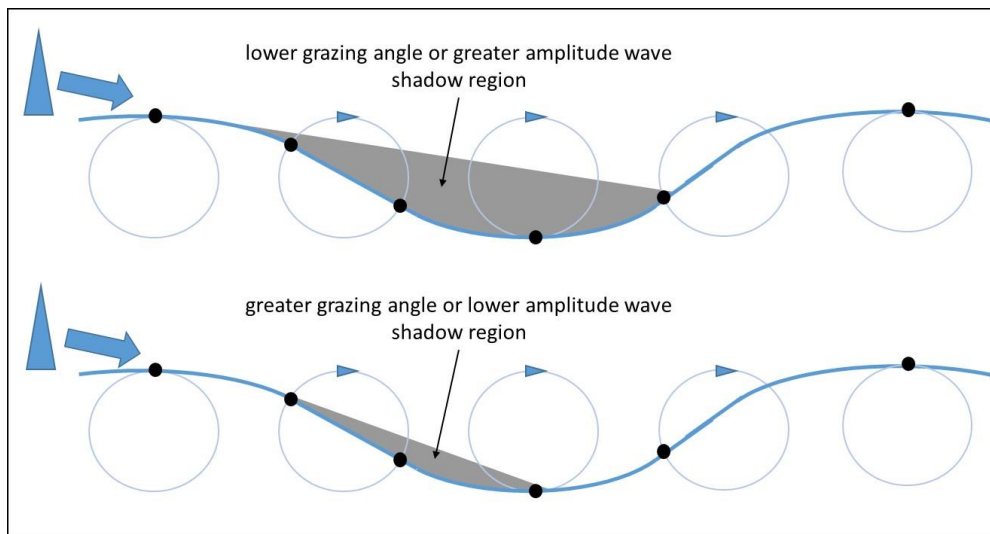


Figure 122: Diagram showing the variation of the impact of shadowing with differing grazing angles.

The two cases given show that when the amplitude of the wave amplitude is great then the shadow region is increased compared to the lower amplitude wave case. A point to note is that this situation is equivalent in the imaging geometry to variation in grazing angle. As the shadow region is located within the trough of the wave, where one of the extremes of along-boresight water particle velocity is found, the affect will be the reduction in visibility of this extreme of velocity and hence the reduction in the envelope of the bloom artefact on the corresponding side determined by the sense of the radial velocity. This can be seen in Figure 123.

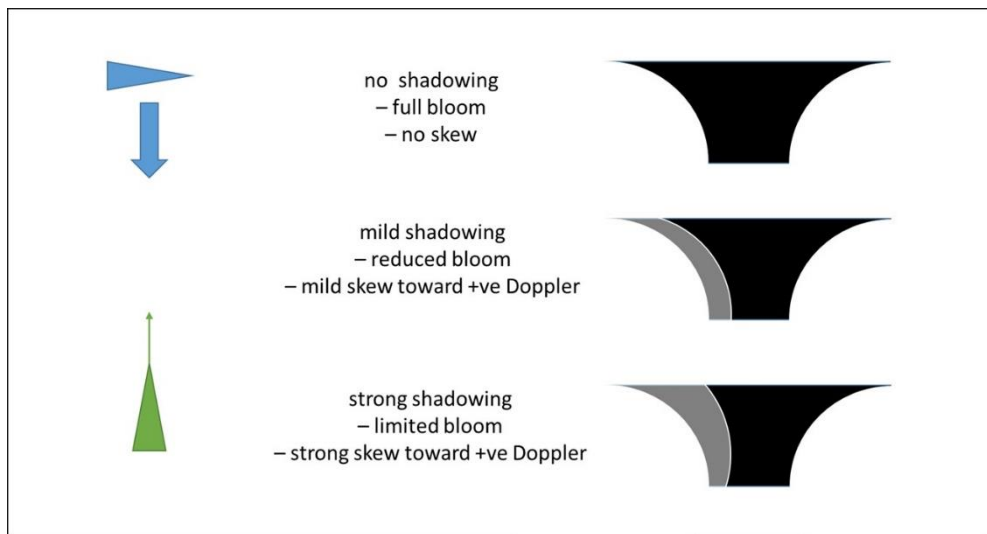


Figure 123: Diagram showing the likely impact of shadowing on the extremes of the wake bloom.

To investigate this possibility further, Figure 124 shows the plot of the amplitude of the transverse wave field directly along the centreline of the Kelvin wake pattern of Figure 104.

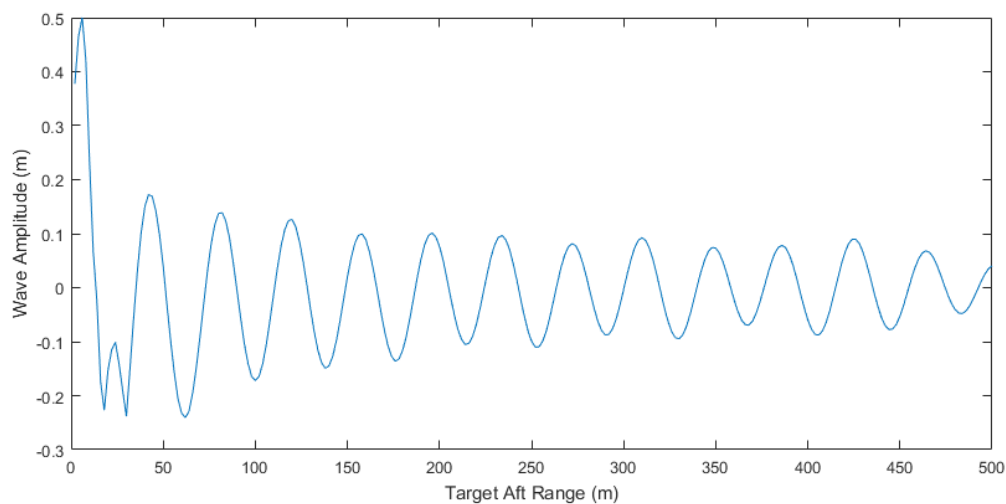


Figure 124: Plot showing the wave amplitude of the transverse waves within the Kelvin wake against aft range from the target vessel. The plot is taken along the centreline of the wake.

A comparison between the wave gradient shown in Figure 125 and the grazing angle of the imaging geometry, 3.5 deg in this case, shows that the nearest 53 m of the wake is likely to suffer from partial shadowing.



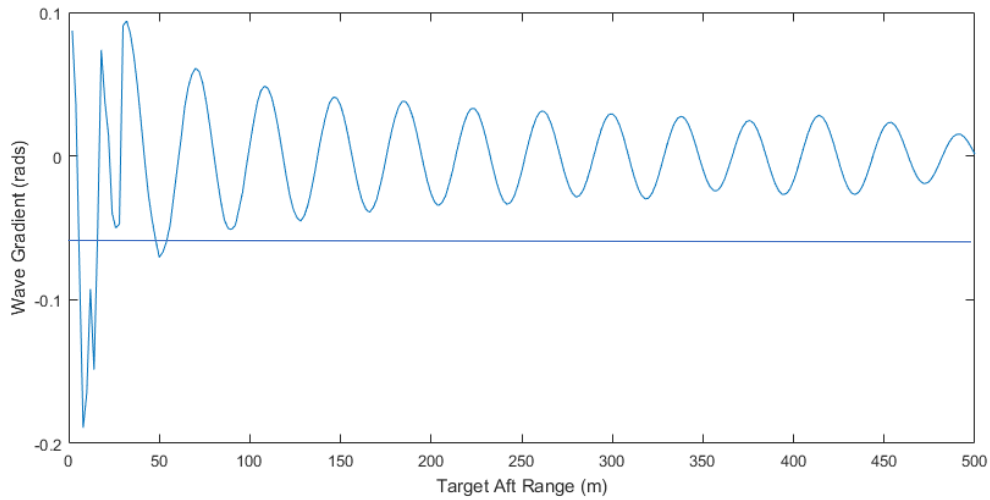


Figure 125: Plot of wave gradient in the along-target-track direction against aft range. The plot is taken along the centreline of the wake. The horizontal threshold at -0.058 shows where the steepness of the wake breaches the criterion for shadowing being present.

In this case, the proportion of the balance of the skew is a calculable quantity given a known amplitude and wavelength. The two limiting cases that relate to the bloom skew in this geometry are shown in Figure 126 where the shadowing either allows the full extent of the Doppler spectrum of the wave to be observable or where the shadowing denies the observation of the lower half of the spectrum and therefore results in full skew.

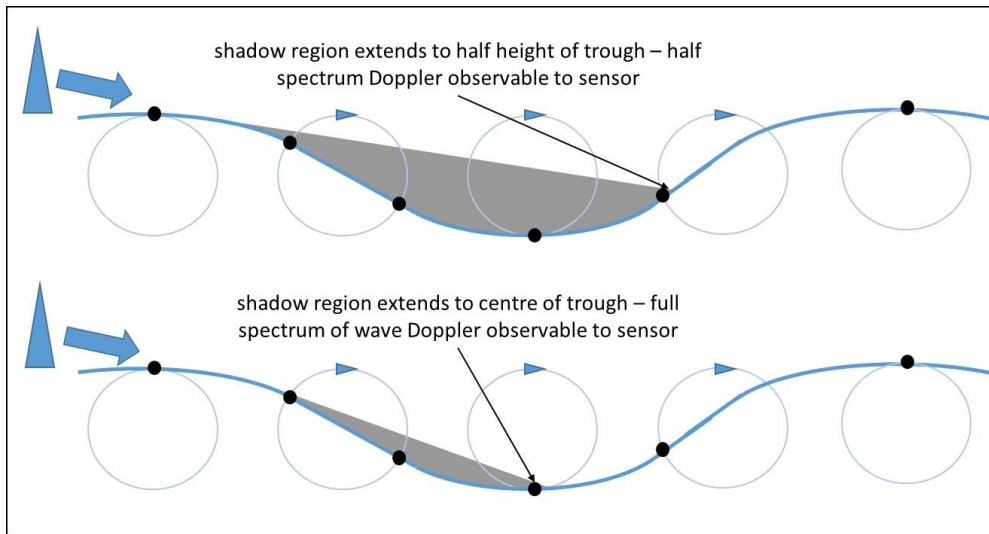


Figure 126: Diagram showing the situations of shadowing where the Doppler spectrum of the wave can be seen to be bounded due to the proportion of the wave phase that is observable by the sensor.

Also, if this mechanism was responsible for the skew then the sense of the skew would be dependent on the aspect of the collection. Using the GF technique where the transverse wake is either fully moving towards or away from the sensor, the shadowing would either have most effect on the receding section of the waves or conversely the approaching sections. In the case of imaging the target vessel from bow to stern, the approaching elements of the wave are predominantly observable and therefore the skew will be towards the positive azimuthal direction of the motion of the sensor. For the case where the target vessel is imaged from stern to bow, the receding elements of the wave are dominant and therefore the skew would be towards the negative azimuthal direction of the sensor's motion, as shown in Figure 127. Both geometries in Figure 127 have been collected somewhat already so could aid future analysis.

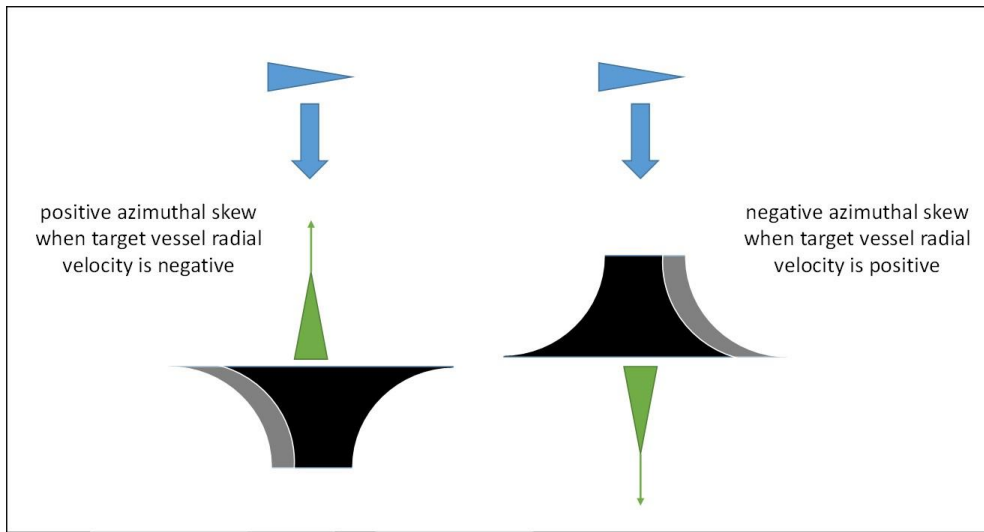


Figure 127: Diagram showing the sense of the impact of the shadowing of the waves on the bloom artefact with relation to the imaging geometry.

An alternative explanation for the source of the skew could be from the significant decay that is seen from the early wave amplitudes that exist just to the rear of the target vessel compared with the amplitudes of the waves further from the vessel. The decay can be visually seen in Figure 124 where, in line with the power law decay prediction that at very small values of target aft range the amplitude is very great. There are, of course, real-world physical limitations that do not allow the wave to follow the true exponential spike at range equal to zero but the smaller the value then the significantly larger the first peak will be compared to the next. If this were the case then similar arguments with regard to the sense of the skew could be made as with the shadowing case as there is a similar predicted reduction in the negative side to the wave's Doppler spectrum. However, as the source is rooted in the power law decay then this would read directly across to the magnitude of the skew. Figure 128 shows a plot of measured values from the wave amplitude of plot at Figure 105 with lines of best fit using the assessed power law relationship in Figure 115, Figure 116 and Figure 117. The mean power coefficient for the three models has been used, -0.44, and the amplitude

factor that was originally arbitrary has been scaled to fit the initial wave amplitude. The fit of the power law relationship has been assessed using a chi-squared test that gives an answer of almost unity. The best fit lines have not been extended beyond the available data for the peak and trough measurements to illustrate the extent, now both aft and beam, of the bloom envelope given the proposed mechanism. A noticeable skew between the positive and negative beam ranges can be seen in the figure. From the measured results, the true target vessel location would plot 86.1 m away from the centreline of the visible bloom in the SAR image with a ratio of 0.64:1 within the bloom frontage. This displacement is pleasingly similar in magnitude and ratio of 0.75:1 to the real image at Figure 63.

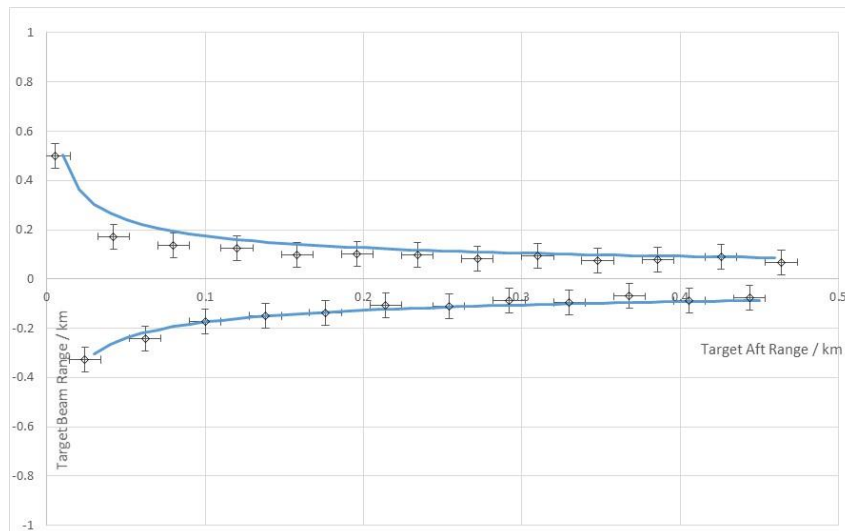


Figure 128: Plot of wave amplitude against aft range taken from the transverse waves along the centreline of the wake. The line of best fit has been derived from the power law decay assessments in Figure 115, Figure 116 and Figure 117.

Applied to a real target, it would be difficult to distinguish between these effects on the skew of bloom. Given the proposed mechanisms of each it would be expected that the skew due to the power law to be evident in all cases as this relationship is ubiquitous for all wakes and imaging geometries. There may also be shadowing superposed that will further affect the bloom skew. This can be predicted to a certain degree with the known parameters of the

imaging geometry but without the knowledge of the amplitude of the waves within the wake then the full effect can only be approximated. Figure 128, through its goodness of fit, suggests that observation of the wake decay by fitting the power law could infer a suitable number to approximate the amplitude of the waves in order to assess the shadowing.

### 8.5 Wake Bloom Striations

Not attempted to be explained by the simple model, evident within the real image, and therefore a lingering question are the striations that run azimuthally through the bloom effect. It was suggested but could not be ascertained whether the striations were isolated elements of the bloom with their own source or scattering mechanism from the remainder of the bloom. Or, whether the striations were simply particularly bright sections of the bloom and that the bloom is a superposition of multiple striations. The model bloom area in Figure 105 is strongly defined by striations as seen within the real image. Figure 129 shows enlargements of the bloom artefact where the phenomenon can be seen.

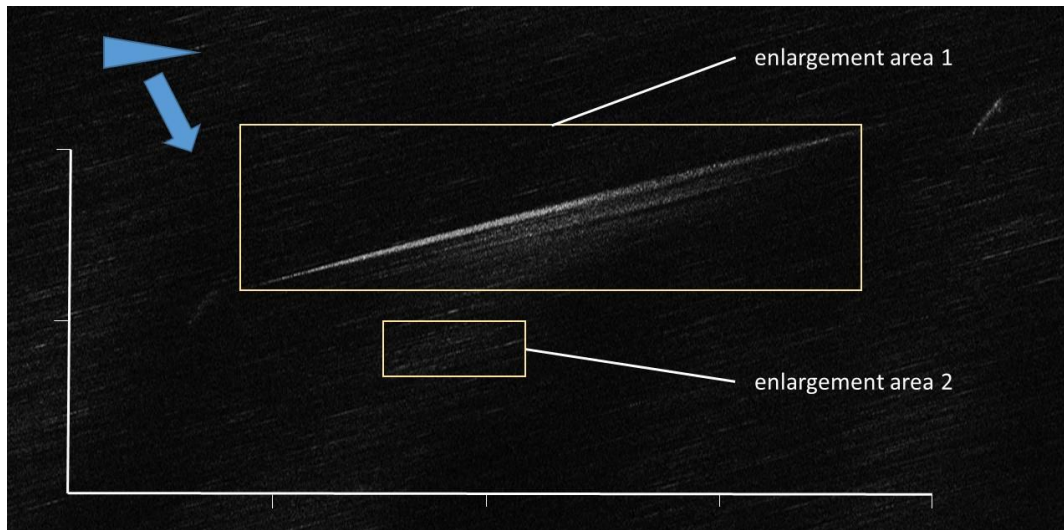


Figure 129: Chip-out of full SAR image annotated to show the zoomed areas for Figure 130.

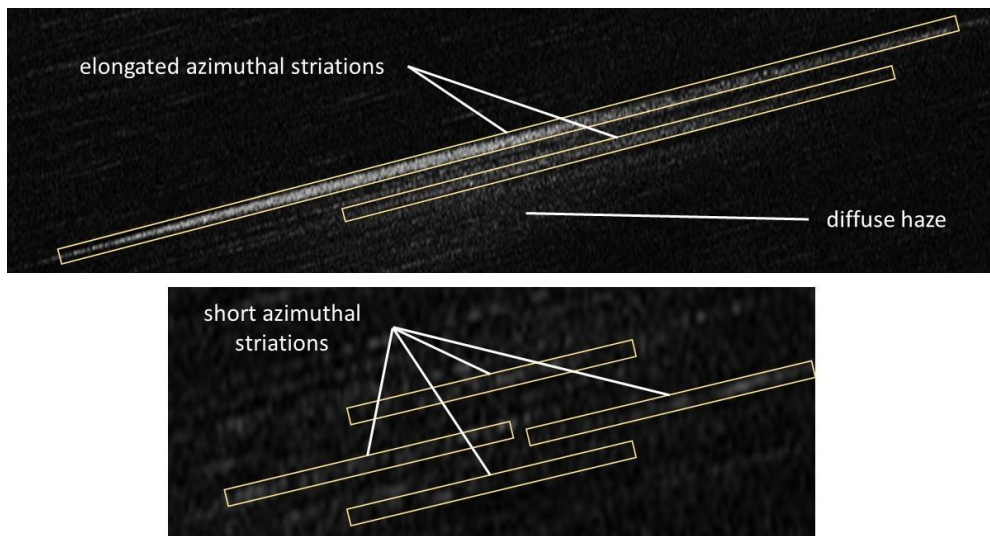


Figure 130: Side-by-side comparison of areas within the wake bloom showing elongated and short azimuthal striation structure. The area of the wake bloom nearest the target vessel also shows a diffuse haze return.

The enlargements in Figure 130 shows three somewhat distinct forms within the bloom that, to varying extents, occur in other images containing the overall artefact. The three forms are the already mentioned striations but are further split here into elongated and shorter versions of what appear to be a similar artefact, and, the diffuse haze that permeates the bloom itself. The sub-aperture analysis, Figure 58, showed deconstruction of the short azimuthal striations as point-like and intense scatterers that have the Doppler spectrum effect of moving a relatively short distance in azimuth during the full aperture. This was described to be akin to the expected returns from burst events. The abundance of the short azimuthal striations, albeit less intense than within the wake area, throughout the remainder of the image would suggest that the source is a common feature of the water surface.

With reference to the elongated striations, given the consideration of the wave steepness at Figure 120 and the expected Doppler spectra from a whitecap return, as shown by Watts et al. (2005), it is entirely reasonable to say that these striations due to their location and the large azimuthal spread, of the order of 600 m compared to the background spreads of the order of

23 m, are a result of whitecap events from the high amplitude waves in the near field wake of the target vessel. The plot in Figure 120 that shows only the first three complete waves of the Kelvin wake will likely show whitecap returns is mirrored in Figure 63 where only two major elongated striations can be readily identified but there are hints of a small number more at much reduced intensity.

The diffuse haze seen in Figure 129 is another common artefact within blooms but is not as distinct in the model plot of Figure 105 as the striations but it appears replicated by the thin ship and surface pressure models shown in Figure 108 and Figure 111. In Figure 105, but both elongated striations appear close to the target vessel and the short striations appear farther from the vessel. The elongated striations are seen within 75 m downstream of the vessel and the short striations beyond 200 m. In the mid region there appears to be signs of the haze artefact. It can be seen where the linear features blur at the edges but do not form the full area effect seen in Figure 129. As the sub-aperture analysis had a limited conclusion as to the source of the haze it was considered that white water may be responsible. The disagreement concerning the expected reflectivity of white-water bubbles floating on a water surface between the likes of Alpers et al. (1981) and Gunn et al. (2018) did not assist in the identification of a true source. The appearance of both the haze artefact in the thin ship et al. and surface pressure models, where it is known that no white-water modelling has been included, would suggest that consideration of the bubble reflectivity is somewhat moot and that the tilt modulation and Bragg effects can account suitably for the haze. This would therefore suggest that the haze is less of a white-water effect and more of a rough water effect.

A final point of note from Figure 105 concerns the plotting of the striations. It would be natural to directly read across the distribution of the transverse wake lines into the simulated

SAR image as the alignment and placing is roughly similar but upon closer inspection it is clear that there are several key differences. The orientation of the strongest parts of each line does not directly follow a line of the transverse wake nor too does the spacing between the striations mirror the wavelength. In fact, the spacing appears roughly double the wavelength of the transverse wavelength. There is nothing that can be seen immediately within the real image of Figure 44 to confirm the modelling. More data would need to be used to corroborate this potential artefact.

### **8.6 Summary**

This chapter has shown that the implementation of the more rigorous mathematical model for describing the wake of the target vessel has been able to provide more probable answers to the questions as to what lies behind the cause of the bloom artefact. This combined with the progress made with previous chapters has resulted in a satisfactorily combined concept of the ship and wake artefact combination. This combined conclusion will be summarised in the final chapter with considerations for possible future work in this particular area of research.



## **9 CHAPTER 9 – CONCLUSIONS AND FUTURE WORK**

### **9.1 Introduction**

Having completed all steps of analysis within this study, this final Chapter collates and summaries the conclusions of the previous sections and identifies specific areas where more work could be done to expand the field or improve the approach taken. The aim of this thesis has been to understand and explain the multiple phenomena that occur in low grazing angle SAR images of moving ships. The methodology used began with application of sub-aperture analysis of the raw SAR imagery then followed by progressively more complex radar and scatterer modelling. The increased fidelity of modelling that improved through stages allowed for the analysis of particular characteristics and phenomena within the collect. Some elements of the imaging have been satisfactorily explained however some questions still remain.

### **9.2 Conclusions**

From the use of the basic model it can be concluded that several of the major artefacts can be explained through the direct employment of well-established SAR imaging phenomenology. This conclusion includes the azimuthal displacement of the target vessel, the azimuthal ambiguity of the target vessel return, the apparent defocus of the primary vessel return and the plot of the range location within the image. The azimuthal displacement is expected as an effect of the bulk motion of the target vessel. As shown in (4.53), the magnitude and orientation of the azimuthal displacement can be determined by the relative velocities of the sensor and the target vessel. It is shown in Chapter 4 that the collection geometry in the case of GF produces azimuthal displacements that are significant in comparison to image size and target vessel size. The related characteristic of azimuthal displacement due to PRF induced ambiguity is also apparent as predicted through SAR image formation process. The relatively

## Chapter 9 – Conclusions and Future Work

low PRF of SAR collection makes ambiguity a risk in standard SAR imagery, although it is normally planned to be avoided by sensor design, but in the instance of a moving target the impact of the radial velocity on the Doppler signature of the target moves the ambiguous returns into view within the image. As shown in (4.54), the PRF induced ambiguity is controlled by the radar signal wavelength, the PRF and the ratio  $\frac{R}{v_{rdr}}$ , which is shown to be a significant determining factor in the character of many of the phenomena demonstrated in this study. Having explained the plotted location of the target vessel return within the image, the defocus of the vessel is also addressed and concluded to be as a result of both the bulk motion of the vessel and the ambiguous nature of the return that appears within the image. Of note, the difference between the simulated image of Figure 85 and a real radar image of the same target would be additional defocus caused by radial and lateral accelerations. Figure 83 also shows the small but apparent range error effect caused to the range plot of the target vessel return mainly as a result of the ambiguous return but also the motion of the vessel through the scene footprint during the collection time.

A common theme associated with the azimuthal displacement of the primary vessel and the azimuthal spread of the wake feature returns is the extent to which they impact the image as opposed to the effects just being present. The individual effects are not only present but commonly have a significant impact on the image – for instance when azimuthal displacement is apparent the magnitude of the displacement is comparable, if not larger, than the total image size. This observation can be considered as a phenomenon in itself. The root cause of this characteristic of this GF imagery is shown to be due the  $\frac{R}{v_{rdr}}$  ratio. The ratio acts to magnify the individual velocity induced phenomena. In certain cases, this acts to make the image harder to interpret and analyse as the ‘true’ sample of the target is significantly

distorted. An example of this is the lack of appearance of the standard Kelvin wake pattern of transverse and cusp waves within the SAR image. The  $\frac{R}{v_{rd}r}$  ratio is high, compared to many other radar systems and imaging geometries, and hence results in highly non-linear azimuthal distortions. As such, the ratio azimuthally distorts the pattern to such an extent that the bunching of the scatterers cannot be readily seen by the image analyst. However, when understood, this ratio characteristic should be considered situationally useful as the effect can be used as a form of microscope to closely and directly examine the velocity induced Doppler signature within the image.

The potential scattering mechanism of white-water has been considered following postulations from previous work but noting the evident disagreement on the topic from certain authors. Ultimately the appearance of the bloom artefact, including many of its key characteristics, within Figure 105 are reproduced from a model that contains no white-water scattering mechanism. This strongly suggests that the white-water itself does not provide a good scatterer in this case. It is important to make the distinction that, in line with the sea clutter scattering phenomena models, this does not fully dissociate the increased scattering magnitude from white-water locations within the wake. This is most notable when considering the whitecap mechanism where a breaking wave event shows a raised return and white-water. Rough water within the breaking event that provides increased RCS and the white-water are often present together. However, it should be understood that the coincidence does not necessarily attribute increased RCS to white-water as the scattering mechanism is associated with the rough water.

Of particular interest, as a novel contribution to this study, was the investigation and explain the appearance of the unusual bloom artefact in the vicinity of the target vessel return.

## Chapter 9 – Conclusions and Future Work

Through use of the hydrodynamic modelling for the Kelvin wake pattern of the ship and use of a low grazing angle SAR radar model it is shown that a bloom artefact can be reproduced in the near field wake region of a moving ship. As such, it is concluded that the bloom artefact is the result of near zero radial velocity rough water scatterers in the near field region of the wake. Through the use of sub-aperture SAR analysis, it is shown that the bloom artefact contains several distinct characteristics. The presence of striated features that extend significantly in azimuth but less so in range suggests the bloom contains breaking wave events that exhibit whitecap scatterer returns. The widespread haze return that accounts for much of the bloom area within an image suggests that the region of the bloom contains rough water that significantly increases the relative reflectivity of the artefact above the average sea clutter level. The shape of the bloom envelope has been considered and shown to follow power law decay in accordance with decay of the orbital velocity of the Kelvin wake cusp and transverse waves.

Through the use of the sub-aperture analysis, sea clutter sea spikes can be identified. The narrow Doppler signature of the spikes is clearly evident along with the representative timeframe of each event. The interesting and novel observation of the slight movement of the Doppler centroid of each event in relation to others was shown through comparison of multiple spikes. Further investigation into the magnitude and nature of this characteristic would be useful further work as the current accepted model suggests the peak should exhibit a constant frequency spike, if the spike is associated with a burst mechanism. The wider modulation of the background clutter is observed across the image and is deduced to be swell related Bragg returns, notably different from the velocity bunching effect seen in high grazing angle SAR imagery of the ocean surface. As the real-time swell was not recorded within the scene, this conclusion cannot be validated further at this stage. Also worth further

investigation is the intensity variation through the sub-image set. It has been argued that the antenna-beam weighting correction within the sub-aperture approach is the most likely cause but the initial image autofocus could not be fully ruled out and may play as a factor.

### **9.3 Suggested Future Work**

The approach taken has proven useful to allow for detailed analysis of the target vessel, bloom artefact and the sea clutter. This is achieved, as planned with the approach, through closer inspection of the Doppler signature progression through the image collection. To that extent the technique, developed and employed, is effective and the user interface allows for flexibility. However, this could be improved by investigating the optimisation of the window that is selected in order to balance the effect on the image and the achieved resolution. Also, the window overlap could be examined and made controllable by the operator as it may prove analytically useful. The approach taken allows for a smooth transition between sub-images with a scalable degradation of resolution but it could prove useful in certain circumstances to provide the user with chronologically displaced, high resolution, Doppler distinct sub-images rather than a sub-image set that are more akin to animation.

The sub-aperture approach could be extended to increase the fidelity of the RDA model applied here. One of the main constraints of the specific RDA model developed in this study is the limitation due to processing load determined by the complexity of the scatterer distribution. The requirement for the load is purposeful in this case as the full fast-time modelling of the scene is desirable for the resultant understanding of the artefacts.

Implementation of a sub-aperture technique like that developed by Moreira in Figure 32 would allow for an increased scatterer model reality without a vastly increased computational load due to the linearised approximations capable with sub-aperture processing.

## Chapter 9 – Conclusions and Future Work

The appearance of the azimuthal skew of the bloom artefact has been considered and explanations are provided using the varying orbital velocity of the waves within the Kelvin wake and also the obscuration due to grazing angle. The current data is insufficient to determine between these possibilities so it is suggested that an expansion to the dataset be collected that specifically looks at varying the collection geometry to include multiple grazing angles. The expansion of the data-set should also look to include a variety of environmental conditions that allow for examination of the change in sea state as well and prevailing wind. The wind strength and direction, with respect to the direction of motion of the target vessel, should also be considered. This data should be able to shed light on the validity of each of the skew hypotheses.

Given the positive results of more realistic ship hull models, such as the slender ship model, as a means of producing an accurate ship and wake model, these methods could be applied with the radar model to investigate the bloom artefact further. This approach could shed light on some of the yet unsure conclusions through the use of different target ship hull models and hence an improved accuracy of the understanding of the wake elevation data that could be fed into the SAR processor.

### **9.4 Summary**

Although the study of the interaction of water with ships goes back centuries into our history, the field is by no means complete. The use of SAR imagery has proven to be particularly fruitful as an investigatory means due to the characteristics of the imaging itself, arising from its underlying modelling assumptions, that produce unique image features as a direct result of scene parameters. The investigation of the scene through use of low grazing angle observation remains one of the least understood environments within the field of sea clutter, mainly due to its non-linearity. This study has focussed on this niche area of research where

## Chapter 9 – Conclusions and Future Work

it has been possible to identify and explain new image artefacts and their phenomenology.

The analytical approach has been to ensure first principles are satisfied and layered modelling complexity in a steady fashion, drawing conclusions progressively throughout. Novel technique approaches have been used in sub-aperture analysis and SAR process modelling to supplement the analysis and demonstrate validation of conclusions. The final analysis has shown that, albeit for some conclusions, there is further work in several areas that could be conducted to follow this research. The study of the affect that ships have on the water through which they travel is still not complete.

## 10 REFERENCES

- [1] Agilent Technologies (2000) 'The fundamentals of signal analysis' (Agilent Technologies: US)
- [2] T. L. Ainsworth, R. W. Jansen, J. S. Lee and R. Fiedler (1999) 'Sub-aperture analysis of high-resolution polarimetric SAR data' *IEEE 1999 International Geoscience and Remote Sensing Symposium. IGARSS'99*, Hamburg, Germany (vol. 1, pp. 41-43)
- [3] T. Ainsworth, M. Sletten, R. Jansen and J. S. Lee (2006) 'SAR Estimation of River Surface Currents: A Sub-Aperture Analysis Approach' *2006 IEEE International Symposium on Geoscience and Remote Sensing*, Denver, CO (pp. 2397-2399)
- [4] H. Akliouat, Y. Smara and L. Bouchemakh (2007) 'Synthetic aperture radar image formation process: application to a region on north Algeria' *Envisat Symposium* (ESA SP-636, Jul 2007)
- [5] M. Albuquerque, P Prats and R. Scheiber (2008) 'Applications of time-domain back projection SAR processing in the airborne case' *European Conference Synthetic Aperture Radar (EUSAR)* (2-5 Jun 2008, Friedrichshafen, Germany, pp. 1-4)
- [6] W. Alpers (1985) 'Theory of radar imaging of internal waves' *Nature* (vol. 314, no. 6008, pp. 245-247)
- [7] W. R. Alpers, D. B. Ross and C. L. Rufenach (1981) 'On the detectability of ocean surface waves by real and synthetic aperture radar' *Journal of Geophysical Research* (vol. 86, no. C7, pp. 6481-6498)
- [8] W. Alpers, R. Romeiser and I. Hennings (1998) 'On the radar imaging mechanism of Kelvin arms of ship wakes' *IGARSS '98. Sensing and Managing the Environment. 1998 IEEE International Geoscience and Remote Sensing. Symposium Proceedings*. Seattle, WA, USA (vol. 4, pp. 1932-1934)



## References

- [9] S. J. Anderson (1991) 'HF Sky Wave Radar Studies Of Ocean Wave Directional Spectra Near Equilibrium' *1991 Fifth International Conference of HF Radio Systems and Techniques*, Edinburgh (pp. 70-72)
- [10] D. B. Andre (2007) 'Radar target-ground interaction' *IET International Conference on Radar* (15-18 Oct 2007, Edinburgh, UK, pp. 1-5)
- [11] D. B. Andre, D. Blacknell, D. Muff and M. R. Nottingham (2011) 'The physics of vibrating scatterers in SAR imagery' *Proceedings of SPIE* (vol. 8051, pp. 1-13)
- [12] D. A. Ausherman, A. Kozma, J. L. Walker, H. M. Jones and E. C. Poggio (1984) 'Developments in radar imaging' *IEEE Transactions on Aerospace and Electronic Systems* (vol. AES-20, no. 4, pp. 363-400)
- [13] S. R. J. Axelsson (1995) 'Frequency and azimuthal variations of radar cross section and their influence upon low-frequency SAR imaging' *IEEE Transactions on Geoscience and Remote Sensing* (vol. 33, no. 5, pp. 1258-1255)
- [14] S. Axelsson (2004) 'Position correction of moving targets in SAR-imagery' *Proceedings of SPIE* (vol. 5236, pp. 80-92)
- [15] M. Balser, C. Harkless, W. McLaren and S. Schurmann (1998) 'Bragg-wave scattering and the narrow-vee wake' *IEEE Transactions on Geoscience and Remote Sensing* (vol. 36, no. 2, pp. 576-588)
- [16] B. C. Barber (1983) 'Theory of digital imaging from orbital synthetic aperture radar' (Technical Report 83079: Royal Aircraft Establishment, MOD)
- [17] M. Y. Bhanumurthy and Y. Mallikarjuna Reddy (2011) 'SAR data processing with range cell migration' *International Journal of Engineering Science and Technology* (vol. 3, no. 1, pp. 388-398)

## References

- [18] D. Blacknell, D. Andre, C. Finch, M. Nottingham and D. Muff (2011) 'Life in the frequency domain: SAR CCD over mountains and the physics of vibrating targets' *Defence Applications of Signal Processing* (pp. 1-6)
- [19] M. L. Boas (1966) 'Mathematical Methods in the Physical Sciences' (John Wiley & Sons, Inc.: London)
- [20] M. Born and E. Wolf (1999) 'Principles of Optics' (Cambridge University Press: UK)
- [21] W. M. Brown and L. J. Procello (1969) 'An introduction to synthetic-aperture radar' *IEEE Spectrum* (vol. 6, no. 9, pp. 52-62)
- [22] W. M. Brown and R. J. Fredricks (1969) 'Range-Doppler imaging with motion through resolution cells' *IEEE Transactions on Aerospace and Electronic Systems* (vol. AES-5, no. 1, pp. 98-102)
- [23] W. M. Brown (1967) 'Synthetic aperture radar' *IEEE Transactions on Aerospace and Electronic Systems* (vol. AES-3, no. 2, pp. 217-229)
- [24] S. Butman, R. Lipes, A. Rubin and T. K. Truong (1981) 'Digital SAR processing using a fast polynomial transform' *IEEE Transactions of Acoustics, Speech and Signal Processing* (vol. 32, no. 2, pp. 419-425)
- [25] C. Cafforio, C. Prati and E. Rocca (1991) 'SAR data focussing using seismic migration techniques' *IEEE Transactions on Aerospace and Electronic Systems* (vol. 27, no. 2, pp. 194-207)
- [26] D. Callaghan, J. Burger and A. K. Mishra (2017) 'A machine learning approach to radar sea clutter suppression' *2017 IEEE Radar Conference*, Seattle, WA (pp. 1222-1227)

## References

- [27] T. M. Calloway and G. W. Donohoe (1994) 'Subaperture autofocus for synthetic aperture radar' *IEEE Transactions on Aerospace and Electronic Systems* (vol. 30, no. 2, pp. 617-621)
- [28] W. Carrara, R. Goodman and R. Majewski (1995) 'Spotlight synthetic aperture radar signal processing algorithms' (Artech House: Boston)
- [29] K. Case, C. Callan, R. Dasher, R. Davis, W. Munk, J. Vesecky, K. Watson and F. Zachariasen (1984) 'SEASAT III & IV' (Defence Technical Information Centre: Vancouver)
- [30] M. Chanteclarc (2005) 'Understanding radar phenomenology of relocatable targets' (ONERA: Palaiseau)
- [31] R. D. Chapman, C. M. Hawes and M. E. Nord (2010) 'Target motion ambiguities in single-aperture synthetic aperture radar' *IEEE Transactions on Aerospace and Electronic Systems* (vol. 46, no. 1, pp. 459-468)
- [32] X. Chen and T. Wu (2009) 'Detection of ships using sub-aperture airborne PolSAR data' *2009 2nd Asian-Pacific Conference on Synthetic Aperture Radar, Xian* (pp. 717-720)
- [33] X. Chen, T. Wu, X. Ruan, H. Zhang and C. Wang (2011) 'Coherent Scatterers Detection with Polarimetric SAR Sub-Aperture Analysis' *2009 2nd Asian-Pacific Conference on Synthetic Aperture Radar, Xian, Shanxi* (pp. 717-720)
- [34] C. Clemente and J. J. Soraghan (2010) 'Range Doppler SAR processing using the fractional Fourier transform' *International Radar Symposium (IRS)* (pp. 1-4)
- [35] D. J. Coe and R. G. White (1995) 'Moving target detection in SAR imagery: experimental results' *IEEE International Radar Conference* (8-11 May 1995, Alexandria, VA, pp. 644-649)

## References

- [36] F. Comblet, A. Khenchaf, M. Parenthoen and A. Ghaleb (2010) 'Ship wake modelling for synthetic aperture radar simulation' (<http://web1.see.asso.fr/ocoss2010>)
- [37] G. Cox and G. Macfarlane (2019) 'The Effects of Boat Waves on Sheltered Waterways - Thirty Years of Continuous Study' *Australasian Coasts & Ports 2019 Conference, Hobart* (pp. 1-7)
- [38] Cumming, F. Wong and K. Raney (1992) 'A SAR processing algorithm with no interpolation' *IEEE International Geoscience and Remote Sensing Symposium (IGARSS)* (vol. 1, pp. 376-379)
- [39] L. J. Cutrona, E. N. Leith, C. J. Palermo and L. J. Porcello (1960) 'Optical data processing and filtering systems' *IRE Transactions on Information Theory* (vol. 6, no. 3, pp. 386-400)
- [40] L. J. Cutrona, E. N. Leith, L. J. Porcello and W. E. Vivian (1966) 'On the application of coherent optical processing techniques to synthetic aperture radar' *Proceedings of the IEEE* (vol. 54, no. 8, pp. 1026-1032)
- [41] Danklmayer (2009) 'Assessment of atmospheric propagation effects in SAR images' *IEEE Transactions on Geoscience and Remote Sensing* (vol. 47, no. 10, pp. 3507-3518)
- [42] M. Dawson (2010) 'Python Programming' (Course Technology Centage Learning: Boston, MA, USA)
- [43] Deng, Y. Qin, H. Wang, X. Li and H. Li (2012) 'Pulse-repetition-interval transform-based vibrating target detection and estimation in synthetic aperture radar' *IET Signal Processing* (vol. 6, no. 6, pp. 551-558)
- [44] N. Didden and I. Hennings (1999) 'Comparison of synthetic aperture radar (SAR) cross section and wave energy density variations above submarine sand waves

## References

- from the C-STAR field experiment' *IEEE International Geoscience and Remote Sensing Symposium (IGARSS)* (vol. 3, pp. 1658-1660)
- [45] M. Do (2006) 'Fundamentals of signal processing' (Creative Comms: <http://cnx.org/content/col10360/1.3/>)
- [46] L. J. Doctors and A. H. Day (2009) 'The generation and decay of waves behind high-speed vessels' (pp. 1-4)
- [47] W. Doerry (2001) 'Performance limits for synthetic aperture radar' (Sandia National Laboratories: Albuquerque, NM)
- [48] W. Doerry (2004) 'Atmospheric loss considerations for synthetic aperture radar design and operation' *Proceedings of SPIE* (vol. 5410, pp. 17-27)
- [49] W. Doerry (2004) 'Performance limits for synthetic aperture radar - second edition' (Sandia National Laboratories: Albuquerque, NM)
- [50] Elachi and W. E. Brown, Jr (1977) 'Models of radar imaging of the ocean waves' *IEEE Transactions of Antennas and Propagation* (vol. AP-25, no. 1, pp. 84-95)
- [51] Elachi, T. Bicknell, R. L. Jordan and C. Wu (1982) 'Spaceborne synthetic-aperture imaging radars: Applications, techniques, and technology' *Proceedings of the IEEE* (vol. 70, no. 10, pp. 1174-1209)
- [52] L. Evans, J. Apel, R. Arvidson, R. Bindshadler, F. Carsey, J. Dozier, K. Jezek, E. Kasischke, F. Li, J. Melack (1995) 'Spaceborne Synthetic Aperture Radar: Current Status and Future Directions' (NASA Technical Memorandum 4679)
- [53] M.-C. Fang, R.-Y. Yang, I. V. Shugan (2011) 'Kelvin Ship Wake in the Wind Waves Field and on the Finite Sea Depth' *Journal of Mechanics* (vol. 27, no. 1)

## References

- [54] R. Fasih, E. Ertin, J. N. Ash and R. L. Moses (2008) ‘SAR focussing performance for moving objects with random motion components’ *Asilomar Conference on Signals, Systems and Computers* (26-29 Oct 2008, Pacific Grove, CA, pp. 1628-1632)
- [55] L. Ferro-Famil, A. Reigber, E. Pottier and W. M. Boerner (2002) ‘Scene characterization using subaperture polarimetric SAR data’ *IEEE Transactions on Geoscience and Remote Sensing* (vol. 41, no. 10, pp. 2264-2276)
- [56] R. Fiedler and R. Jansen (2000) ‘Joint time-frequency analysis of SAR data’ *IEEE Workshop on Statistical Signal and Array Processing* (pp. 480-484)
- [57] G. Franceschetti, A. Mazzeo, N. Mazzocca, V. Pascazio and G. Schirinzi (1991) ‘Time-domain processing of SAR sata in real time’ *IEEE International Geoscience and Remote Sensing Symposium (IGARSS)* (vol. 1, pp. 283-286)
- [58] O. Frey and E. Meier (2008) ‘Combining time-domain back-projection and Capon beamforming for tomographic SAR processing’ *IEEE International Geoscience and Remote Sensing Symposium (IGARSS)* (vol. 2, pp. 445-448)
- [59] W. Fu, J. Ma, P. Chen and F. Chen (2020) ‘Remote Sensing Satellites for Digital Earth’ *Manual of Digital Earth* (pp 55-123)
- [60] M. Furth (2014) ‘The development of a dissipative potential flow model for wave making resistance prediction’ (University of Southampton, Engineering and the Environment)
- [61] A. Garren, J. S. Goldstein, D. R. Obuchon, R. R. Greene and J. A. North (2004) ‘SAR image formation algorithm with multipath reflectivity estimation’ *IEEE Radar Conference* (26-29 Apr 2004, pp. 323-328)

## References

- [62] Gotman (2007) 'Navigating the wake of past efforts' *The Journal Of Ocean Technology - Reviews and Papers* (vol. 2, no. 1)
- [63] K. A. Graf and H. Guthart (1969) 'Velocity effects on synthetic apertures' *IEEE Transactions of Antennas and Propagation* (vol. AP-17, no. 5, pp. 541-546)
- [64] H. Greidanus (2006) 'Sub-aperture Behavior of SAR Signatures of Ships' *2006 IEEE International Symposium on Geoscience and Remote Sensing*, Denver, CO (pp. 3579-3582)
- [65] D. Gu, H. Yue, B. Lu and X. Xu (2018) 'Velocity Estimation for Moving Target Refocusing in the Long-Time Coherent Integration SAR Imaging' *2018 China International SAR Symposium (CISS)*, Shanghai (pp. 1-4)
- [66] L. Guerrierio, F. Intelligente, V. A. Lore and G. Milillo (2005) 'Analysis of algorithms for SAR data processing: an approach in the time domain' *IEEE International Geoscience and Remote Sensing Symposium* (pp. 3337-3340)
- [67] G. E. Gunn (2018) 'Observing Scattering Mechanisms of Bubbled Freshwater Lake Ice Using Polarimetric RADARSAT-2 (C-Band) and UW-Scat (X- and Ku-Bands)' *IEEE Transactions On Geoscience And Remote Sensing* (vol. 56, no. 5)
- [68] D. Guo, X. Gu, T. Yu, X. Li, H. Xu and H. Ma (2009) 'Wave Simulation of SAR Signal for Two-Dimensions Sea Surface' *IEEE Circuits and Systems International Conference on Testing and Diagnosis*
- [69] T. H. Havelock (1934) 'The Calculation of Wave Resistance' *Proceedings of the Royal Society of London. Series A, Containing Papers of a Mathematical and Physical Character* (vol. 144, no. 853, pp. 514-521)

## References

- [70] D. Holliday, L. L. Deraad and G. J. St-Cyr (1998) 'Sea spike back-scatter from a steepening wave' *IEEE Transactions Antennas Propagation* (vol. 46, pp. 108-113)
- [71] Y. Huang and A. Moreira (1993) 'Airborne SAR processing using the chirp scaling and a time domain subaperture algorithm' *IEEE International Geoscience and Remote Sensing Symposium (IGARSS)* (vol. 3, pp. 1182-1184)
- [72] J. R. Huynen (1970) 'Phenomenological theory of radar targets' (Drukkerij Bronder-Offset N.V: Rotterdam)
- [73] V. Jakowatz, Jr and P. A. Thompson (1995) 'A new look at spotlight mode synthetic aperture radar as tomography: Imaging 3-D targets' *IEEE Transactions on Image Processing* (vol. 4, no. 5, pp. 699-703)
- [74] J. K. Jao (2001) 'Theory of synthetic aperture radar imaging of a moving target' *IEEE Transactions on Geoscience and Remote Sensing* (vol. 39, no. 9, pp. 1984-1992)
- [75] M. Y. Jin and C. Wu (1984) 'A SAR correlation algorithm which accommodates large-range migration' *IEEE Transactions on Geoscience and Remote Sensing* (vol. GE-22, no. 6, pp. 592-597)
- [76] O. Karabayir, S. Makal Yucedag, O. M. Yusedag, H. A. Serim and S. Kent (2014) 'Radar cross section and Doppler effects of wind turbines on SAR imaging' *IEEE Proceedings of Radar, Sonar and Navigation* (vol. 9, no. 3, pp. 1-4)
- [77] D. P. Kasilingham and O. H. Shemdin (1990) 'Models for Synthetic Aperture Radar Imaging of the Ocean: A Comparison' *Journal Of Geophysical Research* (vol. 95, no. C9, pp 16263-16276)



## References

- [78] A. F. Kip (1969) 'Fundamentals of Electricity and Magnetism' (McGraw-Hill Kogakusha: Tokyo)
- [79] J. C. Kirk, Jr (1975) 'A discussion of digital processing in synthetic aperture radar' *IEEE Transactions on Aerospace and Electronic Systems* (vol. AES-11, no. 3, pp. 326-337)
- [80] J. C. Kirk, Jr (1975) 'Motion compensation for synthetic aperture radar' *IEEE Transactions on Aerospace and Electronic Systems* (vol. AES-11, no. 3, pp. 338-348)
- [81] J. R. Klauder, A. C. Price, S. Darlington and W. J. Albersheim (1960) 'The theory and design of chirp radars' *Bell System Technical Journal* (vol. 39, no. 4, pp. 745-808)
- [82] L. Knepp and M. A. Hausman (2003) 'Ionospheric propagation effects on ground and space based radars' *IEEE International Radar Conference* (3-5 Sep 2003, pp. 71-76)
- [83] E. Kreyszig (1972) 'Advanced Engineering Mathematics' (John Wiley & Sons, Inc.: London)
- [84] V. Krishnan, C. E. Yarman and B. Yazici (2010) 'SAR imaging exploiting multi-path' *IEEE Radar Conference* (13-16 Dec 2009, Aruba, Dutch Antilles, pp. 1423-1427)
- [85] J. M. Kuo and K. S. Chen (2002) 'Ship wake detection in synthetic aperture radar images using a combination of a wavelet correlator and Radon transform' *Journal of Optical Engineering* (vol. 41, no. 3, pp. 686-696)
- [86] H. Lamb (1932) 'Hydrodynamics' (Cambridge University Press: UK)

## References

- [87] T. P. Leonard, I. Antipov and K. D. Ward (2002) 'A Comparison Of Radar Sea Clutter Models' *The 2002 International Radar Conference - Institution of Electrical Engineers* (pp. 429-433)
- [88] K. Li and W. T. K. Johnson (1983) 'Ambiguities in Spaceborne Synthetic Aperture Radar Systems' *IEEE Transactions On Aerospace And Electronic Systems* (vol. AES-19, no. 3)
- [89] J. Lighthill (1978) 'Waves in Fluids' (Cambridge University Press: UK)
- [90] M. J. Lighthill and G. B. Whitham (1955) 'On kinematic waves I. Flood movement in long rivers' *Proceedings of the Royal Society, Mathematical, Physical and Engineering Sciences* (vol. 229, no. 1178)
- [91] L. Liu, Z. Fan, C. Tao and R. Jia (2012) 'Research of X-Band Radar Sea Clutter Image Simulation Method' *2012 Fifth International Joint Conference on Computational Sciences and Optimization*, Harbin (pp. 793-796)
- [92] P. Lombardo, F. Colone and D. Pastina (2006) 'Monitoring and surveillance potentialities obtained by splitting the antenna of the COSMO-SkyMed SAR into multiple sub-apertures' *Proceedings of IEE Radar Sonar and Navigation* (vol. 153, no. 2, pp. 104-116)
- [93] S. P. Luttrell and C. J. Oliver (1986) 'Prior knowledge in synthetic aperture radar processing' *Journal of Physics D: Applied Physics* (vol. 19, no. 3, pp. 333-356)
- [94] J. D. Lyden (1988) 'Synthetic aperture radar imaging of ship wakes' *Journal of Geophysical Research* (vol. 93, no. C10, pp. 12293-12303)
- [95] J. D. Lyden, D. R. Lyzenga and R. A. Shushman (1985) 'SAR detection of ship-generated turbulent and vortex wakes' (Research Institute of Michigan)

## References

- [96] Lyzenga and N. Malinas (1994) 'Near-field ship wake signature modelling and simulation' (Office of Naval Research: Arlington, VA)
- [97] R. Lyzenga (1986) 'Numerical Simulation of Synthetic Aperture Radar Image Spectra for Ocean Waves' *IEEE Transactions on Geoscience and Remote Sensing* (vol. GE-24, no. 6, pp. 863-872)
- [98] U. Madhow (2008) 'Fundamentals of digital communication' (Cambridge University Press: New York)
- [99] D. D. Madsen (2010) 'Multi-Aperture Coherent Change Detection and Interferometry for Synthetic Aperture Radar' (Department of Electrical and Computer Engineering, Brigham Young University)
- [100] B. R. Mahafza (2011) 'Radar Signal Analysis and Processing using MATLAB' (Chapman & Hall: Boca Raton)
- [101] C. Maingot, A. Soloviev, M. Gilman, S. Matt, J. Fenton, S. Lehner, D. Velotto, S. Brusch, W. Perrie and B. Zhang (2011) 'Observation of natural and artificial features on the sea surface from satellite imagery with in-situ measurements' *IEEE International Geoscience and Remote Sensing Symposium (IGARSS)* (vol. 11, pp. 241-244)
- [102] Margarit, J. J. Mallorqui, J. Fortuny-Guasch and C. Lopez-Martinez (2009) 'Phenomenological vessel scattering study based on simulated inverse SAR imagery' *IEEE Transactions on Geoscience and Remote Sensing* (vol. 47, no. 4, pp. 1212-1223)
- [103] M. Marghany (2004) 'Velocity Bunching Model For Modelling Wave Spectra Along East Coast Of Malaysia' *Journal of the Indian Society of Remote Sensing* (vol. 32, no. 2)

## References

- [104] D. Martin and A. W. Doerry (2005) 'SAR polar format implementation with MATLAB' (Sandia National Laboratories: Albuquerque, NM)
- [105] C. C. Mei and M. Naciri (1991) 'Note on Ship Oscillations and Wake Solitons' *Mathematical and Physical Sciences* (vol. 432, no. 1886, pp. 535-546)
- [106] W. Melief, H. Greidanus, P. van Genderen and P. Hoozeboom (2006) 'Analysis of sea spikes in radar sea clutter data' *IEEE Transactions on Geoscience and Remote Sensing* (vol. 44, no. 4, pp. 985-993)
- [107] J. Meyer and J. B. Nicoll (2008) 'Prediction, detection, and correction of Faraday rotation in full-polarimetric L-band SAR data' *IEEE Transactions on Geoscience and Remote Sensing* (vol. 46, no. 10, pp. 3076-3086)
- [108] J. H. Michell (1898) 'The wave resistance of a ship' *Philosophical Magazine* (ser. 5, vol. 45, pp. 106-123)
- [109] S. Mirbolouk, M. Maghsoodi, E. Torabi and M. Mahdavi (2013) 'Synthetic aperture radar data processing' *International Journal of Advanced Research in Computer Science and Software Engineering* (vol. 3, no. 5, pp. 805-809)
- [110] L. M. Mitnik and V. A. Dubina (2012) 'Satellite SAR sensing of oceanic dynamics in the Kuril Straits area' *IEEE International Geoscience and Remote Sensing Symposium (IGARSS)* (vol. 12, pp. 7632-7635)
- [111] A. Moreira and Y. Huang (1994) 'Airborne SAR processing of highly squinted data using a chirp scaling approach with integrated motion compensation' *IEEE Transactions on Geoscience and Remote Sensing* (vol. 32, no. 25, pp. 1029-1040)

## References

- [112] A. Moreira (1992) 'Real-time synthetic aperture radar (SAR) processing with a new subaperture approach' *IEEE Transactions on Geoscience and Remote Sensing* (vol. 30, no. 4, pp. 714-722)
- [113] A. Moreira, T. Misra and S. Chowdhury (1992) 'Modelling and performance evaluation of a new subaperture approach for real-time SAR processing' 92 *International Conference on Radar*, Brighton, UK, (pp. 399-402)
- [114] W. H. Munk, P. Scully-Power and F. Zacariasen (1987) 'The Bakerian Lecture 1986, Ships from Space' *Proceedings of the Royal Society of London. Series A, Mathematical and Physical Sciences* (vol. 412, no. 1843, pp. 231-254)
- [115] D. C. Munson, Jr, J. D. O'Brien and W. K. Jenkins (1983) 'Tomographic formulation of spotlight-mode synthetic aperture radar' *Proceedings of the IEEE* (vol. 71, no. 8, pp. 917-1005)
- [116] F. Noblesse, F. Huang and C. Yang (2013) 'The Neumann–Michell theory of ship waves' *Journal of Engineering Mathematics* (no. 1)
- [117] J. Oliver (1991) 'Information from SAR images' *Journal of Physics D: Applied Physics* (vol. 24, no. 9, pp. 1493-1514)
- [118] C. Oliver and S. Quegan (1998) 'Understanding Synthetic Aperture Radar Images' (Artech House: Boston)
- [119] K. Ouchi (1985) 'On the multilook images of moving targets by synthetic aperture radars' *IEEE Transactions of Antennas and Propagation* (vol. AP-33, no. 8, pp. 823-827)
- [120] K. Ouchi (1993) 'On the SAR imaging mechanisms of oceanic internal waves' *IEEE International Geoscience and Remote Sensing Symposium (IGARSS)* (vol. 2, pp. 357-360)

## References

- [121] K. Ouchi (1994) 'Modulation of waveheight spectrum and radar cross section by varying surface currents' *IEEE Transactions on Geoscience and Remote Sensing* (vol. 32, no. 5, pp. 995-1003)
- [122] K. Oumansour, Y. Wang and J. Saillard (1996) 'Multifrequency SAR observation of a ship wake' *IEEE Proceedings of Radar, Sonar and Navigation* (vol. 143, no. 4, pp. 275-280)
- [123] R. P. Perry, R. C. DiPietro and R. L. Fante (1999) 'SAR imaging of moving targets' *IEEE Transactions on Aerospace and Electronic Systems* (vol. 35, no. 1, pp. 188-200)
- [124] R. Peltzer, W. Garrett and P. Smith (1985) 'A remote sensing study of a surface ship wake' *OCEANS '85 - Ocean Engineering and the Environment*, San Diego, CA, USA (pp. 277-286)
- [125] R. Pethiyago (2016) 'Mathematical and computational analysis of Kelvin ship wave patterns' (Queensland University of Technology)
- [126] F. D. Queen and E. E. Maine, Jr (1971) 'Radar cross section of surface ships at grazing incidence' (Naval Research Laboratory: Washington, DC)
- [127] L. R. Rabiner and B. Gold (2014) 'Theory and Application of Digital Signal Processing' (PHI Learning: Delhi)
- [128] R. K. Raney (1970) 'Synthetic aperture imaging radar and moving targets' *IEEE Transactions on Aerospace and Electronic Systems* (vol. AES-7, no. 3, pp. 499-505)
- [129] R. K. Raney, H. Runge, R. Bamler, I. G. Cumming and F. H. Wong (1994) 'Precision SAR using chirp scaling' *IEEE Transactions on Geoscience and Remote Sensing* (vol. 32, no. 4, pp. 786-799)

## References

- [130] R. K. Raney, I. G. Cumming and F. H. Wong (1993) 'Synthetic aperture radar processor to handle large squint with high phase and geometric accuracy' (Patent Number 5179838: United States Patent)
- [131] R. K. Raney and G. J. Princz (1987) 'Reconsideration of Azimuth Ambiguities in SAR' *IEEE Transactions on Geoscience and Remote Sensing* (vol. GE-25, no. 6, pp. 783-787)
- [132] M. Reed and J. H. Milgram (2002) 'Ship wakes and their radar images' *Annual Review of Fluid Mechanics* (vol. 34, pp. 469-502)
- [133] Reigber, M. Jager, A. Dietzsch, R. Hansch, M. Weber, H. Przybyl and P. Prats (2007) 'A distributed approach to efficient time-domain SAR processing' *IEEE International Geoscience and Remote Sensing Symposium* (pp. 582-585)
- [134] Ribalta (2011) 'Time-domain reconstruction algorithms for FMCW-SAR' *IEEE Geoscience and Remote Sensing Letters* (vol. 8, no. 3, pp. 396-400)
- [135] M. A. Richards (2005) 'Fundamentals of Radar Signal Processing' (McGraw-Hill Education: New Delhi)
- [136] M. A. Richards, J. A. Scheer and W. A. Holm (2010) 'Principles of modern radar' (Scitech Publishing, Inc: Rayleigh, NC)
- [137] F. Rocca (1989) 'Synthetic aperture radar: a new application for wave equation techniques' *Geophysical Prospecting* (vol. 37, no. 7, pp. 809-830)
- [138] Rohde and Schwarz (2012) 'Introduction to radar system and component tests' (Rohde and Schwarz: Munich)
- [139] W. Rosenthal, F. Ziemer, K. Raney and P. Vachon (1989) 'Removal of 180/spl deg/ ambiguity in SAR images of ocean waves) *12th Canadian Symposium on*

## References

- Remote Sensing Geoscience and Remote Sensing Symposium*, Vancouver, Canada (pp. 2342-2345)
- [140] M. Ruegg, E. Meier and D. Nuesch (2005) 'Constant motion, acceleration, vibration and rotation of objects in SAR data' *Proceedings of SPIE* (vol. 5980, pp. 1-12)
- [141] L. Rufenach, R. A. Schuchman and N. P. Malinas (1991) 'Ocean wave spectral distortion in airborne synthetic aperture radar imagery during the Norwegian continental shelf experiment of 1988' *Journal of Geophysical Research* (vol. 96, no. C6, pp. 10453-10466)
- [142] Runge and R. Bamler (1998) 'Prf Ambiguity Resolving For Sar' *12th Canadian Symposium on Remote Sensing Geoscience and Remote Sensing Symposium*, Vancouver, Canada (pp. 2572-2575)
- [143] P. A. Ryan and K. S. Wilson (1999) 'Phenomenology metric development for SAR scene modelling tools' *Proceedings of SPIE* (vol. 3721, pp. 582-588)
- [144] R. A. Schuchman and O. H. Shemdin (1983) 'Synthetic aperture radar imaging of ocean waves during the Marineland experiment' *IEEE Journal of Oceanic Engineering* (vol. OE-8, no. 2, pp. 83-90)
- [145] S. R. Schurmann (1989) 'Radar characterization of ship wake signatures and ambient ocean clutter features' *Proceedings of the IEEE National Radar Conference*, Dallas, TX, USA (pp. 182-187)
- [146] M. Scott, A. Rezaizadeh and M. Moore (2001) 'Phenomenology study of HERMES ground penetrating radar technology for detection and identification of common bridge deck features' (Office of Infrastructure Research and Development: McLean VA)



## References

- [147] J. Sharma and M. J Collins (2014) 'Simulation of SAR signals from moving vehicles' (<http://www.researchgate.net/publication>)
- [148] J. Sharma, C. H. Gierull and M. J. Collins (2006) 'The influence of target acceleration on velocity estimation in dual-channel SAR-GMTI' *IEEE Transactions on Geoscience and Remote Sensing* (vol. 44, no. 1, pp. 134-147)
- [149] S. Sharma, P. Jena and R. Kuloor (2011) 'Mathematical analysis of interpolation step of omega-k algorithm for GPR and its implementation' *International Conference on Communications and Signal Processing (ICCSP)* (10-12 Feb 2011, Calicut, pp. 46-50)
- [150] W. Sherwin, J. P. Ruina and R. D. Rawcliffe (1962) 'Some early developments in synthetic aperture radar systems' *IRE Transactions on Military Electronics* (vol. MIL-6, no. 2, pp. 111-115)
- [151] Shin and J. Lim (2012) 'Omega-K algorithm for spaceborne spotlight SAR imaging' *IEEE Geoscience and Remote Sensing Letters* (vol. 9, no. 3, pp. 343-347)
- [152] S. Singh, M. Soccorsi and M. Datcu (2010) 'SAR complex image analysis: A Gauss Markov and a multiple sub-aperture based target characterization' *IEEE International Geoscience and Remote Sensing Symposium, IGARSS 2010*, July 25-30, 2010, Honolulu, Hawaii, USA, Proceedings (pp. 1585-1588)
- [153] Singh and M. Datcu (2010) 'Target Analysis using a 4-D Representation based on Sub- Aperture Decomposition of SAR Images' *8th European Conference on Synthetic Aperture Radar*, Aachen, Germany (pp. 1-3)
- [154] M. I. Skolnik (1980) 'Introduction to Radar Systems' (McGraw-Hill, Inc.: New York)

## References

- [155] T. Soomere (2006) 'Nonlinear ship wake waves as a model of rogue waves and a source of danger to the coastal environment: a review' *Oceanologia* (vol. 48)
- [156] Soumekh (1995) 'Reconnaissance with ultra wideband UHF synthetic aperture radar' *IEEE Signal Processing Magazine* (pp. 21-40)
- [157] M. Spigai, C. Tison and J-C, Souyris (2008) 'Time-frequency analysis of point target behaviour in high resolution single polarization SAR images' *EUSAR 2008* (pp. 1-4)
- [158] N. R. Stapleton (1997) 'Ship wakes in radar imagery' *International Journal of Remote Sensing* (vol. 18, no. 6, pp. 1381-1386)
- [159] N. R. Stapleton (1989) 'Bright narrow V-shaped wakes observed by the NASA/JPL AIRSAR during the Loch Linnhe experiment 1989' *1995 International Geoscience and Remote Sensing Symposium, IGARSS '95. Quantitative Remote Sensing for Science and Applications*, Firenze, Italy (vol. 3, pp. 1646-1648)
- [160] G. W. Stimson (2014) 'Introduction to Airborne Radar' (Sci Tech Publishing Inc.: New York)
- [161] J. J. Stoker (1957) 'Water Waves – The Mathematical Theory with Applications' (Interscience Publishers Inc.: New York)
- [162] M. Stuff, M. Biancalana, G. Arnold and J. Garabrino (2004) 'Imaging moving objects in 3D from single aperture synthetic aperture radar' *IEEE Radar Conference* (26-29 Apr 2004, pp. 94-98)
- [163] E.H. Suller and J.K.E. Tunaley (1989) 'The effect of ship's screws on the ship wake and its implications for the radar image of the wake' *12th Canadian Symposium on Remote Sensing Geoscience and Remote Sensing Symposium*

## References

- [164] R-Q. Sun, G. Luo, M. Zhang and C. Wang (2011) 'Electromagnetic scattering model of the Kelvin wake and turbulent wake by a moving ship' *Waves in Random and Complex Media* (vol. 21, no. 3, pp. 501-514)
- [165] V. Swanson, J. R. Bennett and F. J. Tanis (1988) 'The Influence Of Surfactants On The Remote Sensing Of Ocean Internal Waves And Ship Wakes' *International Geoscience and Remote Sensing Symposium, 'Remote Sensing: Moving Toward the 21st Century'*, Edinburgh, UK (pp. 1079-1080)
- [166] J. C. Toomay and P. J. Hannen (2004) 'Principles of Radar' (PHI Learning: New Delhi)
- [167] V. Toporkov, P. A. Hwang, M. A. Sletten, G. Farquharson, D. Perkovic and S. J. Frasier (2011) 'Surface velocity profiles in a vessel's turbulent wake observed by a dual-beam along-track interferometric SAR' *IEEE Geoscience and Remote Sensing Letters* (vol. 8, no. 4, pp. 602-606)
- [168] W. Thompson (1847) 'On the Theory of Oscillatory Waves' *Transactions of the Cambridge Philosophical Society* (vol. 8, pp. 197-238)
- [169] W. Thompson (1887) 'On Ship Waves' *Proceedings of the Institute of Mechanical Engineers* (vol. 38, no. 1, p. 409)
- [170] E. O. Tuck (1975) 'Low aspect ratio flat ship theory' *Journal of Hydronautics* (vol. 9, pp. 3-12)
- [171] E. O. Tuck, D. C. Scullen and L. Lazauskas (2002) 'Wave Patterns and Minimum Wave Resistance for High-Speed Vessels' *24th Symposium on Naval Hydrodynamics, Fukuoka, Japan*
- [172] E. O. Tuck (2004) 'Computation and Minimisation of Ship Waves' *Applied Mathematics Entering the 21st Century: Invited Talks from the ICIAM 2003 Congress*

## References

- [173] J. K. E. Tunaley, E. H. Buller, K. H. Wu and M. T. Rey (1991) 'The simulation of the SAR image of a ship wake' *IEEE Transactions on Geoscience and Remote Sensing* (vol. 29, no. 1, pp. 149-156)
- [174] J. K. E. Tunaley, J. R. Dubois and J. B. A. Mitchell (1989) 'The Radar Image Of The Turbulent Wake Generated By A Moving Ship' *12th Canadian Symposium on Remote Sensing Geoscience and Remote Sensing Symposium*, Vancouver, Canada (pp. 343-346)
- [175] USN (1998) 'Navy electricity and electronics training series – Modulation' (Naval Education and Training: Professional Development and Technology Centre)
- [176] Veneziani and R. Vitulli (1995) 'Sub-aperture Doppler rate estimation and SAR data focalization' *1995 International Geoscience and Remote Sensing Symposium, IGARSS '95. Quantitative Remote Sensing for Science and Applications*, Firenze, Italy (vol.3, pp. 2292-2294)
- [177] V. T. Vu, T. K. Sjogren and M. I. Pettersson (2013) 'Fast time-domain algorithms for UWB bistatic SAR processing' *IEEE Transactions on Aerospace and Electronic Systems* (vol. 49, no. 3, pp. 1982-1994)
- [178] J. L. Walker (1980) 'Range-Doppler imaging of rotating objects' *IEEE Transactions on Aerospace and Electronic Systems* (vol. AES-16, no. 1, pp. 23-52)
- [179] Walker (2001) 'Doppler modelling of radar sea clutter' *IEE Proceedings - Radar, Sonar and Navigation* (vol. 148, no. 2, pp. 73-80)
- [180] Wang, L. Zhen and Y. Guan (2010) 'Novel space-time processing method for airborne SAR to detect and image the slowly moving targets' *IEEE International Conference on Computational Science and Optimization* (28-31 May 2010, Huangshan, Anhui, vol. 2, pp. 435-439)

## References

- [181] Wang, Z. Xu, M. Zhang and C. Chen (2013) 'Effects of ionospheric high-order dispersion and multiple scattering on space-based SAR imaging' *IET International Radar Conference* (14-16 Apr 2013, Xi'an, pp. 1-4)
- [182] K. D. Ward (1989) 'Radar imaging of ships at sea' *IEEE Colloquium on SAR* (pp. 7/1-7/5)
- [183] K. Ward, R. J. A. Tough and S. Watts (2006) 'Sea Clutter: Scattering, the K Distribution and Radar Performance' (IET: London)
- [184] K. D. Ward and R. D. Hill (2018) 'Notes on SAR imagery of the Kelvin Wake using the Thin Ship model' (Igence Radar Ltd.: Malvern, UK – from personal correspondence)
- [185] Watson, R. D. Chapman and J. R. Apel (1992) 'Measurements of internal wave wake of a ship in highly stratified sea loch' *Journal of Geophysical Research* (vol. 97, no. C6, pp. 9689-9703)
- [186] S. Watts, K. D. Ward and R. J. A. Tough (2005) 'The physics and modelling of discrete spikes in radar sea clutter' *IEEE International Radar Conference, 2005.*, Arlington, VA (pp. 72-77)
- [187] G. Weinblum (1959) 'Application of Wave Resistance Theory to Problems of Ship Design' *Technische Universität Hamburg-Harburg, Hamburg* (no. 1244)
- [188] S. Werness, W. Carara, L. Joyce and D. Franczak (1990) 'Moving target imaging algorithm for SAR data' *IEEE Transactions on Aerospace and Electronic Systems* (vol. 26, no. 1, pp. 57-67)
- [189] W. C. S. Wigley (1926) 'Ship wave resistance. A comparison of mathematical theory with experimental results' *Transactions of the Institute of Naval Architects* (vol. 68, pp. 124-137)

## References

- [190] A. Wiley (1985) 'Synthetic aperture radars: A paradigm for technology evolution' *IEEE Transactions on Aerospace and Electronic Systems* (vol. AES-21, no. 3, pp. 440-443)
- [191] Z. Wu (1991) 'On the estimation of a moving ship's velocity and hull geometry information from its wave spectra' (Defence Technical Information Centre: Vancouver)
- [192] K. h. Wu and M. R. Vant (1985) 'Extensions to the Step Transform SAR Processing Technique' *IEEE Transactions on Aerospace and Electronic Systems* (vol. AES-21, no. 3, pp. 338-344)
- [193] Yang, B. Li, L. Chen, C. Wei, Y. Xie, H. Chen and W. Yu (2017) 'A Spaceborne Synthetic Aperture Radar Partial Fixed-Point Imaging System Using a Field- Programmable Gate Array—Application-Specific Integrated Circuit Hybrid Heterogeneous Parallel Acceleration Technique' *Sensors (Basel)*. (vol. 17(7), no. 1493)
- [194] Tat Soon Yeo, Ngee Leng Tan, Cheng Bo Zhang and Yi Hui Lu (2001) 'A new subaperture approach to high squint SAR processing' *IEEE Transactions on Geoscience and Remote Sensing* (vol. 39, no. 5, pp. 954-968)
- [195] T. Yoshida (2012) 'SAR signal simulation in time domain for velocity bunching by ocean wave' *EUSAR 2012; 9th European Conference on Synthetic Aperture Radar*, Nuremberg, Germany, (pp. 466-469)
- [196] Z. Yueting, D. Chibiao, Y. Hongjian and Q. Xiaolan (2009) 'The effects of multi-path scattering on the SAR image of cylindrical cavity' *IEEE International Geoscience and Remote Sensing Symposium (IGARSS)* (vol. 4, pp. 609-612)

## References

- [197] S. Zhang, W. Zheng and L. Kong (2010) 'SAR Raw Signal Simulation Based on Sub-aperture Processing' *IEEE National Radar Conference - Proceedings*
- [198] J. Zhang, J. Xu, Y. Peng and X. Wang (2005) 'Speckle filtering of SAR images based on sub-aperture technique and principal component analysis' *IEEE International Symposium on Communications and Information Technology, 2005. ISCIT 2005.*, Beijing (pp. 1217-1222)
- [199] Zilman, A. Zapolski and M.Marom (2014) 'SAR imaging of ship wakes and inverse ship wake problem' (<http://www.iwwwfb.org>)
- [200] Zilman, A. Zapolski and M.Marom (2004) 'The speed and beam of a ship from its wake's SAR images' *IEEE Transactions on Geoscience and Remote Sensing* (vol. 42, no. 10, pp. 2335-2343)